Evolution of the Tonga-Kermadec forearc in response to seamount subduction

FUNNELL, MATTHEW,JAMES

Evolution of the Tonga-Kermadec forearc in response to seamount subduction

Matthew James Funnell

Department of Earth Sciences

Durham University

A thesis submitted for the degree of

Doctor of Philosophy

August 2017

Software used:
This thesis was written using LaTeX. The references and citations were produced using BibTeX. *Seismic Unix (Stockwell, 1999; 2011)* was used in conjunction with *GLOBE Claritas*^{TM} to process and manipulate seismic data prior to plotting. All figures were plotted using *Generic Mapping Tools (GMT)*, written by Wessel & Smith (1991; 1995; 1998). *Adobe Illustrator* was used for image conversion and manipulation post-plotting.

Abstract

Subducting plate characteristics are recorded as temporal variations in overriding plate deformation. Downgoing bathymetric anomalies superimpose enhanced tectonic erosion on pre-existing forearc crustal and sedimentary structural variations. Existing models of inherited forearc crustal structure along the Tonga-Kermadec subduction system are simplistic and neglect along-strike variability, which has resulted in a limited understanding of margin evolution and Louisville Ridge seamount chain (LRSC) subduction.

In this study, robustly tested, velocity-depth and density-depth models are synthesised with existing data from the Tonga-Kermadec margin to reveal along-strike variations in the subducting and overriding plate structure. In regions north and south of the point of LRSC subduction, the incoming Pacific plate displays >2 km-throw bend faults and reduced seismic velocity throughout the crust and upper mantle by ∼1.0 km s^{-1} and ∼0.5 km s^{-1}, respectively. Around the LRSC-trench intersection, the trench axial depth decreases by 4 km and normal fault throw is reduced to <1 km, suggesting the seamounts reduce subducting plate deformation. The forearc structure is dominated by the extinct (∼51 Ma) Tonga arc, defined by a high velocity (7.0-7.4 km s^{-1}) and density (3.30 ± 0.10 g cm^{-3}) lower crustal anomaly. Increases in Tonga-Kermadec forearc crustal thickness from 12 to >18 km over 300 km along-strike are coincident with variations in bathymetry and free-air gravity anomaly that reveal a broader trend of northward-increasing crustal thickness between 18°S and 32°S, predating LRSC subduction at the margin. Beyond this region, the overriding crust formed as the south Fiji Basin opened ∼35 Ma. Within this framework of existing crustal structure, LRSC subduction promotes erosion of the overriding crust, forming a steep unstable lower-trench slope. Following seamount subduction, trench-slope stability is re-established by the collapse of the extinct Tonga arc, suggesting that seamount subduction commenced at 22°S along the margin.

Declaration

This thesis describes my original work except where acknowledgement is made in the text. It does not exceed the word limit and is not substantially the same as any work that has been, or is being, submitted to any other university for any degree, diploma, or any other qualification.

Matthew James Funnell
August 2017

Acknowledgements

My thanks go first and foremost to Christine, your guidance and encouragement since I first joined the project has been inspiring and truly invaluable. This thesis would certainly not be the product it is today without your support and keen eye for typographical errors. I would also like to thank Richard for his continuing guidance and support, and for always providing interesting points for discussion. To Adam, thank you for living and surviving every moment of the PhD alongside me, and for always being there to discuss science no matter how relevant.

This research project was funded by the Natural Environmental Research Council (NERC) grant NE/F004273/1 (Peirce & Watts, 2011). I would like to thank all involved in the planning and acquisition of data during research cruise S0215, including the officers and crew of the R/V Sonne, the scientific party, and all seagoing technicians. The NERC Ocean-Bottom Instrumentation Facility (Minshull *et al.*, 2005) and GEOMAR provided the OBSs used in this project, and their technical support at sea.

I would like to thank the other members of the Postgraduate community in the department, for helping me to remain *relatively* sane, and always being able to provide a different outlook on science and broader life. In particular, 'Geophysics bay' (all members past and present) has provided a reliable source of entertainment and a continuous flow of strong, stimulating, ~~scientific discussion~~ coffee. I hope that, long after I have moved out, the coffee sessions continue to enable the group both socially and scientifically.

A huge thank you goes to all who have supported me, knowingly or not, through their friendship over the last four years: members of St. John's College, Group 13, all my friends across the country, and those even further afield. Thank you to my family, for encouraging me to follow this path and for always listening. Lastly, I thank Carys, for her never-ending support and belief in me.

This thesis is dedicated to Carys

Contents

List of Figures

List of Tables

List of abbreviations and acronyms

1D - One-dimensional
2D - Two-dimensional
3D - Three-dimensional
AGC - Automatic gain control
CMP - Common mid-point
CVA - Claritas^{TM} velocity analysis
CVG - Constant velocity gather
CVS - Constant velocity stack
FAA - Free air-anomaly
FAST - First Arrival Seismic Tomography
GEBCO - General bathymetric chart of the oceans
GMT - Generic Mapping Tools, written by Wessel & Smith (1991; 1995; 1998)
GPS - Global Positioning System
LRSC - Louisville ridge seamount chain
MCS - Multichannel seismic
NMO - Normal moveout
OBS - Ocean bottom seismograph
QC - Quality control
RMS - Root mean squared
SEG-D - Society of exploration geophysicists D-type file format
SEG-Y - Society of exploration geophysicists Y-type file format (Barry *et al.*, 1975)
SNR - Signal-to-noise ratio
SU - Seismic Unix (Stockwell, 1999; 2011)
TWTT - Two-way traveltime
VGG - Vertical gravity gradient
VSP - Vertical seismic profile
WA - Wide-angle
XBT - Expendable bathymetric thermograph
Phase arrivals:
$\mathbf{W_w}$ - Waterwave arrivals
$\mathbf{P_s}$ - Sediment P-wave refractions
$\mathbf{P_g}$ - crustal P-wave refractions
$\mathbf{P_mP}$ - Moho P-wave reflections
$\mathbf{P_n}$ - Mantle P-wave refractions

Chapter 1

Introduction and geological setting

1.1 Structure and evolution of subduction zones

Subduction zones are sites where oceanic lithosphere is recycled into the mantle. The oceanic lithosphere subducts at deep water trenches located in front of volcanic chains and, in the present-day global system, are predominantly focussed around the Pacific ocean (Figure 1.1). These zones are typically divided into two different types: accretionary, where more than 30% of the sediment cover is scraped from the top of the incoming plate and accumulates at the front of the overriding plate in an accretionary wedge; and erosional, where effectively all incoming sediment is subducted and the frontal region of the overriding plate crust is highly fractured and deformed (von Huene & Scholl, 1991; Lallemand *et al.*, 1994; von Huene *et al.*, 2004). The total length of the global subduction system is ∼43,500 km, comprising ∼19,000 km of strongly erosional margins, ∼8,200 km with an accretionary wedge, and ∼16,300 km that display a small accretionary wedge and are considered as intermediate margins (von Huene & Scholl, 1991). This makes erosional margins the most prevalent in the current global system.

Subduction processes result in a typical set of morphological features seaward of the trench. The incoming plate has a broad bathymetric high, known as the outer rise, which forms as a result of the bending and flexure it undergoes as it enters the trench. This shallower bathymetry is mirrored by a free air-anomaly (FAA) high (Figure 1.1; Watts & Talwani, 1974). As the incoming plate bends, large extensional stresses are generated throughout the top of the plate across the outer rise, forming normal faults (e.g. Aubouin, 1989; Naliboff *et al.*, 2013). This faulted oceanic plate is underthrust beneath the overriding plate along deep water trenches that can reach up to 11 km below sea surface (Taira *et al.*, 2005). Immediately arcward of the trench axis is either an accretionary wedge comprising sediments scraped from the

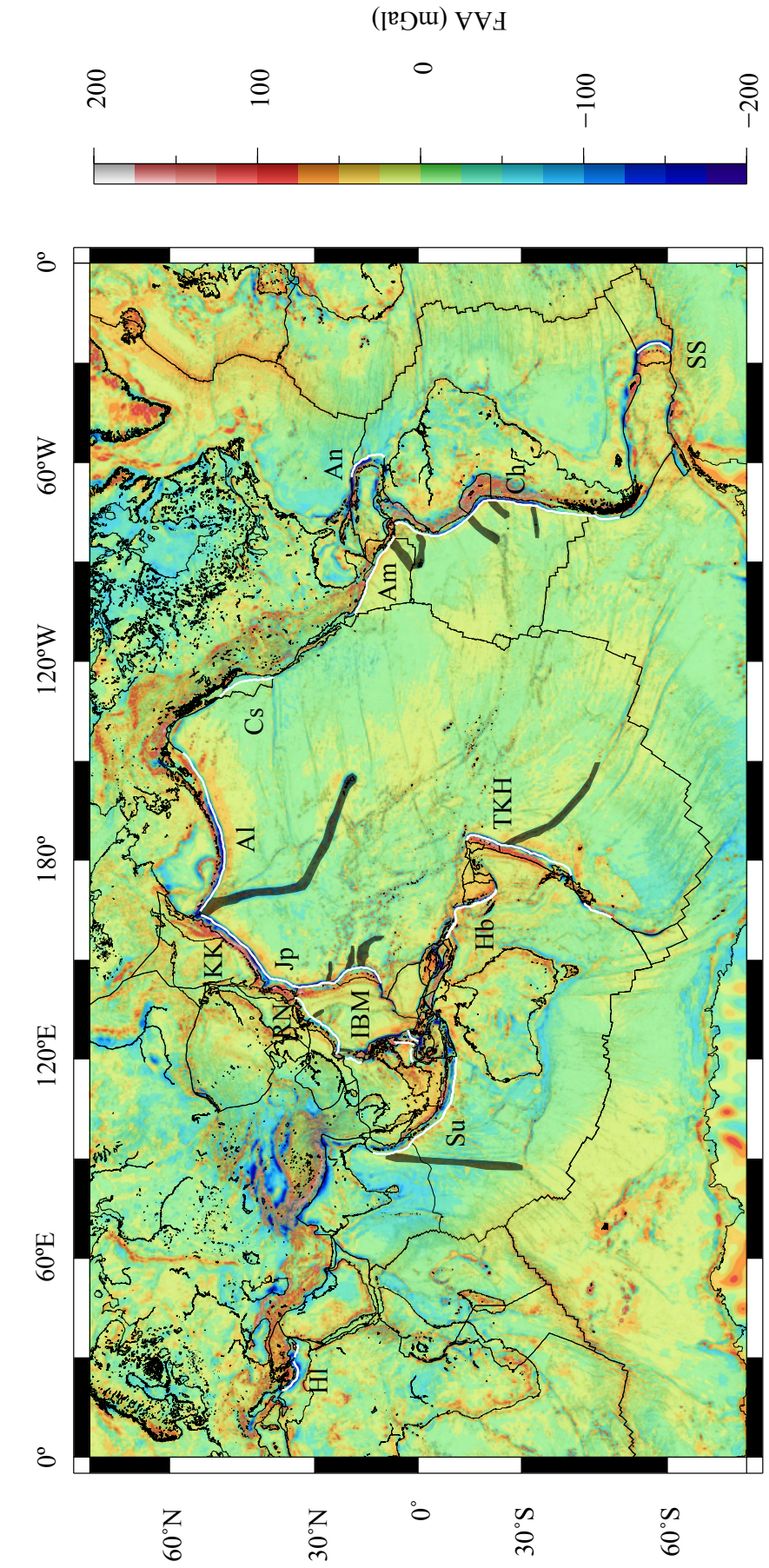

Figure 1.1: Global overview of subduction zones and subducting bathymetric anomalies. Free air-anomaly (FAA) map, overlain with plate boundaries (thin black lines), highlighting major subduction system trenches (white lines), and significant bathymetric anomalies intersecting with subduction systems (thick black lines). Major trenches are labelled with short names for clarity, including: Al - Aleutian, Am - American, An - Antilles, Ch - Chile, Cs - Cascadia, Hb - New Hebrides, Hl - Helenic, IBM - Izu-Bonin-Mariana, Jp - Japan, KK - Kuril-Kamchatka, RN - Ryukyu-Nankai, Su - Sumatra, SS - South Sandwich, TKH - Tonga-Kermadec-Hikurangi.

incoming plate, or steep, poorly sedimented, and highly deformed crustal blocks. The predominant controls on the presence and volume of an accretionary wedge are the quantity of incoming sediment and the rate of subduction (Clift & Vannucchi, 2004). Behind the frontal region of the overriding plate, more structurally consolidated crust forms the forearc and arc, which are morphologically prominent ridges often parallel to their deep water trenches. Along the active volcanic arc new material is generated, with intrusives locally increasing crustal volume, and extrusives distributed as sedimentary material to the surrounding basins through volcanic eruptions and mass wasting. Backarc basins are present behind some volcanic arcs, opening in response to the relative seaward migration of the trench, and generally separating an older extinct volcanic backarc from the currently active arc.

Subduction alters the downgoing and overriding plates over a range of timescales. Forearcs generally evolve and deform in response to changes in the rate, angle and obliquity of subduction, as well as the strength and roughness of the subducting plate (Dickinson & Seely, 1979; von Huene & Scholl, 1991). Variations in these characteristics are manifest in physical properties, including the dominant stress regime and seismicity (Bonnardot *et al.*, 2007; Ide, 2013; Schellart & Rawlinson, 2013; Nishikawa & Ide, 2014), the rate of frontal and basal erosion (Clift & Vannucchi, 2004; von Huene *et al.*, 2004), and other crustal deformation processes (Lallemand *et al.*, 1992; Martinod *et al.*, 2005; Sallarès & Ranero, 2005). Such variations in subduction characteristics are recorded in the island arc-backarc systems over time as changes in the sedimentary and crustal structures observed on the overriding plate (Dickinson & Seely, 1979; von Huene & Scholl, 1991; Reagan *et al.*, 2013). Although trench proximal regions of the overriding plate at erosive margins are predominantly controlled by the deformation and removal of material, new crust and sedimentary material is generated and distributed from the active arcs into the surrounding basins (Clift *et al.*, 1994; Suyehiro *et al.*, 1996; Clift *et al.*, 1998; Holbrook *et al.*, 1999). Forearcs continually evolve in response to these erosive and constructive processes, often generating significant variation in structure not only between different subduction systems (Ide, 2013; Schellart & Rawlinson, 2013), but also along individual margins (e.g. Larter *et al.*, 2003; Calvert *et al.*, 2008; Kodaira *et al.*, 2010; Bassett & Watts, 2015b). Of the controls on overriding plate deformation and evolution, perhaps the most poorly understood is the subduction of seamounts and aseismic ridges.

1.2 Seamount and aseismic ridge subduction

Seamounts, which are typically defined in plan view as sub-circular bathymetric highs, pervade the global seafloor with >200,000 estimated to exist throughout the oceans with a height of 0.1-6.7 km above seafloor (Hillier, 2007; Hillier & Watts, 2007). These bathymetric anomalies vary in size, in crustal and sub-crustal structural support, and in geochemical composition (Richards *et al.*, 2013), but are characterised as discrete features that may either be part of a chain (e.g. Watts, 1978; Lonsdale, 1988; Kaneda *et al.*, 2010) or completely isolated (e.g. Dominguez *et al.*, 1998b; Huhnerbach *et al.*, 2005; Oakley *et al.*, 2007; Hirano *et al.*, 2008). In contrast, aseismic ridges are continuous bathymetric highs that tend to cover larger areas of the seafloor and predominantly form at intra-plate hotspots. These features can either maintain a relatively constant depth and along-ridge structure, such as the Cocos Ridge (Walther, 2003), or consist of a continual chain of bathymetically isolated seamounts that are located on a less prominent ridge of thickened oceanic crust, such as the Hawaiian-Emperor seamount chain (Watts, 1978). Aseismic ridges vary in size from <10 to ∼500 km-wide, and can be thousands of kilometres long (e.g. Lonsdale, 1988; Dominguez *et al.*, 1998a; Walther, 2003).

Such bathymetrically anomalous features subduct at most subduction systems (Figure 1.1). They are proposed to influence inter-plate seismicity (Kelleher & McCann, 1976; Habermann *et al.*, 1986; Wang & Bilek, 2014), control overriding plate deformation (Dominguez *et al.*, 1998b; Wang & Bilek, 2011; Zeumann & Hampel, 2015), and can alter the shape of the margin (Vogt, 1973; Lallemand *et al.*, 1992). Early studies into seamount subduction proposed that seamounts act as strong asperities within the subduction interface, generating large earthquakes as they shear from the downgoing plate along a zone of inherent internal weakness (Cloos, 1992; Cloos & Shreve, 1996; Figure 1.2). Scholz & Small (1997) suggested that shearing is unlikely and, instead, seamounts tend to subduct whole and are accommodated by the flexure of the overriding crust, effectively increasing the local interplate coupling to generate large but irregular earthquakes (Scholz & Campos, 1995). More recent research observed that subducting seamounts tend to generate radial faulting patterns as well as normal and thrust faults throughout the accretionary wedge (Dominguez *et al.*, 1998b; Bell *et al.*, 2010), which led to the proposal that seamounts are predominantly accommodated through extensive faulting and fracturing of the overriding plate (Figure 1.2), generating only small earthquakes or subducting completely aseismically (Dominguez *et al.*, 2000; Wang & Bilek, 2011; 2014). This most recent theory is only generally applied to the subduction of isolated seamounts at heavily sedimented margins, and does not consider the effect on more structurally

robust erosive margins or the subduction of broader as well as more long-lived aseismic ridges.

As aseismic ridges subduct they are observed to alter the nature and magnitude of bend-related faulting of the incoming oceanic crust and significantly deform the overriding plate (Dominguez *et al.*, 1998a; Grindlay *et al.*, 2005; Ranero *et al.*, 2005; Rosenbaum & Mo, 2011). Analogue modelling of subducting aseismic ridges suggests that these relatively strong and buoyant ridges reduce the downgoing slab dip locally, exerting a strong control on the morphology of the trench where subduction is oblique to the margin (Martinod *et al.*, 2005; 2013). These results are generally supported by numerical models that also predict significant uplift and deformation of the frontal region of the overriding plate as ridges subduct (Figure 1.2), with the effect on erosive or accretionary margins being comparable, except for the inherent strength of the overriding material implying a likely difference in deformation style (Zeumann & Hampel, 2015; 2016). Observations and models of aseismic ridge subduction typically neglect the effect of morphological complexities, or seamounts combined with the ridges, on the deformation of the overriding plate.

1.3 Current questions

Considerable variability between and within subduction systems is thought to be controlled by the changing nature of the subducting crust, including the amount of sediment cover, convergence obliquity, subducting plate age, extent of faulting, and the presence of bathymetric anomalies. Generally, subduction systems are classified according to whether they display dominant accretive or erosive processes, forming either broad prisms of accreted sedimentary material or steep and highly irregular trench slopes at the front of the overriding plate. At erosive margins, typically located further from land and therefore less well studied, the processes governing forearc evolution and structural variability along strike are poorly understood. In particular, seamount and aseismic ridge subduction is a process that is spatially limited and relatively uncommon along the total length of the global subduction system and, although widely documented and modelled at accretionary margins, is poorly constrained along erosive systems. Consequently, the nature of seamount subduction process at erosive margins requires further research, in particular focussing on how they actively interact with and deform the overriding plate, and whether the forearc recovers following seamount subduction. Before it is possible to ascertain a more detailed understanding of how seamounts subduct at erosive margins, it is

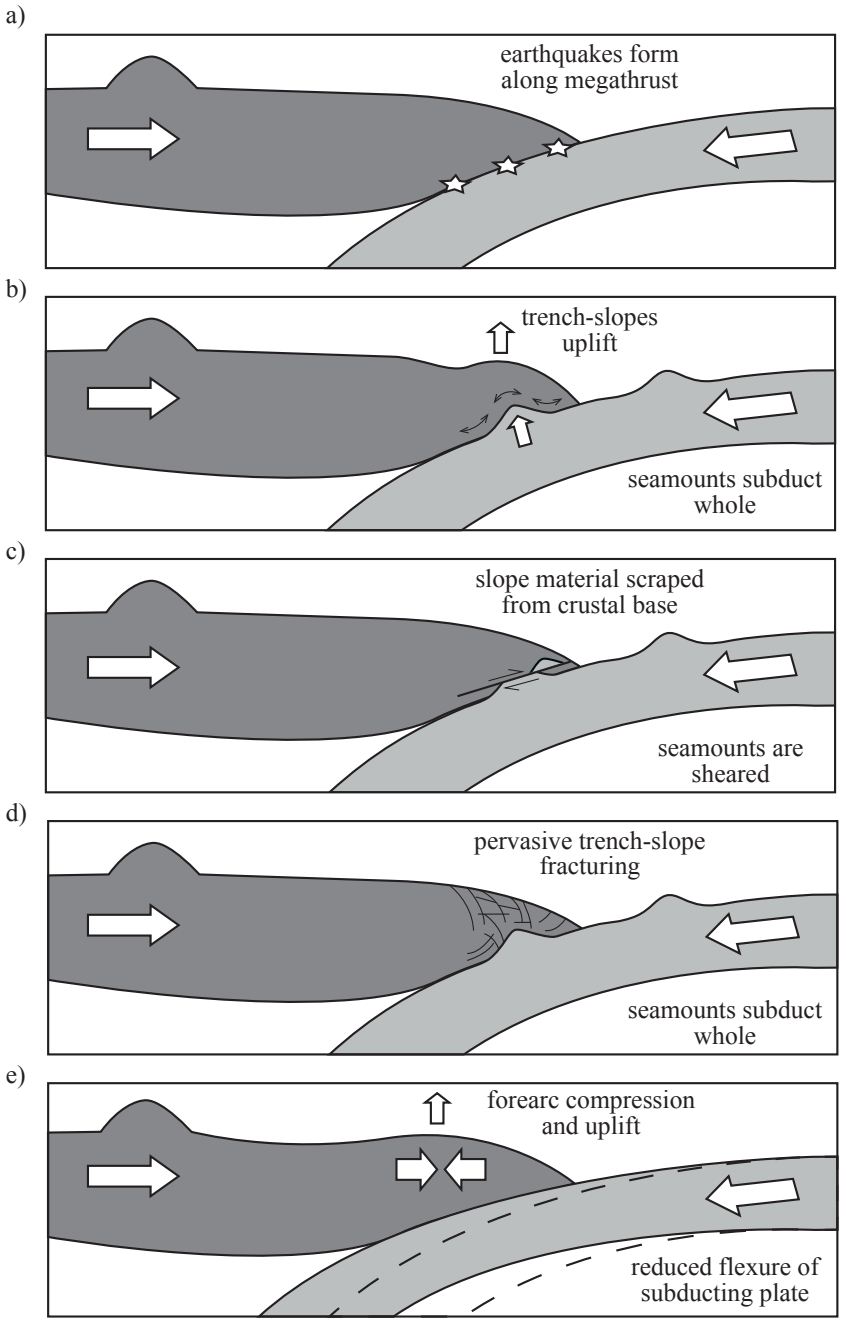

Figure 1.2: Schematic diagrams of seamount and aseismic ridge subduction models. a) Simple model depicting typical oceanic crustal subduction. b) Model of overriding plate flexure as a seamount subducts, locally increasing stress and seismic coupling (Scholz & Campos, 1995; Scholz & Small, 1997). c) Seamount shear model, where seamount summits are incorporated into the overriding plate (Cloos, 1992; Cloos & Shreve, 1996). d) Model of seamount subduction accommodated by fault and fracture networks (Wang & Bilek, 2011; 2014), based on observations at accretionary margins (Dominguez *et al.*, 1998a; 2000). e) Aseismic ridge subduction, with a broad reduction in plate flexure relative to typical subduction (dashed line), causing uplift and compression of the overriding plate (Martinod *et al.*, 2005; 2013; Zeumann & Hampel, 2015; 2016).

important to determine the significance of seamount subduction relative to steady-state processes acting on subduction systems and the natural variability in structure likely along a forearc.

This study aims to determine how overriding plates at erosive subduction systems evolve, in particular addressing the influence of seamount subduction on forearc structure. These aims can be considered through the following questions:

- What are the main features of a forearc, and where do they form?
- How do forearcs vary along a subduction system, and what are the primary controls on this variation?
- How do seamounts subduct at erosive margins?
- How does the effect of seamount subduction compare to other controls on overriding plate evolution, and which processes dominate long-term forearc structure?

These key questions can be primarily addressed by sampling a forearc at different points along a subduction zone to directly determine the major crustal features and structural variability. The resulting model of subduction system variation can be compared to the tectonic history and current subduction inputs to determine how specific features have formed and evolved over the lifetime of the margin. To address these questions, the Tonga-Kermadec subduction system was selected for a geophysical investigation into the effects of seamount subduction. The Tonga-Kermadec subduction system is the longest and most linear example of an erosive intra-oceanic margin (Figure 1.1). Seamount subduction is also a major process acting on the margin as the Louisville Ridge Seamount Chain (LRSC) is currently intersecting the trench and is widely proposed to have been subducting since at least 5 Ma. The linearity of the trench-oblique seamount chain results in the partitioning of the subduction system into regions where the LRSC has already subducted, where seamount subduction is ongoing, and a region where the LRSC has not yet subducted but is expected to in the future. Previous studies of the region have revealed a number of significant discontinuities and variable structures along-strike, but have been unable to conclusively determine an origin for them. Further, these features have generally been considered as isolated, so no margin-wide structural framework exists. As a result, the Tonga-Kermadec subduction system is an ideal location to study forearc variability, the importance of inherited structural features, and the control of seamount subduction on the evolution of a margin.

Although this setting provides an excellent opportunity to study seamount subduction at an erosive margin, it does not account for all possible variations in structure or different styles of anomalous bathymetric feature. Future studies at different margins, or more comprehensive research at the Tonga-Kermadec subduction system may reveal structures and controls that are not described or considered in this thesis.

1.4 Geological setting of the Tonga-Kermadec subduction zone

The ∼2700 km-long Tonga-Kermadec subduction system is a typical example of an erosive intra-oceanic margin, located in the southwest Pacific Ocean (Figure 1.3). West-dipping subduction along the trench initiated ∼51 Ma (Meffre *et al.*, 2012; Michibayashi *et al.*, 2016), with evidence of active volcanism at the Tonga, Lau-Colville, and Tofua-Kermadec arcs continually throughout the Eocene and to the present-day (Parson, 1992; Bloomer *et al.*, 1995). The onset of subduction at the Tonga-Kermadec subduction system is thought to be concurrent with that of the Izu-Bonin-Mariana margin (Ishizuka *et al.*, 2011; Reagan *et al.*, 2013); both margins displaying similar morphological structure described by an extinct frontal arc, active arc, and extinct backarc separated from the active system by a backarc basin (Figure 1.3). During subduction initiation, volcanism was focussed along the subaerial Tonga arc, which now forms the extinct forearc ridge (Figure 1.3; Wright *et al.*, 2000; Meffre *et al.*, 2012). Between 45 and 34-32 Ma, active volcanism migrated to the Lau-Colville arc, and the arc system rapidly subsided to ∼3 km below sea level, tilting sediments trenchward (Parson, 1992; Clift & MacLeod, 1999). Volcanism along the Lau-Colville ridge continued until ∼17 Ma, as the subduction system migrated eastward and rotated anticlockwise causing the South Fiji Basin to open (Parson, 1992; Herzer *et al.*, 2011; Bassett *et al.*, 2016). An erosional unconformity and arcward tilting of forearc sediments at this time is associated with the subduction of a seamount (MacLeod, 1994; Clift & MacLeod, 1999). By ∼5.5 Ma volcanism had ceased along the Lau-Colville ridge and, following a 2 Myr hiatus as the Lau Basin and Havre Trough began to open (Malahoff *et al.*, 1982; Taylor *et al.*, 1996; Ruellan *et al.*, 2003), volcanism restarted to form the currently active Tofua-Kermadec arc (Clift *et al.*, 1994; Bloomer *et al.*, 1995). Since the onset of backarc basin opening ∼5.5 Ma, the northern Lau Basin has undergone the greatest rates of spreading to form an ∼500 km-wide basin with complex microplate structure in the north, and a much narrower basin (∼150 km) to the south (Zellmer & Taylor, 2001; Conder

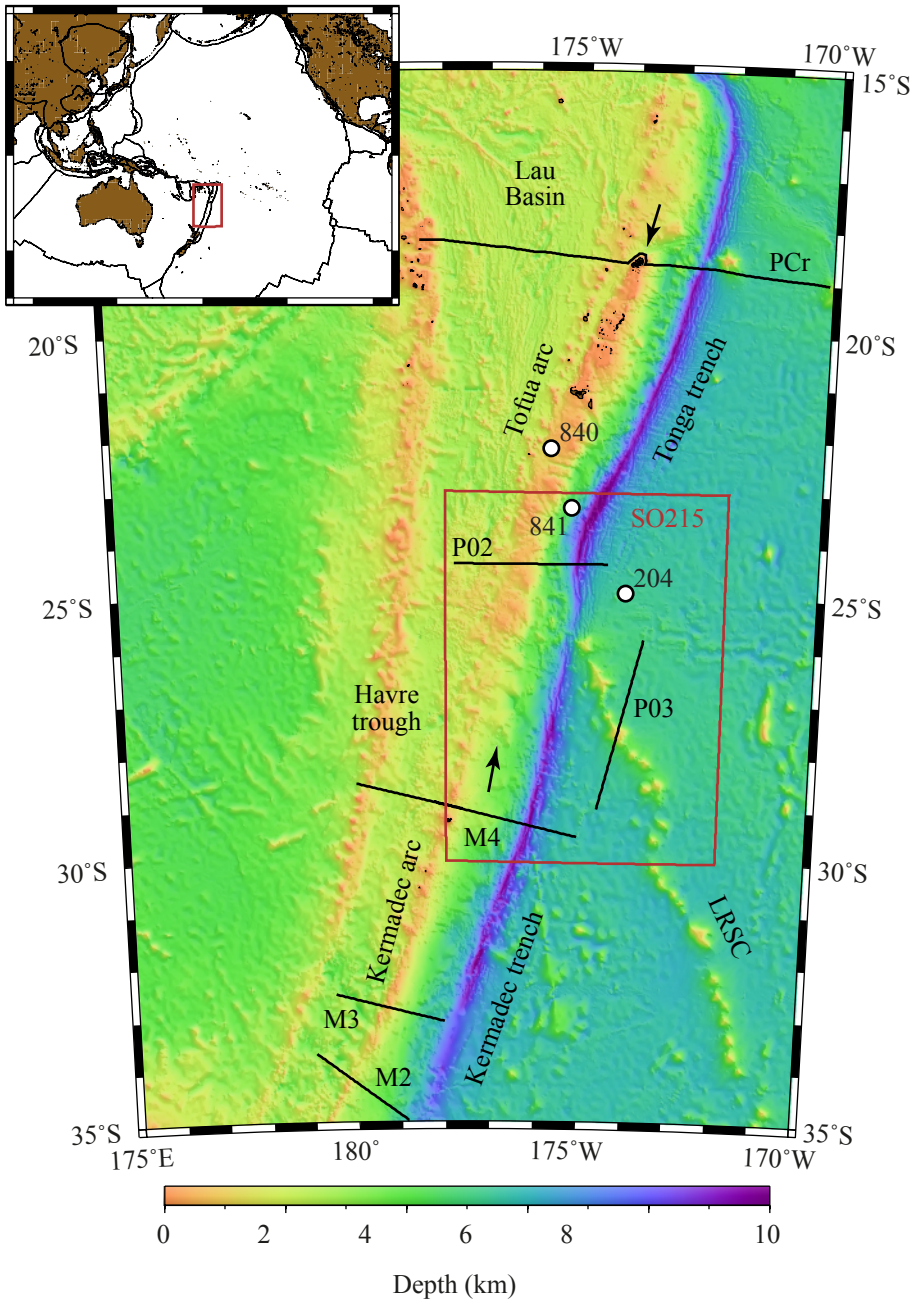

Figure 1.3: Geological setting of the Tonga-Kermadec subduction system. Black arrows indicate the extent of the bathymetrically expressed extinct Tonga arc (18-28°S). Major geophysical and geological datasets acquired along the Tonga-Kermadec subduction system and northwestern end of the LRSC are indicated. Profiles P02 and P03 were acquired during R/V Sonne cruise SO195 (TOTAL), Profiles M2, M3, and M4 during cruise SO192 (MANGO), and PCr during the R/V Melville WESTWARD cruise (Crawford *et al.*, 2003). DSDP borehole 204, and ODP holes 840 and 841 are indicated as white circles. The red box indicates the primary study region of cruise SO215. The inset map shows the location of the Tonga-Kermadec subduction zone region.

& Wiens, 2011). The subduction of the LRSC is proposed to have initiated 5-4 Ma (Lallemand *et al.*, 1992; Ruellan *et al.*, 2003) or >7 Ma (Timm *et al.*, 2013), based on the tectonic history of the Lau Basin and the expected volcanic recycling times of subducted material, respectively. Regardless, the seamount chain is widely agreed to have been subducting since 5 Ma, and is associated with an increase in the trenchward rotation of the forearc at ODP site 841 between 1.5-0 Ma (Figure 1.3; MacLeod, 1994; Clift & MacLeod, 1999). Today, the Tofua-Kermadec arc trends parallel to the strike of the Tonga-Kermadec trench, with the Lau-Colville ridge separated from the active arc by the backarc basin, and the initial Tonga arc forming the extinct forearc ridge (Figure 1.3).

The oceanic plate currently subducting along the Tonga-Kermadec trench formed at the intermediate-slow Osbourn spreading centre prior to 90 Ma (Billen & Stock, 2000; Downey *et al.*, 2007). As this plate bends and subducts to the west (DeMets *et al.*, 2010), large extensional faults form parallel to the trench throughout the crust and upper mantle (Pelletier & Dupont, 1990; Contreras-Reyes *et al.*, 2011). Comparable normal extensional faults are observed at other trenches, such as Chile and Costa Rica (Figure 1.1), and are attributed with increasing the hydrothermal circulation, actively hydrating and serpentinising the crust and upper mantle (Ranero *et al.*, 2003; Ivandic *et al.*, 2010; Moscoso & Grevemeyer, 2015; Korenaga, 2017). These physical and chemical alterations weaken the plate, reducing the flexural rigidity (Billen & Gurnis, 2005; Arredondo & Billen, 2012).

Currently intersecting with the Tonga-Kermadec trench at ∼26°S, the LRSC is an ∼4300 km-long ridge of seamounts that formed as the Pacific plate migrated over the Louisville hotspot through the Late Cretaceous and Cenozoic (Lonsdale, 1988; Castillo *et al.*, 2009; Koppers *et al.*, 2011; Vanderkluysen *et al.*, 2014). At the northwestern end of the extant chain, the typically >3 km high seamounts formed shortly after the oceanic crust (Watts *et al.*, 1988). This young host-plate age (<10 Myr) is proposed to have enabled the shallow intrusion of the mafic-ultramafic magmatic material within the seamount edifices, and also prevented significant thickening or magmatic underplating of the surrounding crust (Contreras-Reyes *et al.*, 2010; Richards *et al.*, 2013). During their emplacement, large volumes of volcaniclastic material were erupted and distributed over the surrounding region (Koppers *et al.*, 2011; Vanderkluysen *et al.*, 2014), supplementing the <200 m of sediment cover that is typically observed in the southwest Pacific ocean today (e.g. at DSDP site 204; Burns & Andrews, 1973).

Along the Tonga-Kermadec subduction system, the structure of the overriding plate varies perpendicular and parallel to the trench (Figure 1.3). The steeply dip-

ping (>10°) lower-trench slope is characterised by <0.1 km sediment cover and extensive fracturing and faulting that results in a highly irregular seabed and basement morphology (Karig, 1970; Ballance *et al.*, 1999). Further west, the mid-trench slope is predominantly observed with an ∼25 km-wide basin, that accumulates sedimentary material as it is transported away from the volcanic arc and towards the trench (Ballance *et al.*, 1999; Wright *et al.*, 2000; Funnell *et al.*, 2014). Proximal to the present-day LRSC-trench intersection at ∼26°S, the lower- and mid-trench slopes are even more deformed and irregular, with the mid-slope basin reducing in width or being completely absent (Figure 1.3; Contreras-Reyes *et al.*, 2011; Stratford *et al.*, 2015). Pervasive normal faulting observed in drill cores from the lower-trench slope at ODP site 841 (Clift *et al.*, 1994), and remarkably low seismic velocities (3.5-4.0 km s^{-1}) up to 5 km below the seafloor (Contreras-Reyes *et al.*, 2011; Stratford *et al.*, 2015; Bassett *et al.*, 2016), suggest that subduction erosion dominates the lower-trench slope and causes it to undergo extension (von Huene & Ranero, 2003; von Huene *et al.*, 2004; Sallarès & Ranero, 2005). Arcward of the mid-trench slope, the overriding plate is either defined by a steep upper-trench slope and forearc ridge or a broad concave-up forearc basin. At the northern end of the subduction system, between 18°S and ∼28°S, the forearc ridge is the bathymetrically expressed extinct Tonga arc that was active from 51 Ma (Ballance *et al.*, 1999; Wright *et al.*, 2000; Crawford *et al.*, 2003; Contreras-Reyes *et al.*, 2011). The morphological expression of the volcanic arc reduces in prominence to the south and, at 28°S, gives way to an ∼2 km-deeper, broad, sediment-filled forearc basin (Karig, 1970). Active volcanism along the Tofua and Kermadec arcs, 170-200 km west of their trenches (Figure 1.3), generates and distributes volcaniclastic material into the surrounding forearc and backarc basins (Karig, 1970; Gillies & Davey, 1986). Most of this volcanic activity occurs along prominent ridges; however, south of ∼32°S, volcanism has migrated west of the bathymetric ridge and into the deep backarc basin at the south of the Havre Trough. The Lau Basin and Havre Trough are currently opening, with the greatest spreading rates observed in the north, resulting in the funnel-shaped backarc basin with highly complex plate structure in the northern Lau Basin (Zellmer & Taylor, 2001; Ruellan *et al.*, 2003; Conder & Wiens, 2011). Along the Tonga-Kermadec subduction system there are three major changes in structure of the overriding plate that demarcate significant tectonic boundaries: the 32°S Discontinuity; the LRSC-trench intersection at ∼26°S; and, the Fonualei Discontinuity at 18°S.

At 32°S, the forearc, which displays a broad basin to the north, increases in depth by ∼0.5 km southwards. The trench slopes also change from a dominant

erosive regime to accretionary (Pelletier & Dupont, 1990), documented to coincide with a marked change in the structure of the subducting plate, displaying >1.5 km vertical throw horst and graben and an up to 10 km deep trench in the north compared to <0.2 km throw normal faults and <8 km axial trench depth in the south (Figure 1.3). Pelletier & Dupont (1990) ascribed the changes in forearc structure to the dominant erosive or accretionary processes acting on either side of the 32°S Discontinuity, proposing the maximum observed depth of the subducting oceanic plate as the primary control (∼550 km to the north, <350 km to the south). Collot & Davy (1998b) alternatively proposed that the boundary indicates the initial point of Hikurangi Plateau subduction, which is currently intersecting the trench south of 36°S, and more recently Bassett *et al.* (2016) suggested that this discontinuity marks the southern extent of the extinct Tonga arc.

Further north, at ∼26°S, the LRSC intersects the trench, enhancing subduction erosion of the overriding plate (Ballance *et al.*, 1989), and significantly reducing inter-plate seismicity (Bonnardot *et al.*, 2006; 2007). At the LRSC-trench intersection, the trench axis shallows by 4 km (from ∼10 km) relative to regions of typical subduction (Figure 1.3; Lonsdale, 1986; Ballance *et al.*, 1989). Arcward of the present-day LRSC-trench intersection, the steep lower-trench slope displays extensive normal faulting and a highly irregular morphology, appearing to also encompass the frontal region of what is typically the stable mid-slope basin (Contreras-Reyes *et al.*, 2011; Stratford *et al.*, 2015). Increased tectonic erosion following the subduction of the seamount chain is attributed with removing significant quantities of overriding plate material, causing the trench axis to migrate ∼80 km west (Clift & MacLeod, 1999), and form the deepest part of the trench (10.87 km at Horizon Deep Bight; Ballance *et al.*, 1989).

A tectonic boundary at 18°S is manifest as a less prominent aseismic discontinuity than that observed arcward of the LRSC (Bonnardot *et al.*, 2006; 2007) and an ∼2 km-deep canyon through the forearc (Figure 1.3). This boundary, termed the Fonualei Discontinuity by Bonnardot *et al.* (2007), occurs at the northern extent of the bathymetrically expressed Tonga ridge (Wright *et al.*, 2000; Crawford *et al.*, 2003), and separates older dredged rock samples (<51 Ma) to the south, from younger (<35 Ma) samples in the north (Meffre *et al.*, 2012). In the backarc, complex microplate structure is observed north of the boundary, and the Fonualei Rift terminates at the discontinuity (Zellmer & Taylor, 2001; Ruellan *et al.*, 2003; Conder & Wiens, 2011). The greatest density of earthquakes along the Tonga-Kermadec subduction system occurs at the very northern end of the Tonga trench, ∼15°S, where the Pacific plate tears (Bonnardot *et al.*, 2007).

1.4.1 Existing regional datasets

Initial geophysical studies of the Tonga-Kermadec subduction system (e.g. Raitt *et al.*, 1955; Brodie & Hatherton, 1958; Talwani, 1961) were conducted prior to the application of plate tectonic theory to subduction zones (Wilson & Burke, 1972), but revealed basic variations in crustal structure across the trench, and variability in the overriding plate along the margin. Since then, local geophysical studies have focussed on specific features such as LRSC subduction (Ballance *et al.*, 1989), the 32°S boundary (Ballance *et al.*, 1999), and the north Tonga arc structure (Crawford *et al.*, 2003). More recent large-scale projects, such as MANGO (Flueh & Kopp, 2007; Schwarz-Schampera, 2007), which investigated the southern Kermadec arc structure, and TOTAL (Grevemeyer & Flueh, 2008), which independently explored the Tonga forearc and the structure of individual seamounts of the LRSC, have provided high quality datasets that reveal variations in crustal and upper mantle structure (Figure 1.3).

1.5 Cruise SO215

In collaboration with the German TOTAL group, the UK's Natural Environment Research Council funded a research cruise aboard the R/V Sonne that took place between 25th April and 11th June 2011, sailing from Auckland, New Zealand, to Townsville, Australia (Peirce & Watts, 2011). During cruise SO215, five integrated geophysical profiles were acquired in the vicinity of the intersection between the Tonga-Kermadec subduction system and the LRSC (Figures 1.3 and 1.4).

Wide-angle (WA), and multichannel seismic (MCS), gravity, magnetic, and bathymetry data were acquired coincidently along Profiles A, B, C, and G. No ocean bottom seismographs (OBSs) were deployed along Profile D, so the profile has no associated WA seismic dataset (Figure 1.4). Expendable bathymetric thermographs (XBTs) were deployed to determine the sound-velocity profile of the water column to a maximum depth of 1800 m below sea surface at a number of discrete locations on each profile during OBS deployment. In addition to the data acquired along the main profiles, multibeam bathymetry data were acquired throughout the cruise to improve regional coverage. The observation of active volcanism at the Monowai volcanic centre led to a repeat swath survey of the volcano, as indicated by the dense region of grey tracklines near 26°S 177°W on Figure 1.4 (Watts *et al.*, 2012). Gravity measurements were made continuously, port-to-port, to enable the gravity data acquired at sea to be tied with the absolute gravity base stations. A more

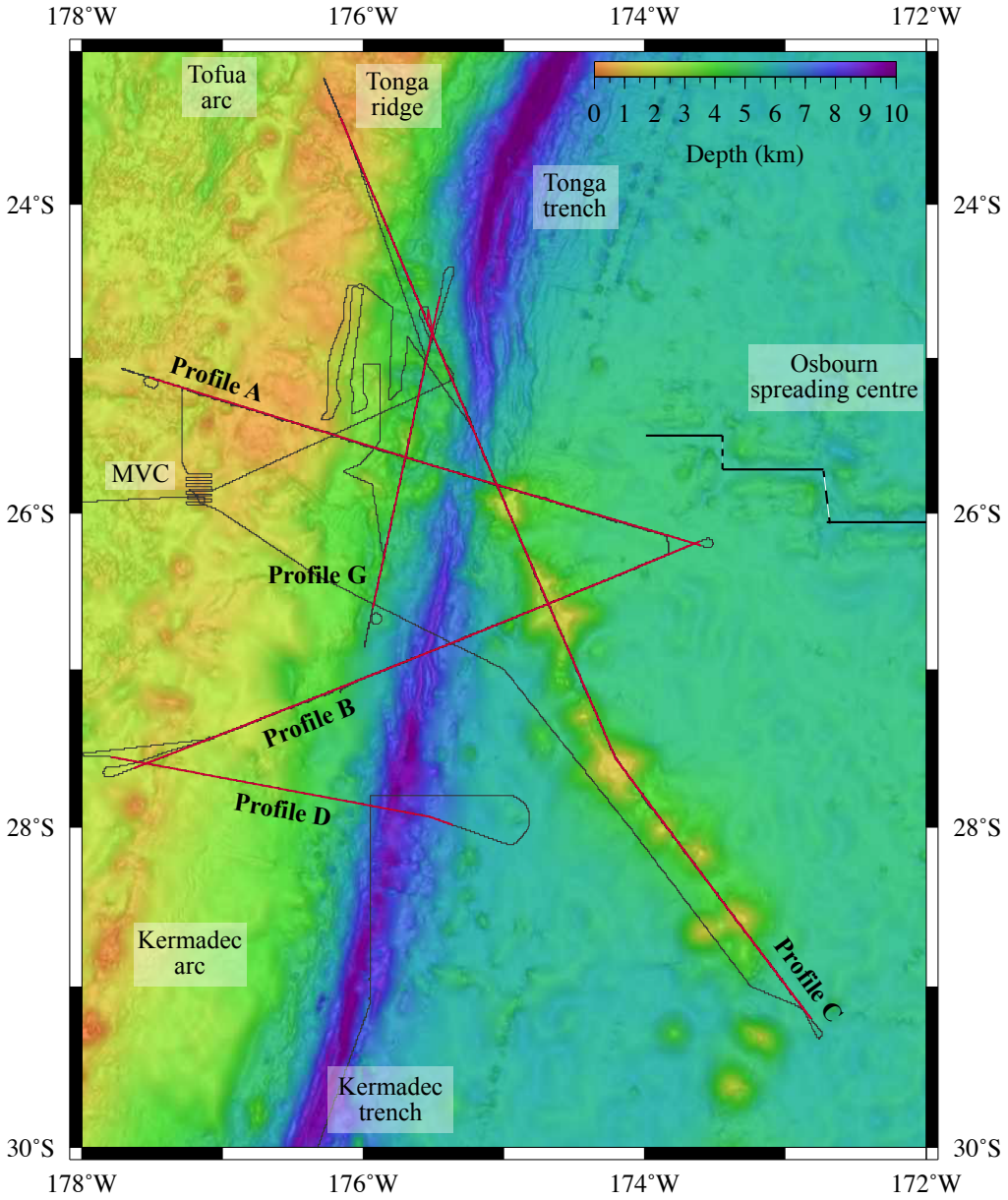

Figure 1.4: Cruise SO215 study area and acquired geophysical profiles. The five profiles are indicated by labelled red lines, and overlie the satellite-derived regional bathymetry map (Sandwell *et al.*, 2014). The ship track is shown by the continuous grey line, highlighting the repeat swath survey of Monowai volcanic centre (MVC; ~26°S 177°W). Major tectonic features are labelled on the map.

detailed overview of the data acquired during cruise SO215 can be found in Peirce & Watts (2011).

1.5.1 Profile B

Profile B is orientated northeast-southwest, and crosses Canopus seamount as well as the Kermadec trench, forearc, and arc perpendicular to the strike of the LRSC. This profile, which is ∼430 km long (Figure 1.4), intersects a number of other profiles, including: Profile D at the southwestern end; Profile C along the LRSC at Canopus seamount; as well as Profile A and P03 at the northeastern end.

Profile B was designed to image the sedimentary, crustal, and upper mantle structure associated with the LRSC, and the Kermadec forearc south of the present-day LRSC-trench intersection point. Profile B is complimented for this purpose by the data acquired along Profile D, as both sample the forearc south of the present-day LRSC-trench intersection point. As such, Profile D represents the background system structure upon which, seamount-related deformation is superimposed.

1.5.2 Additional profiles

Four other profiles were acquired during SO215 (Figure 1.4). Whilst these are not the focus of this study, the additional data acquired along them provides further constraint on the structure of the Pacific plate, LRSC, and Tonga-Kermadec forearc. The results of the data acquired along these profiles are presented and compared to Profile B throughout this thesis. These profiles can be summarised as:

- Profile A - An ∼400 km-long profile that crosses the present-day LRSC-trench intersection point. The profile was designed to image the structure of the collision zone and determine the extent and nature of deformation related to seamount subduction. The processing, modelling, and interpretation of the Profile A datasets are discussed by Stratford *et al.* (2015);

- Profile C - A 725 km-long transect over the oldest bathymetrically-expressed seamounts in the LRSC and the Tonga forearc, continuing along-strike of the exposed seamount chain. This profile was designed to image the crust and upper mantle structure of the seamounts and determine how the overriding forearc crust deforms in response to their subduction. The processing, modelling, and interpretation of data acquired along Profile C are presented by Robinson (2017);

- Profile D - An MCS-only profile that crosses the Pacific plate and Kermadec forearc, perpendicular to trench strike, south of the present-day point of LRSC-trench intersection. This ∼250 km-long profile was acquired to image the sedimentary and top-basement structures of the overriding and subducting plates associated with typical subduction of the Pacific plate along the Tonga-Kermadec subduction system. Funnell (2013) provides a detailed description of the data processing, while the results and interpretation of these data are discussed by Funnell *et al.* (2014); and,

- Profile G - An ∼240 km-long trench-parallel profile, across the lower-trench slope of the overriding plate immediately landward of the present-day point of LRSC-trench intersection. This profile was planned during the cruise to make best use of the remaining ship time and consumables. Therefore, only nine OBSs were deployed along this profile. The profile was acquired to determine along-strike variation in the crustal structure of the forearc and the top of the subducting Pacific plate in the immediate vicinity of present-day seamount subduction. The results from Profile G are presented by Bassett (2014).

1.6 Swath bathymetry data

Global bathymetry datasets, such as the General Bathymetric Chart of the Oceans (GEBCO; IOC *et al.*, 2003), offer full coverage at relatively low resolutions to as good as 30 arc-seconds (Weatherall *et al.*, 2015). Whilst these data provide valuable insights into regional-scale structures (e.g. Figure 1.3), they lack the detail necessary to accurately represent seabed morphology for the purposes of WA data modelling, or to laterally extend the interpretation of shallow local structures imaged by MCS data in three-dimensions. Multibeam bathymetry data, acquired using ships' hull-mounted transducer arrays, determine the depth of the seabed at much higher spatial resolutions than the global datasets, although are limited to swathes centred on the ship's track. Both the spatial resolution and swath sampling width are dependent on the chosen swath array beam angles and seabed depth.

1.6.1 Swath bathymetry data acquisition and processing

Swath bathymetry data were acquired throughout cruise SO215 using the onboard Kongsberg EM120 multibeam echosounder (Peirce & Watts, 2011). The EM120 system consisted of 191 hull-mounted transducer pairs that sampled overlapping along- and across-track areas of 20° and 2° respectively, resulting in a variable spatial

resolution of <50-200 m depending on seabed depth, which, for cruise SO215 was between 0.1-10 km.

Acquisition artefacts, typically observed as unusually deep or shallow depth reading spikes, were removed using an automated filter designed to flag datapoints that deviated more than 100 m from the local median depth. These cleaned bathymetric data were combined with 25 other swath datasets from other cruises throughout the region (see Appendix A) to increase the high resolution bathymetry coverage in the study area. Where multiple soundings exist for the same location from different cruises, the most recently acquired was used. This combined dataset was gridded at 50 m intervals, which enables detailed seabed structures to be resolved and interpreted at shallower water depths whilst ensuring even coverage of the sparser data at greater seabed depths, such as around the Tonga-Kermadec trench.

Within the broader region (20-35°S 170-180°W; Figure 1.5), coverage of the swath dataset is relatively sparse (<25%), although it is much greater within the cruise SO215 study area (∼55%), and almost complete in the region of the present-day LRSC-trench collision (>85%). Although the 30 arc-second satellite-derived bathymetry data (Weatherall *et al.*, 2015) fails to reveal many of the small-scale structures clearly imaged by the swath bathymetry data, it does provide constraint on features of >1 km wavelength (Sandwell *et al.*, 2014; Weatherall *et al.*, 2015).

The resulting combined swath bathymetry dataset reveals the small-scale variations in seabed structure along the subduction system. It highlights the varying nature and extent of the incoming oceanic plate bend-faulting along the margin, and shows the irregular morphology of the inner-trench slopes (Figure 1.6). The LRSC volcanic edifices, which are poorly defined in the satellite-derived bathymetry (Figure 1.4), appear stellate, and the slopes are revealed to be steep-sided with scarps indicative of mass wasting events. Swath coverage over the forearc and arc along the margin is poor, primarily due to shallow seabed depths preventing broad swathes of data from being acquired where traversed by a ship track. In all future bathymetry maps presented at profile-scale, swath data will be preferentially used, where there is sufficient seafloor coverage, over satellite-derived data (Sandwell *et al.*, 2014).

1.7 Summary of this study

This chapter has introduced the purpose of the study, describing current understanding of the major controls on forearc structure and evolution and, in particular, the subduction of seamounts and aseismic ridges. The inherent spatial and temporal limitations associated with seamount and aseismic ridge subduction at

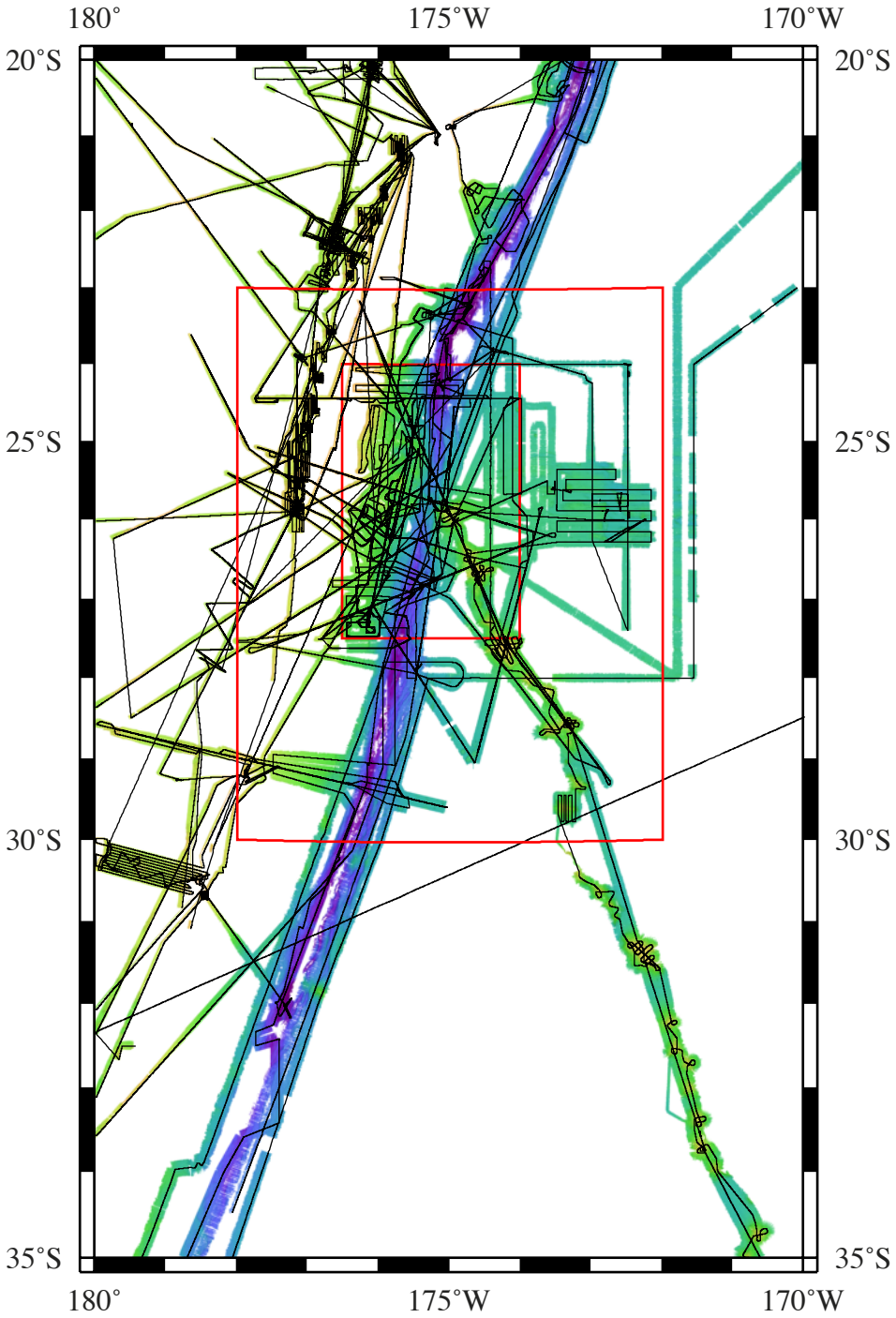

Figure 1.5: Combined swath bathymetry survey datasets from the Tonga-Kermadec subduction system. Swath coverage is limited over the entire region (<25%), but is better in the area covered by cruise SO215 (outer red box; 55%), and almost complete in the region immmediately around the LRSC-trench intersection point (inner red box; 85%). Black lines indicate the ship tracks for each of the cruises (Appendix A).

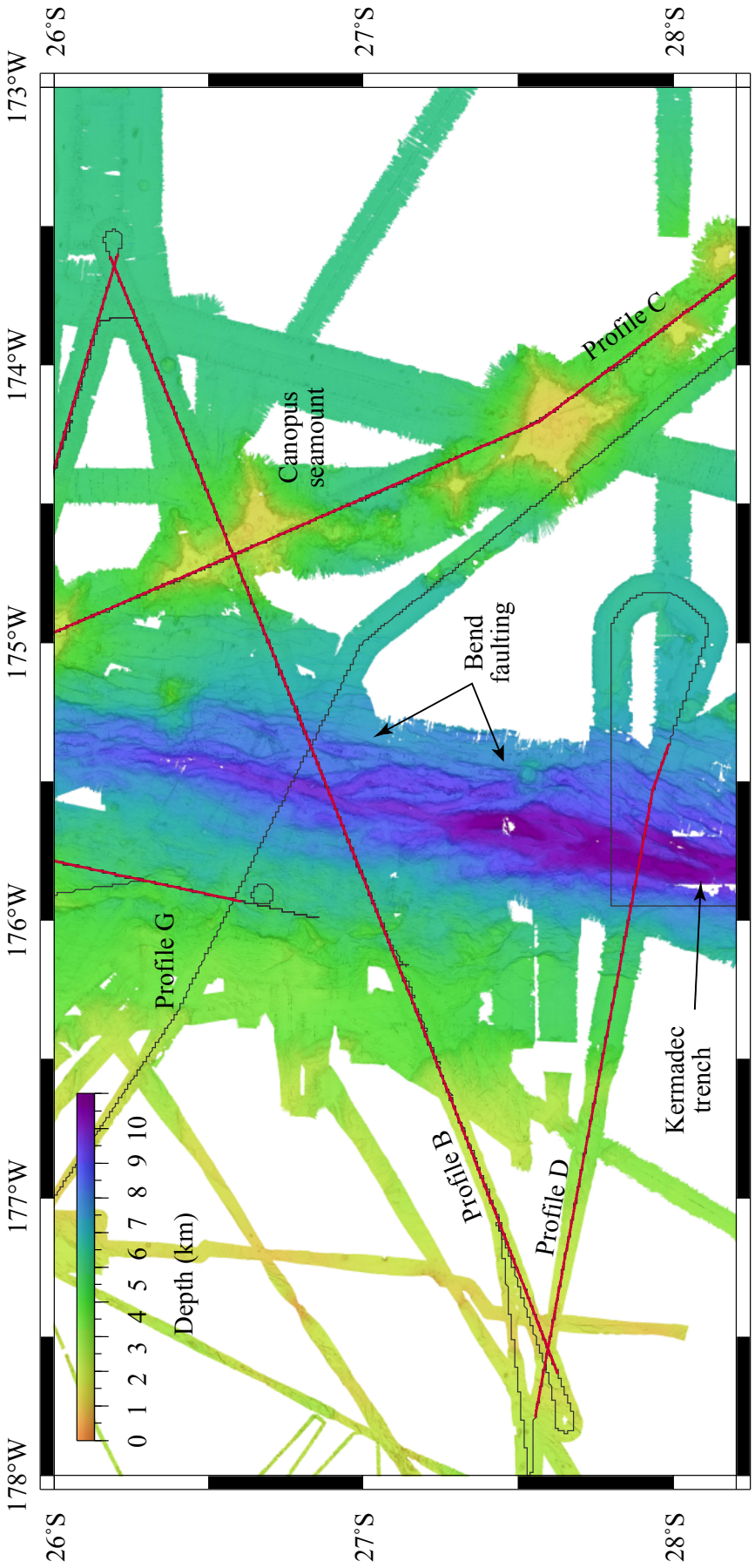

Figure 1.6: Swath bathymetry map of the region surrounding Profile B and D. The map demonstrates the detail of bathymetric structure constrained by the combined swath dataset. The LRSC and Kermadec trench are particularly well imaged, highlighting the steep-sided slopes of the seamounts and the pervasive extensional faulting of the incoming oceanic crust. Black lines indicate cruise SO215 ship tracks, and labelled red lines show acquired profiles.

erosive margins makes it one of the most poorly understood subduction processes. This chapter also raised a number of key questions about inherited overriding plate structure and how the subduction of anomalous bathymetric features superimposes deformation structures. In Section 1.4 the geological setting and tectonic history of the Tonga-Kermadec subduction system was described as an ideal location to study the subduction of seamounts. Cruise SO215, which targeted the Tonga-Kermadec subduction system with five distinct geophysical profiles, was introduced in Section 1.5.

This study focusses on the processing, modelling, and interpretation of data along Profile B, to develop a model of crust and upper-mantle structure across the LRSC and Kermadec forearc south of the present-day LRSC-trench intersection. The results will be discussed in the context of previous research to constrain inherited forearc structure, develop a structural framework for the region, and reveal the evolution of the subduction system. There are seven chapters in this thesis. Chapters 2, 3, and 4 present data processing, modelling, and testing, and Chapters 5 and 6 describe the resulting models and discuss them in the regional context.

In Chapter 2, the MCS acquisition parameters and processing scheme are described, detailing how the different processes improve the final stacked section. This seismic section is interpreted to quantitatively inform the initial forward WA velocity model and highlight interesting geological features that may control the sub-seabed seismic velocity structure.

Chapter 3 presents the processing, analysis, and forward modelling of the WA dataset to develop a velocity-depth model across the subduction system south of the LRSC-trench intersection. The model was initially constrained by swath bathymetry data and velocity and depth information from the MCS data processing, prior to model development using a dense coverage of sub-seabed reflected and refracted arrivals from the WA seismic dataset. The resulting final velocity-depth model was directly assessed for constraint through sensitivity testing and reprocessing of the MCS profile.

The final forward velocity-depth model from Chapter 3 is then independently tested in Chapter 4 to highlight the regions of the model that are most well constrained, determine the model resolvability, and test for modeller bias. Inversion modelling of the WA seismic dataset tests whether the modelling programme or user has incorporated any unnecessary features by resolving the minimum required velocity structure. Checkerboard testing of this model enables the size of velocity anomalies recoverable with the acquisition geometry and modelling parameters to be determined. Subsequently, the forward velocity-depth model is converted into

density-depth models to assess whether the forward model fits the observed gravity to within the uncertainties as a further test of model constraint, and to determine sub-surface composition.

In Chapter 5, the results from Chapters 2, 3, and 4 are synthesised to develop a combined best-fit model for the Profile B sub-surface structure. This is primarily achieved using the forward velocity-depth model and the understanding of resolvability provided by the direct and indirect testing of it, supplemented by the seismic reflection data and density model. Interesting and more complex sub-surface features are discussed in the context of other published datasets to provide additional constraint.

This combined model is synthesised with published models and datasets from along the Tonga-Kermadec subduction system in Chapter 6 to develop a framework of structural variations along the margin. LRSC subduction at the margin is then discussed in the context of this model to determine the likely effects and history of seamount subduction along the subduction zone. The results of this study are summarised, and suggestions are made for future research at the margin in Chapter 7.

Chapter 2

Multichannel seismic data acquisition, processing, and interpretation

2.1 Introduction

In Chapter 1 the background, purpose, and aims of this project were outlined in the context of cruise SO215. The acquisition of swath bathymetry data throughout the cruise, its processing, and merging with existing datasets from the region were described to demonstrate the development of a high resolution image of the seabed. Chapter 2 introduces and discusses the detailed analysis, processing, and interpretation of the Profile B MCS data.

Along Profile B, the WA seismic and MCS data were acquired contemporaneously with the configurations outlined in Section 2.2. Following seismic data acquisition, different processing techniques were applied to enable the analysis of the MCS dataset characteristics and generate a detailed and robust sub-surface reflection image (Section 2.3). This fully processed MCS section is interpreted in the context of previous studies and datasets from along the Tonga-Kermadec subduction system, and key features highlighted (Section 2.4). From this processing and interpretation the sediment column thickness and seismic velocity structure are used to initialise and enhance the modelling of the WA seismic data acquired contemporaneously along the profile (Chapter 3).

2.2 Seismic data acquisition

Seismic data acquisition geometries and parameters were chosen to produce optimal datasets for the geological target to be imaged along each profile. The acquisition of geophysical data throughout the cruise followed the same general equipment configuration, although adjustments were made to the configuration of the airgun array between seismic profiles to improve the source signature.

The acquisition parameters for Profile B can be divided into three main components: the airgun source array (Section 2.2.1); the MCS streamer (Section 2.2.2); and the seabed instruments (presented in Chapter 3). Along Profile B (Figure 2.1) the MCS and WA seismic data were acquired contemporaneously. This joint acquisition required a trade-off in parameters to achieve a suitable shot spacing, and source amplitude, signature, and frequency band, to ensure that both the WA seismic and MCS datasets could be processed, modelled, and interpreted effectively.

2.2.1 Airgun source array

The seismic source consisted of 12 Sercel G-guns with volumes of 260, 380 and 520 in^3 (4.3, 6.2, and 8.5 l respectively) divided into two sub-arrays (Figure 2.2).

The resulting airgun array had a combined volume of 5440 in^3 (89.1 l), and was towed 43 m astern, and at 7.5 m water depth. The inclusion of larger airgun chambers aimed to enhance the low frequency component of the source signature and enable signal propagation through the sub-surface to the OBSs at greater offsets (Peirce & Watts, 2011). Whilst the low frequency signal aids signal propagation to greater depths and over larger distances, it does not aid the resolution of finer-scale sedimentary depositional and deformational structures in the MCS reflection dataset.

A shot interval of 60 s was chosen to avoid wrap-around of the direct waterwave obscuring the sub-seabed arrivals of later shots. At an average survey speed of 4.5 kn, this resulted in a shot spacing of ∼150 m along-profile. An electronics mismatch between the airgun firing trigger and streamer recording systems resulted in a 560 ms static advance between MCS trace start and shot fire aim point.

2.2.2 MCS streamer

The multichannel streamer was 3 km-long and comprised 240 channels at 12.5 m group interval. The first active channel was located 204 m astern (161 m from airgun array centre; Figure 2.2). The streamer was towed at 10 m below sea surface to minimise the effect of swell noise during heavy sea conditions. With a CMP

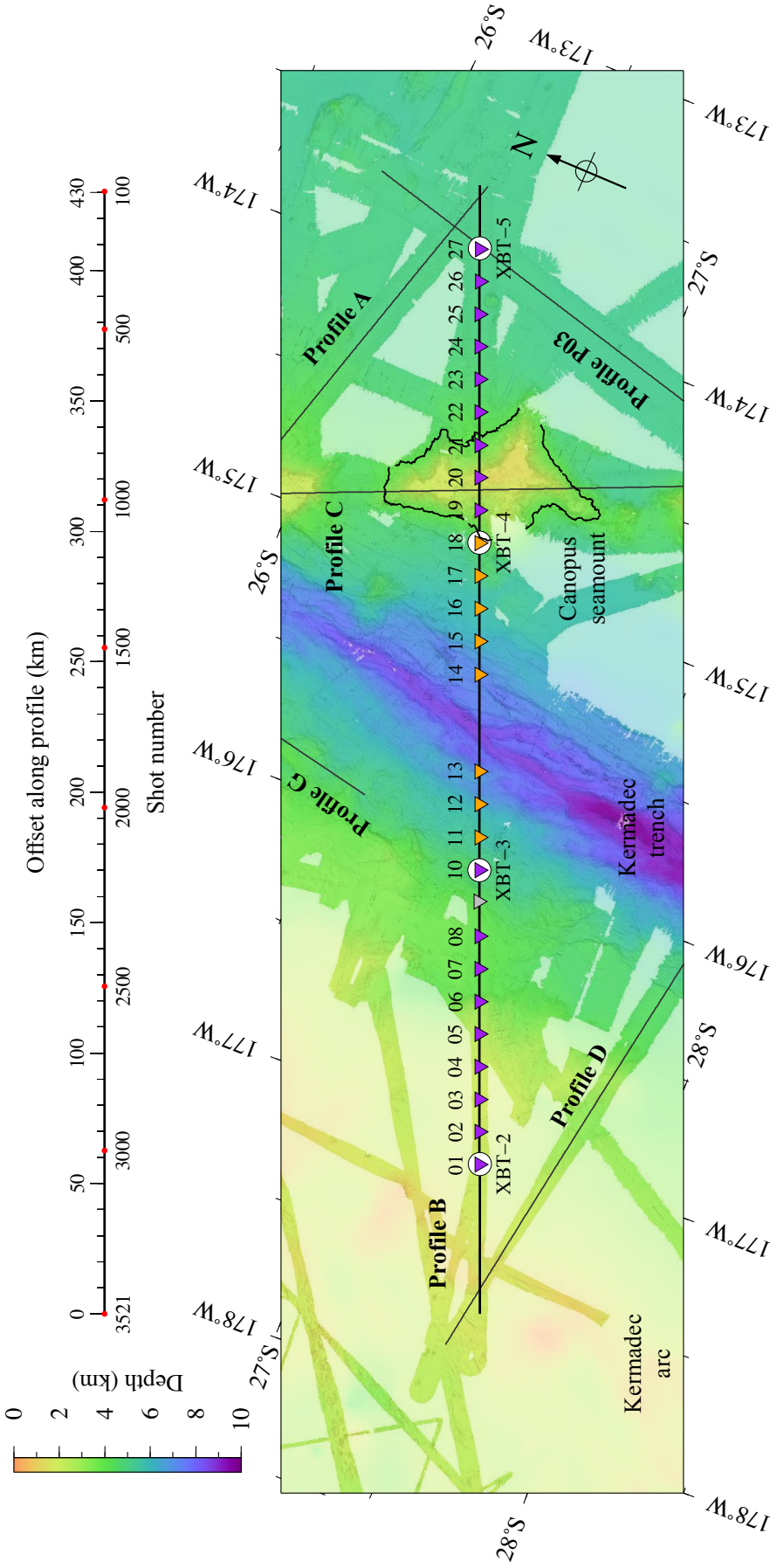

Figure 2.1: Overview of the Profile B acquisition geometry. This joint WA seismic and MCS profile crosses the subducting Pacific and overriding Indo-Australian plate. LC- (purple) and KUM deep water-type (orange) OBSs deployed along Profile B (thick black line) are numbered. XBT sampling locations are shown by the numbered white circles. The background bathymetry map consists of high-resolution swath and illuminated satellite-derived data where swath data are absent.

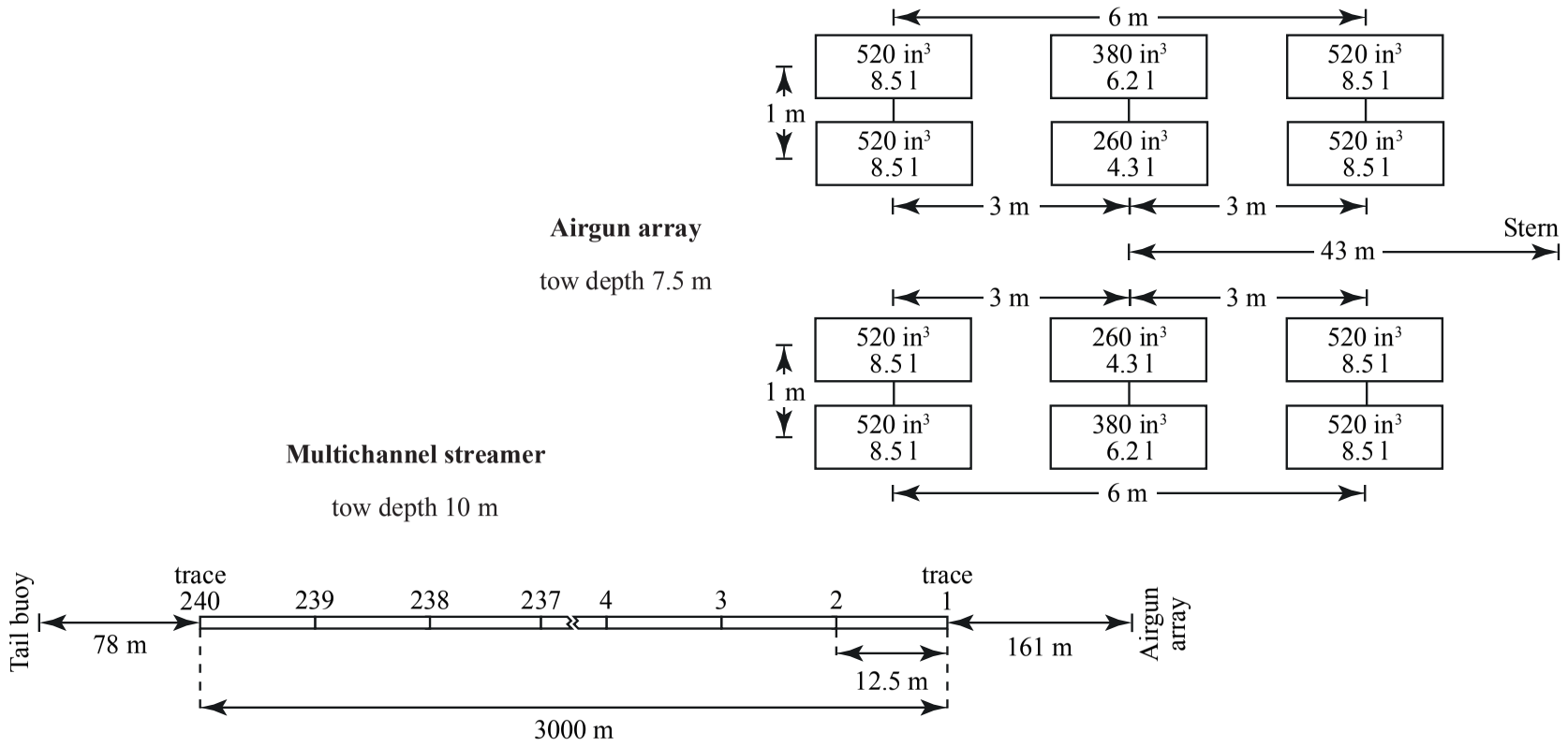

Figure 2.2: Combined MCS acquisition array schematic. The airgun array was towed at 7.5 m depth below sea surface and had a combined volume of 5440 in^3 (89.1 l). Below, the MCS streamer was towed at 10 m depth below sea surface to reduce the effect of swell noise during quite heavy sea conditions (Peirce & Watts, 2011). The streamer is offset 161 m from the centre of the airgun array, with spring sections at the front and back of the active sections to reduce the effect of cable tug propagating down the streamer.

spacing of 6.25 m, and a shot interval of 150 m, the nominal fold-of-cover is 10. Seismic data were recorded at 2 ms sampling interval in SEG-D format.

2.3 Multichannel seismic data processing

MCS data processing was initially undertaken to inform the initial thickness and seismic velocities of the sedimentary column for WA velocity modelling (Chapter 3), and provide insight on the sediment deposition and deformation structures along the profile. To generate a representative and robust sub-surface image, processing was divided into four main stages:

1. pre-processing (Section 2.3.1) - raw SEG-D data files were quality control (QC) checked and combined to create a complete SEG-Y format dataset;

2. brute stack (Section 2.3.2) - first-pass processing to generate an indicative image of geological structures. The resulting brute stack was then used to highlight regions of interest and determine the processing steps necessary to improve sub-seabed reflectivity (Section 2.3.3);

3. full processing (Section 2.3.4) - detailed processing resulting in a final high-quality seismic reflection image, absent of processing artefacts, focussing on regions and features of interest highlighted by the brute stack; and,

4. WA velocity model restacking (Section 3.8.2) - reprocessing using the final WA velocity-depth model to test not only the fit of that model but also to improve the imaging of any previously unresolvable features beneath the acoustic basement. As this stage relies on the result of the WA data modelling, it is presented in Chapter 3.

The processing sequence applied is summarised in Table 2.1. Each process sub-stage number is included in section headers to enable quick reference to the processing summary table. Seismic data processing was undertaken using *GLOBE Claritas*^{TM} and *Seismic Unix (SU)*, while the data plots were produced using the *Generic Mapping Tools* package (*GMT*; Wessel & Smith, 1991; 1995; 1998).

2.3.1 Pre-processing

Pre-processing of the raw data comprised file format conversion, geometry assignment, QC, and resampling.

Profile B MCS processing sequence summary

No.	Stage	**Processor**	Details
1	Pre-processing	**Generate SEG-Y**	Convert SEG-D files into a single shot-sorted SEG-Y
2	Pre-processing	**Input geometry**	Insert geometry (e.g. CMP number) into headers
3	Pre-processing	**Quality Control**	Remove dead traces, highlight regions of low SNR
4	Pre-processing	**Resample**	Resample from 2 to 4 ms
5	Processing	**Bulk static**	Apply recording delay static (-560 ms)
6	Processing	**Bulk static**	Apply source-streamer static (+12 ms)
7	Processing	**Filter**	Apply 3-10-100-110 Hz Butterworth band-pass filter
8	Processing	**Sort**	Convert from shot- to CMP-sorted gathers
9	Brute stack	**NMO**	Apply NMO correction at 1.5 km s^{-1}
10	Brute stack	**Stack**	Stack into CMP traces
11	Processing	**Velocity analysis**	Determine NMO correction velocities
12	Processing	**NMO**	Apply NMO correction determined from velocity analysis
13	Processing	**Stack**	Stack into CMP traces
14	Processing	**Migration**	Post-stack Kirchhoff time migration at 1.5 km s^{-1}; 10 km sliding window
15	Plotting	**AGC**	Scale for plotting (2000 ms window)
16	Plotting	**Muting**	Mute above seabed for display

Table 2.1: Summary of steps followed during MCS data processing for Profile B. The sequence is divided into the major stages of pre-processing, brute stack, and full processing. The WA velocity model restacking stage is presented in Section 3.8.2.

2.3.1.1 File format conversion *(1)*

During cruise SO215 the MCS data were acquired in SEG-D format, with one shot per file and the GPS location of the ship loaded into the header. The first task in the MCS data processing was to combine each of the SEG-D files into a single, shot-sorted, SEG-Y format file. For each of the 3422 (from shot 100-3521) shot gathers

the first channel was an auxiliary trace, which was removed during this conversion process to generate 240-trace gathers.

2.3.1.2 Geometry *(2 and 3)*

True shot and receiver locations were calculated from the ship's GPS navigation data taking account of the known distances from the ship navigational datum to the airgun array and each channel along the streamer. This information was loaded into the Geometry toolkit in Claritas^{TM} and used to calculate the common mid-point (CMP) locations for each shot-receiver pair. Initial analysis of the CMP gathers indicated a very low signal-to-noise ratio (SNR), most likely due to the low fold-of-cover (10) along Profile B, which was a result of the compromise between shot firing rate and signal wrap-around in the seabed instrument data. Due to this low SNR, the CMPs, which were nominally spaced at 6.25 m intervals, were grouped into 25 m superbins to increase the effective fold-of-cover to ∼40. These CMP superbin locations, numbers, and shot-receiver offsets were loaded into the headers of each trace prior to resampling.

2.3.1.3 Resampling *(4)*

Following anti-alias filtering, the 2 ms-sampled traces were downsampled to a 4 ms sampling interval to reduce processing time and file size (Figure 2.3). While resampling halved the Nyquist frequency to 125 Hz, no useful signal components were expected, or found, to have been recorded above this frequency (Peirce & Watts, 2011), so any significant sub-seabed reflections should still be well resolved at the reduced sampling rate.

2.3.2 Brute stack

A brute stack constitutes the first pass at MCS data processing, and highlights not only areas of the dataset that demonstrate interesting sub-surface structures, but also areas likely to require more detailed analysis and focussed attention during subsequent full processing.

2.3.2.1 Static shift corrections *(5 and 6)*

To ensure that the seabed plots at its true depth in two-way traveltime (TWTT), bulk static shifts were applied to the data to account for known delays in the signal recording and instrument locations.

Two static shift corrections were applied to the entire Profile B dataset:

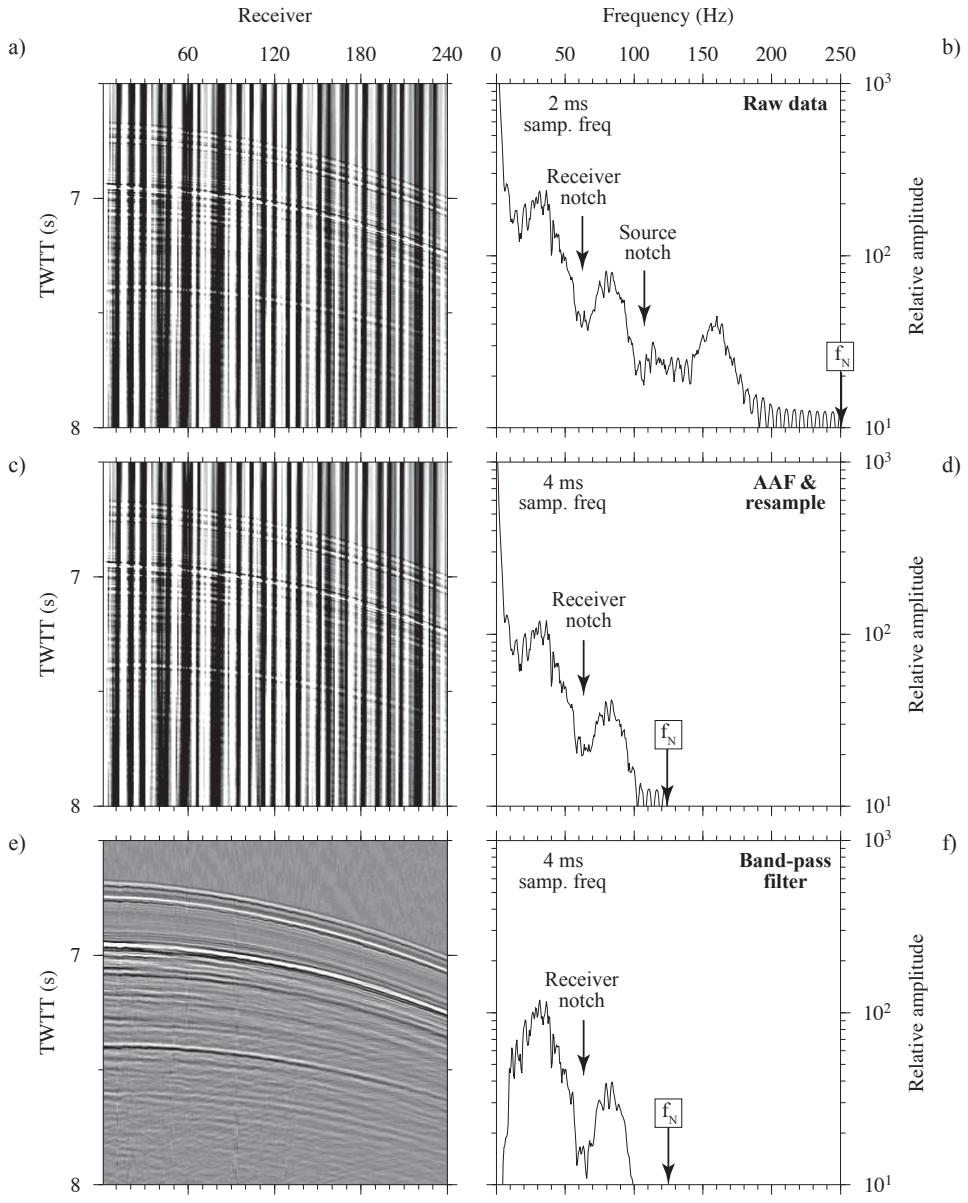

Figure 2.3: Resampling and filtering of the MCS shot-gathers. a) Raw shot gather (shot 500) at the original sampling interval of 2 ms. The seabed reflection is barely visible (∼6.75 s TWTT) beneath the high-amplitude noise. b) Frequency spectrum of the unfiltered data shown in a). Note how the low frequency region (<5 Hz) has the highest amplitude, and the acquisition notches are present. c) Shot gather (shot 500) anti-alias filtered (AAF) and resampled to 4 ms. d) Frequency spectrum of data shown in c) following the application of the AAF and resampling. Note that the signal >125 Hz has been effectively removed. e) Shot gather (shot 500) filtered using a Butterworth band-pass filter (3-10-100-110 Hz), indicating clear seabed and sub-seabed reflectivity. f) Frequency spectrum of data shown in e) following the application of the Butterworth filter with the low frequency noise significantly attenuated.

- -560 ms - this shift accounts for the 560 ms triggering mismatch between the recording system and the firing of the airgun array; and
- +12 ms - this shift accounts for the combined depth of the acquisition array components beneath the sea surface survey datum. Together the 7.5 m-deep airguns and 10 m-deep streamer combine to give a 17.5 m-thickness of water that is not accounted for in the seismic traveltimes. At 1.5 km s^{-1}, this 17.5 m equates to 12 ms in TWTT.

When combined, these static corrections add 548 ms to the start of each seismic trace.

2.3.2.2 Frequency-domain filtering *(7)*

Initial analysis of the raw shot gathers showed that the recorded data had a low frequency noise content that was equivalent to the amplitude of the seabed reflection, which is expected to be the highest amplitude primary geological reflector below sea surface (Figure 2.3).

This noise is predominantly <5 Hz and most likely results from the significant swell experienced during cruise SO215. Boosting of the SNR in the useful bandwidth was achieved through the application of a Butterworth band-pass filter (3-10-100-110 Hz). The filter corner frequencies were chosen to maximise admittance of the expected, and thus useful, signal bandwidth, whilst attenuating the effects of the high-amplitude and low-frequency swell noise.

2.3.2.3 Sorting, NMO, and stacking (*8, 9, and 10*)

Once the static correction and frequency filtering had been applied, the shot gathers were sorted into CMP gathers based on the geometry assigned in the trace headers (Section 2.3.1.2). The normal moveout (NMO) correction, using a single velocity of 1.5 km s^{-1} was then applied and the CMP gathers stacked.

2.3.3 Brute stack results

The brute stack (Figure 2.4) shows that thin sedimentary sequences (<1 s TWTT-thick) are present in the moat on either side of Canopus seamount, although there are no clear sub-seabed reflections on the steep flanks of the seamount (Figure 2.4). Coherent sub-seabed reflectivity indicates sedimentary sequences ∼2 s TWTT-thick are present on the forearc (30-120 km offset). Along the remainder of the profile the sediment cover varies in thickness and is, in places, completely absent. Strong

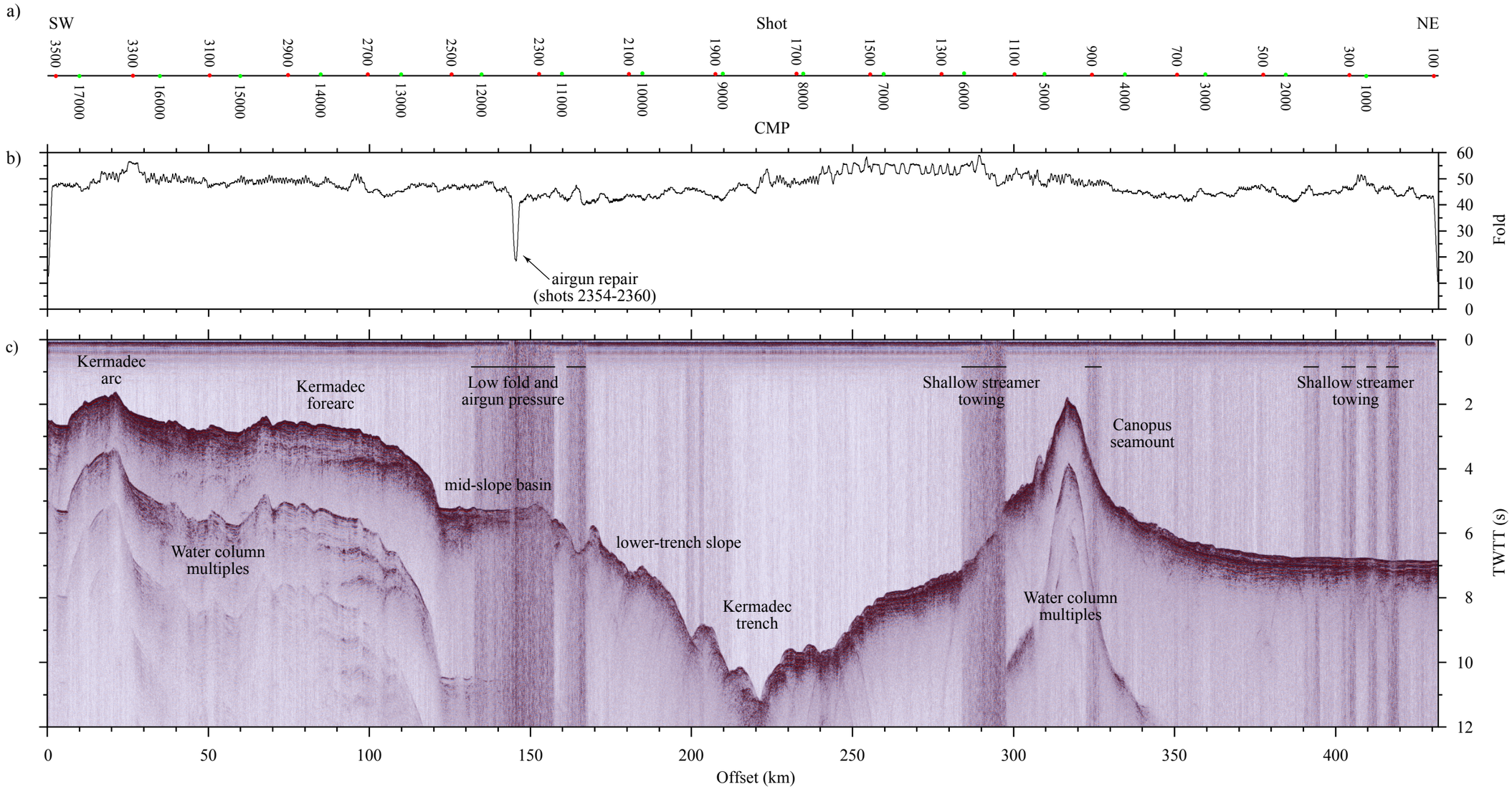

Figure 2.4: Profile B MCS acquisition geometry and brute stack. a) Acquisition geometry, showing a representative sample of shot point (red dots) and CMP bin locations (green dots). b) Fold-of-cover for each CMP along the profile, highlighting slight variability and the significant fold drop off between shots 2354-2360. Along the rest of the profile, minor variations in fold are a function of slight changes in ship speed over the ground caused by the heavy sea conditions. c) Brute stacked section of Profile B. Note that the strong bands of persistent noise, indicated on the section, are caused by either shallowing of the MCS streamer or the short period of gun downtime and low airgun pressure.

diffraction hyperbolae are observed at the seabed that cross-cut deeper reflections along the entire profile. The diffractions are most prominent on the inner- and outer-trench slopes (170-270 km offset) and the flanks of Canopus seamount (290-330 km offset). Water column multiple energy is also observed close to the top-basement reflection on the Kermadec forearc.

This variable structure and clarity of imaging along the profile highlights that further processing is required to improve the SNR of sub-seabed reflectivity and to better resolve laterally coherent and incoherent structures. The main MCS processing sequence needed to address:

- sub-seabed reflection signal - sub-seabed reflectivity varies in apparent amplitude and lateral coherence. Further data processing would aim to improve the clarity of sedimentary reflections and structures to enable the accurate assessment of sediment thickness along the profile for input into the initial WA velocity-depth model;

- diffraction hyperbolae - diffractions form at sharp sub-vertical velocity discontinuities, often indicating faulting of the seabed and sub-surface interfaces. These diffraction tails limit the interpretability of the seismic section by cross-cutting primary reflectivity, such as intra-sediment reflections. Further processing would aim to refocus the diffracted energy to its point of origin, improving reflection coherence and sharpening lateral discontinuities;

- multiple energy - long-path (water column) and short-path multiples can mask primary sub-surface reflectivity. Although there are no clear examples of multiples superimposed on the useful sediment column data, further processing would, if possible, eliminate them. Such multiple suppression would be especially effective beneath the forearc where the seabed multiple is observed just below the basement reflection, and risks introducing artefacts as part of processing; and

- noise - despite frequency filtering there are a number of persistent bands of noise throughout the section. These apparent increases in noise in the frequency band of interest may originate from periods of low airgun pressure and the streamer being towed though the heaviest swell conditions. The application of standard processing techniques would aim to enhance signal, and thus increase SNR, in these regions.

2.3.3.1 Persistent noise

Between 130-170 km along-profile offset, the SNR appears to be reduced as there is reduced apparent reflectivity of the seabed and sub-seabed, and noise is persistent along the trace. This region of low SNR coincides with a period of reduced air pressure that resulted in equipment maintenance during shots 2354-2360. The consequence of this is a broad band of significantly reduced signal amplitude and transmittance through the sub-surface as well as a reduction in the fold-of-cover to <20 (Figure 2.4b). Smaller and less prominent bands of low SNR occur at 285-295 km offset on the flanks of Canopus seamount, and again around 410 km offset. At these offsets the streamer did not maintain the planned tow depth of 10 m, and was instead at ∼2 m, increasing the influence of the heavy swell on the streamer, and reducing the apparent SNR.

2.3.4 Full processing

The generation of a brute stack (Figure 2.4) highlighted the need to further process the MCS dataset to generate a more geologically representative and interpretable seismic reflection image. The full processing sequence, therefore, continued with the full velocity analysis of the CMP-sorted data (stage 8).

2.3.4.1 Velocity analysis *(11)*

Correctly determined velocity for NMO correction improves the primary geological reflectivity and also attenuates long-path multiple energy. The brute stack (Figure 2.4) highlights the extreme geological heterogeneity along Profile B, with an undulatory seabed, regions of significant faulting, and highly variable sediment thickness. To more clearly resolve these features, a laterally and vertically variable velocity model was needed that represented the seabed and sub-surface at smaller intervals than their lateral variability along profile. Significant seabed offsets are observed at scales down to ∼2 km laterally, so velocity analysis intervals were chosen to be at least every 50 CMP (1.25 km), with a smaller spacing in regions of greater geological complexity. At each 50 CMP interval, velocity analysis was undertaken using semblance plots, constant velocity gathers (CVG), and constant velocity stacks (CVS) using the inbuilt *Claritas*^{TM} Velocity Analysis (CVA) tool (Figure 2.5).

The combined use of semblance plots and CVGs enabled the accurate determination of stacking velocities for primary reflection events at the chosen interval, whilst the CVSs showed the effect of the velocity profile on the surrounding CMPs. The

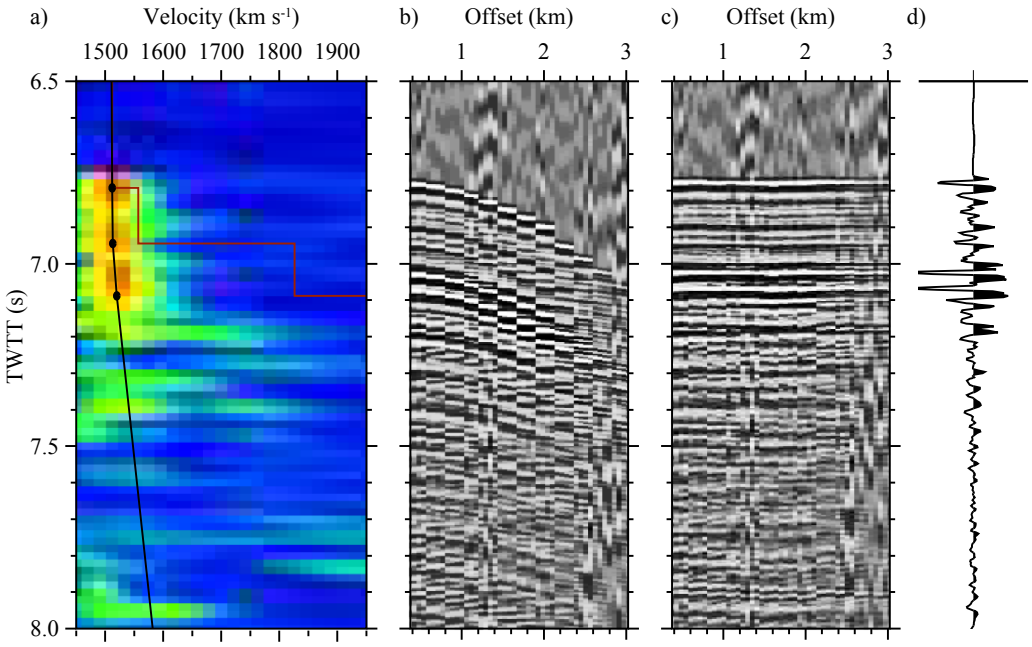

Figure 2.5: Example velocity analysis applied to a single CMP supergather (CMP 1000). a) Semblance plot, with the stacking velocity picks indicated by the black dots and profile, and the interval velocities shown by the red line. b) CMP supergather with no NMO applied. c) CMP supergather with NMO correction applied using the velocity profile shown in a). d) Single stacked trace following the application of NMO corrections.

velocities were analysed iteratively, starting in regions with relatively thick sedimentary deposits where clear semblance profiles could be determined (such as on the forearc, between 50-120 km offset along profile), before moving to regions of reduced or no sediment cover where reflections were unclear or absent. In some regions, such as on the lower-trench slope (190-220 km offset along profile), only the seabed reflection was evident. A varying water column velocity, which was mainly dependent on the depth of the seabed (from 1.3-8.5 km), was applied along profile (1.48-1.51 km s^{-1}). Below the seabed, stacking velocities were gradually increased according to the picked velocity profiles (e.g. Figure 2.5), with a positive velocity gradient assumed from the top-basement reflection down to the bottom of the velocity model.

2.3.4.2 NMO and stacking *(12 and 13)*

The stacking velocity model was interpolated between sample locations, and applied to each CMP supergather as the NMO correction prior to stacking (Figure 2.5). The summing of well-corrected CMP supergathers enhances the SNR, as shown in

Figure 2.5, which demonstrates how the random noise in the water column has been significantly reduced relative to the seabed reflection.

2.3.4.3 Migration *(14)*

Post-stack Kirchhoff time migration was applied to attenuate the high level of diffracted energy observed originating at the faulted regions of the seabed and in the sub-surface. A constant migration velocity of 1.5 km s^{-1} and 10 km sliding window were found to be the most effective parameters after testing. Although other processors were tested, Kirchhoff post-stack time migration was found to introduce fewer artefacts whilst being computationally inexpensive. Variable velocity migration processors introduced distortions to the data, most likely as a result of the high lateral variability of the stacking velocity model generated through velocity analysis, and the poor constraint on velocity beneath the top-basement reflection.

Post-stack Kirchhoff migration sums energy along diffraction hyperbolae and relocates it to the apex, refocussing signal to the origin of the diffraction. Figure 2.6 demonstrates how the application of the post-stack Kirchhoff migration improves the lateral definition of normal faults on the subducting Pacific plate along Profile B. The reflection located ∼200 ms below the seafloor, which exhibits smaller diffraction tails than the seabed, becomes much more clearly defined and of a higher amplitude than the seabed reflection following migration. Faulting of the seabed and sub-seabed reflections also becomes much clearer. In some locations, multiple minor faults are resolved that were previously unobserved, i.e. extensive small-offset normal faults throughout the subducting Pacific crust fault blocks (e.g. compare Figures 2.6a and b between 225 and 240 km offset along profile). The apparent seabed echos observed above the seabed following the application of the Kirchhoff migration are low amplitude artefacts that are cosmetically removed from the section with a top mute prior to plotting.

2.3.4.4 Plotting *(15 and 16)*

After the top mute, an automatic gain control (AGC) scalar was applied over a 2000 ms-long rolling window to balance the reflection amplitudes over the full trace length. Although more computationally expensive, a median scaling function is used as it introduced fewer low amplitude bands (white spots) above and below bright reflections. The long AGC window length also minimises the negative effects of the AGC trace scaling to create a well-balanced seismic section (Figure 2.7).

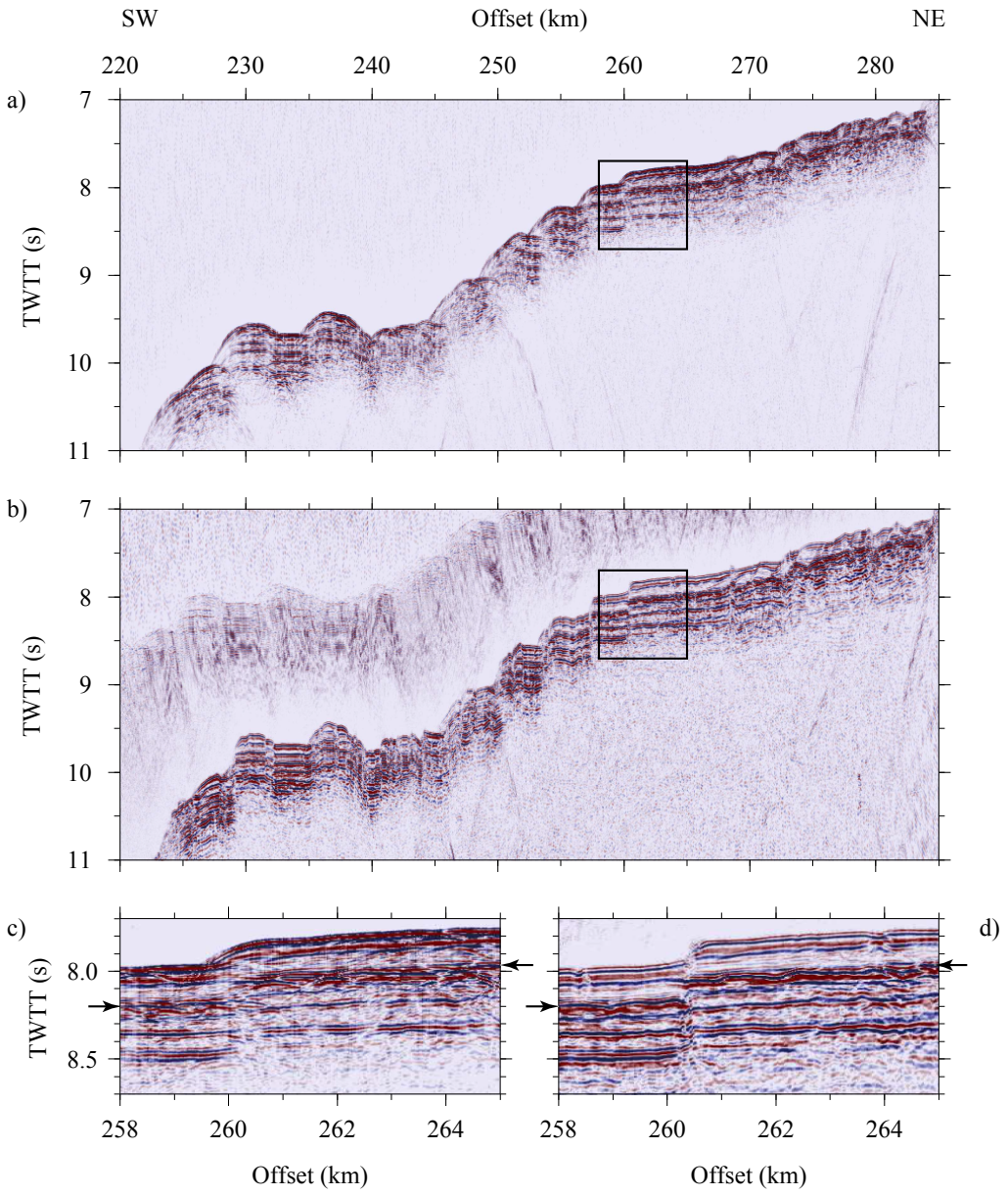

Figure 2.6: Example application of post-stack Kirchhoff migration on the outer-trench slope. a) Pre-migration stack with strong seabed and sub-seabed diffractions masking primary reflectivity. b) Post-migration stack showing much clearer seabed and sub-seabed reflections and faults, with the detrimental effects of the diffracted energy significantly reduced. c) Data window indicated by the black box in a), highlighting diffraction tails that occur at the seabed and a high amplitude internal sediment reflection ∼200 ms below the seabed (indicated by black arrows). d) Comparison data window indicated by the black box in b), with the seabed and sedimentary reflection ∼200 ms below the seabed more clearly defined following migration.

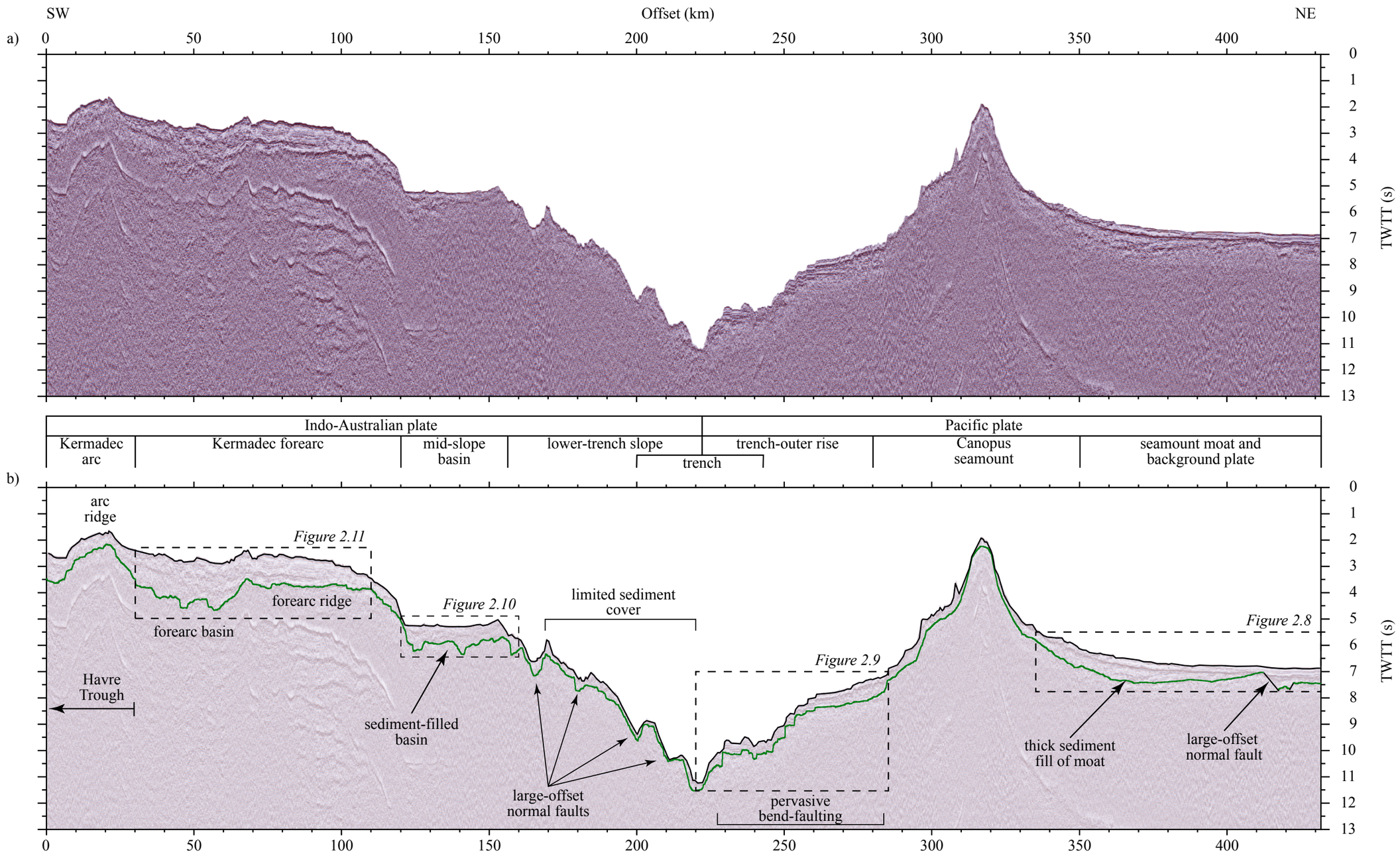

Figure 2.7: Final stack and initial interpretation of the fully processed MCS data. a) Final stack following detailed velocity analysis and the application of a standard processing sequence (see Table 2.1). b) Initial interpretation of the data presented in a), with major tectonic features indicated, seabed (black line) and basement reflections (green line) plotted and significant sedimentary and structural features labelled.

2.3.5 Processing summary

The application of the optimised processing sequence to the Profile B MCS dataset significantly improves the clarity of the reflections and faults throughout the seismic section. Detailed velocity analysis sharpens the seabed, internal sediment, and top basement reflections, whilst reducing the amplitude of the water column multiple reflections observed below the basement. The application of post-stack time migration refocuses diffracted seismic energy to its origin, further enhancing reflection strength and lateral continuity. Finally, trace scaling and the muting of signal above the seabed improves the image for the final plotting. The final stacked section is shown in Figure 2.7.

2.4 Initial interpretation

In this section, the initial interpretation of the final processed Profile B MCS section is presented. The interpretation is used not only to provide qualitative information about the nature of the material deposited and deformed over the history of subduction at the margin, but also to determine the thickness and indicate seismic velocities of the sediments for construction of the initial forward WA seismic model (Section 3.6.4). For the initial interpretation of the processed section, the results are considered in the context of the surrounding bathymetry (Figure 2.1), as well as previously acquired MCS and borehole data from the margin. As the MCS section has not been depth converted, the 'depth' and 'thickness' estimates for different reflection events are quoted in TWTT.

2.4.1 Profile B

The thickness of sediment observed on the flat-lying regions of the Pacific plate along Profile B varies between 0.2 and 0.9 s TWTT (e.g. 370-410 km offset, Figure 2.8). At ∼415 km offset along profile, a 0.6 s TWTT-throw normal fault delimits a heavily faulted, sediment-filled basement to the northeast. This fault is located ∼150 km from the trench, which, together with the significant sediment fill (>0.6 s TWTT) and extensive internal faulting indicates it most likely predates the emplacement of the LRSC, which is the major sediment source for the region at the time (Figure 2.8). A fracture zone with a strike in line with this fault suggests the feature may have originated at the Osbourn spreading centre (<20 km to the north), and been subsequently infilled, with possible fault reactivation during seamount formation. Reflections internal to the sedimentary succession observed in the moat

of Canopus seamount typically dip away from the seamount, onlap onto deeper reflections, and display a relatively chaotic internal structure. This internal structure and high variability in sediment thickness (up to ∼1 s TWTT) indicates that the sediments imaged in the moat of Canopus seamount are most likely generated and redistributed volcaniclastic material from the volcanic centres (e.g. Koppers *et al.*, 2011; Vanderkluysen *et al.*, 2014). Sediment is absent from the flat top and steep (up to 40°) flanks of Canopus seamount sampled. This suggests that the steep seamount flanks promote the transportation of sediments down-slope, and do not enable their accumulation.

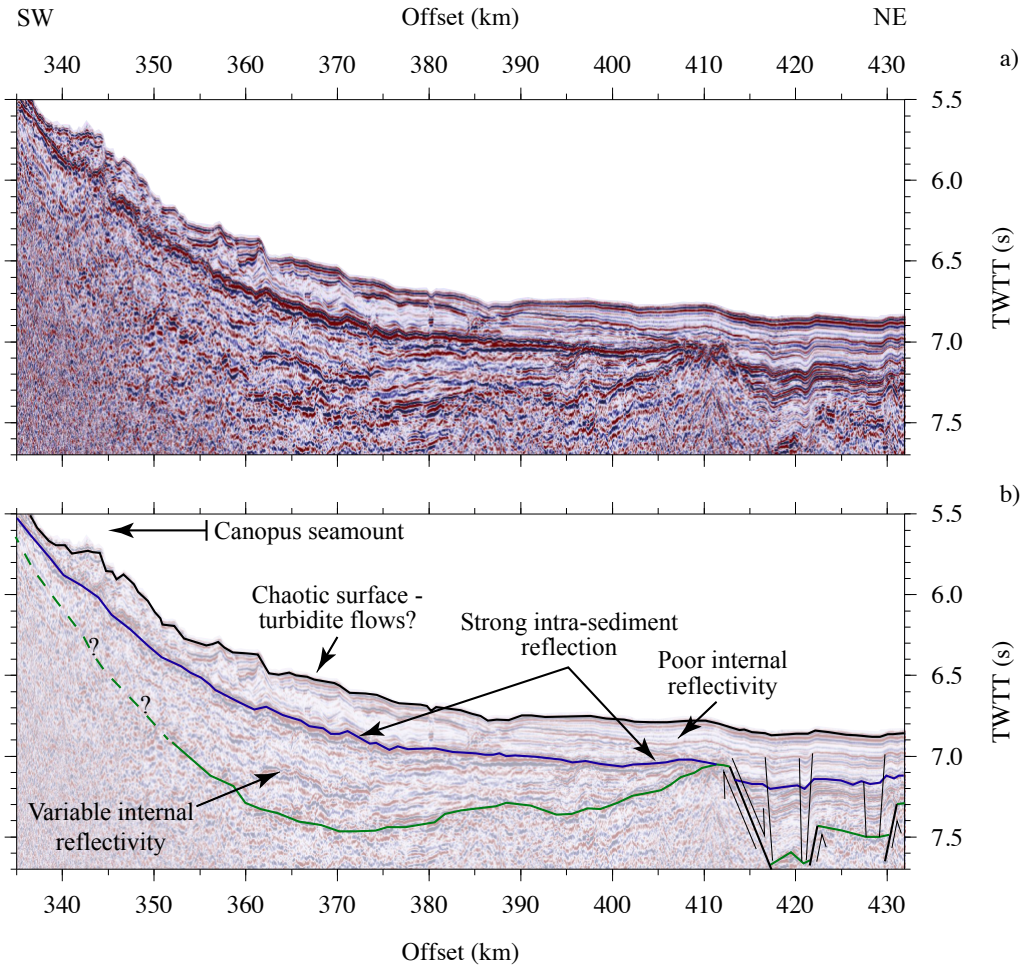

Figure 2.8: Interpretation of processed MCS data across the background Pacific plate and Canopus seamount flexural moat. a) Window centred on the Canopus seamount moat. b) Interpretation of the data presented in a). Seabed and sedimentary reflections are coherent east of ∼375 km offset, but are more chaotic in nature with increasing proximity to Canopus seamount.

Between the seamount and the trench, sediments appear to reach ∼0.6 s TWTT-thick, but are disturbed by pervasive nomal faulting (Figure 2.9). The normal faulting is manifest as <0.1-0.3 s TWTT vertical offsets that are dominantly trenchward-dipping and preserve a sub-horizontal seabed. This deformation pattern is significantly different to the 2 s TWTT-throw horst and graben structures on Profile D, documented by Funnell *et al.* (2014), that coincide with an increased plate dip of ∼5°. No sediments are observed in the trench axis.

The lower-trench slope is morphologically rough, dominated by large fault blocks with 0.7 s TWTT throw and minimal sediment cover (<0.1 s TWTT; Figure 2.7). Further west, a large normal fault (∼1.0 s TWTT-high) at ∼160 km offset, offsets

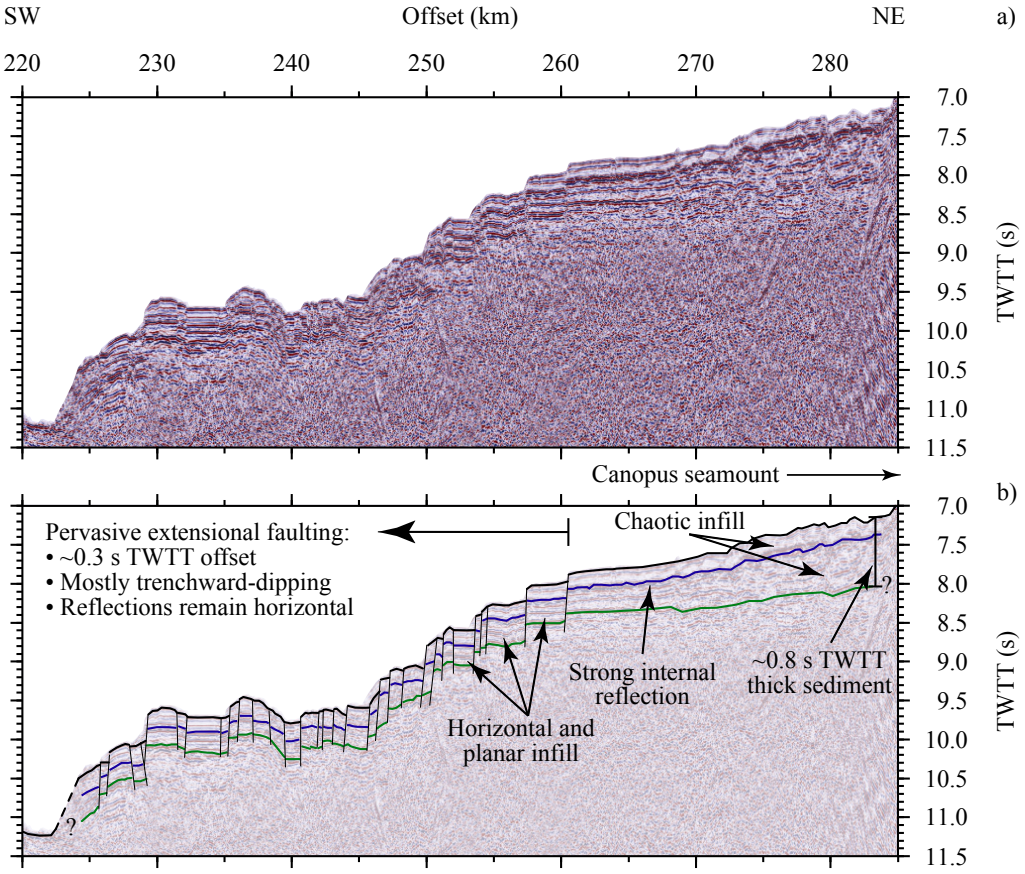

Figure 2.9: Interpretation of processed MCS data across the bend-faults of the subducting Pacific plate. a) Window centred on the bend-faults of the subducting Pacific plate. b) Interpretation of the data presented in a). The pervasive extensional faults through the Pacific plate sediments are typically ∼0.3 s TWTT in vertical offset, and predominantly dip towards the trench. Sediment thickness increases slightly with proximity to the base of Canopus seamount.

the lower-trench slope from a poorly imaged 25 km-wide mid-slope basin (Figure 2.10). The eastern end of the basin, ∼143-155 km offset, was poorly imaged due to the locally limited fold-of-cover and reduced airgun array pressure. Despite this, the sediment is observed to tilt slightly arcward, and appears to be pervasively faulted, although does not clearly demonstrate a change in sediment thickness. This mid-slope basin starves the lower-trench slope and trench axis by acting as a sediment pond.

Between 30-110 km offset the Kermadec forearc is defined by a ridge and basin morphology (Figure 2.11). The forearc ridge is ∼45 km in trench-perpendicular

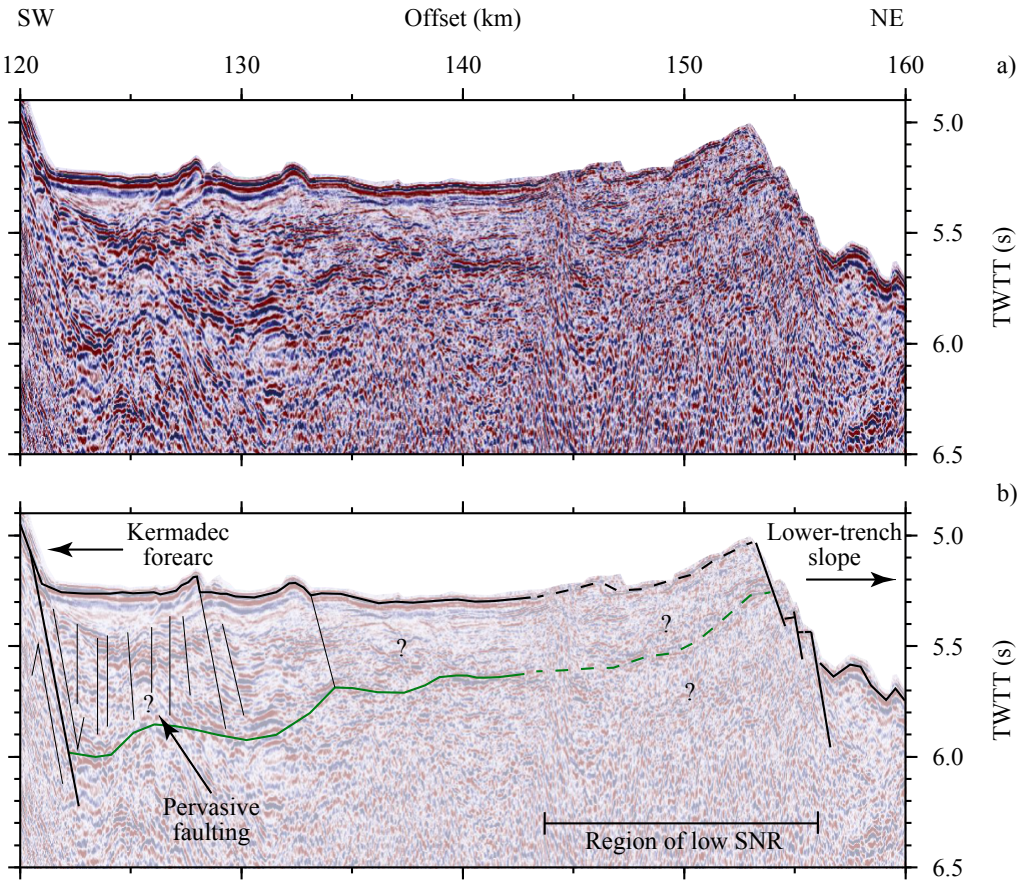

Figure 2.10: Interpretation of the processed MCS data across the mid-slope basin of the overriding plate. a) Window centred on the mid-slope basin of the overriding plate. b) Interpretation of the data presented in a). The mid-slope basin demonstrates pervasively faulted sediments reaching ∼0.7 s TWTT thick between 120-130 km offset along profile. At the eastern end of the mid-slope basin (∼143-155 km offset), low SNR, caused by reduced fold-of-cover and airgun pressure, prevents sub-seabed reflectivity from being observed.

width, and at 2.5 s TWTT water depth, so appears to be a less bathymetrically pronounced form of the Tonga ridge in the north (Wright *et al.*, 2000; Contreras-Reyes *et al.*, 2011; Stratford *et al.*, 2015). The sediments located on top of the bathymetric ridge (65-100 km offset) are ∼1 s TWTT thick and relatively horizontal, although broken up by pervasive <0.1 s TWTT-throw normal faults. Between this ridge and the volcanic arc, an ∼40 km-wide bathymetric basin exhibits sediments that reach ∼2 s TWTT-thick. A high amplitude intra-sediment reflection 0.5-0.7 s TWTT below the seabed is observed across the forearc basin and ridge, terminating at ∼95 km offset. That this high amplitude reflection is underlain by more sediment in the forearc basin than the ridge suggests that the underlying morphology predates

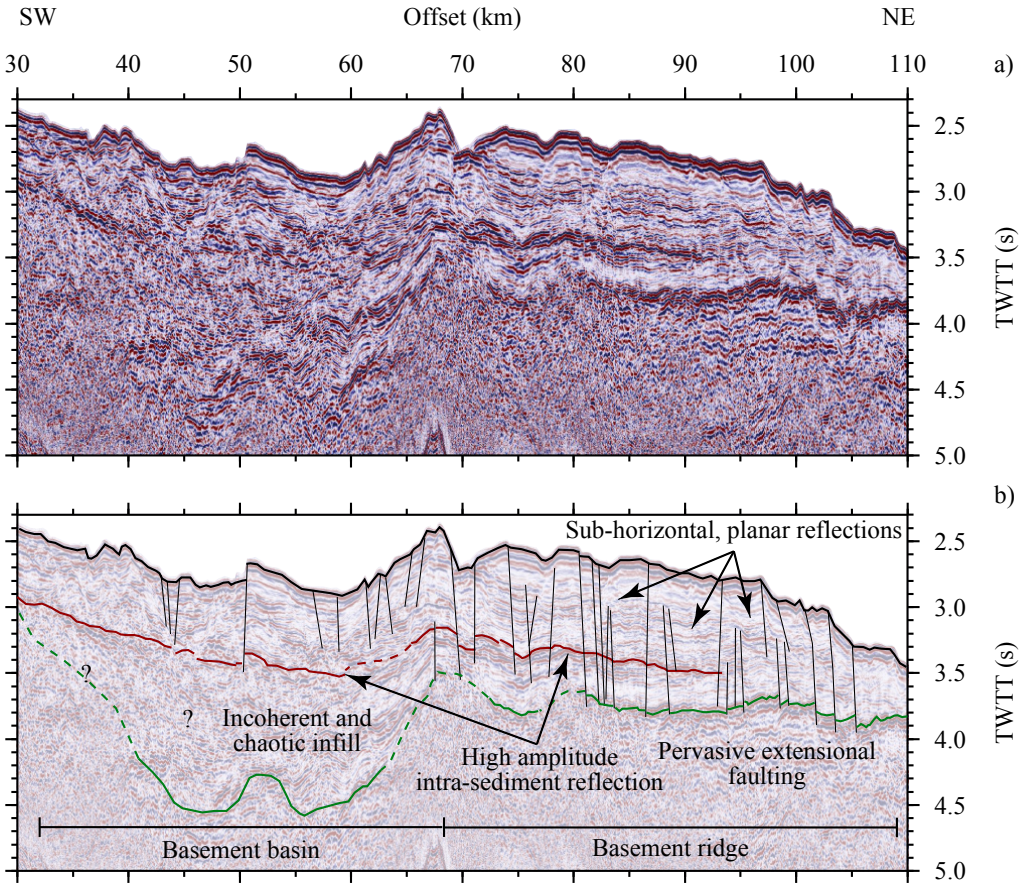

Figure 2.11: Interpretation of the processed MCS data across the Kermadec forearc. a) Window centred on the Kermadec forearc. b) Interpretation of the data presented in a). Sediments reach up to 2 s TWTT-thick in the region with a basement basin structure, shallowing to ∼1 s TWTT-thick on the basement ridge. Small-offset (<0.1 s TWTT) normal faulting pervades the forearc sedimentary sequence and basement.

the seismo-stratigraphic boundary. Intra-sediment reflectivity is typically horizontal and planar, suggesting prolonged accumulation of material, although chaotic reflectivity proximal to the arc indicates turbiditic flows that redistributes volcaniclastic material down the forearc slopes (e.g. Gillies & Davey, 1986; Clift *et al.*, 1994).

2.5 Summary

In this chapter the parameters for acquiring and processing the MCS data along Profile B were presented and the final processed seismic section described.

Profile B images highly variable sediment thicknesses across the Pacific oceanic crust and Tonga-Kermadec forearc south of the present-day LRSC-trench collision zone. Sedimentation is greatest in flat-lying regions of crust that are proximal to a source of material, such as the Kermadec forearc, and the moat surrounding Canopus seamount. Subduction bend-related faulting is pervasive, but relatively small in scale (<0.3 s TWTT-throw). The inner-trench slope of the overriding plate imaged along Profile B is dominated by extensional faulting and poor sedimentation, except for a large mid-slope basin (25 km-wide, <1 s TWTT-deep). Extensive faulting of the ∼2 s TWTT-thick Kermadec forearc basin and ridge morphology indicates a complex deposition and deformational history.

The interpretation of the profile was considered to provide valuable qualitative insights and shallow quantitative constraints on the velocity structure of the subsurface imaged along Profile B. In Chapter 3, a crust and upper mantle velocity-depth structure model is developed using a forward modelling technique that is initialised using the Profile B swath bathymetry and MCS reflection data.

Chapter 3

Wide-angle seismic data analysis and forward modelling

3.1 Introduction

Chapter 1 introduced the various geophysical datasets acquired during cruise SO215, and presented the merging of multibeam swath bathymetry data to generate a high resolution seabed map. Chapter 2 focussed on the acquisition and processing of the MCS data along Profile B, before concluding with an initial interpretation of the seismic reflection data to inform the initial WA forward velocity-depth model.

In this chapter the WA seismic data are analysed and forward modelled to develop a seismic velocity-depth model of the crust and upper mantle velocity structure along Profile B. The acquisition of the WA seismic data is described in Section 3.2. Before modelling is undertaken, the OBS WA dataset is analysed (Sections 3.3, 3.4, and 3.5) to determine data quality and inform the forward modelling process. The forward model is initialised (Section 3.6) using swath bathymetry data (Section 1.6) as well as the sediment interval velocity (Section 2.3.4.1) and thickness (Section 2.4) derived from the processing and interpretation of the MCS data respectively. Forward traveltime modelling follows the method of Zelt (1998) and Zelt & Smith (1992), and is used in the first instance because of the degree of lateral heterogeneity of the sub-surface velocity structure typical of subduction zones (Section 3.7). The results and initial interpretation of the final forward velocity-depth model are presented in Section 3.7.4 to provide the context for determining the fit of the model (Section 3.7.5). Lastly, the final forward velocity-depth model is directly assessed for goodness of fit and robustness through sensitivity testing (Section 3.8.1) and used to restack the MCS dataset (Section 3.8.2).

3.2 OBSs and wide-angle seismic data acquisition

Twenty-seven OBSs were deployed along Profile B (Figure 2.1), at ∼15 km spacing except for a 30 km gap around the trench due to the extreme water depth exceeding the maximum instrument depth rating (>8 km). Although OBS 09 was successfully recovered, it did not record any usable data. The WA seismic data acquisition was contemporaneous with that of the MCS data, so OBSs recorded seismic signals from the same source array with a shot interval of 60 s (Section 2.2.1). The LC- and KUM-type OBSs recorded seismic signals at 4 and 5 ms sampling intervals respectively (see Figure 2.1) on hydrophone and geophone (one vertical and two horizontal) components. The data from each component have an anti-alias filter applied to remove signal above the Nyquist frequency, which is 125 Hz for the LC-type, and 100 Hz for the KUM deep water-type instruments. Seismic data recorded on the OBSs are stored in a raw format until the instruments are recovered and the data extracted at the end of the shooting phase.

3.3 Wide-angle data

WA traveltime modelling is primarily concerned with accurately determining the sub-surface seismic velocities that govern the arrival traveltimes recorded by OBSs. Such a sub-surface seismic velocity-depth model is achieved by comparing the recorded arrival traveltimes with the calculated traveltimes of rays that have been traced through a theoretical seismic velocity model. Updates are made to this model after the assessment of the fit between the recorded and calculated arrival times by a modeller (forward modelling), or statistically (inversion modelling). Thus it is essential that each 'pick' accurately represents the recorded traveltime of the unaltered seismic signal generated at a known time by the airgun source. Unlike MCS data processing, where the primary objective is to determine the primary reflectivity of the sub-surface with the effective source signature removed (e.g. Section 2.3), the WA seismic dataset is only enhanced to improve data usability and accuracy without altering the characteristics of the source signature. As a result, WA data enhancement here is limited to:

- OBS relocation - data are shifted so that the shots are offset relative to the true OBS location on the seabed, instead of the OBS deployment location (Section 3.3.1); and

- signal enhancement - at greater shot-receiver offsets where the SNR is low, frequency filtering is applied to facilitate traveltime picking through signal enhancement (Section 3.3.2).

The following sections describe how these data enhancement techniques are applied to the OBS records.

3.3.1 Seismograph positioning

Prevailing currents cause an OBS to drift laterally during descent and ascent through the water column, and as a result OBSs are often recovered at significant distances from where they were deployed. As a result of this drift, the true location of an OBS on the seabed is unknown, so the location applied to the headers following OBS recovery is, most likely, incorrect (e.g. Figure 3.1). The implications of this are two-fold:

- profile-parallel shifting - the shot-receiver offsets are miscalculated, and therefore the seismic traces do not correctly represent the true profile-parallel distances traversed by the seismic signal; and

- profile-perpendicular shifting - movement of an OBS out-of-plane of the acquired profile not only results in the sampling of out-of-plane sub-seabed structures, but can also significantly alter the depth of the seabed on which the OBS is located.

Both of these shifts have the potential to introduce errors greater than are acceptable for velocity modelling. The most clear manifestation of OBS mislocation is in the asymmetry of the waterwave, which should display the shortest travel time when the seismic source is closest to the instrument (i.e. shot-receiver offset=0 km). If an OBS drifts in the along-profile direction during the deployment, the waterwave will appear asymmetric on the resulting record section (e.g. Figure 3.1c). If an OBS drifts out-of-plane of the acquisition profile, and lands on a seabed at a different depth, arrivals are shifted in time. Consequently the first stage in OBS data analysis is to determine OBS locations and depths on the seabed and apply appropriate corrections to shot-receiver offsets and traveltimes as shown in Figure 3.1 (Appendix B).

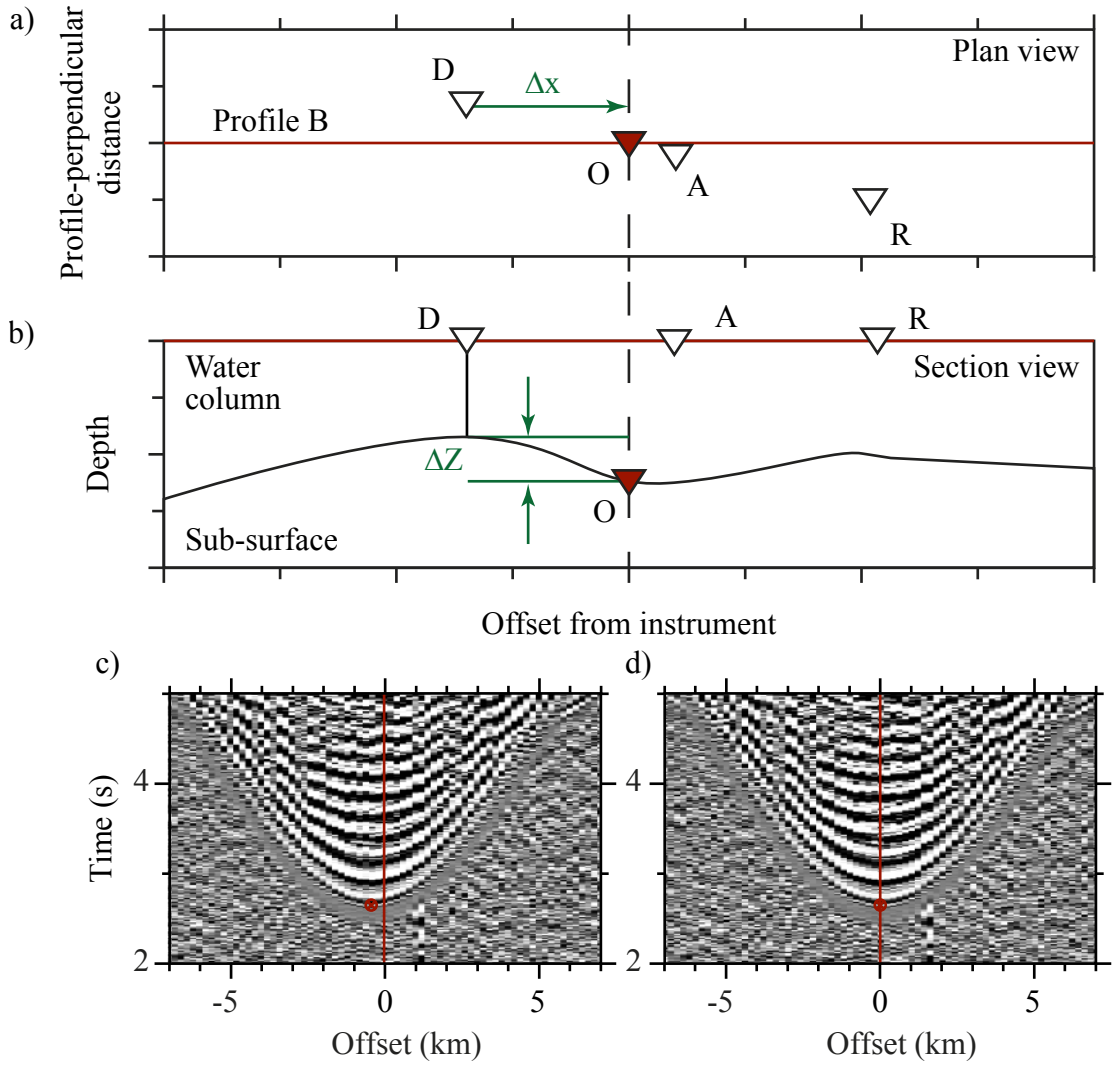

Figure 3.1: OBS relocation schematic diagram. a) OBS relocation in plan view, and b) section view. Deployment (D), recovery (R), average (A), and true (O) OBS locations are indicated. c) Original OBS 07 data, with the peak of the waterwave indicated by the red circle, initially ∼0.5 km laterally from the origin of the instrument. d) Relocated OBS 07 data, with the peak of the waterwave now centred on 0 km offset. Note that there is minimal temporal shifting (50 ms) of the waterwave on OBS 07, although for some instruments this can reach 100s of ms (see Appendix B).

3.3.2 Frequency analysis and filtering

Seismic energy that propagates over large distances through the crust and upper mantle is naturally filtered, predominantly at higher frequencies, by the attenuative properties of the sub-surface. To maximise the frequency bandwidth of the recorded data, particularly at lower frequencies, hydrophone components are preferentially chosen for data analysis and traveltime picking (Figure 3.2), although in some cases the SNR of the hydrophone component is poor so that the geophone component is

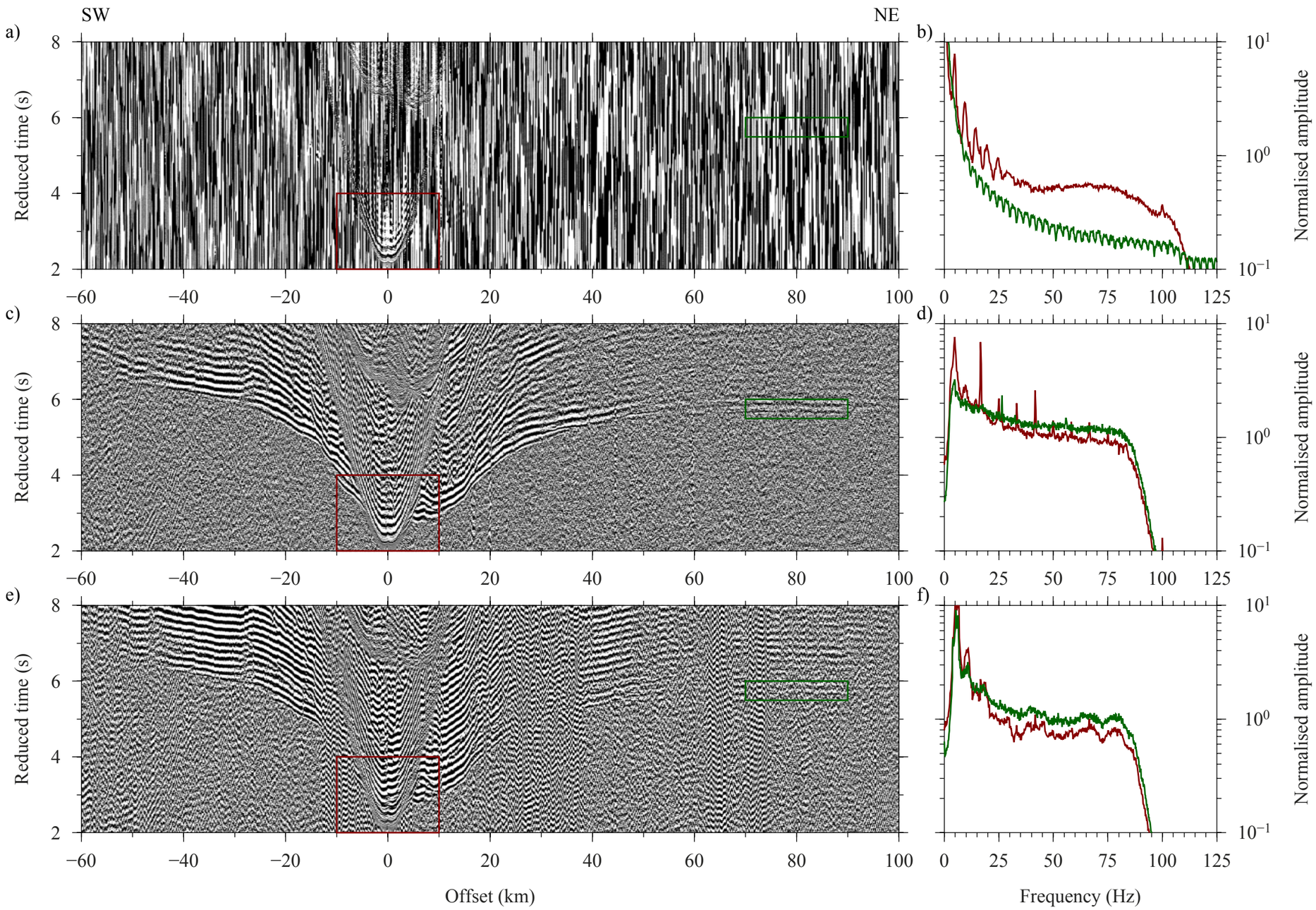

Figure 3.2: Filtering of OBS 19 record sections with frequency spectra. a) Unfiltered hydrophone data, with the red and green boxes showing the subset of waterwave and mantle refractions sampled to determine the frequency spectra (represented by the same colours) in b). Note how only a waterwave is readily observed in a), with low frequency (<2 Hz) high amplitude noise masking all sub-surface arrivals. c) Hydrophone data with a minimum-phase Butterworth filter applied (band-pass 2-4-80-100 Hz). Sub-surface arrivals are now clear up to 100 km offset, and the frequency spectra in d) highlights the increase in SNR across the useful bandwidth for the mantle refractions (green line) relative to those in b). e) and f) Vertical geophone data and frequency spectra with a minimum-phase Butterworth filter applied (low-pass 80-100 Hz), highlighting the natural low-frequency filtering effect of the geophone component.

used instead.

During WA data analysis the dataset was preferentially assessed and traveltime picked using the raw data. However, the relatively low SNR at longer offsets makes phase identification and picking difficult. Consequently, to enable reliable picking at longer offsets, the data were frequency filtered with parameters tailored to phases, offset ranges, and instrument locations. As such, the band-pass filter applied would start relatively broad (e.g. 2-4-80-100 Hz; Figure 3.2) and the high-pass and stop frequencies were gradually decreased with increasing offset from the instrument. Decreasing filter pass bandwidths has an increasingly large effect on the apparent onset time and signal characteristics of an arrival, which was accounted for by increasing the uncertainty assigned to the picks (described in Section 3.5).

3.4 OBS wide-angle dataset phase identification

The WA dataset consists of 26 OBSs, with data of variable quality recorded on all four channels. The SNR and type of seismic phases recorded on each of these instruments are controlled by:

- instrument-seabed coupling - for example, instruments located on the lower-trench slopes of the overriding plate, where there is only minimal (<0.1 km) sediment cover, generally exhibit lower SNR and shorter offsets to which sub-surface arrivals are observed;
- instrument component - hydrophones tend to observe higher SNRs than the geophone components (e.g. Figure 3.2);
- shallow sub-surface geology - in regions such as northeast of Canopus on the Pacific plate where there is significant sediment cover, relatively planar seabed topography, and a less deformed sub-surface, OBSs exhibit higher SNR and longer shot-receiver offset arrivals as the seismic signal attenuates less; and
- large scale geology - the phases recorded on each OBS are primarily determined by the geological layers and features that the arrivals propagate through. For example, OBSs on or near Canopus seamount observe highly irregular and asymmetric arrival geometry controlled by the perturbation of rays through the seamount edifice.

The OBSs are divided into three groups according to significant changes in the major geology along Profile B: instruments 01-10 on the Kermadec forearc, 11-15 in the trench, and, 16-27 on the Pacific Plate.

Traces are stored with the relocated instrument-shot offsets relative to each OBS, with positive offsets to the northeast and negative offsets to the southwest. OBS positions along-profile are defined by their distance increasing from the most south-western shot point, which is considered as 0 km offset. For most instruments, the hydrophone component was used for WA data analysis as it typically displayed the highest SNR, and displayed readily observable arrivals to the longest offsets. For OBS 11 and 18, which had poor signal on the hydrophone component, the geophone component was used instead, with the traveltime pick uncertainty adjusted accordingly.

The arrivals recorded by each OBS were identified initially by their offset from the instrument and their apparent velocity, set in the context of the expected underlying geology. Waterwaves are observed as the first arrival at the shortest offsets on all instruments, up to an offset that is a function of the seabed depth of the instrument. At greater offsets, sediment turning waves become the first arrival, although this is only the case where the sediment column is thicker than ∼1.5 km (e.g. on the Kermadec forearc, 50-100 km offset along profile; Figure 2.7). These arrivals display apparent velocities of 2.5-3.5 km s^{-1}. At greater offsets, and where the sediment is less thick, crustal turning waves are observed as the first arrival (4.0-7.0 km s^{-1}). Beyond this, mantle turning waves are observed as the first arrival (>7.5 km s^{-1}). Only OBS located on relatively flat-lying seabed record Moho reflections, at a range offsets behind the crustal and upper mantle refractions. These are typically more difficult to identify and assign a traveltime pick for because they are embedded within the refracted arrival wavetrain.

In order to ensure consistency in arrival picking, each arrival is assigned its own phase designation. These are:

W_w - direct waterwave arrival;

P_s - sediment P-wave refraction;

P_g - crustal P-wave refraction;

P_mP - Moho reflected arrival; and

P_n - mantle P-wave refraction.

Picking of the first and secondary arrivals was undertaken on each instrument with the phase identifications in mind, although in areas of highly variable bathymetry and regions of low SNR, the assignment of phases was more challenging. For such cases, phase identifications were made for each pick based on which was

the most appropriate, and these were subsequently tested against the arrivals that were forward modelled, enabling the iterative reassignment of misassigned picks. Example phase identifications are shown in Figure 3.3 for the Kermadec forearc, Figure 3.4 for the Kermadec trench, and Figure 3.5 for the Pacific plate OBSs.

3.4.1 Kermadec forearc (OBSs 01-10)

OBSs 01-10 were deployed on the Kermadec forearc in seabed depths between 2 and 5 km (Figure 2.1). The arrivals on these OBSs generally have a good SNR and display a varying arrival geometry, suggesting that the sub-seabed velocity structure in this region is quite laterally variable. This indicates that there may be significant variations in the velocity structure and thickness of the forearc crust sampled.

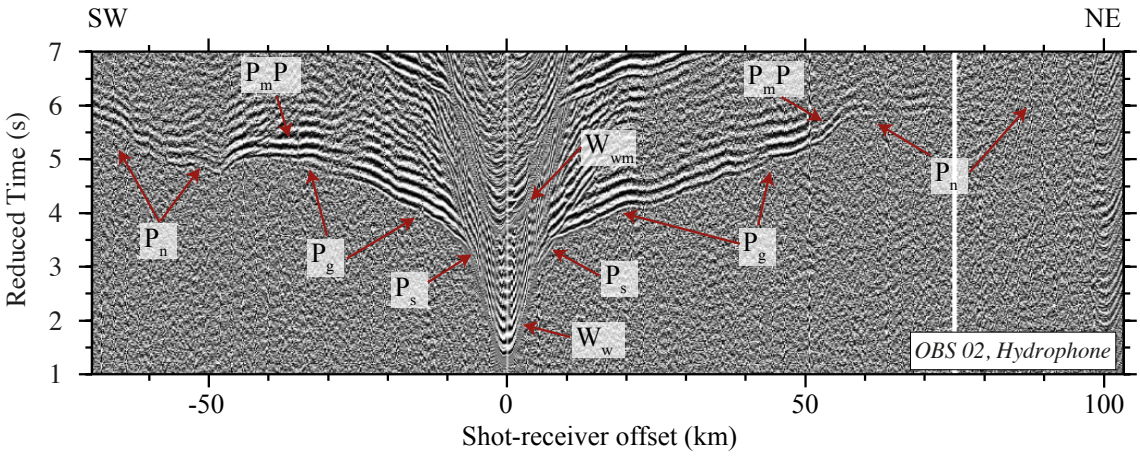

Figure 3.3: Filtered hydrophone data from OBS 02 located on the Kermadec forearc, reduced at 8 km s^{-1} (see Figure 2.1). Identified phases are annotated. Note that P_g arrivals are observed to ~60 km-offset northeast of the instrument, but to less than 50 km to the southwest.

P_s arrivals (2.2-3.5 km s^{-1}) are only observed on OBS 01-04 (e.g. OBS 02, Figure 3.3). The observation of these arrivals coincides with the ~2 s TWTT-thick sedimentary sequences imaged by the MCS data between 40 and 100 km offset along profile on the Kermadec forearc (Figure 2.7). Further northeast along Profile B where the sediment cover is significantly thinner, P_g arrivals (4.0-7.0 km s^{-1}) are observed as the shortest-offset (at <4.5 km shot-receiver offset) refracted arrivals. These arrivals are observed to varying offsets on the forearc instruments, although typically reach 50-70 km from the instrument. At greater offsets, P_n arrivals (7.5-8.0 km s^{-1}) are observed, although these are much less evident than those for instruments located on the Pacific crust. Reflections from the forearc Moho, P_mP, are observed as a secondary phase arrivals. These are the most inconsistently observed arrival,

which may indicate varying degrees of signal attenuation in the forearc crust or lateral variation in geometry of the forearc Moho.

3.4.2 Kermadec trench (OBSs 11-15)

OBSs 11-15 were deployed on both the overriding and subducting plates in the vicinity of the trench (180-260 km profile offset) at seabed depths of between 5.5 and 7.5 km. The trench OBSs generally display arrivals with the lowest SNR and most complex arrival geometry of the entire WA dataset, making phase identification more challenging (e.g. Figure 3.4).

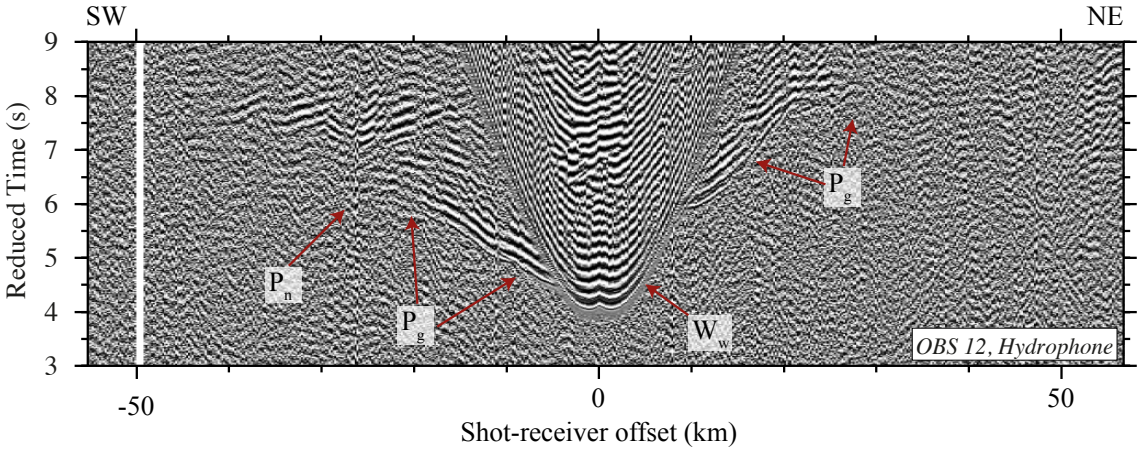

Figure 3.4: Filtered hydrophone data from OBS 12 located on the lower-trench slope of the Kermadec forearc (see Figure 2.1), reduced at 8 km s^{-1}. In the Kermadec trench region arrivals have significantly lower SNR, and are rarely observed beyond 50 km-offset from the instrument. The data gap at -50 km offset was a result of the 6-shot airgun downtime described in Section 2.3.3.

P_g arrivals display abnormally low apparent velocities (3.6-6.5 km s^{-1}) for OBSs located on the inner-trench slope (150-220 km offset along profile). At the outer-trench slope, P_g arrivals are observed with more typical apparent velocities between 4.0-7.0 km s^{-1}. P_n arrivals (>7.0 km s^{-1}) are rarely observed. Arrivals tend only to be observed by trench-located instruments to typical offsets for a given phase if they pass through the plate on which the OBS is located. Arrivals that pass through the subduction interface are significantly attenuated, resulting in the apparent rapid reduction in SNR beyond the trench axis. For example, OBS 12, located ~25 km southwest of the trench, only displays clear arrivals northeast of the instrument to <30 km, whereas signal is observed to at least 40 km to the southwest (Figure 3.4).

3.4.3 Pacific plate (OBSs 16-27)

OBSs 16-27 were deployed on the Pacific plate, in a range of water depths (1.5-6.0 km) traversing Canopus seamount. The OBSs located on the Pacific plate typically had the highest SNRs of the entire OBS dataset, indicating a very consistent arrival geometry.

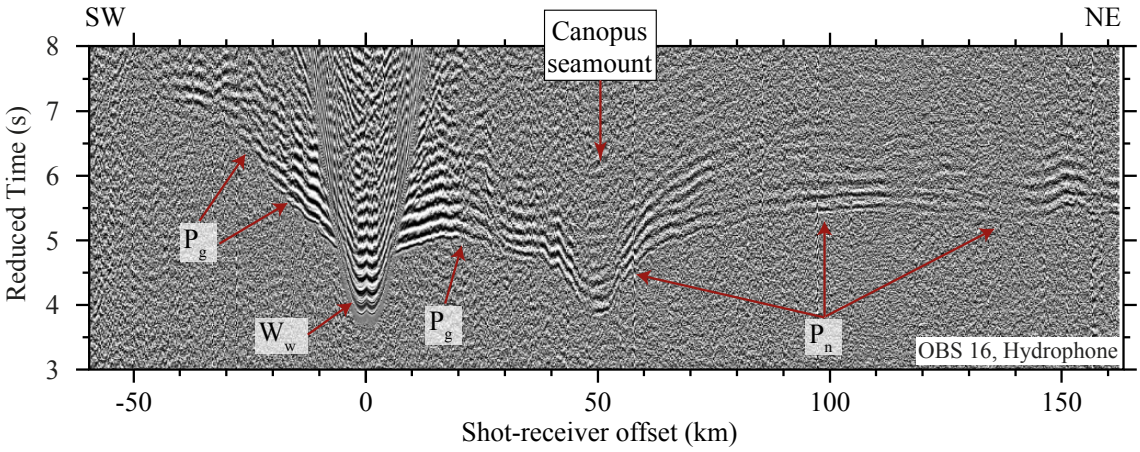

Figure 3.5: Filtered hydrophone data from OBS 16 located on the Pacific plate, reduced at 8 km s^{-1} (see Figure 2.1). The effect of Canopus seamount on arrival traveltimes is demonstrated between 40-70 km offset. OBS 16 highlights how long-offset P_n arrivals are observed on most of the Pacific plate instruments.

Although thick sediment accumulations up to ~1 s TWTT-thick are observed on the MCS reflection section in the moat around Canopus seamount (Figure 2.8), no P_s phases are observed as first arrivals on Pacific plate OBSs (Figure 3.5). Instead, low velocity (4.0-5.0 km s^{-1}) P_g phases are the shortest offset first arrivals. These crustal refractions increase in apparent velocity up to 7.4 km s^{-1}, at 30 km from the instrument. At offsets greater than 30 km, the first arrival observed is P_n, with apparent velocities of >7.4 km s^{-1}. The rapid and significant change in bathymety associated with Canopus seamount perturbs the travel times of arrivals propagating through it, causing them to arrive earlier than those at adjacent offsets (e.g. between 40-70 km offset on Figure 3.5). OBSs on the Pacific plate recorded P_n arrivals up to 200 km from the OBS although, as with the Kermadec trench OBS group (Section 3.4.2), few arrivals were observed beyond the trench axis (e.g. southwest of -40 km on Figure 3.5). Observing arrivals for up to 200 km with the Pacific plate instruments suggests that signal was attenuated less through the crust and mantle of this region compared to that of the Kermadec forearc, where P_n arrivals are rarely observed beyond 100 km shot-receiver offset.

3.5 Wide-angle data traveltime picking

Wide-angle phase arrival traveltime picking was undertaken using *zplot*. This software facilitates the assignment of phase type as well as uncertainty to each pick, and enables user-defined data windowing and filtering, to minimise the potential for incorporating systematic picking errors.

For the purpose of traveltime modelling, the traveltime of each arrival, and the degree of certainty to which that time is known, must be quantified. Traveltime picks were made for each clearly identifiable phase on a trace, according to the predetermined method for phase identification (Section 3.4), and an independent pick uncertainty value is assigned (Figure 3.6).

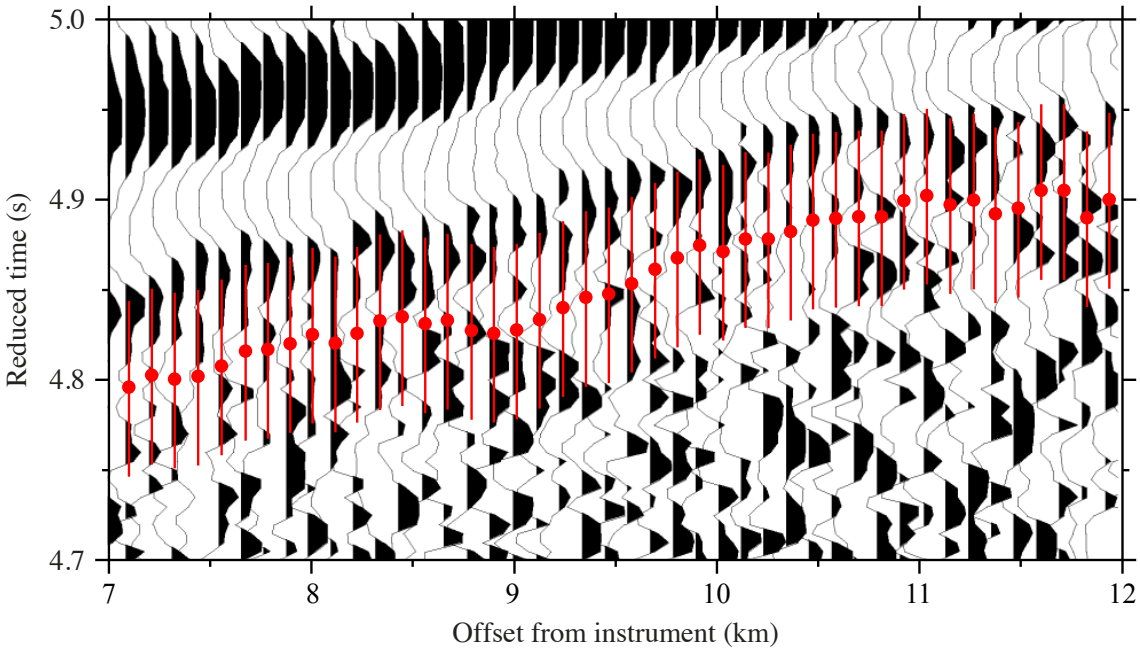

Figure 3.6: Example of filtered data from OBS 16, reduced at 8 km s^{-1}. P_g picks are shown by red circles, and red vertical lines represent the uncertainty (50 ms) associated with each pick. Note that because the data are filtered for plotting, the picks may not perfectly align with the onset of seismic energy on a trace.

There are a number of errors and uncertainties involved in the WA seismic method that are carried through to the data. The magnitude of the combined error is considered for each pick to enable statistical analysis of model fit. The total uncertainty for any given pick is defined by a number of instrument-dependent and pick-specific uncertainties. Instrument-dependent uncertainties include:

- sampling interval - for the LC- and KUM-type OBSs, this is 4 and 5 ms, respectively (Peirce & Watts, 2011);

- shot location - shots were fired on time at 60 s intervals, and shot locations were determined from GPS navigation to an accuracy of ±10 m given the limited constraint on the location of the airgun array during towing; and
- OBS location - following the relocation of each OBS (Section 3.1), this is the uncertainty in the determined OBS location.

The uncertainty associated with each specific pick includes bias introduced by the picker as well as the qualitatively assessed uncertainty in determining the onset of the arrival embedded in background noise, as a function of the SNR, and varies for each shot recorded by each instrument as well as on an instrument-by-instrument basis. The pick specific uncertainty is also influenced by the shot-receiver offset of the pick and the location of the instrument along profile relative to the underlying geological structure. Greater instrument deployment depths and shot-receiver offsets, and hence longer ray-paths, typically yield lower signal-to-noise ratios, resulting in a larger pick uncertainty. The combined error is the total pick uncertainty for each phase on each trace, and is applied to the picks made for each OBS (summarised in Table 3.1).

3.6 Forward wide-angle velocity-depth model construction

Subduction systems typically display extremely laterally heterogeneous seismic velocity structure, and so to ensure that a suitable model is developed, forward ray-tracing was chosen as the primary velocity-depth modelling technique. Before a forward model can be developed, a starting model is required with as much input constraint as is possible at this point to simplify and aid the modelling process. 2D forward modelling assumes all shots and receivers are located on-profile, such that all shot and instrument locations are represented by their offset along profile, and not their true geographic location. Construction of the initial velocity-depth model, therefore, followed the method:

- projection - shot points, OBS locations, and bathymetry data were projected from geographical coordinates into a linear model space (Section 3.6.1);
- bathymetry - swath bathymetry data were downsampled to the model node spacing, whilst accurately representing the seafloor depth (Section 3.6.2);

Instrument	W_w	P_s	P_g	P_mP	P_n
01	13	32	48	48	80
02	13	32	48	48	80
03	13	32	48	48	80
04	13	32	48	48	80
05	13	-	48	48	80
06	13	-	48	48	80
07	13	-	48	48	80
08	13	-	48	48	80
09	-	-	-	-	-
10	13	-	48	48	80
11	15	-	60	75	80
12	15	-	60	75	80
13	15	-	75	90	90
14	15	-	50	60	80
15	15	-	50	60	80
16	15	-	50	60	80
17	15	-	50	60	80
18	20	-	55	60	80
19	13	-	40	48	80
20	18	-	44	52	80
21	13	-	40	48	80
22	13	-	40	48	80
23	13	-	40	48	80
24	13	-	40	48	80
25	13	-	40	48	80
26	13	-	40	48	80
27	18	-	44	52	80
Group					
Pacific plate	13	-	44	52	80
Trench	15	-	54	64	83
Forearc	15	32	46	48	80
Full dataset	14	32	46	51	80

Table 3.1: Pick uncertainties for each phase, summarised for each OBS as well as the different instrument groups as outlined in Section 3.4. Note that OBS 09 had no recorded data and, therefore, no assigned picks or uncertainties. Only OBSs 01-04 recorded P_s arrivals that were not masked by the waterwaves, so are the only OBSs with these picks.

- water column - the seismic velocity structure of the water column was determined to 1.8 km below the sea surface using an XBT at four locations along Profile B (Figure 2.1), with a constant gradient applied below this to the seabed; and

- sediments - initial sediment thickness and velocity were determined from the processed and interpreted MCS data (Section 3.6.4).

3.6.1 Profile projection

The WA velocity model was initialised by projecting airgun shots and relocated OBS positions onto the profile with offset increasing, from the origin at the southwestern end of the profile, to give a full length of 431.88 km (Figure 3.7). Projecting a 2D profile into a 1D space introduces a spatial error, by assuming that the y-dimension, which varies by up to 300 m along Profile B, has no length. Despite this simplification, the error introduced is negligible, because in the worst case scenario a path-length change over a short (e.g. 40 km-long) profile segment is ∼1 m. Longer offset shot-receiver pairs are subject to even smaller relative path-length changes.

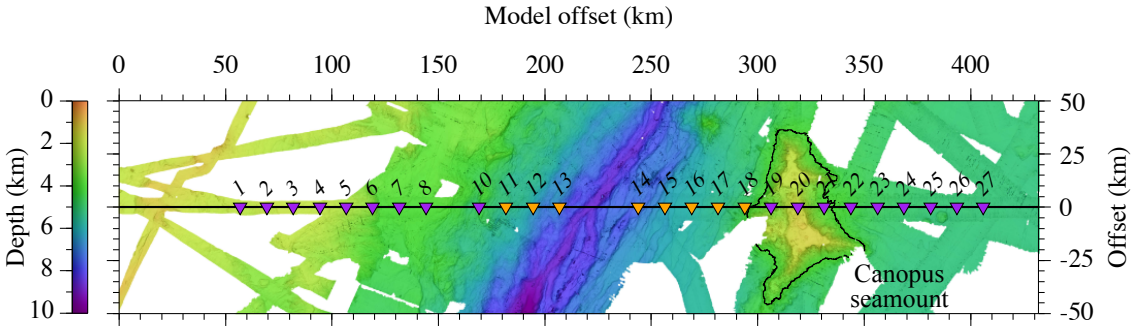

Figure 3.7: Profile B (black line) and surrounding swath bathymetry projected into model space. OBSs are the numbered inverted triangles along the profile (orange are KUM-type and purple are LC-type).

3.6.2 Seafloor bathymetry

Seafloor bathymetry has a first-order influence on the traveltime of WA arrivals. This influence is evident in the significant variation in waterwave arrival onset time (e.g. Section 3.4) and regions of extreme seafloor bathymetric variation, such as in the vicinity of the Kermadec trench and Canopus seamount, where the refracted and reflected arrival travel times effectively mirror the shape of the seafloor (e.g. Figure 3.5).

The regional bathymetry information provided by the GEBCO dataset is too insensitive to small-scale (<1 km) changes in seabed depth to provide suitable constraint for modelling purposes. In contrast, the swath bathymetry dataset (Section 1.6) has the highest depth and lateral resolution of the datasets available (at ∼50 m

node spacing), and so was used to define the seabed in the initial model by filtering and then downsampling to ∼2 km intervals (Figure 3.8). The downsampled model bathymetry adequately represents the variations in seabed bathymetry for modelling purposes, with the average residual misfit between the model and swath profiles of 50 m, introducing an error in the modelled traveltime of an arrival of up to 13 ms (assuming water of 1.5 km s^{-1}, juxtaposed against rock with a seismic velocity of 2.5 km s^{-1}). While this potential error is large relative to the instrument sampling rate (4 or 5 ms), it is not significant compared to the assumptions already incorporated into the modelling process, such as instrument relocation errors and the assigned pick uncertainties.

3.6.3 Water column velocity structure

The speed of sound in seawater is relatively consistent at ∼1.5 km s^{-1}, although does vary by up to 3% due to changes in temperature, salinity (density), and pressure. Generally in the oceans, the seismic velocity decreases to the bottom of the thermocline, and increases below this to the base of the water column.

The suitability of a water column velocity model can be tested by comparing the direct waterwave arrivals observed on each OBS with the equivalent modelled phases. Although single-velocity water column models did produce a fit within error to the short-offset arrivals (<5 km offset) for most instruments, they could not fit observed waterwaves at greater offsets (Figure 3.9) due to the relatively long travel path of each seismic wave through the water column.

A more realistic representation of the water column seismic velocity structure was derived from the XBT dataset, acquired during the deployment of the OBS instruments. The XBTs sampled to ∼1.6 km depth below sea surface along Profile B (Figure 3.10), and measured temperature-depth profiles that were converted to seismic velocity and groundtruthed against a seismic velocity probe profile acquired in the work area to 3.0 km depth below sea surface (Peirce & Watts, 2011). Each XBT profile was simplified to just four points that sufficiently recreated the measured velocity curve to 1.6 km depth and projected to the seabed. In between XBT sample locations the water column velocity profile was interpolated to create a laterally smooth velocity model across the model space. The resulting water column velocity model (Figure 3.11a) generates calculated waterwave arrivals that closely match the observed picks for each OBS, fitting to an average misfit of just 17 ms for over 7105 waterwave traveltimes for the 26 OBSs (Figure 3.11b). Seismic velocities are expected to reach 1.59 km s^{-1} at the bottom of the Kermadec trench (>8 km depth) which, although much higher than is typically observed in the oceans, is comparable

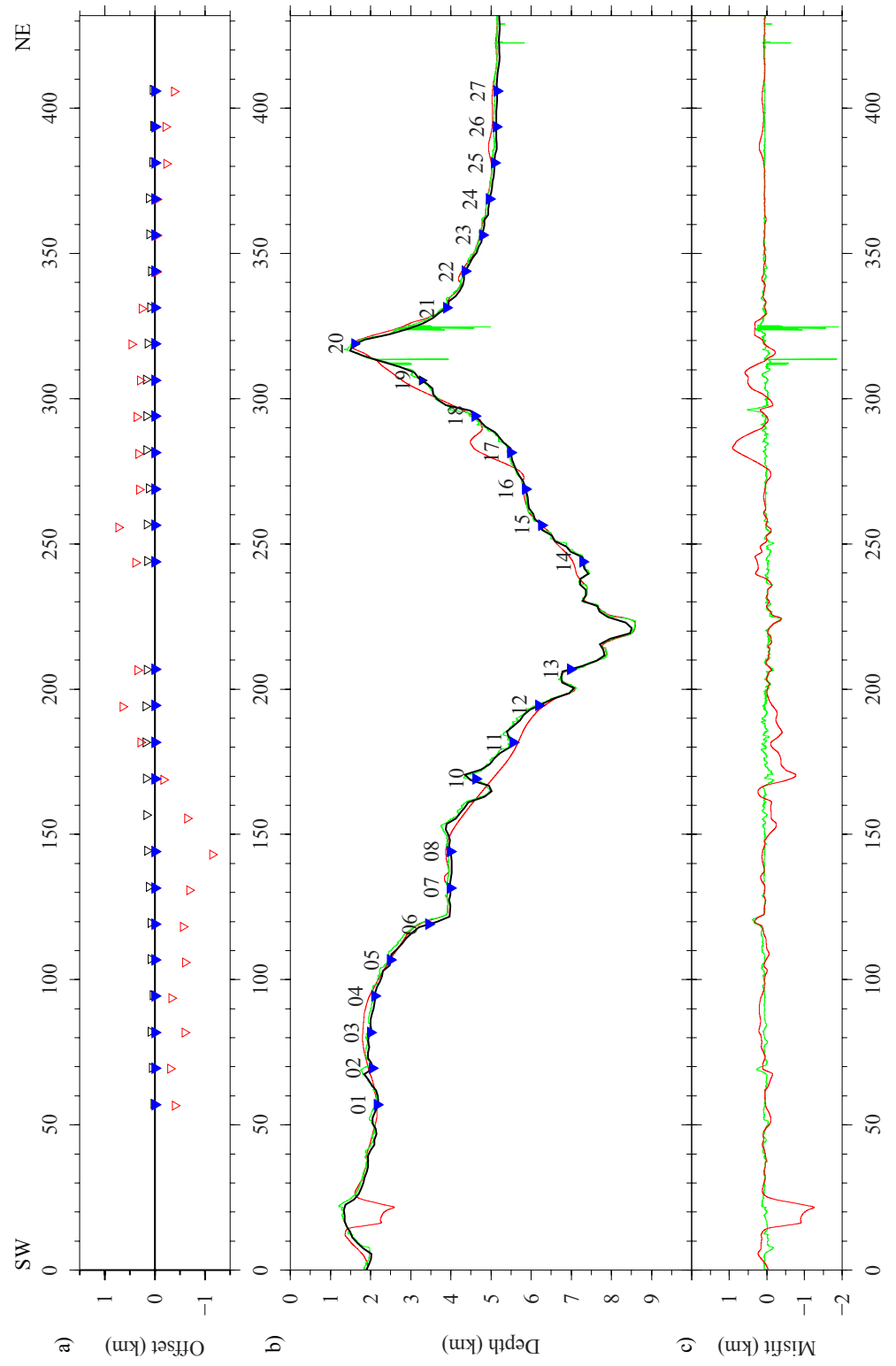

Figure 3.8: Caption next page.

Figure 3.8: (Previous page) Overview of bathymetry and OBS locations along Profile B. a) Plan view of the profile with the deployment (black inverted triangle) and recovery (red inverted triangle) OBS locations indicating instrument drift through the water column, while solid blue inverted triangles show relocated final model positions. Note that although OBS 09 was successfully deployed and recovered, it is not included in the model space because no usable seismic data were recorded by this instrument. b) Bathymetry derived from GEBCO (red line; IOC *et al.*, 2003), swath (green line), and as determined for WA modelling (black line). OBS are shown in their relocated positions. c) Residual bathymetry between the model and the GEBCO 30 arcsecond and swath profiles, resulting in average misfits of ∼150 and 50 m respectively. Bathymetric spikes are residual acquisition artefacts not removed through swath data processing.

to measurements made at Challenger Deep in the Mariana trench (1.60 km s^{-1} at ∼8 km-deep; Taira *et al.*, 2005). At the bottom of the Mariana trench (∼11 km depth), Taira *et al.* (2005) observed the water column seismic velocity reach over 1.65 km s^{-1}.

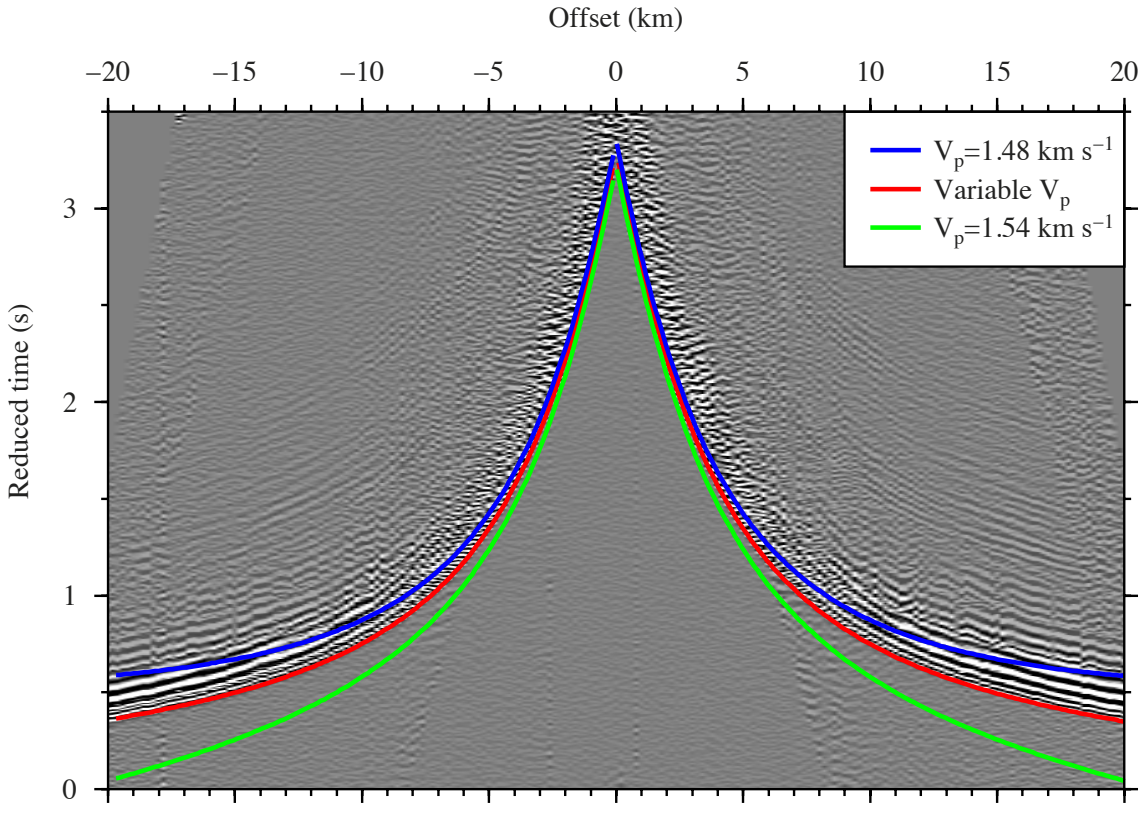

Figure 3.9: Waterwave arrivals for OBS 24, reduced at 1.5 km s^{-1}. The calculated waterwaves through different water column velocity models are overlain. Fixed water column velocity models are able to replicate the arrival well at short offsets, but diverge at longer offsets. A variable (4-layer) water column velocity structure, which accounts for the thermocline, visually fits the observed arrival at all offsets.

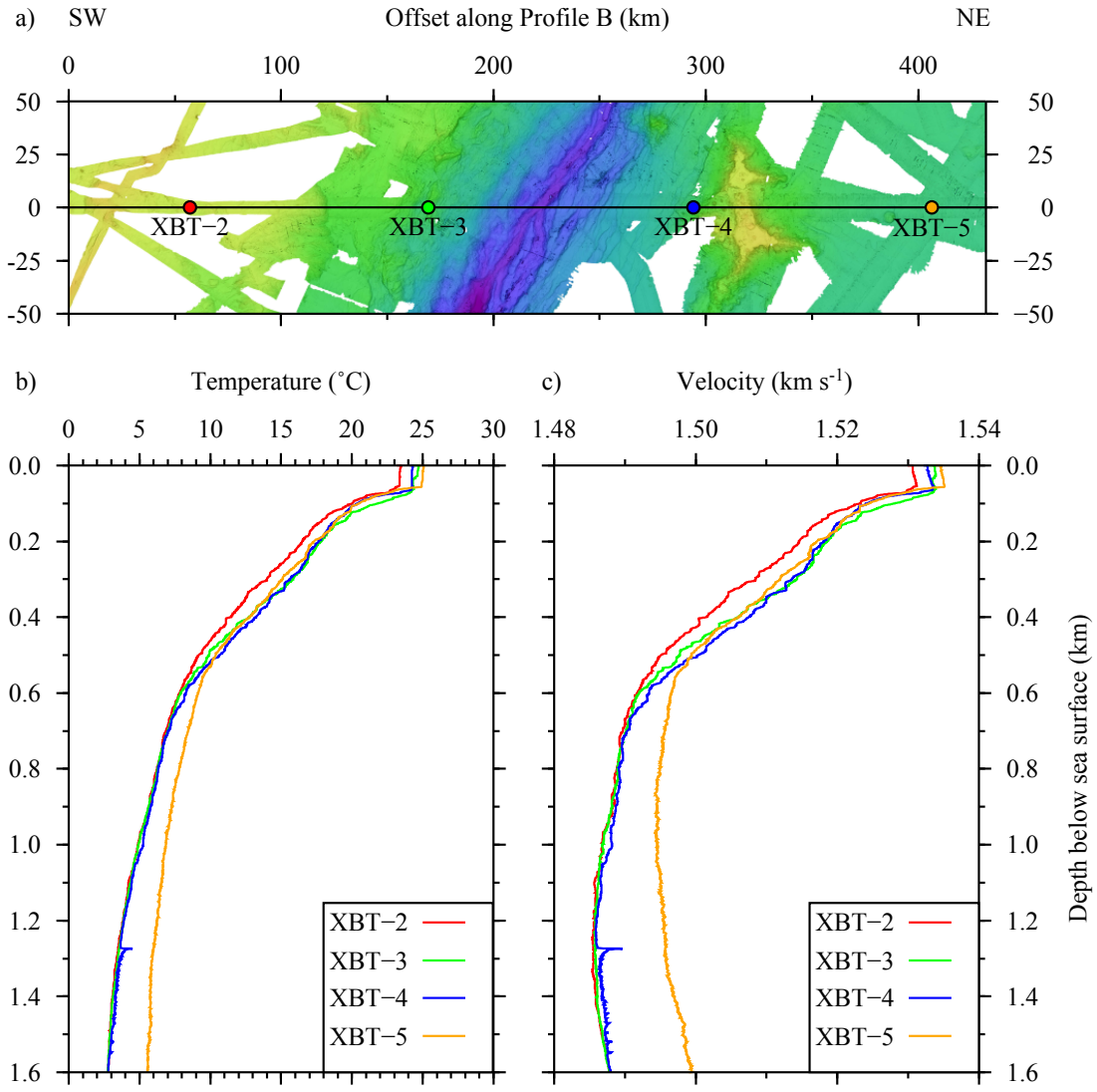

Figure 3.10: Seismic velocity profiles through the water column along Profile B. a) Map showing the location of XBT profiles. b) Temperature profiles through the water column to 1.6 km depth. c) Seismic velocity profiles through the water column to 1.6 km depth.

3.6.4 Sediment layer thickness and velocity

Sediment layer seismic velocity and thickness were constrained by the velocity analysis and interpretation of the MCS dataset, respectively (Section 2.3.4 and 2.4). The stacking velocities for the reflections sampled at each CMP-gather (see Section 2.3.4.1), were converted to interval velocities using the Dix equation (Dix, 1955):

$$V_{int} = \left(\frac{\left({V_{RMS2}}^2 \times t_2 \right) - \left({V_{RMS1}}^2 \times t_1 \right)}{t_2 - t_1} \right)^{1/2} \tag{3.1}$$

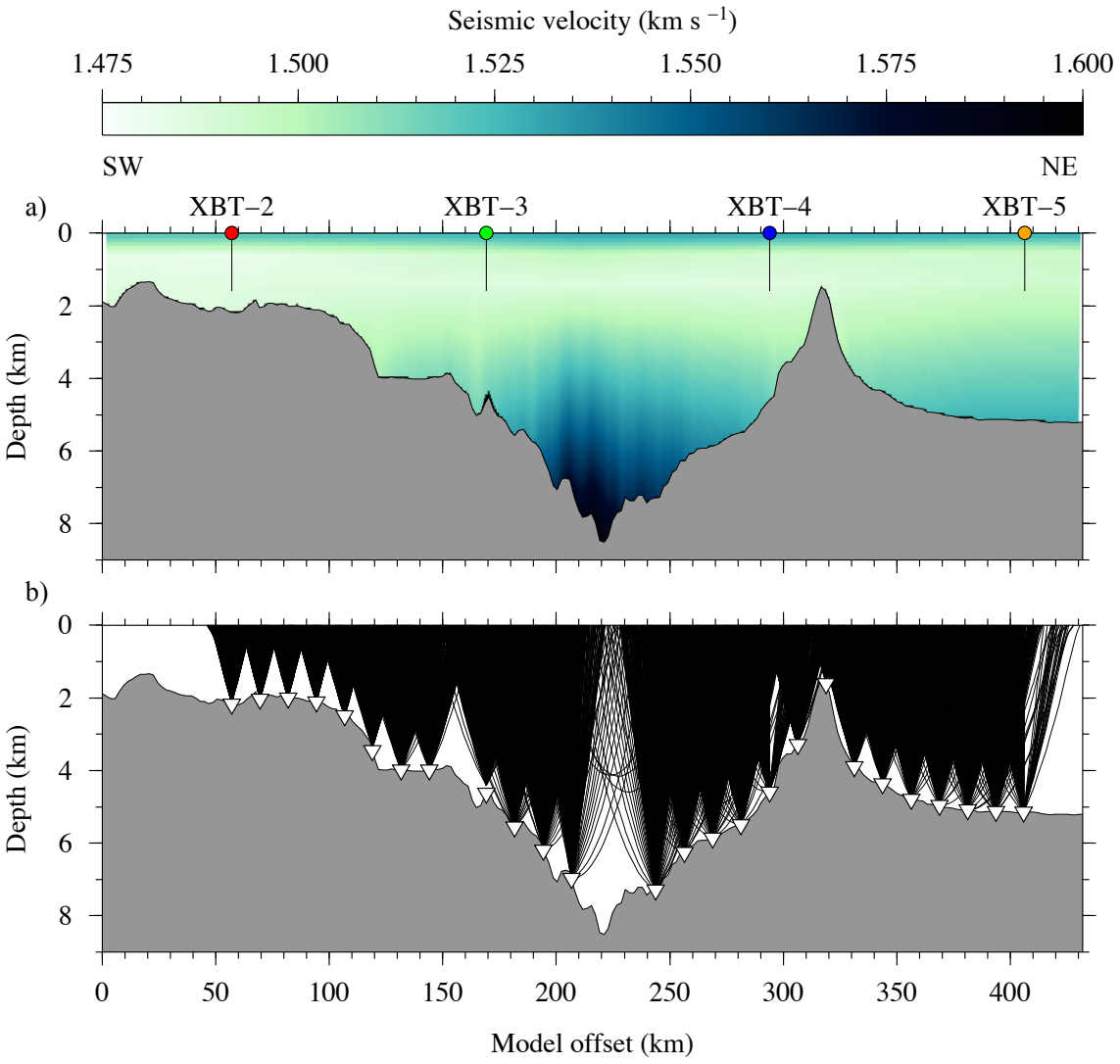

Figure 3.11: Profile B water column velocity-depth model and waterwave tracing. a) Water column velocity-depth model, interpolated between XBT-cast locations (indicated by the circles, where the colour matches the XBTs presented in Figure 3.10). Maximum cast depths below sea surface are indicated by the vertical black lines. Seismic velocities decrease from the sea surface through the thermocline, but then increase to the bottom of the model. b) Traced waterwaves for each OBS (inverted triangles) through the water column velocity model, with a combined T_{RMS} misfit of 17 ms.

where V_{int} is the interval velocity, and V_{RMSn} is the RMS velocity for a given sample in time, t_n.

These interval velocities were averaged at the seabed and basement for the sediments located on the Pacific and Kermadec forearc crusts to provide a simplified velocity structure for both of the two major regions of sediment accumulation in the model (Figure 3.12). Sediment layer thickness, determined from the interpreted seabed and top-crust reflections (Section 2.4), was then converted from TWTT to

depth using this velocity structure and draped beneath the corresponding seabed depth nodes, with the node velocity assigned to match (Figure 3.12).

The forearc crust is covered by sediments that vary between ~0.1 km-thick in the lower-trench slope region to 2.2 km-thick in the forearc basin, with seismic velocity of 1.6 and 2.5 km s^{-1} at the seabed and basement respectively. Sediments on the Pacific crust are more consistent, reaching 1.2 km thick in the moat of Canopus seamount, with seismic velocity increasing from 1.8 km s^{-1} at the seabed to 3.2 km s^{-1} at the basement. On average, the sediment column is 0.8 km thick.

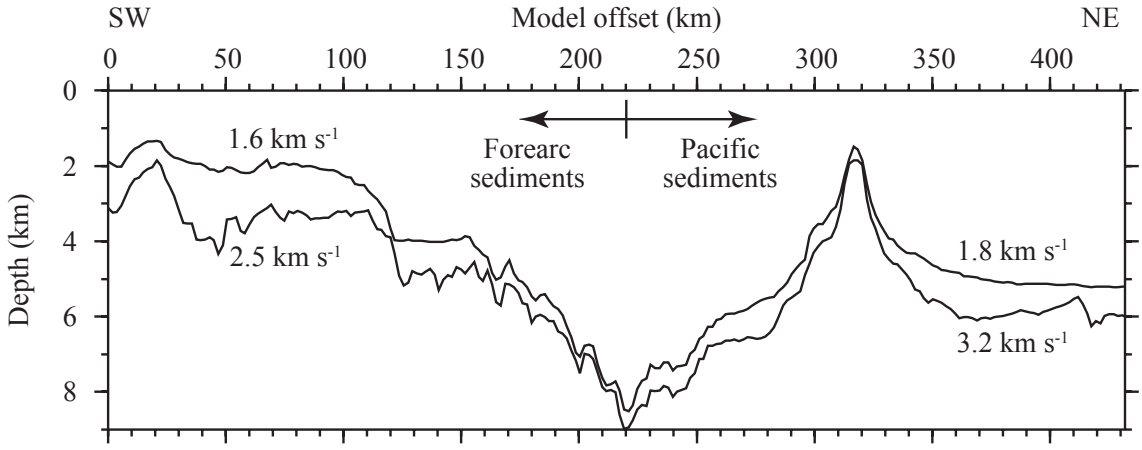

Figure 3.12: Initial model sediment thickness and seismic velocity structure draped beneath the seabed determined in Figure 3.8. Sediment thickness was obtained by converting the MCS-interpreted layer TWTT values to depth using the simplified sediment interval velocity model shown.

3.7 Forward travel-time modelling

The WA seismic data were modelled following the forward modelling technique of Zelt & Smith (1992), embedded in the programme *rayinvr*. Forward modelling enables the user to iteratively improve a velocity model by comparing the computed arrival traveltimes to those that are observed. The use of this method is preferable to that of traveltime and full waveform inversion in regions of extreme lateral velocity heterogeneities, such as at a subduction system, as it enables a greater control over the lateral and vertical division of the velocity model. For example, *rayinvr* allows layers to pinch out to zero thickness and have a first-order velocity discontinuity at the layer boundaries. Layers are defined by a series of depth as well as upper and lower velocity nodes at any point along the model space, i.e. the nodes do not need to be equally spaced, and can vary in interval with depth. Velocity nodes

for the upper and lower layers are laterally independent of the depth nodes, so can occupy a point along a layer that has been interpolated between two depth nodes. The modelling capabilities are thus extensive although, because of the user-driven improvement of the model, are open to human bias and subjectivity. As a result it is important that these models are robustly tested against independent modelling techniques as well as other datasets, to highlight any regions where the user has strongly influenced the model and to determine the limitations of the model and the dataset.

The velocity-depth model is improved using an iterative top-down approach. The shallow layers are altered so that the modelled arrivals produce a good fit to the observed data before moving on to the next layer down. For each layer, arrivals are analysed for a subset of instruments in a sliding window from one end of the model, or section of the model, to the other. Layer depths and upper and lower seismic velocities are altered to minimise the arrival misfit, and only if a reasonable fit was not achievable with the existing model parameters was an additional model layer included. Model improvements were generally made so that large vertical or horizontal changes in velocity and layer thickness were not introduced. To ensure the robust development of the forward velocity-depth model, the modelling process was undertaken by:

- refining sub-seabed velocity-depth structure - with well located OBSs and constrained water column velocities, the sub-seabed structure was improved iteratively to minimise the misfit between modelled and observed arrivals;
- sensitivity testing of the forward velocity-depth model - after a good fit was achieved between the forward modelled and observed data, the sensitivity of the model fit to changes in layer depths and velocities was tested; and
- restacking of MCS data to improve sub-basement reflectivity - the final forward velocity-depth model was converted into stacking velocities and used to restack the MCS dataset, improving the velocity constraint on deeper reflections such as the Moho.

3.7.1 Assessing model improvement

The fit of the observed to the calculated arrival traveltimes was initially assessed visually, to determine a good fit of the broad data trends for each instrument. Having determined a good visual fit for a set of arrivals, the traveltime fit was assessed more robustly using the root mean square misfit (RMS) calculation:

$$T_{RMS} = \sqrt{\frac{1}{n}(T_1^2 + T_2^2 + T_3^2 + ...T_n^2)} \tag{3.2}$$

Where T_x is the difference between the observed and calculated traveltimes for a given trace.

Using the uncertainties associated with each pick (α_i), a statistical estimate of the fit between the observed (O_i) and expected (E_i) traveltimes can be determined relative to the uncertainties applied to each pick α_i:

$$\chi^2 = \frac{1}{n}\sum_{k=1}^{n}\frac{(O_i - E_i)^2}{\alpha_i^2} \tag{3.3}$$

A χ^2 value of 1 indicates a perfect fit, with higher values indicating an increasingly less good fit. Values under 1 imply that there is an overfit, suggesting the model is more detailed than is necessary to explain the observed dataset.

With a good fit achieved in both an absolute (T_{RMS}) and statistical (χ^2) sense for each of the instruments sampling a particular layer, the modelling process moved onto the next set of arrivals and repeated. Three example OBSs are presented to show the fit of the modelled arrivals to the recorded data (Figures 3.13-3.15), with the remaining OBSs presented in Appendix C.

3.7.2 OBS location in the forward velocity-depth model

OBSs are placed at their relocated position along Profile B following the construction of the forward velocity-depth model (Section 3.6). The depth of the instrument is shifted slightly in the model space so that it is located at the seabed. Waterwave arrivals were then modelled for each instrument, and the misfit between these arrivals and the observed water wave was applied as a static shift to the instrument to ensure that the sub-surface arrivals would be modelled at the correct time relative to the instrument location. To prevent the introduction of artefacts or problems with modelling, the OBSs were placed just above or below the seabed for modelling rays through the water column and sub-surface, respectively.

3.7.3 Sub-seabed velocity structure modelling

Modelling of the sub-seabed seismic velocity-depth structure was undertaken in four parts because of the observed variations in the WA dataset, and because of the large lateral changes in crustal structure along the profile. Modelling was undertaken in the following order:

1. Kermadec forearc crust and upper mantle, except in the vicinity of the Kermadec trench, from southwest to northeast;

2. Pacific crust and upper mantle, except in the vicinity of the Kermadec trench, from northeast to southwest;

3. Kermadec trench crust and upper mantle, for both the subducting and overriding crusts; and

4. minor improvements, focussing on regions where the above three sections overlap, whilst refining the statistical fit of the entire model.

The following sections describe the process used to iteratively improve each of these regions in more detail.

3.7.3.1 Kermadec forearc modelling

The sub-seabed velocity-depth model initially consisted of the MCS-derived sediment thickness and velocity structure (Section 3.6) with a gradient hung below this reaching typical lower-crustal velocities at the base. P_s arrivals were only observed on OBSs 01-04 on the forearc (Section 3.4.1), which were located on top of the broad forearc ridge, where sediments reach ∼2 km-thick in the MCS section (Section 2.4). Despite this constraint, the WA data indicated that the layer was closer to 1.5 km-thick in the basin (Figure 3.13). Below this layer the P_g arrivals were most effectively modelled with a three-layer crust: layer 1, 3.0-4.5 km s^{-1}, between 1-2 km thick; layer 2, 5.0-6.3 km s^{-1}, also 1-2 km thick; and layer 3, ∼7 km thick up to about 120 km model offset (coincident with the eastern edge of the forearc ridge), where it thins to 5 km. Velocities in layer 3 increase from the velocity of the lower boundary of layer 2, to 7.0 km s^{-1} along most of the well constrained forearc Moho (by P_mP and P_n arrivals), except for in the centre of the forearc ridge, ∼100 km model offset, where velocities reach 7.4 km s^{-1}. The OBS record sections typically exhibited high noise levels at greater shot-receiver offsets, with P_mP and P_n arrivals not clearly observed on most of the instruments. This resulted in the Moho and mantle being sampled by only a few sets of crossing rays from different instruments, most notably at the sharp change in Moho depth at 80-100 km model offset (Figure 3.13).

3.7.3.2 Pacific plate modelling

Modelling of the Pacific plate shallow sub-surface seismic velocities was limited by the lack of short-offset sediment layer refractions. These P_s arrivals were obscured by the high energy direct waterwave arrivals on the Pacifc plate OBSs due to the relatively deep seabed (4-5 km below sea surface) and thin sediment cover. As a result, the sediment velocity structure remained largely unchanged from the initial velocity structure derived from the MCS data analysis and interpretation (Section 3.6).

Although the crustal refracted arrivals are picked as a single P_g phase on the OBSs, the Pacific crust is subdivided into three main units for the purpose of modelling (Figure 3.14). In general, away from the direct influence of Canopus seamount (i.e. >370 km model offset), the oceanic crust exhibits layer velocities (3.3-7.2 km s^{-1}) and thicknesses (∼6.0 km) that are typical of Pacific crust (Spudich & Orcutt, 1980; White *et al.*, 1992). The uppermost crustal layer has no observed arrivals due to its thickness of <0.5 km, and relatively low seismic velocity (4.5 km s^{-1}), but was required in the model to accurately calculate the traveltimes of arrivals from the deeper crustal layers. Below this, the mid-crustal layer remains consistently ∼1 km thick throughout the Pacific section of the model, with velocities increasing from 5.8 to 6.4 km s^{-1}. Together, the upper two crustal layers most likely represent basaltic and doleritic units of the oceanic crust (layers 2a/b and 2c, respectively), as they match published compilations of these layers (Carlson & Raskin, 1984; Carlson & Herrick, 1990). The lower crustal unit, which displays an increase in seismic velocity from ∼6.5-7.2 km s^{-1} over its 4.0 km thickness, most likely represents layer 3 of traditional oceanic crustal velocity models.

The crust thickens significantly beneath Canopus seamount by ∼6 km (from 6.0 to 12.0 km) with only a slight increase in the depth of the Moho constrained by P_mP and P_n arrivals (Figure 3.14). Most of this crustal thickening appears to be accommodated in the upper crustal layer, the base of which maintains an approximately constant depth in the model space irrespective of the significant seabed shallowing (∼4 km). This is markedly different from observations beneath other seamounts in the LRSC that display elevated velocities within the seamount edifices (e.g. Contreras-Reyes *et al.*, 2010; Stratford *et al.*, 2015). The P_n phases indicated that the Pacific mantle velocities are relatively low, and do not vary to an observable degree beneath the background Pacific crust or Canopus seamount (7.6-7.7 km s^{-1}).

3.7.3.3 Kermadec trench modelling

The Kermadec trench region of the WA velocity-depth model was developed last because: i) observed arrivals exhibited a remarkably low SNR (e.g. Section 3.4.2); ii) the gap in instrumentation around the trench (Figure 3.7) naturally reduced the number of arrivals recorded; and, iii) the region is expected to be very geologically complex.

On the forearc side of the trench, minimal sediment cover resulted in low-velocity P_g phases being observed as the shortest-offset sub-surface arrivals (Figure 3.15). The morphological complexity of the seabed, and the remarkably low apparent velocities of the observed arrivals made forward modelling more challenging in the trench region. Low seismic velocities were required throughout the crust, with velocities reaching just 6.5 km s^{-1} at the base of the forearc crust (compared to typical values of 7.0 km s^{-1}). A lack of observed P_mP and P_n phases resulted in poor model ray coverage throughout the forearc Moho and mantle closest to the trench, with mantle velocities assumed to be comparable to those found beneath the rest of the forearc crust (7.8 km s^{-1}).

On the Pacific plate side of the Kermadec trench, the sediments were slightly thicker, and more comparable to those across the rest of the Pacific plate; however, the sediments remained too thin to generate an observable P_s first arrival on the trench OBSs (Section 3.4.3). Instead, the sediment column remained largely unchanged from the structure derived from the MCS dataset, except where necessary to fit the shortest offset P_g arrivals (Figure 3.15). The velocity structure of the oceanic crust in this region remained comparable to that determined for the background section of the Pacific crust (Section 3.7.3.2), but was slightly reduced in velocity to account for the lower apparent seismic velocities observed for the P_g arrivals on the OBSs (Section 3.4.3). This feature is manifest in the model as a thickening of the upper crustal layer (3.3-5.5 km s^{-1}) from ∼0.5 to 1.5 km thick. The middle crustal layer (5.5-6.4 km s^{-1}) maintained its ∼1 km thickness, whilst the lower crustal layer (6.5-7.1 km s^{-1}) was effectively thinned by 1 km. The total crustal thickness of 6.0 km, supported by P_mP arrivals, is maintained from the regions of background crust to the trench region of the Pacific crustal model. Although there were fewer mantle refractions observed due to a lower SNR on these instruments, the mantle velocity had to be reduced by 0.3 km s^{-1} (from 7.7 to 7.4 km s^{-1}) to fit the observed P_n phases.

Modelling of the inter-plate region was initially conducted with the crustal layers of the subducting and overriding plates simply joined, to reduce initial modelling

complexity and minimise modeller preconceived bias. As the seismic velocity structures of the different crusts began to diverge, this became increasingly challenging, and so the model was broken up into overriding and subducting crustal blocks (see Figure 3.15). To facilitate this, the top-slab depths provided by the Slab1.0 model (Hayes *et al.*, 2012) were projected into the model space, and the depths along the profile were extracted (Figure 3.16). The top of the oceanic crust was merged with the Slab1.0 depths to a maximum of 35 km depth (the lower limit of the model required to correctly model all P_n arrivals), with the mid- and lower-crustal layer thickness adjusted for the increasing slab dip, and draped beneath the upper crustal layer. The sediment column remained continuous along the profile, and the overriding crust pinches out and follows the base of the sediment column to the northeastern edge of the model. From this point, the observed P_g, P_mP, and P_n arrivals could be modelled across the inter-plate boundary, although they had relatively large pick uncertainties due to the low SNR of these phases (Section 3.4.2). Reflections predictively modelled from the top and bottom of the subducting slab, even at depth, match observed arrivals on certain instruments. Despite this, the number of observed reflections from the slab was too limited to reliably model slab depth.

Following the modelling of the Kermadec forearc, Pacific plate, and Kermadec trench as independent datasets and models, the regions were combined with minor alterations made to iteratively improve the fit between the overlapping datasets. This modelling was undertaken with an increasing reliance on the statistical fit of the data, as determining changes visually became more challenging given the size of the model and dataset.

3.7.4 Forward velocity-depth model initial interpretation

The final best-fit forward velocity-depth model for Profile B was developed by the iterative improvement of a starting model based on the fit of traced rays to over 45,300 traveltime picks for different sub-seabed phases recorded by 26 OBSs spaced evenly along the 432 km-long profile (Figure 3.17). The complete, annotated, final velocity-depth model, in the *rayinvr* v.in file format, is presented in Appendix D.

This final model comprises a total of four water column and nine sub-seabed layers: a single sediment layer, three crustal layers and a single mantle layer that are discrete and split between the subducting and overriding plates in the model. Seabed and sediment layer nodes were laterally spaced at ∼2.5 km intervals, with node spacing intervals increasing to >10 km at the Moho. In this section, the results and initial interpretation of the forward velocity modelling process are presented to

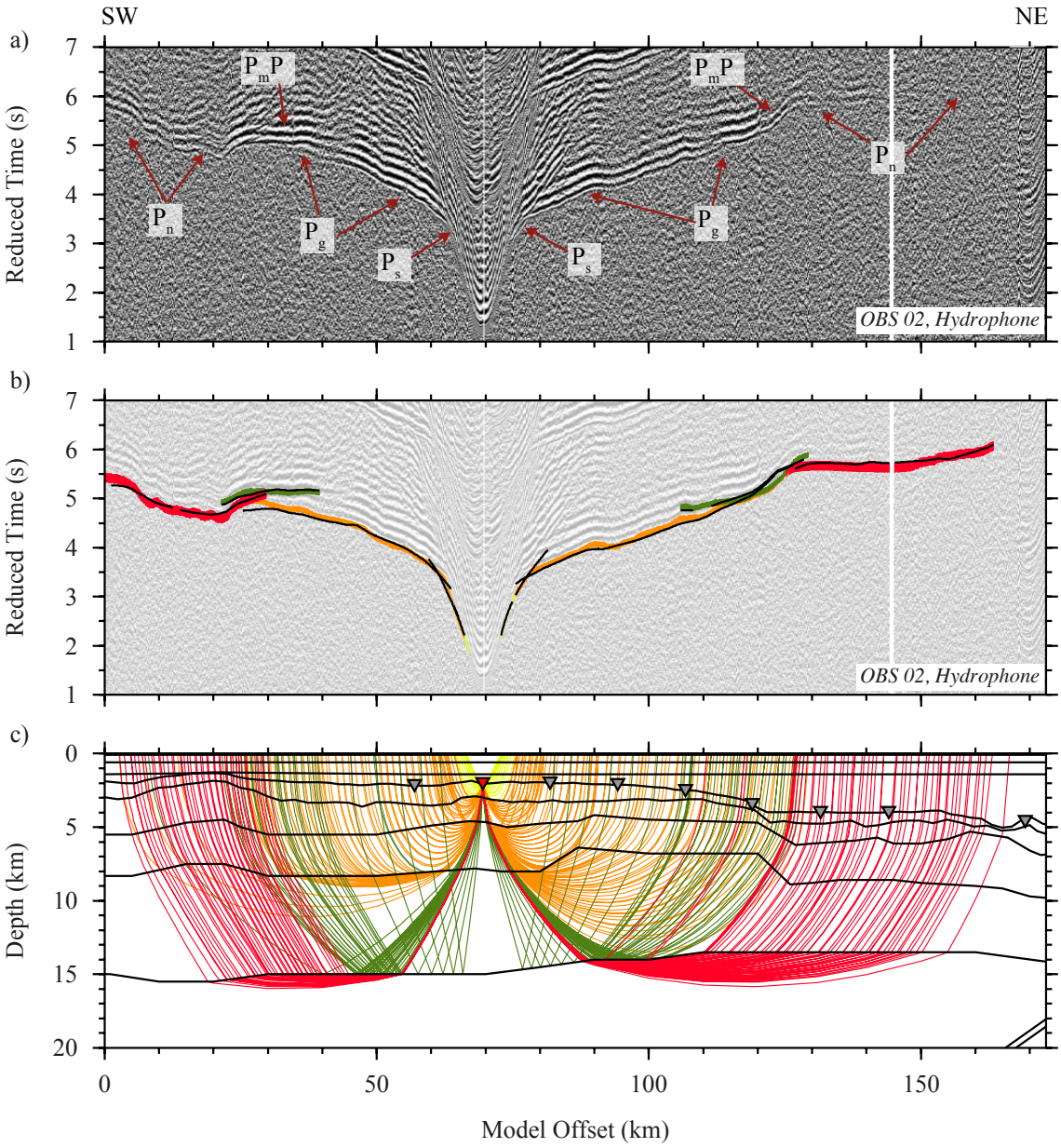

Figure 3.13: WA seismic data and modelled arrival comparison for OBS 02. a) Filtered hydrophone data from OBS 02 reduced at 8 km s^{-1}, with phase identifications annotated. b) Picked phases are indicated by vertical coloured bars (P_s - yellow; P_g - orange; P_n - red; P_mP - green). The height of the coloured bar represents the pick uncertainty, the black lines on top are the modelled arrival times. c) Calculated refracted and reflected rays traced through the velocity-depth model (layer boundaries indicated by the black lines). Ray colours match the assigned pick phases (in b), the location of OBS 02 is indicated by an inverted red triangle, and other OBSs are depicted as inverted grey triangles.

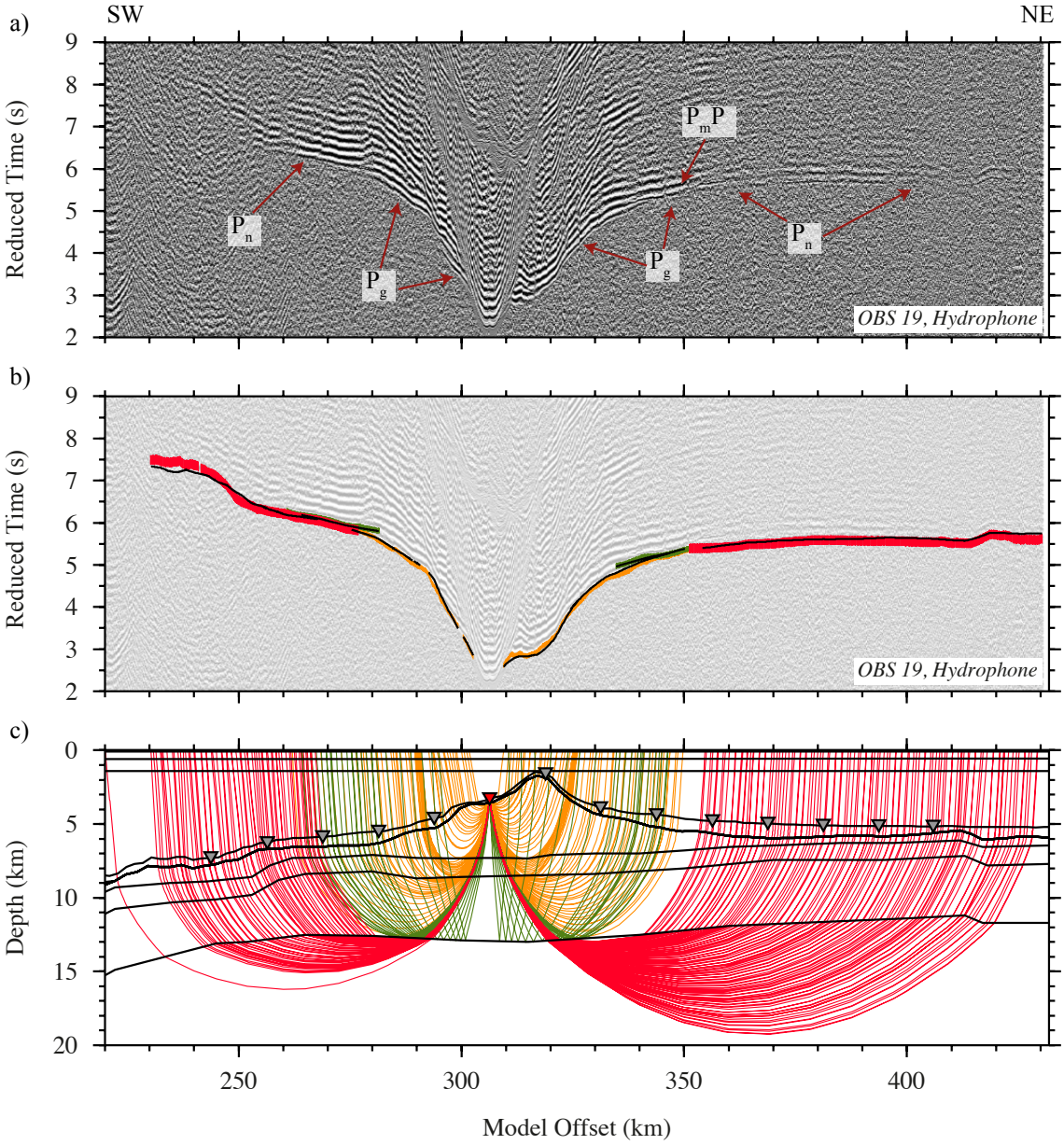

Figure 3.14: WA seismic data and modelled arrival comparison for OBS 19. a) Filtered hydrophone data from OBS 19 reduced at 8 km s^{-1}, with phase identifications annotated. b) Picked phases are indicated by vertical coloured bars (P_s - yellow; P_g - orange; P_n - red; P_mP - green). The height of the coloured bar represents the pick uncertainty, the black lines on top are the modelled arrival times. c) Calculated refracted and reflected rays traced through the velocity-depth model (layer boundaries indicated by the black lines). Ray colours match the assigned pick phases (in b), the location of OBS 19 is indicated by an inverted red triangle, and other OBSs are depicted as inverted grey triangles.

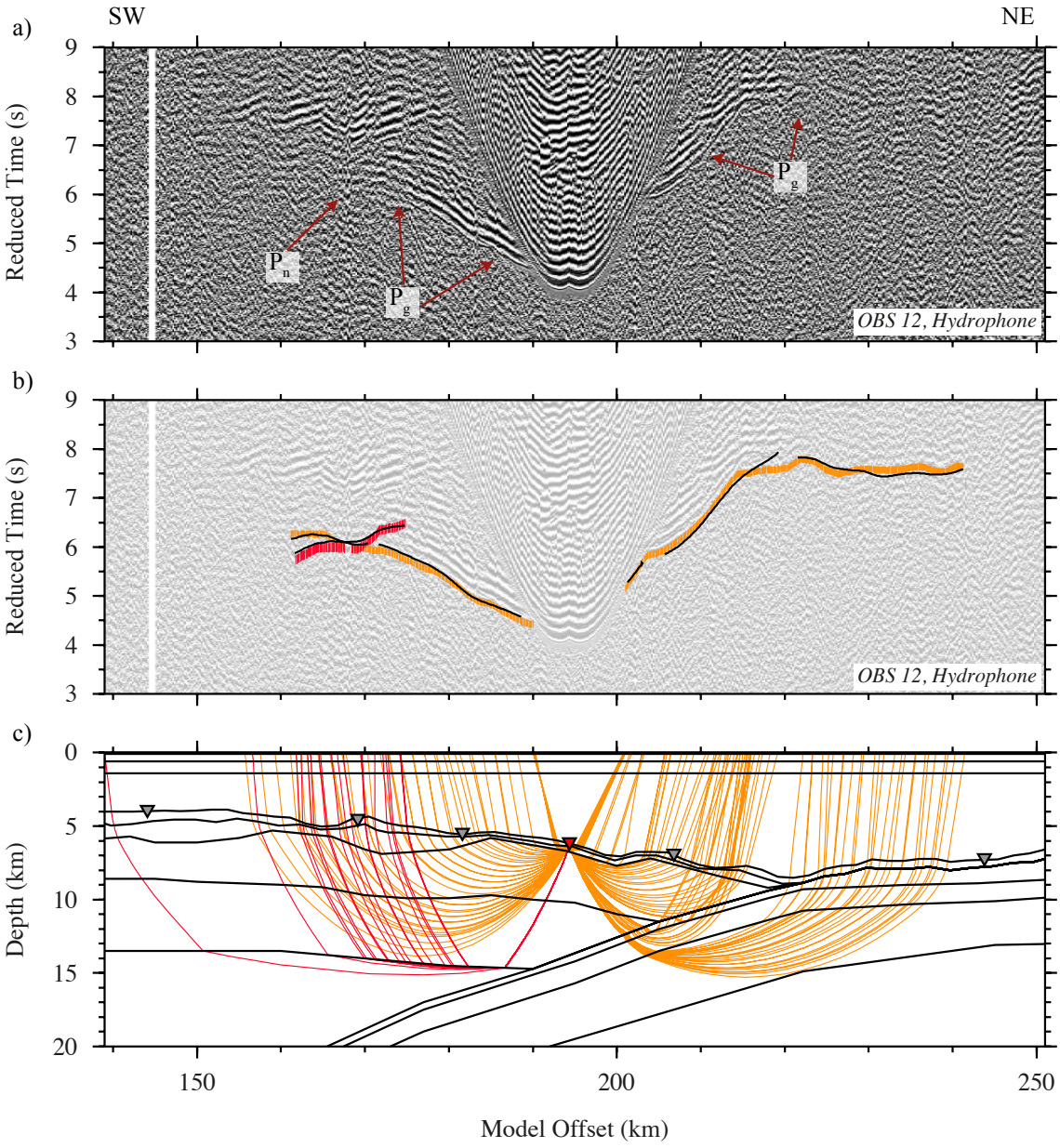

Figure 3.15: WA seismic data and modelled arrival comparison for OBS 12. a) Filtered hydrophone data from OBS 12 reduced at 8 km s^{-1}, with phase identifications annotated. b) Picked phases are indicated by vertical coloured bars (P_s - yellow; P_g - orange; P_n - red; P_mP - green). The height of the coloured bar represents the pick uncertainty, the black lines on top are the modelled arrival times. c) Calculated refracted and reflected rays traced through the velocity-depth model (layer boundaries indicated by the black lines). Ray colours match the assigned pick phases (in b), the location of OBS 12 is indicated by an inverted red triangle, and other OBSs are depicted as inverted grey triangles.

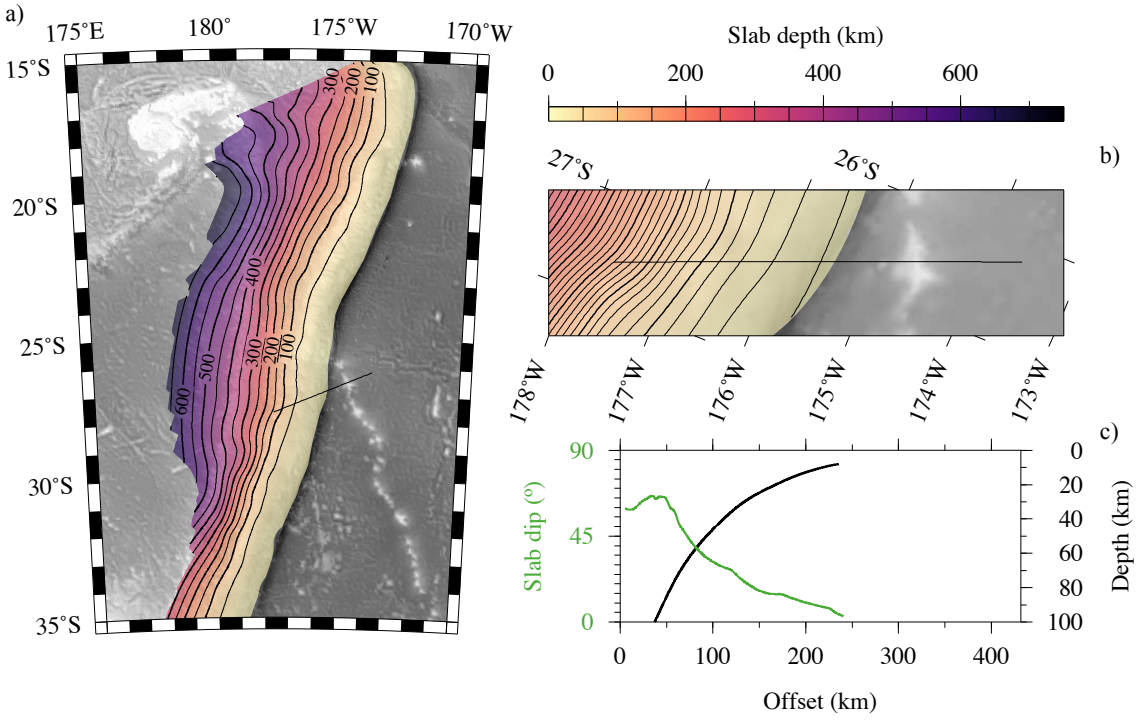

Figure 3.16: Slab1.0 model across the Tonga-Kermadec subduction system and along Profile B. a) Regional map of the Tonga-Kermadec subduction system with the Slab1.0 model of the Pacific plate overlain (Hayes *et al.*, 2012). b) Slab1.0 model rotated into the Profile B model space. Profile B is indicated by the black line in parts a) and b). c) Slab dip (green line) and depth (black line) to the top of the Pacific plate along Profile B, extracted from Slab1.0.

reveal the broad scale structure of the final velocity-depth model to provide the context for understanding the model fit (Section 3.7.5) and testing (Section 3.8), as well as informing gravity modelling (Section 4.4). A detailed interpretation of the final forward velocity-depth model will be presented in Chapter 5.

The Profile B final forward velocity-depth model (Figure 3.17) broadly consists of two major plates: the overriding plate, or Kermadec forearc and mantle, and the subducting Pacific plate. Sediments are relatively limited in thickness across the model and were, therefore, mainly constrained by the MCS data processing and interpretation. P_s arrivals observed on some forearc OBSs, and other regions that were sampled by deeper turning refractions, enabled minor changes to the sediment column thickness and seismic velocity.

The forearc crust and mantle exhibit seismic velocities that are closer to standard oceanic velocity profiles (Spudich & Orcutt, 1980; White *et al.*, 1992) than the continental crustal properties proposed to be present at other intra-oceanic subduction systems such as the Izu-Bonin-Mariana (IBM) system (Takahashi *et al.*, 2008;

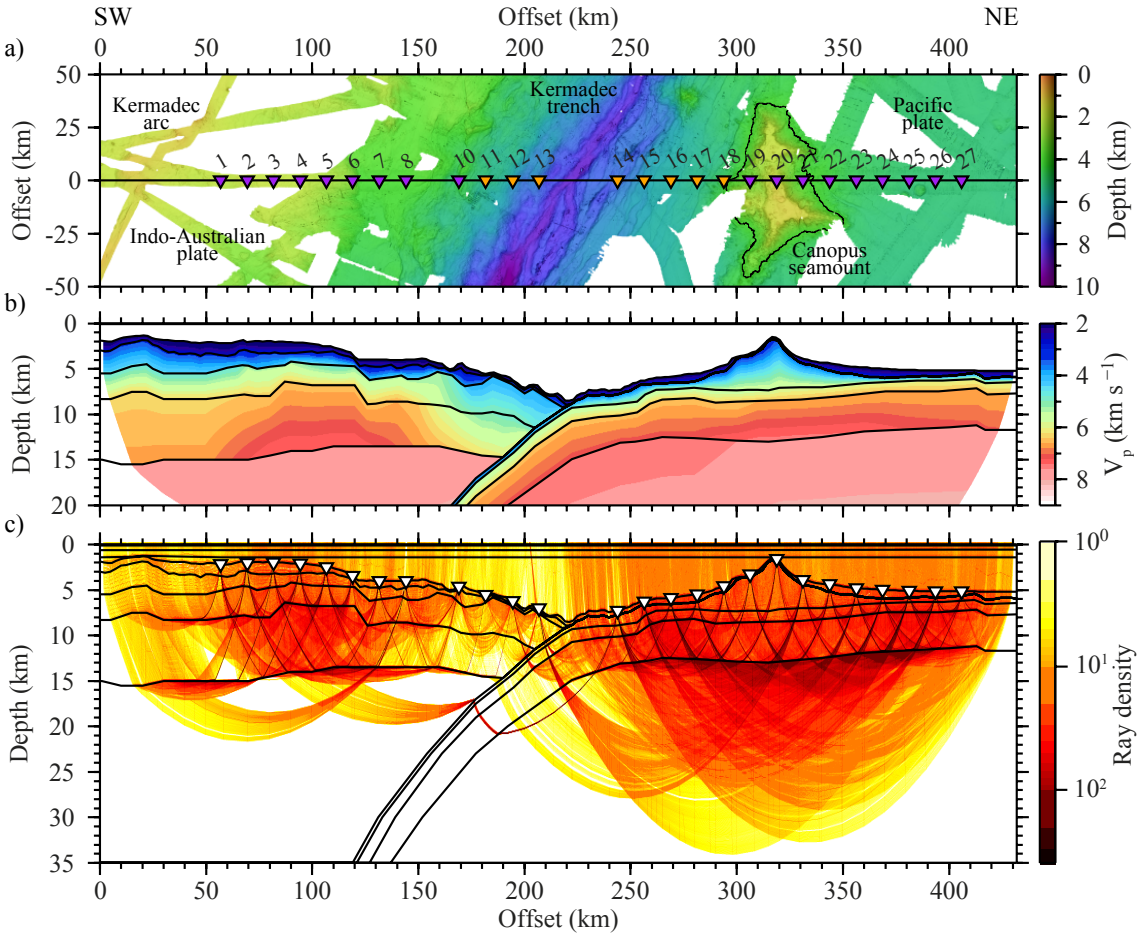

Figure 3.17: Final Profile B best-fit forward velocity-depth model. a) Swath bathymetry map around Profile B, which crosses the Pacific plate and Kermadec forearc. b) Final forward WA velocity-depth model, with the water column and regions of the sub-surface with no ray coverage masked out. c) Ray density through the final model. Model layer boundaries are indicated by black lines in b) and c), and OBS locations are shown as inverted triangles. Note how the ray coverage is greatest through the Pacific crust and upper mantle, but poor in the trench region and the southwestern-most section of the Kermadec forearc.

2009). Whilst the velocities are close to standard oceanic profiles, the crust is significantly thicker, being more comparable to previous studies through intra-oceanic arc settings (Larter *et al.*, 2003; Kodaira *et al.*, 2010). At the northeastern end of the profile, the Pacific crust and upper mantle exhibit a typical structure for oceanic crust, but this is significantly perturbed beneath Canopus seamount. Internal to the seamount edifice, velocities are very low (<6.0 km s^{-1}), and comparable to an ~6 km-thick sequence of the typical upper oceanic crust (i.e. layer 2a/b). Between the seamount and the trench, seismic velocities reduce slightly throughout the crust and upper mantle (Figure 3.17), coinciding with the bend-related faulting observed in

the MCS data (Section 2.4).

3.7.5 Final forward velocity-depth model fit

Forward modelling resulted in a good visual fit between the observed and calculated arrival phases (e.g. Section 3.7.3), although throughout the process the dataset fit was being tested through the absolute and statistical measures presented in Section 3.7.1. Anaylsis of the fit between the traveltimes of all observed and modelled sub-seabed turning phases gives a total T_{RMS} misfit of 86 ms and a χ^2 of 2.0 (Table 3.2).

Model region	Phase	Uncertainty (ms)	Number of picks	T_{RMS} misfit (ms)	χ^2
Pacific plate	P_g	44	6,362	45	1.2
	P_mP	52	4,643	51	1.2
	P_n	80	15,199	109	1.9
Trench	P_g	54	1,748	71	1.7
	P_mP	64	728	83	2.1
	P_n	83	3,291	145	3.8
Forearc	P_s	32	133	21	0.5
	P_g	46	6,155	78	2.9
	P_mP	48	2,863	64	1.9
	P_n	80	4,183	98	1.7
Full model	P_s	32	133	21	0.5
	P_g	46	14,265	62	2.0
	P_mP	51	8,234	58	1.5
	P_n	80	22,673	112	2.2
Overall values:	-	-	45,305	86	2.0

Table 3.2: Summary of the fit of modelled phases through different regions of the final forward velocity-depth model. Phases through different model sections are listed separately to highlight the variation in data quality and modelling certainty across the model space. The final model compares over 45,300 seabed-penetrating traced rays with observed phase arrivals, achieving a χ^2 of $\sim$2.0. Note that the <1 χ^2 value for the forearc sediments most likely results from the small number of rays traced and relative simplicity of the velocity structure.

Although the total fit of the modelled data to the observed arrivals is very good, there are clear variations in the quality of fit along the profile. The Pacific oceanic crust has the highest coverage of the model regions (>26,000 rays). Modelled P_g and P_mP arrivals from the Pacific crust fit the observed dataset to within a T_{RMS} misfit of 45 and 51 ms, respectively, which is the best fit throughout the model

(both with a χ^2=1.2). Pacific P_n arrivals have a surprisingly high misfit (T_{RMS}=109 ms, χ^2=1.9) considering the good fit for the crust, although this may be largely a function of the large number of rays traced (>15,000) through the much more coarsely defined Moho and mantle (Figure 3.17). Although a similar number of P_g and P_mP arrivals constrain the forearc and Pacific crustal layers, the forearc crust has a much higher misfit (T_{RMS}=78, χ^2=2.9 and T_{RMS}=64 ms, χ^2=1.9, respectively). The forearc mantle has approximately a quarter of the number of refracted rays traced through it compared to the Pacific crust mantle. This relatively low number of traced rays (∼4,000) reduces the chance for conflict between sets of rays from different instruments that need to be resolved, so less compromise is required to achieve a reasonable fit (T_{RMS}=98, χ^2=1.7). In short, whilst the fit appears to be better for the forearc mantle than the Pacific plate mantle, the Pacific mantle is constrained by a greater density of rays that indicates the fit will be most likely more sensitive to changes in the model than the forearc mantle (Section 3.8.1).

All phases recorded by instruments in the trench region have a high level of misfit. This is expected as the OBSs in the region consistently exhibit the lowest SNR of the entire Profile B dataset (Section 3.4.2), and the MCS data indicated that the region was highly faulted and heterogeneous at the shallowest level. Whilst the fit of the crustal constraining arrivals is perhaps surprisingly good, with a T_{RMS} of 71 ms (χ^2=1.7) for P_g arrivals and a T_{RMS} of 83 ms (χ^2=2.1) for P_mP arrivals, this is most likely aided by the very limited number of arrivals for each phase (1,748 and 728, respectively), which is approximately one quarter of the number of arrivals used to constrain the Pacific crustal structure (see also Figure 3.17). The limited number of arrivals is purely a result of the low SNR observed on the OBS record sections (Section 3.4.2). P_n arrivals from the trench OBSs have the highest misfit (T_{RMS}=145 ms, χ^2=3.8), most likely a function of the geological complexity of the inter-plate zone.

3.8 Testing the forward velocity-depth model

While the final forward velocity-depth model is considered to be of a good fit, with a total T_{RMS} of 86 ms and a χ^2 of ∼2, it is potentially not the only model that could produce a good fit between the calculated and observed arrival traveltimes. In this section the forward velocity-depth model is tested to determine:

- model sensitivity - perturbations are applied to the final forward velocity-depth model, to test the fit between the calculated and observed arrivals until a statistical fit threshold is broken; and,

- inter-dataset fit - the MCS dataset is restacked using an RMS velocity model derived from the final forward WA velocity-depth model. This process tests whether: i) previously imaged reflections are better resolved; ii) there is any new or enhanced sub-surface reflectivity; and, iii) any processing artefacts are introduced by the WA velocity-depth model or vice versa removed.

These tests were undertaken at this point in the modelling process to help constrain the fit of the model and its applicability to previously presented datasets, and to provide a sense of the control and robustness of the model. Further and more detailed testing of the final forward velocity-depth model, through velocity inversion and density modelling, will be presented in Chapter 4.

3.8.1 Sensitivity testing

One approach for testing the uniqueness of the final forward velocity model is to test the sensitivity of the fit between the calculated and observed datasets to enforced perturbations of it. An estimate of this sensitivity can be determined by altering the model until it becomes geologically unrealistic or statistically invalid, i.e. when the fit exceeds a pre-determined χ^2.

Analysis of the difference between the observed and calculated traveltimes suggests that the model has a good absolute and statistical fit. For the entire model, the traced rays fit to within 86 ms T_{RMS}, and a χ^2 value of $\sim$2. However, these are average values that include significant variation along the profile, with the rays traced through the Pacific crust region of the model fitting much better than either the overriding crust and the trench. There is also a large discrepancy in the amount of constraint provided by each phase type, for example, the sediment layer has every ray passing through it, but only a handful turn in this layer. This gives only minimal meaningful control on the layer despite being 'overfit' because of the small number of traced rays (Table 3.2) and a good starting point provided by the MCS dataset.

Minor changes to the final forward velocity-depth model can provide a similar fit to the best-fit model presented in Section 3.7. Further to this, an equally good fit can be achieved by systematically decreasing and increasing velocities in alternating layers, by decreasing a layer velocity but increasing the layer thickness, or vice versa. As a result, the final forward velocity-depth model is not a perfect and unique solution, but rather one of a spectrum of suitable models that could, within the assumptions of the ray tracing method, statistically explain the data. It is important to understand how much the model can be varied before the calculated arrivals no longer fit the observed dataset within the imposed uncertainties.

Maximum model variation, or model sensitivity, is calculated by systematically adjusting individual layer thickness, upper and lower boundary velocity (variable velocity gradient), and bulk layer velocity (constant velocity gradient) until a pre-defined misfit threshold is exceeded. Initially the whole model was tested against a single threshold value of χ^2=3.5. This was found to allow regions of relative geological simplicity and better fit, such as the Pacific plate, more variability before exceeding the limit, resulting in such layers appearing less sensitive to perturbations in the model than parts that originally fit less well. This result can be misleading as the different regions of the forward WA velocity-depth model have varying levels of uncertainties applied and geological complexities expected. An improved understanding of the true model sensitivity was achieved by dividing the tests into the major model regions, with more realistic thresholds chosen to match the set of instruments represented (Section 3.4). Figure 3.18 highlights the importance of dividing up the model for testing, with the base-level misfit significantly different between the Pacific (χ^2=2.0) and overriding crust (χ^2=3.5) regions of the forward model. By setting the same sensitivity threshold, either the overriding crust region would exceed this point too early, or the Pacific crust too late, to determine a reasonable estimate of the sensitivity for the different model regions.

The results of the sensitivity testing are summarised in Table 3.3. Generally, the fit of the intra-crustal regions of the subducting and overriding plates of the model are sensitive to relatively small changes in layer depth ($\sim$0.3 km), upper or lower boundary velocity ($\sim$0.3 km s^{-1}), and bulk layer velocity (0.2 km s^{-1}). Within the trench region, the crustal fit appears to be almost half as sensitive to model variations than is typical for the intra-crustal layers of the rest of the model (i.e. the layer boundary needs to be adjusted by twice as much before the pre-defined threshold is broken). Such a result may be expected as the phase picks for most of the trench instruments were assigned much higher uncertainty values than their non-trench counterparts due to the low SNR (see Section 3.4.2).

The sediment layer demonstrates similar sensitivities to changes in seismic velocity as the intra-crustal units for each section (Table 3.3). The absence of turning rays through the Pacific plate sediments gives minimal control on the shallow velocity structure (allowing up to a 0.5 km s^{-1} adjustment in upper or lower seismic velocity). Low numbers of rays turning through the sediment layer, and its typically $<$2 km thickness, results in it being relatively poorly constrained.

Pacific plate phase traveltimes are relatively sensitive to upper mantle velocity and Moho depth (0.3 km s^{-1} and 0.5 km, respectively; Figure 3.18). The fit of traveltimes through the forearc mantle is, however, significantly less sensitive to changes

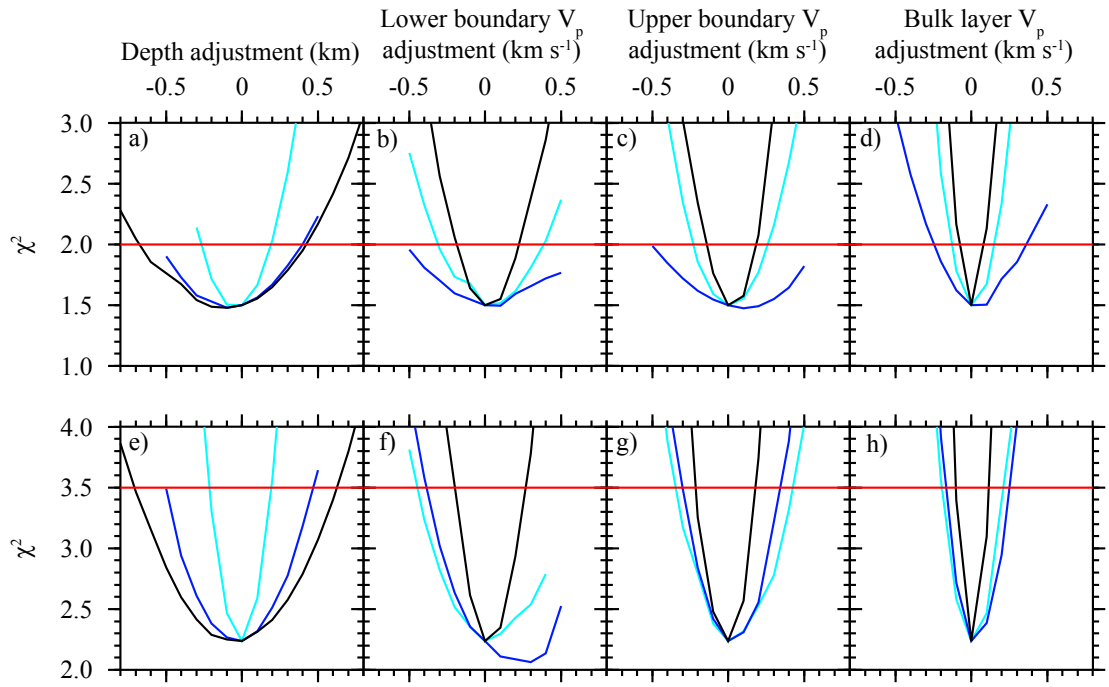

Figure 3.18: Example forward WA velocity-depth model sensitivity test plots. a) Tests of the Pacific crustal layer depths, b) lower boundary velocity, c) upper boundary velocity, and d) bulk layer velocity. e) Tests of the overriding plate crustal layer depths, f) lower boundary velocity, g) upper boundary velocity, and h) bulk layer velocity. The different lines correspond to the lower boundary of a given layer: the upper crustal layer (light blue), the middle layer (dark blue), and the lower crustal boundary (black line). Note that for each layer, tests stop at the point that *rayinvr* stops tracing rays through the model because of layer crossing violations. For all examples, the sensitivity threshold is indicated by the red line.

(0.7 km and 0.8 km s^{-1}, respectively; Figure 3.18), most likely as a result of the reduced ray coverage compared to the Pacific plate (Figure 3.17). For example, the Pacific plate mantle is constrained by two and four times as many Moho reflections and mantle refractions (Table 3.2), respectively, than the forearc mantle, despite covering a similar lateral distance.

After splitting the sensitivity tests into the major model sections, the results must still be considered critically, as statements are made concerning the fit of an entire layer boundary. This assumption is inherently incorrect as, for example, there are some regions of the Pacific plate Moho that are constrained by no rays due to the calculated turning geometries, but others may have thousands of rays pass through them. While these results are limited, they still provide an objective means for comparing the assessed sensitivities for each characteristic of a layer boundary. Henceforth, final forward model layer depth and upper and lower velocity values will

Forearc, OBSs 1-10, $\chi^2 < 3.5$					
Layer	Model side	Lower ΔZ (km)	Upper V_p (km s^{-1})	Lower V_p (km s^{-1})	Const. V_p Grad.
Sediment	Forearc	0.1	0.3	0.2	0.1
Intra-crustal	Forearc	0.5	0.3	0.3	0.1
Mantle	Forearc	-	0.8	0.3	0.2

Trench, OBSs 11-15, $\chi^2 < 3.5$					
Layer	Model side	Lower ΔZ (km)	Upper V_p (km s^{-1})	Lower V_p (km s^{-1})	Const. V_p Grad.
Sediment	Both	-	-	-	-
Intra-crustal	Forearc	-	0.6	0.7	0.6
Mantle	Forearc	-	0.2	0.2	0.6
Intra-crustal	Pacific plate	-	0.5	0.3	0.4
Mantle	Pacific plate	-	0.2	0.1	-

Pacific plate, OBSs 16-27, $\chi^2 < 2$					
Layer	Model side	Lower ΔZ (km)	Upper V_p (km s^{-1})	Lower V_p (km s^{-1})	Const. V_p Grad.
Sediment	Pacific plate	0.1	0.5	0.3	0.2
Intra-crustal	Pacific plate	0.3	0.3	0.3	0.2
Mantle	Pacific plate	-	0.3	0.1	0.1

Table 3.3: Summary of the forward velocity model sensitivity test results. Empty cells indicate tests that were not undertaken, either because that part of the model does not exist (e.g. the lower mantle depth boundary is the base of the model) or because they violated the modelling code (e.g. trench boundary variations cause layer overlap).

be quoted with their respective sensitivities where appropriate.

3.8.2 Restacking of the MCS data

The standard processing of the Profile B MCS data involved applying NMO-correction velocities determined from detailed analysis of CMP gathers that rely on assumptions, such as reflectors being horizontal and planar, that are overly simplistic in an area as geologically complex as a subduction system. The application of such a velocity model to the MCS dataset produced an optimised stacked section

in which the reflections at each CMP were flattened by ideal, but not necessarily representative, sub-surface seismic velocities.

The final forward velocity-depth model represents the best achievable representation of the crust and upper mantle seismic velocity structure to within the limits determined through sensitivity testing (Section 3.8.1). This velocity-depth model should represent the true sub-surface seismic structure, and so the model can be used to restack the MCS CMP gathers to generate a more geologically representative seismic reflection image. Restacking of the MCS dataset had two main purposes:

1. to test the fit of the velocity-depth model to the MCS dataset; and
2. to improve reflectivity in regions of the MCS data that were poorly constrained by standard velocity analysis.

The Profile B MCS WA-stack processing sequence should generate a similar image to the original fully-processed stacked section in regions where the sub-surface velocities could be readily determined through velocity analysis. Further to this, the additional constraint on sub-surface velocities provided by the final forward WA velocity-depth model might sharpen reflections that were previously poorly resolved or completely unobserved because of limited sediment cover, depth, or steep dip angle. If the final forward seismic velocity-depth model poorly represents the true sub-surface structure, the restacked MCS section will exhibit poorly focussed reflections and more processing artefacts, such as reflection smearing.

Restacking was achieved by applying an updated processing sequence to account for the use of a different velocity model (Table 3.4). As with the full processing sequence presented in Section 2.3.4, the MCS restacking was applied to the data after the initial processing sequence (Section 2.3.2).

3.8.2.1 Velocity model conversion *(11)*

The final forward seismic velocity-depth model was converted from depth to two-way traveltime using the velocity samples at known depths. Following this, the time domain velocity model was converted from interval to RMS velocities using the Dix equation (Equation 3.1; Dix, 1955).

3.8.2.2 NMO and stacking *(12 and 13)*

Seabed and sediment layer nodes for the forward seismic velocity-depth model were spaced at ∼2.5 km intervals. The lateral node spacings increase with depth, reaching >10 km at the Moho. This lateral spacing is less frequent than the CVA velocity

No.	Stage	**Processor**	Details
11	Restack	**Velocity model conversion**	Convert final forward P-wave velocity model from interval velocities in depth to RMS velocities in time
12	Restack	**NMO**	Apply NMO correction using updated velocity model
13	Restack	**Stack**	Stack into CMP traces
14	Restack	**Migration**	Post-stack finite difference time migration, using updated model
15	Plotting	**AGC**	Automatic Gain Control (2000 ms window)
16	Plotting	**Muting**	Mute above seabed for display

Table 3.4: Summary of steps used to restack the MCS data using the WA forward velocity-depth model derived seismic velocities. This processing scheme replaces stages 11-16 in the original processing sequence (Table 2.1).

model (with 1.25 km sample spacing), although the forward model incorporates sharp vertical discontinuities such as at the inter-plate boundary and Moho.

Vertical and horizontal smoothing was applied to the RMS-converted WA forward model to reduce the potential for processing artefacts to be introduced to the restacked MCS section due to these sharp velocity discontinuities. This smoothed velocity model was interpolated to each CMP and applied to the gathers to correct for normal moveout. Each NMO-corrected gather was summed to generate a single stacked trace at the CMP location.

3.8.2.3 Migration *(14)*

During the full MCS processing sequence (Section 2.3.4) a single velocity (1.5 km s^{-1}) Kirchhoff post-stack time migration was applied to reduce the effect of diffraction hyperbola on the seabed and sedimentary reflections. With the improved constraint on the true sub-seabed velocity structure provided by the forward WA velocity model, a finite-difference post-stack migration was applied during reprocessing.

3.8.2.4 Plotting and results *(15 and 16)*

To enable direct comparison between the velocity analysis-determined and forward velocity model-derived stacked MCS sections, the same seabed mute and AGC (median normalised, 2000 ms window) were applied to the restacked dataset. The

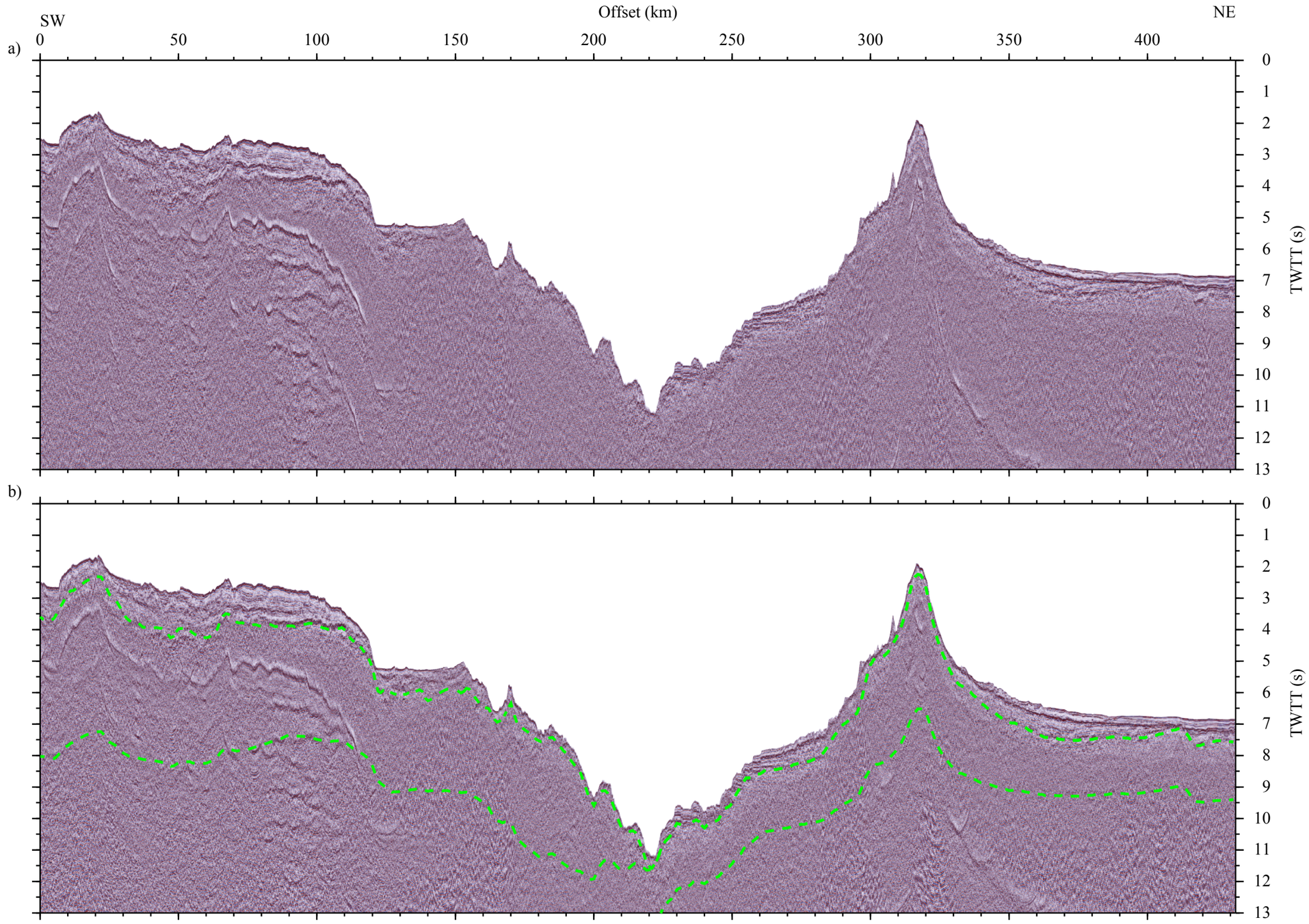

Figure 3.19: Comparison of fully processed and WA velocity-depth model restacked MCS data over the entirety of Profile B. a) Profile B MCS section processed as described in Section 2.3.4. b) Restacked MCS dataset, using the velocity model developed by forward WA modelling for the NMO-correction and post-stack migration. Note that the sedimentary structures remain largely unchanged between the sections, except for in the mid-slope basin where reflections are clearer following restacking. Forward WA velocity model layer boundaries are indicated by the dotted green lines.

restacking sequence generated an MCS section that displays the same sedimentary and deformation structures as were imaged in the original processing sequence (Figure 3.19).

As a test, the restacking shows that despite the lower lateral resolution of the forward WA velocity-depth model it performs as well as the CMP gather-derived velocity model in imaging the seabed and sedimentary reflections (e.g. Figure 3.20).

Figure 3.20 demonstrates that the Kermadec forearc, which is the region of greatest sediment accumulation along the profile, has not had processing artefacts introduced through reprocessing, but also that the clarity of the reflections has not been significantly improved by the forward velocity model-based stacking and migration. This may be a result of the original stacking velocity model sufficiently replicating the sedimentary velocity structure, and also a function of the significant diffractors having an apparent velocity close to 1.5 km s^{-1}. The top-crust reflection fits within 0.1 km of the forward model sediment-crust boundary, except in the thick upper forearc basin. This is most likely due to lateral variations in the basement velocity structure being below the lateral sensitivity of the forward modelling method, exemplified by the apparent complexity of the deeper reflections in the forearc basin (Figure 3.20).

During the initial processing of the MCS dataset, velocity analysis was most challenging in regions where there were no clear sub-seabed reflections. Whilst this was typically limited to regions of minimal sediment cover, the forearc mid-slope basin displayed unclear and low SNR sub-seabed reflections because of reduced fold-of-cover during a short break in firing, and a prolonged period of low airgun pressure (Figure 3.21a.). Reprocessing of the MCS data with the RMS-converted WA forward velocity model improved the clarity of the sedimentary structures in this basin (particularly between 145-155 km offset) where there was previously strong noise and no readily apparent reflectivity (Figure 3.21b). Throughout the basin the forward velocity model top-crust boundary is within 0.2 s TWTT of the basement reflection, except in regions of extreme noise where this reflection is not clearly resolved (e.g. 140-145 km offset).

No seismic Moho was easily observed in the initial processing and velocity analysis of the Profile B MCS reflection data (Figure 3.22). Restacking with the forward WA velocity model focused a band of deeper reflectivity beneath the flat-lying segments of the Pacific crust, at ∼9 s TWTT. The expected depth of this reflection, and the fit to within 0.5 km of the forward velocity model crust-mantle boundary, suggests that this reflectivity is generated by the Moho. Although it is readily observed at the northeastern end of the profile beneath relatively 'typical' oceanic crust

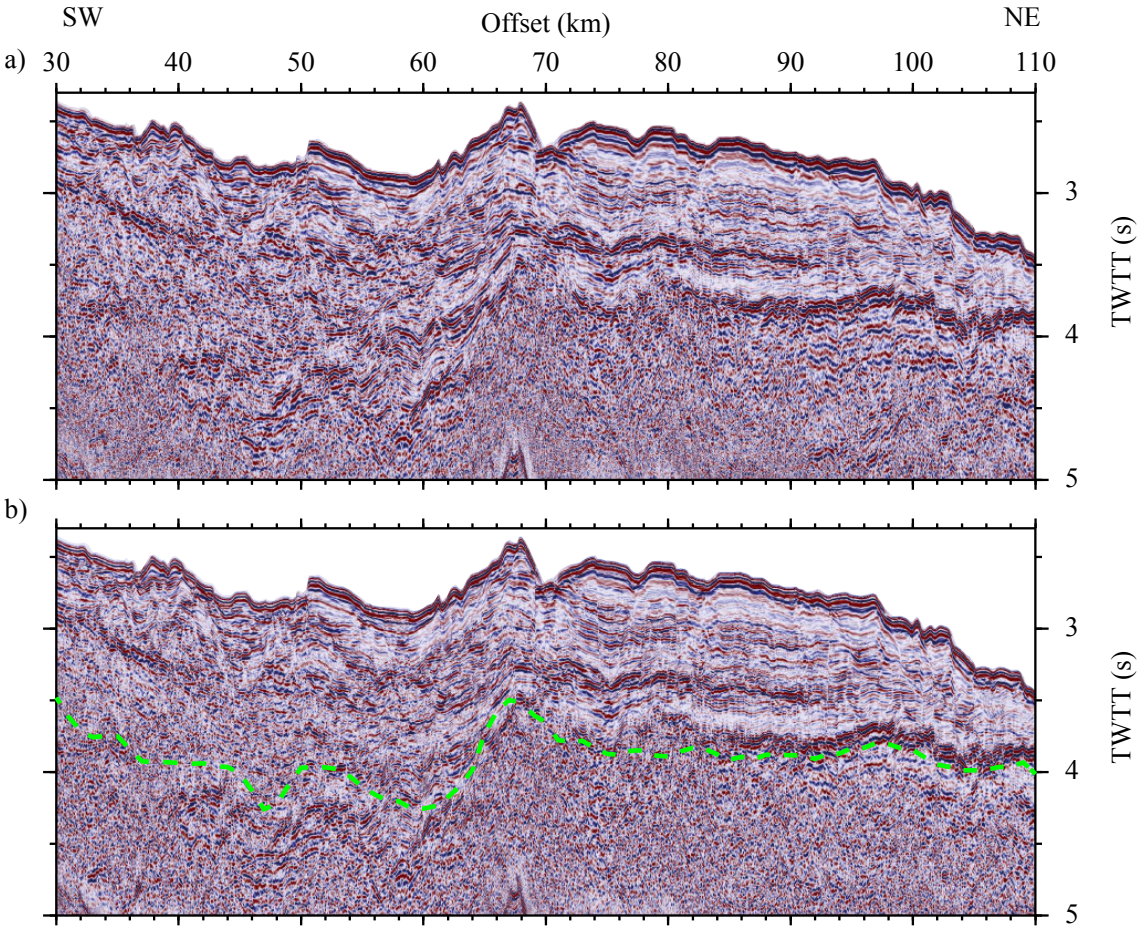

Figure 3.20: Comparison of fully processed and WA velocity-depth model restacked MCS data across the Kermadec forearc basin. a) Fully processed Profile B MCS data (see Section 2.3). b) Forward WA velocity-depth model restacked MCS section over the same region as a), with the forward model top-crust layer boundary indicated by the dashed green line. Intra-sediment reflectivity is not significantly altered following the stacking with the lower-resolution, but more geologically representative velocity model.

(Figure 3.22), the Moho is not observed across the rest of the MCS section because of the high amplitude water column multiple or increased seismic signal attenuation through more geologically complex regions.

3.9 Summary

In this chapter the detailed analysis and robust modelling of the Profile B WA dataset has been discussed. Further to this, the final velocity-depth model has been robustly tested to ensure a good fit with the observed data, determine the sensitivity of the data to changes in the model, and ensure the model could be used to effectively restack the MCS dataset initially presented in Chapter 2.

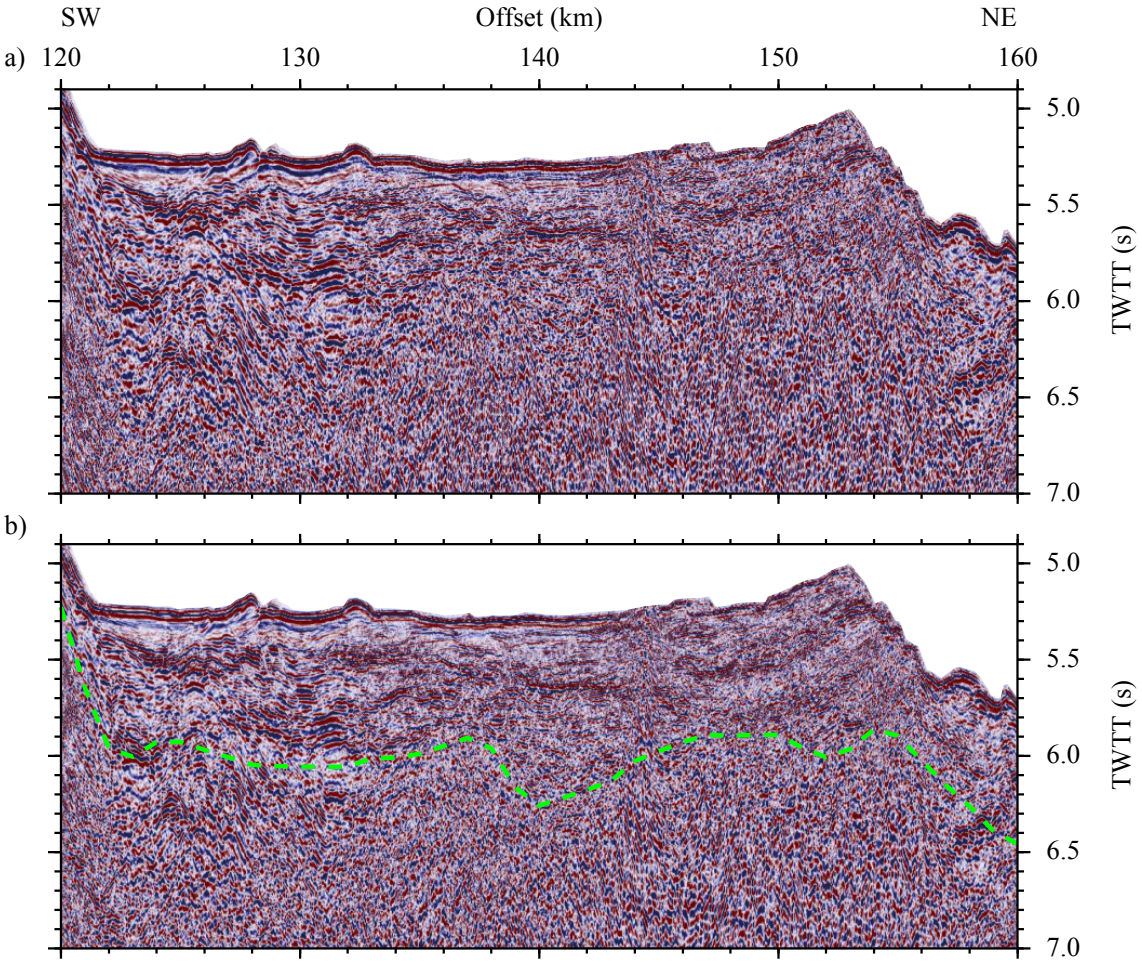

Figure 3.21: Comparison of fully processed and WA velocity-depth model restacked MCS data across the Kermadec mid-slope basin. a) Fully processed Profile B MCS data (see Section 2.3). b) Forward WA velocity model restacked MCS section over the same region as a), with the forward mode top-crust layer boundary indicated by the dashed green line. The restacking of the MCS data in this region not only preserves existing reflectivity, but enhances reflections at the eastern edge of the basin (145-155 km offset) where poor SNR prevented the picking of a suitable velocity profile for the sub-surface.

The final forward velocity-depth model was found to fit well for the Pacific plate, with typical oceanic crust and mantle velocities observed at the northeastern end of the profile. Beneath Canopus seamount, the upper crustal unit appears to thicken (by ∼6 km) to accommodate the extra crustal thickness, and crustal and upper mantle velocities reduce slightly (<0.3 km s^{-1}) in the bend-faulted outer rise region of the Pacific plate. The lower-trench slope region of the overriding plate is poorly constrained and relatively insensitive to changes in velocity structure, although it exhibits surprisingly low seismic velocities throughout the crust (<6.5 km s^{-1}). More typical forearc crustal velocity is observed further southwest, reaching up to 7.4

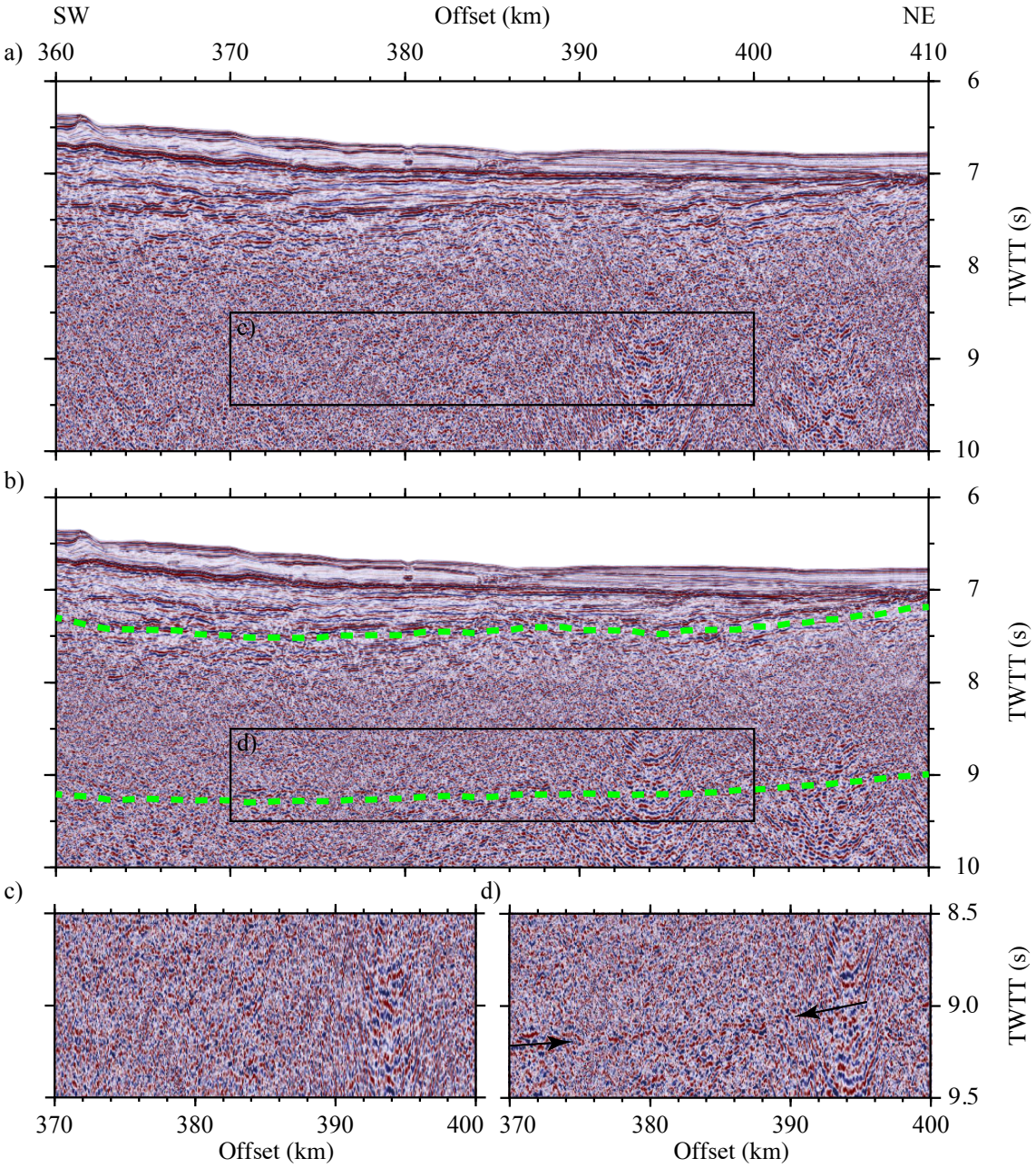

Figure 3.22: Comparison of fully processed and WA velocity-depth model restacked MCS data across the Pacific plate at the northeastern end of Profile B. a) Fully processed Profile B MCS data (see Section 2.3). b) Forward WA velocity-depth model restacked MCS section over the same region as a), with forward model layer boundaries indicated by the dotted green lines (sediment-crust layer boundary at 7-7.5 s TWTT and crust-mantle boundary at ∼9 s TWTT). Black boxes in a) and b) indicate the subsets of data presented in c) and d), respectively. Coherent reflectivity is absent below the basement in the fully processed MCS section shown in parts a) and c), but, following restacking with the WA velocity model, a band of reflectivity is enhanced at ∼9.2 s TWTT (see part d), coinciding with the forward velocity model crust-mantle boundary shown in part b). This reflection most likely represents the Moho.

km s^{-1} at the base of the crust beneath the forearc morphological ridge. Forearc mantle velocity is poorly constrained due to a limited number of observed mantle refractions, and relatively high assigned uncertainties for the phases observed by the forearc instruments.

In Chapter 4 the uniqueness of the forward velocity-depth model will be tested and modeller bias assessed, using the OBS dataset to generate an inversion velocity model for Profile B. This inversion-derived model will, in turn, also be tested to determine the ability of the OBS WA dataset to resolve the sub-surface velocity structure. A final independent test of the forward velocity-depth model structure will be achieved by generating a series of density models, and comparing the fit between the calculated and observed gravity anomalies.

Chapter 4

Independent model testing

4.1 Introduction

Chapter 3 investigated the processing and analysis of the OBS WA dataset to enable the forward modelling of the seismic velocity-depth structure of the water column, sediments, crust, and upper mantle along Profile B. This modelling built upon the sedimentary structures imaged by the MCS data that were presented in Chapter 2. The forward WA model effectively constrains the Pacific and forearc crust and upper mantle velocity structure. The reliability and robustness of this model was directly assessed in Chapter 3 through sensitivity testing and was supported by the restacking the MCS dataset.

This chapter presents a series of methods for independently testing the final forward velocity-depth model resolution and validity. First inversion modelling is undertaken, utilising only the most objective data from the WA dataset to constrain a velocity model of minimum structure (Section 4.2). This indicates which features of the forward model are most robust and reveals whether modeller bias has influenced the model outcome. In the following section (Section 4.3), the resulting inversion model is checkerboard tested to determine the size of features that can be resolved throughout the model space. Lastly, the final forward model is converted into a series of density models using standard velocity-density relationships, and the gravity anomalies calculated for those models compared to the observed anomaly along Profile B to test model structure and sensitivity (Section 4.4).

4.2 Modeller-independent inversion

A series of user-imposed constraints and data from a range of sources informed the development of a geologically realistic forward model, representative of the sub-

surface structure imaged along Profile B (Section 3.7). The forward modelling approach improves model constraint and interpretability whilst minimising non-uniqueness; however, it relies on a number of factors that are subjective or utilise assumptions that can limit the model reliability. These limits and assumptions include:

- phase assignment - the assigning of specific phases corresponding to discrete model layers is a subjective process dependent on layer definitions. Further, arrivals such as reflections are more challenging to identify and can be ambiguous in terms of the interface at which they originate;
- supplementary data - additional data constraints, such as MCS-derived sediment thickness and seismic velocity, introduce structure that is not necessarily required to fit WA traveltime picks;
- modelling approach - modelling codes rely on assumptions and simplifications that can introduce systematic errors into the model. Forward model layer definitions can vary between modellers, for example, as model boundaries can be defined by either a single velocity contour or represent a geological interface with a variable velocity; and
- modeller control - experience of modelling and preconceptions of the velocity structure can alter the modelling outcome.

While the sensitivity testing of the final forward velocity-depth model determined the regions of the model that were best constrained (Section 3.8.1), and the restacking of the MCS dataset demonstrated a slight improvement in reflection clarity (Section 3.8.2), these testing methods suffer from the same subjective limitations as the modelling technique itself. It is important to test the forward model against independent and objective datasets and models. An alternative robust and significant test of the forward model is to, therefore, remove all of the subjective components and test for the simplest velocity structure required by the most objective data. The forward model may be further tested by comparing the model to other, independent datasets such as gravity since density and velocity are inherently related (as will be presented in Section 4.4).

The *First Arrival Seismic Tomography (FAST)* software (Zelt & Barton, 1998) was used to undertake the inversion as it utilises a different approach to generating a seismic velocity model. *FAST* iteratively minimises the fit between the modelled and observed first arrivals, without subjective phase assignments, as they are the

most objective record of the sub-surface seismic velocity structure. As the velocity model generated by *FAST* is solely constrained by refracted arrivals, and the process iterates over user-defined cell sizes with spatial smoothing applied in all model dimensions, the method is incapable of developing sharp interfaces that might be expected in the geologically realistic sub-surface. The result is that *FAST* produces a sub-surface velocity model that describes the minimum structure required to satisfy the first arrival traveltime picks (Zelt & Barton, 1998). *FAST* was not expected to produce a velocity model that replicates the structures observed in the forward velocity model, but instead highlight which regions of the model were robustly constrained and free from modeller and additional data bias (Zelt *et al.*, 2003).

It is worth noting that other seismic tomographic inversion software is available, e.g. *TOMO2D* (Korenaga *et al.*, 2000; 2001), but these require greater initial parameterisation, and thus constraint. The relative simplicity of the *FAST* inversion code, and its sole purpose of determining the minimum objective velocity structure, makes it a more appropriate tool for these tests.

4.2.1 Inversion modelling setup

As is the case with the forward velocity modelling procedure, the inversion velocity model requires initialising. The initial inversion velocity model and modelling parameters can strongly control the inversion procedure and impact on the final model. As the only constraints on the modelling procedure are the input velocity model, input traveltime picks, pick uncertainties, and modelling parameters, it is important that each parameter is carefully tested and chosen to ensure that the model was developed in the most stable and unbiased way (i.e. minimal introduction of artefacts). The modelling parameters include:

- λ - controls the weighting of data misfit compared to the constraint equations;
- α - controls the importance of fitting the smallest perturbation relative to ensuring model smoothness;
- S_z - controls the ratio of vertical to horizontal smoothing;
- S_{edge} - controls the weighting at the edge of the model space, i.e. the imposed structure at the model edges is either kept static, or varied if the modelling requires it;
- V_p reset - limits the degree to which upper and lower node velocity values in each model can deviate from the initial model, preventing perturbations occurring above the seabed; and

- inversion cell size - controls the size and aspect ratio of the cells used in the inversion operation.

Each of these parameters were varied within typical ranges (e.g. Zelt *et al.*, 2003), and chosen to produce the smoothest model of the finest resolvable velocity structures, without acquisition geometry artefacts. In all cases, this led to preferentially choosing harsher smoothing parameters. For example, α was chosen to be 0.95, which increases the weighting of model smoothness (α=1) over fitting the smallest model perturbations (α=0). The range of S_z values tested indicated that a value of 0.25 was optimum to account for the more extreme horizontal variation in seismic velocity across the model space (typically in the range of 0.1-0.3; Zelt & Barton, 1998; Zelt *et al.*, 2003). V_p reset values were chosen to prevent the velocity structure of the model reaching velocities that are geologically unreasonable. Although this parameter needed to accommodate large changes in velocity, it regardless had to have a lower seismic velocity limit of 1.5 km s^{-1} and upper limit of 8.5 km s^{-1}. As no prior velocity structure information would be included in the model, the edge constraint, S_{edge}, was set to allow the model edge velocity structure to vary as much as the modelling algorithm required (S_{edge}=0). Values for the inversion cell size and λ were found to have a variable effect on the model and were applied with different values throughout, and so are discussed separately in Section 4.2.2.

The starting model for inversion must be carefully set to ensure that it only reflects the broadest-scale velocity structure of the sub-surface as the inversion linearisation relies on the assumption that only relatively small perturbations from the starting model need to be determined (Zelt, 1998; Zelt *et al.*, 2003; Rawlinson & Spakman, 2016). Velocity models that are overly simplistic (e.g. 1D from the sea surface downwards), that import pre-existing subjective constraints (e.g. MCS-derived sediment layer velocity structure), or that are too detailed (e.g. a smoothed version of the final forward model), are more likely to introduce modelling artefacts or be so close to minimising the misfit between the observed and calculated arrivals that no meaningful changes are made to the model.

Initially a simple velocity model was built that had a velocity gradient from 1.5 to 8.0 km s^{-1} draped to 8 km below the seabed. Following inversion runs with different cell sizes, the deeper regions of the model were found to retain the morphological structure of the seabed. A further starting model, that imposed a first-order velocity discontinuity at Moho-type depths (i.e. by an increase from 7.0-8.0 km s^{-1} over a single node) also failed to move the sharp boundary, resulting in output models with first-order discontinuities in middle crust-type depths (6.0-7.0 km s^{-1}). The testing of these models indicated that a simpler structure, without any imposed first order

velocity discontinuity was required. In both examples, the models were also unable to increase the velocity sufficiently in the sediment and shallow crust region of the model, so this basic structure has to be imposed in the starting model.

To account for these variations, the initial inversion velocity model was built with an increase in seismic velocity from 1.5 to 6.0 km s^{-1} over 1.5 km below the seabed. Beneath this, the velocity increases further to reach 8.0 km s^{-1} at a fixed depth of 15.0 km below model (sea) surface (Figure 4.1a). The velocity model thus matches the broad structure of the forward velocity model, particularly on the forearc and in regions of background oceanic crust (Figure 4.1b and d). This simple relationship does not impose a low internal velocity structure for the Canopus seamount edifice (Figure 4.1c) and, whilst failing to match the structure determined through forward velocity modelling, this provides an ideal opportunity to independently test for modeller bias.

Finally, the input picks to the *FAST* modelling software were extracted directly from the pick files produced for *rayinvr*, selecting only the first arrival phases with the shortest traveltimes. For each selected pick phase assignments were removed, leaving only the assigned uncertainty values (Section 3.5).

4.2.2 Inversion modelling and fit testing

Prior to running the modelling sequence, the initial model was tested to determine the starting point fit between the calculated and observed picks. A first-pass run of the finite difference code, which calculates the traveltimes of the first arrivals through the velocity models, indicated the initial input velocity model had a total T_{RMS} misfit of 492 ms, (χ^2=157; Figure 4.2). This extremely high misfit indicates this initial model is a good starting point for inversion modelling, with no region of the modelled arrivals showing a good fit to the observed data (Figure 4.2a). The modelling code was also tested at this point using a range of inversion cell sizes, with the smallest cells capable of producing a stable velocity structure with this initial model identified as 10 km x 1 km, using a λ of 100.

During inversion run 1, a suitable misfit minimum was found after five iterations of the non-linear inversion, producing a velocity model with a broadly similar structure to the forward model, and a significantly reduced total T_{RMS} misfit of 99 ms (χ^2=6.8; Figure 4.3). Analysis of the difference between the initial velocity model (Figure 4.2b) and the result of run 1 (Figure 4.3b), shows that most of the overriding plate and internal Canopus seamount velocities are significantly reduced by up to 2 km s^{-1} (Figure 4.3d). Only slight changes were made to regions of background oceanic crust and mantle (>360 km model offset). The plot of misfit against model

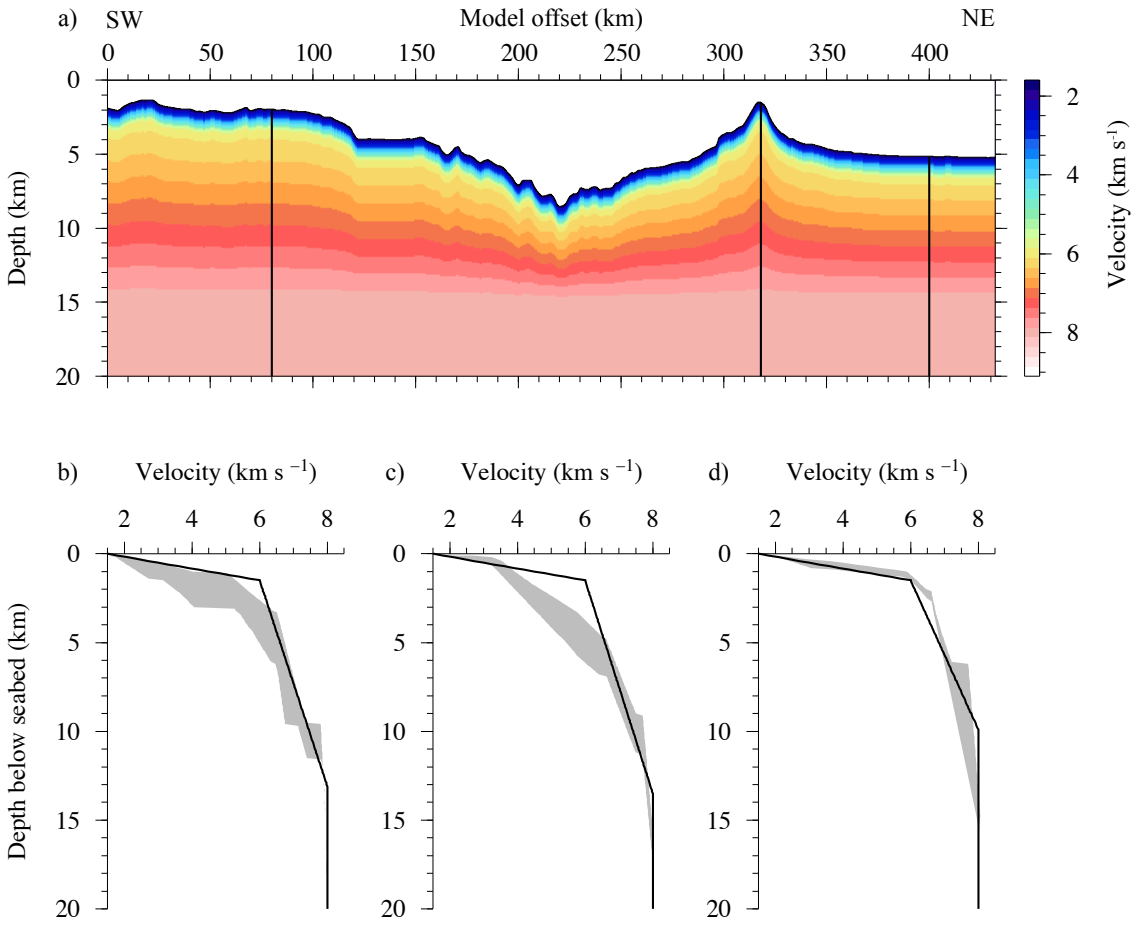

Figure 4.1: Comparison of different initial velocity models for inversion modelling. a) Initial velocity model for inversion modelling. Below the seabed the velocity increases from 1.5 to 6.0 km s^{-1} over 1.5 km in depth, and then increases to 8.0 km s^{-1} at 15.0 km model depth. The black lines through the model indicate the velocity profiles shown in b)-d) compared with the velocity-depth envelope derived from the respective region of the final forward model. Velocity profiles through b) the forearc, c) Canopus seamount, and d) 'background' Pacific oceanic crust.

offset (Figure 4.3a), highlights the overriding plate as the region with the greatest misfit between the calculated and observed arrivals. Furthermore, most of these arrivals with large misfits have a short shot-receiver offset (<20 km), suggesting that the shallow sub-surface has not been adjusted sufficiently as part of the inversion. This is perhaps not unsurprising because the 10 km x 1 km inversion cell size would be insensitive to the large amplitude but spatially limited relative velocity variations in the shallow sub-surface (i.e. the initial forward model sediment layer was 0.8 km thick on average; Section 3.6.4).

An attempt to reduce the misfit for arrivals turning through the shallow sub-surface of the model by running the inversion starting with a 5 km x 0.5 km cell

size resulted in an unstable velocity model that showed velocity inversions and acquisition geometry-related smearing artefacts. The modelling procedure clearly required a large inversion cell size to stabilise the linearisation for the longer wavelength velocity structure before being able to correct for the shallower and smaller structure-limiting misfits. To enable the inversion model to further improve the smaller wavelength velocity structures without introducing modelling artefacts, the result of the run 1 inversion was taken as the starting model for a second inversion run, with the inversion cell size of 5 km x 0.5 km (Figure 4.4). Again, a stable misfit minimum was found after five iterations. The fit between the calculated and observed traveltimes was reduced to a total T_{RMS} of 70 ms (χ^2=3.1), with a marked improvement in the fit of the shortest shot-receiver offset arrivals through the overriding plate crust (Figure 4.4a). As run 1 improved the longer wavelength velocity structures, run 2 was able to correct for the shorter wavelength features, particularly in the shallow sub-surface (Compare the 4.5 km s^{-1} contour on Figures 4.3b and 4.4b between 20-100 km offset). In the shallow forearc crust and the lower-trench slope seismic velocity is reduced by ∼1 km s^{-1} compared to the result of inversion run 1. Throughout the overriding plate crust and mantle, at >5 km depth below model surface, changes in the seismic velocity following run 2 are relatively small (<0.3 km s^{-1}; Figure 4.4d). The subducting plate crust and mantle remain largely unchanged following inversion run 2, although the shallow crust beneath Canopus seamount is slower by ∼0.2 km s^{-1} compared to the result of inversion run 1. Reductions in the seismic velocity around the region represented by the subducting slab interface in the forward model, particularly >10 km depth, are controlled by a limited number of traveltime picks. Following run 2, the lower-trench slope crust arrivals display the greatest misfit, most likely as a result of the limited numbers of rays through this region failing to provide a significant weighting to enable model updates here, compared to the degree of smoothing applied.

4.2.3 Inversion result

After only two runs of five non-linear inversion iterations, the inversion velocity model broadly matches the velocity structure of the final forward model, and the arrival traveltimes exhibit a low total T_{RMS} misfit of 70 ms (χ^2=3.1). The T_{RMS} misfit is lower than that of the final forward velocity model (86 ms), but the χ^2 is higher (2.0 for the forward model). This apparent disparity in statistical fit most likely results from the removal of >8,000 Moho reflected picks for inversion modelling (Section 4.2.1), making it inappropriate to directly compare the statistical

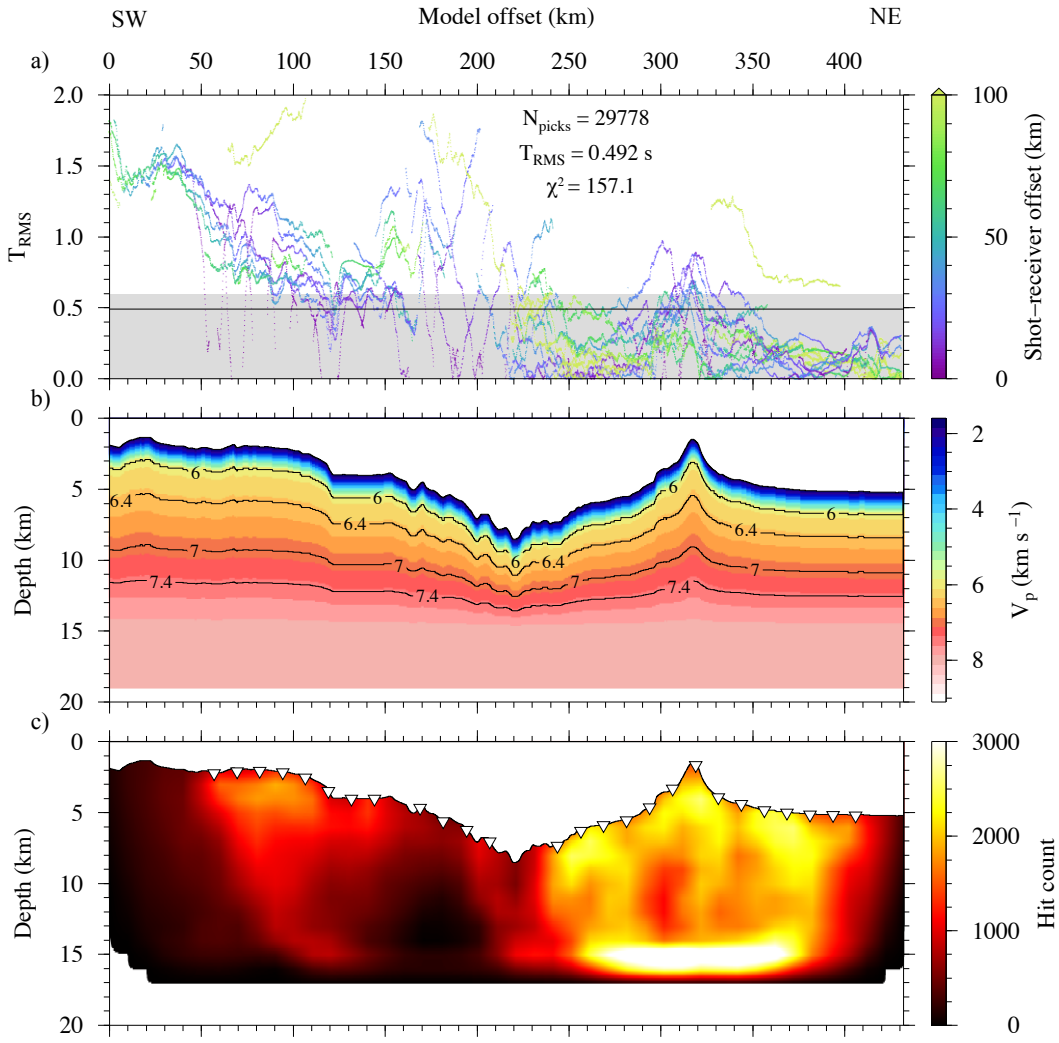

Figure 4.2: Initial inversion velocity-depth model. a) Misfit between the observed and calculated arrivals. These values are generally very high (average T_{RMS}=492 ms), particularly on the forearc and around Canopus seamount, because of the simplistic nature of the velocity model. The grey shaded region indicates the misfit area plotted in the subsequent figures showing how the inversion iterates to a best-fit solution (Figures 4.3 and 4.4). The black line indicates the average T_{RMS} value of the model. b) Initial inversion velocity model, as presented in Figure 4.1, with a velocity increase from 1.5 to 6.0 km s^{-1} over 1.5 km below the seabed, and a further increase to 8.0 km s^{-1} at 15.0 km depth. c) Hit count per inversion cell over the model space, showing significantly greater ray coverage through the Pacific plate than the overriding plate, and almost no coverage through the trench axial and lower-trench slope regions of the model.

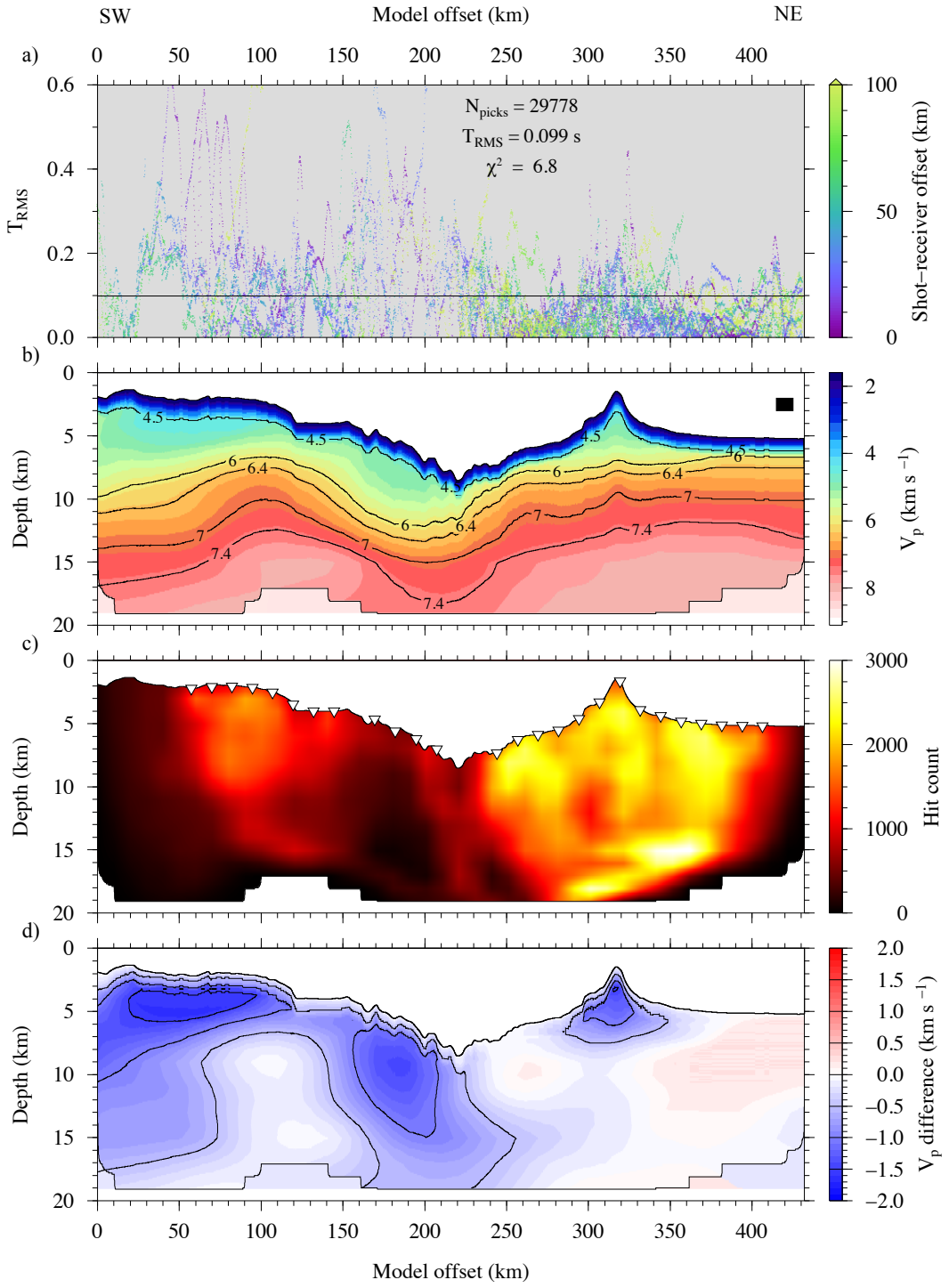

Figure 4.3: Run 1 inversion velocity-depth model. a) Misfit between the observed and calculated arrivals. Arrivals from instruments on the forearc, and those with shorter shot-receiver offsets, display the greatest misfits. The black line indicates the average T_{RMS} value of the model. b) Inversion velocity model following five iterations of non-linear inversions with a 10 km x 1 km inversion cell (indiciated by solid the black box). c) Hit count per inversion cell over the model space. d) Difference from the initial inversion velocity model (Figure 4.2b). Blue colours show net velocity reductions, red indicate increases.

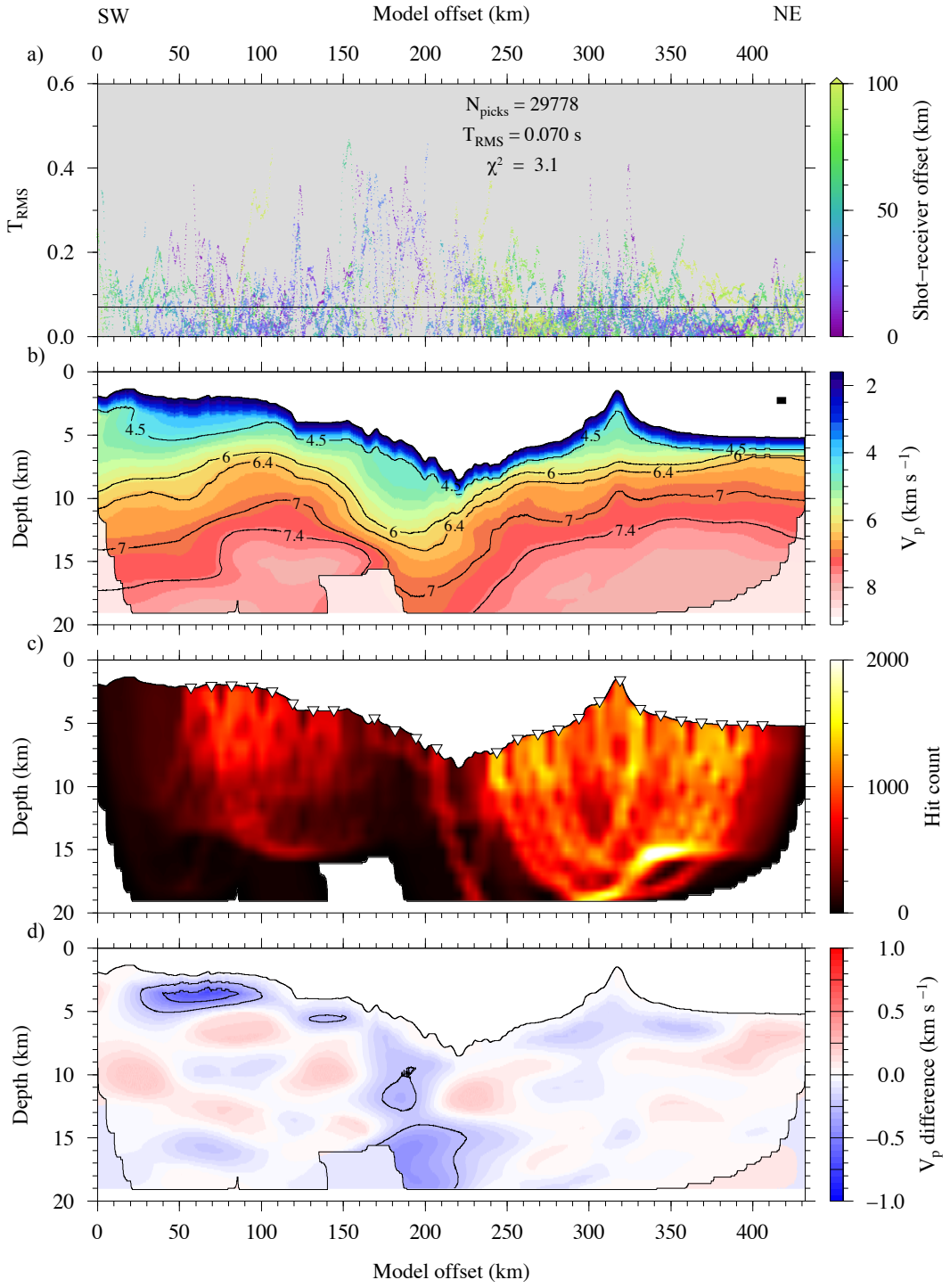

Figure 4.4: Run 2 inversion velocity-depth model. a) Misfit between the observed and calculated arrivals, showing that the forearc instrument misfits have been improved from the result of the run 1 inversion (Figure 4.3). The black line indicates the average T_{RMS} value of the model. b) Inversion velocity model, following a further five iterations of non-linear inversions with a 5 km x 0.5 km inversion cell (indiciated by the solid black box). c) Hit count per inversion cell over the model space. d) Difference from the result of run 1 inversion velocity model (Figure 4.3b). Colours are as in Figure 4.3, but the colour palette has been changed to reflect the smaller velocity perturbations.

fit of the different models. The inversion velocity modelling iterated to a best-fit solution following two runs of five non-linear inversions, where run 1 improved longer wavelength velocity structure with large (10 x 1 km) inversion cells, and run 2 primarily improved the shallower velocity structure with smaller (5 x 0.5 km) inversion cells. Following run 2, the inversion model fits well throughout, but particularly for arrivals travelling through the Pacific plate. The greatest misfit is observed in the trench axis and lower-trench slope, which is perhaps unsurprising given the extremely low ray coverage through these model regions (Figure 4.4).

4.2.4 Comparison with forward model

The final inversion velocity-depth model (Figure 4.5a) differs from the final forward velocity-depth model (Figure 4.5b) most in the shallow sub-surface (<2 km below seabed) and along the inter-plate region of the forward velocity model (Figures 4.5c and d). The inversion modelling procedure is most likely limited in the shallow sub-surface by the imposed velocity structure of the initial model (1.5-6.0 km s^{-1}), and the strong smoothing parameters (Section 4.2.1) that prevent strong lateral and vertical changes in velocity (Zelt *et al.*, 2003). Large differences in the seismic velocity of the forward and inversion models across the inter-plate region are mostly controlled by the low seismic velocity imposed in the upper layer of the forward model subducting oceanic crust. This low velocity is poorly constrained, and only included in the forward velocity model to ensure geological consistency throughout the trench region of the subduction system. The mid- and lower-crustal units of the subducting crust between 170-230 km model offset fit remarkably well between final models (<0.5 km s^{-1}), given the limited ray coverage through both models in this region (Figures 3.17 and 4.4c, respectively).

The velocity models closely match (to <0.5 km s^{-1}) throughout most of the crust and upper mantle across the model space (Figure 4.5c). Generally, the best comparative fit is found in regions where seismic velocity is elevated at the base of the crust, such as beneath the Kermadec forearc ridge and Canopus seamount (at 110 km and 318 km model offset, respectively; 4.5d), where the inversion model is not required to generate a strong first-order velocity discontinuity at the Moho. In regions where the forward model exhibit a strong first-order velocity discontinuity at the Moho (such as <80 km, 150-250 km, and >370 km model offset; Figure 4.5), the inversion model fails to reproduce the velocity-depth profile most likely as a result of the harsh smoothing parameters and the inability for the approach to invert P_mP arrivals (Zelt *et al.*, 2003). Importantly, the inversion velocity model (4.5a) successfully reproduces the longer wavelength velocity structures of the final forward

model. The forearc exhibits low seismic velocities through the shallow (<3 km) subsurface, and also demonstrates that the higher seismic velocities beneath the forearc ridge (∼6.0 km s^{-1} at 7 km model depth, 100 km model offset) are replicated from the forward velocity model. Seismic velocities throughout the lower-trench slope crust are typically low (<6.5 km s^{-1} down to ∼15 km model depth), supporting the observations made in the forward model. The background Pacific crust and upper mantle (>360 km model offset) displays typical oceanic seismic velocity structure, although it is unclear whether the velocities are reduced significantly in the vicinity of the trench-outer rise region (220-270 km model offset) as is the case with the forward velocity model. Despite the high seismic velocity naturally imposed on the crust internal to Canopus seamount in the starting inversion velocity model (6.0 km s^{-1} at 1.5 km depth below seabed; Figure 4.2b), the inversion modelling has reduced the velocity in this region to match those that were observed in the forward velocity model (6.0 km s^{-1} at 5.5 km depth below seabed; Figure 4.5). This indicates that the seismic velocity within the Canopus seamount edifice is most likely remarkably low compared to other regional examples (e.g. Contreras-Reyes *et al.*, 2010) and not a result of any modeller bias.

The final forward velocity-depth model remains the 'preferred' model because it is better constrained by additional datasets (MCS-derived information and WA-reflected phases), is better resolved, and is more geologically representative. The inversion velocity model indicates the minimum structure required by the first arrival data set and, thus, highlights the most robust features that are shared by both models (e.g. Zelt *et al.*, 2003). Whilst these results are significant and indicate the final forward model features are robustly constrained and free from modeller bias, it is important to consider what scale of feature the inversion velocity modelling is capable of resolving.

4.3 Inversion model checkerboard testing

The final inversion velocity-depth model demonstrates a good fit to the first arrival traveltimes and a similar long wavelength structure to that of the forward velocity model. As with the forward velocity model, it is important to assess how reliable and well constrained the inversion model is and determine the parts of the model that may not be resolvable with the acquisition geometry of the experiment, the reduced number of traveltime picks, and the modelling method. However, because the inversion model is formed of a velocity grid and not discretely defined layers, the sensitivity approach to testing is not applicable here. Instead, the resolvability

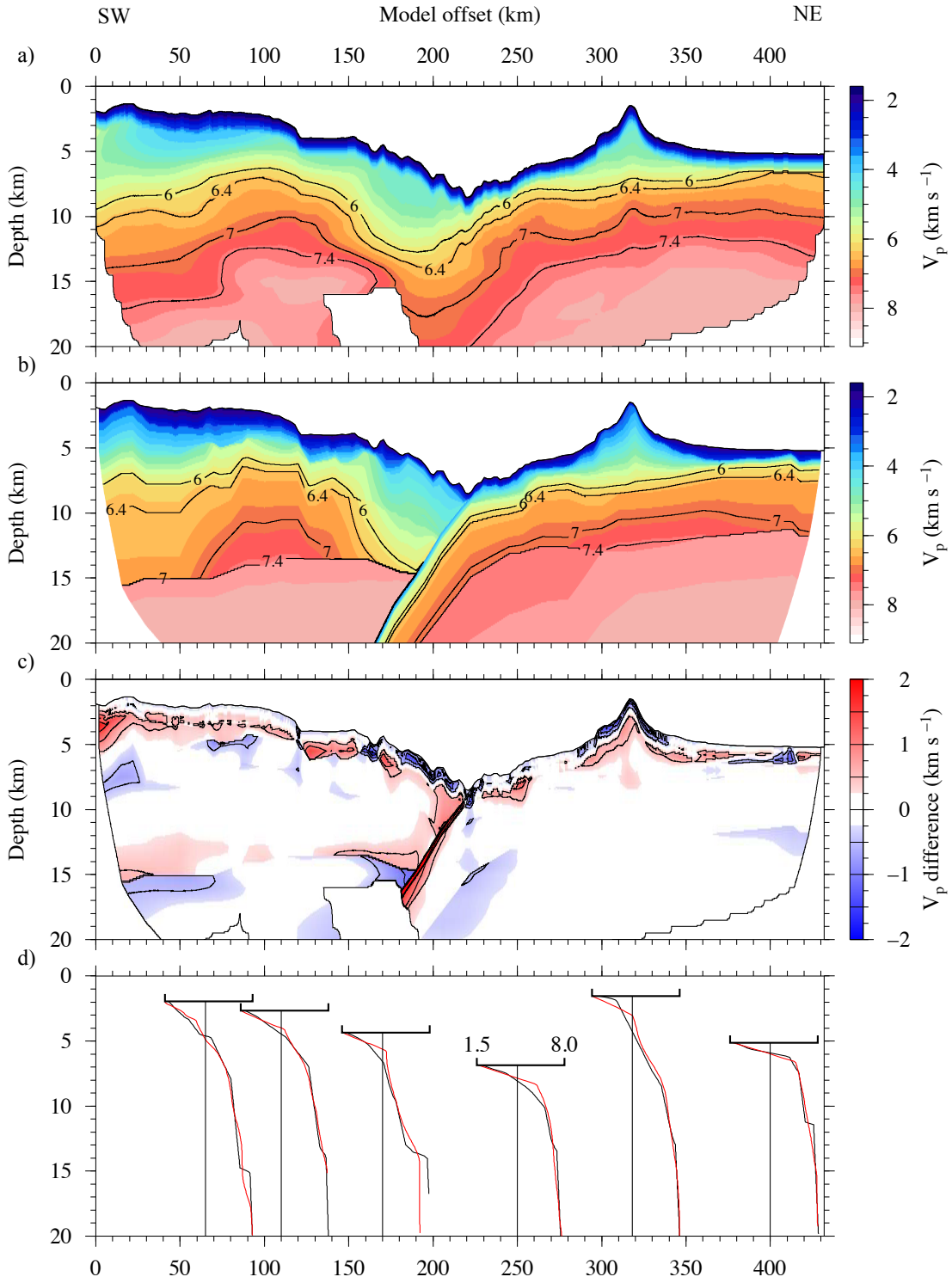

Figure 4.5: Inversion velocity modelling result and comparison with the final forward model. a) Inversion velocity-depth model with significant velocity contours overlain. b) Final forward velocity-depth model for comparison. c) Difference between the inversion (a) and forward (b) velocity-depth models. Blue colours indicate regions where the inversion model is slower than the forward model. Contours mark velocity differences in 0.5 km s^{-1} increments. d) V_p velocity-depth profiles through the sub-seabed of the forward (blue) and inversion (red) models for comparison located at the marked points on the profile. All profiles have the same scale (1.5 to 8.0 km s^{-1}).

of different regions of the inversion model was determined through checkerboard testing, following the method of Zelt (1998) as it is consistent with the modelling approach used for the inversion modelling process itself (Zelt & Barton, 1998), and is widely utilised (Calvert *et al.*, 2008; Takahashi *et al.*, 2008; 2009; Kaneda *et al.*, 2010; Kodaira *et al.*, 2010; Rawlinson & Spakman, 2016). Monte Carlo tests can provide a more direct measure of model uncertainty (e.g. Contreras-Reyes *et al.*, 2011), but are most appropriate for models developed using the Monte Carlo inversion method (Korenaga *et al.*, 2000; 2001).

4.3.1 Checkerboard testing method

Checkerboard testing is a common approach that follows a standardised method, although alternatives have been proposed to test for different types of anomalies, such a discrete spikes (e.g. Rawlinson & Spakman, 2016). Although Zelt (1998) considers a 3D example for checkerboard testing, the method for the 2D case is the same. For clarity, the checkerboard testing was applied as follows:

1. apply a checkerboard velocity anomaly - a checkerboard of a user-defined spatial dimension and percentage anomaly is applied to the final inversion velocity model (M), to yield a checkerboard perturbed input velocity model (M_c);

2. calculate new traveltimes - for each shot-receiver pair used to generate the final inversion velocity model (T) traveltimes are calculated through the checkerboard perturbed input velocity model (T_c);

3. apply noise to the new traveltimes - the applied noise (n) is defined by a Gaussian distribution, with one standard deviation equal to the uncertainty assigned to each pick (T_{cn});

4. set up the checkerboard inversion - the final inversion velocity model (M) is set as the starting model for checkerboard anomaly recovery, with the noise-added traveltimes input as the traveltime 'picks' (T_{cn}); and

5. run the standard non-linear inversion - keeping the same parameters used to develop the inversion velocity model (Section 4.2.1), the inversion was then run to recover the checkerboard perturbed input velocity model (M_c).

Each checkerboard test alters the path of the traced rays (i.e. is a non-linear inversion), predominantly focussing rays along bands of higher relative velocity, introducing a smearing pattern that may not have been present in the initial inversion

model (Rawlinson & Spakman, 2016). Whilst Zelt (1998) notes that such an effect is negligible for small percentage velocity anomaly checkerboards (i.e. <10%), a robust method for assessing a checkerboard anomaly is to test the anomaly size with a range of lateral and vertical node offsets applied to mitigate the potential limitations of this test. For the 2D case, with the model tested at each checkerboard half wavelength in both model directions, this can be achieved with eight tests of the checkerboard (Figure 4.6).

To develop a more complete understanding of the variations in inversion modelling resolvability, different checkerboard sizes were tested. The checkerboards that were successfully resolved to different degrees ranged from 20 to 50 km laterally, and 2 to 5 km vertically, and these were used to determine the size and aspect ratios of seismic velocity features that were capable of being resolved given the acquisition geometry (density and location of different shot-receiver offsets), pick uncertainties, and modelling parameters. It is pertinent to note that checkerboard tests only provide an indirect quantitative assessment of anomaly recovery and model resolvability and, further, that this analysis method only reliably highlights regions that lack resolution and not the true degree of model recovery (Rawlinson & Spakman, 2016).

4.3.2 Checkerboard testing results

The first checkerboard inversion test set, 50 km x 5 km with a 5% velocity anomaly, qualitatively demonstrates relatively good recovery of the input anomaly throughout most of the model (Figure 4.7c-j). Each offset checkerboard indicates the general shape of each checker is recovered for every board in regions shallower than 15 km, and at >50 km model offset. This is perhaps to be expected as there are no instruments located in the first 50 km of the model, and therefore only minimal ray coverage. No significant velocity anomaly smearing, indicative of acquisition geometry-introduced inversion bias, is observed in any of the model regions with dense ray coverage. However, there are slight smears apparent in some checkerboards at the bottom of the velocity model (>15 km model depth) and around the lower-trench slope. Generally a velocity anomaly is only recovered up to 3.5% and does not reach the applied 5%, because the inversion approaches $\chi^2 = 1$. This level of recovery is considered good, as a 1.5% unrecovered velocity anomaly would equate to 0.045 and 0.12 km s^{-1} at background velocities of 3.0 and 8.0 km s^{-1}, respectively. Full recovery of the anomaly may be expected with a reduction of the traveltime uncertainty. However, reducing the uncertainties would not be representative of the original inversion so was not undertaken.

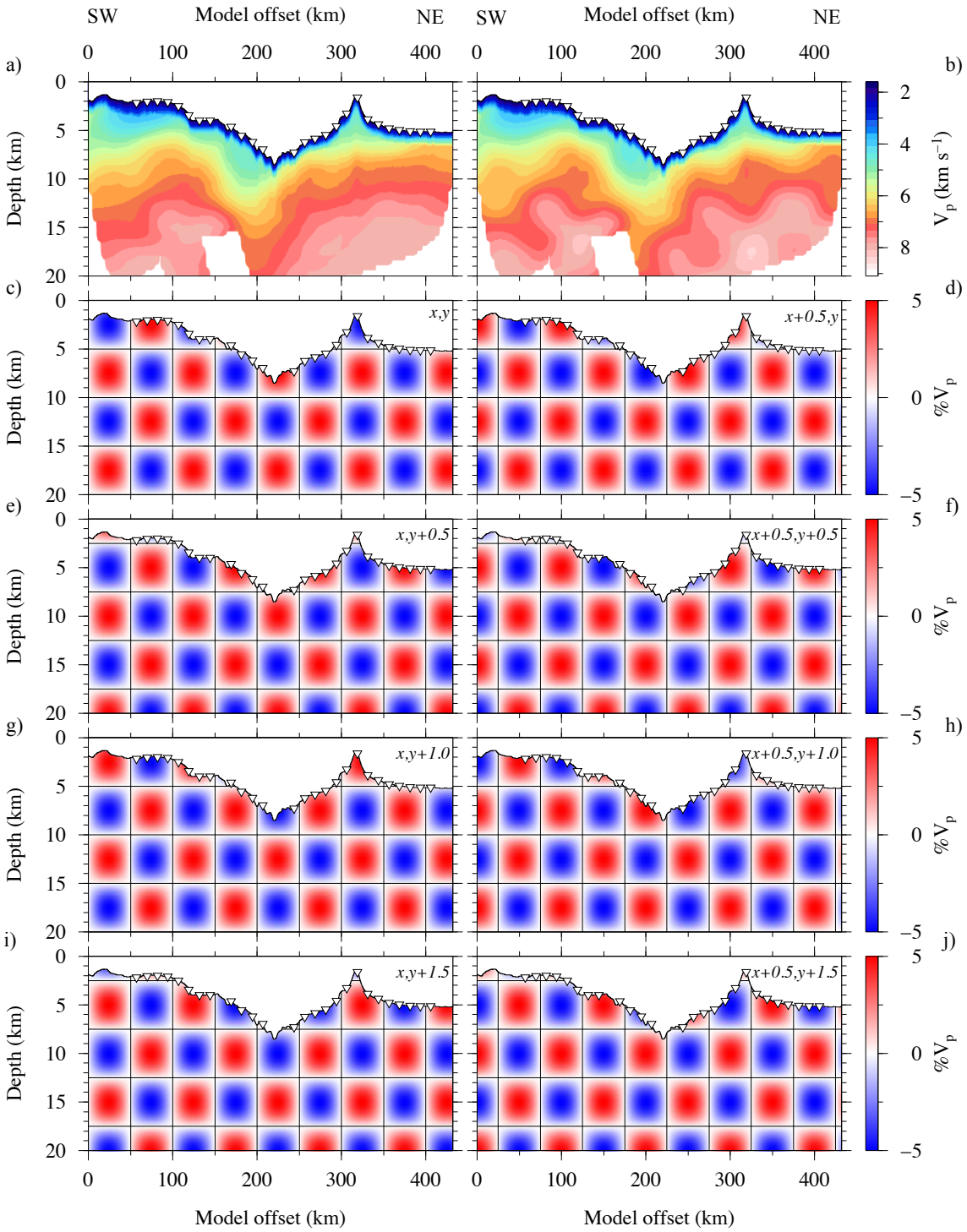

Figure 4.6: Example input velocity anomaly checkerboards testing the resolving capability of the inversion method. a) Final inversion velocity model. b) Final inversion velocity model from a), with a 50 km x 5 km, 5% velocity anomaly checkerboard (c) applied. d)-j) The same checkerboard pattern applied with lateral and vertical checkerboard offsets, indicated in the top-righthand corner of each panel, in checkerboard wavelengths. Note that the grid overlay for c)-j) indicates the expected boundary of individual checkers within each of the eight test patterns.

The results of checkerboard testing are generally considered as purely qualitative and, as such, only a few examples of anomaly recovery are typically shown (e.g. Calvert *et al.*, 2008; Takahashi *et al.*, 2008; 2009; Kaneda *et al.*, 2010; Kodaira *et al.*, 2010). This form of checkerboard presentation significantly limits the ability to critically analyse the true variability of model resolvability, and can lead to general and uninformative statements such as "the model is well resolved". However, checkerboard resolvability, a measure of how well the recovered anomalies match the input checkerboard averaged over a spherical area (Equation 4.1), attempts to provide a more useful, quantitative, assessment of checkerboard tests (Zelt & Barton, 1998; Zelt, 1998). The checkerboard resolvability, R, is defined by:

$$R = \frac{\sum_{j=i}^{N} (Mi_j + Mr_j)^2}{2 \sum_{j=i}^{N} (Mi_j^2 + Mr_j^2)} \tag{4.1}$$

where Mi_j and Mr_j are the percentage anomalies at point j on the input and recovered checkerboards, respectively, with the operators summed over an area consisting of N nodes. A value of 1 indicates perfect recovery, 0 the recovery of a perfect inverse of the input checkerboard (i.e. switched polarity), and 0.5 the effective recovery of nothing.

By calculating the resolvability function for each of the checkerboards in a test set of a given checkerboard size, and averaging over each model node, a quantitative estimate of the broad resolvability of the different model regions can be determined (e.g. Figure 4.7b). Values exceeding 0.7 are considered to be regions of the model that can be regarded as well resolved (Zelt, 1998), which indicates, in the 50 km x 5 km checkerboard anomaly case, that most of the model with good ray coverage (Figure 4.4c), above 15 km depth and to the northeast of 50 km model offset was resolved by the inversion. Whilst the resolvability limit of 0.7 is an arbitrarily defined threshold, it does enable the objective analysis of a large test dataset that can otherwise only be qualitatively assessed.

Following testing of the 50 km x 5 km checkerboard anomaly, a range of other checkerboard inputs were tested, demonstrating anomaly recovery to different degrees, with the larger spatial anomalies typically returning the best resolvability values. For the 40 km x 4 km checkerboard anomaly, the resolvability through the forearc and Pacific crust and mantle remains above the resolvability threshold (Figure 4.8b). The lower-trench slope crust and mantle, however, falls below it. In the recovered checkerboards (Figure 4.8c-j) significant smearing of the velocity anomalies is observed around the lower-trench slope and, in some cases (Figures 4.8c-f)

there is almost no recovery of the input anomaly. Below this checkerboard size, other parts of the model begin to be less well recovered, so resolvability falls below the threshold. For example, the 30 km x 3 km checkerboard tests (Figure 4.9b) are no longer able to sufficiently recover the amplitude of the anomalies through the forearc crust and mantle, but still partially recover the anomalies through the subducting crust where the ray density is greatest (Figure 4.4). Generally checkerboards were found to be recoverable only if the lateral extent of the anomaly was >20 km, and for smaller lateral anomaly sizes, larger vertical anomalies were required (e.g. 20 km x 5 km; Figure 4.10). Again, velocity anomalies throughout the Pacific crust were well recovered and thus retained a resolvability value above the threshold even when the forearc crust and upper mantle did not. Checkerboard anomalies that were smaller than 2 km vertically were consistently not recoverable regardless of the horizontal anomaly size.

4.3.3 Model resolvability results

In total, 16 different checkerboard sizes were tested (Figures 4.7-4.10 and Appendix E), with 20-50 km horizontal and 2-5 km vertical anomaly half-wavelengths incrementing by 10 and 1 km, respectively. To determine a meaningful understanding of the final inversion velocity model resolvability, the values for the different checkerboard resolvability grids for each vertical anomaly size were interpolated to calculate the minimum horizontal anomaly that passed the 0.7 resolvability threshold. The resulting grid is an assessment of the minimum spatial extent of a velocity anomaly necessary to be resolved at a given point in the model space (Figure 4.11). Features smaller than those indicated by the minimum resolvability plots are not resolvable given the modelling parameters, acquisition geometry, and pick uncertainties.

The minimum resolvability plots (Figure 4.11) indicate that the smaller a velocity anomaly vertically, the larger it must be horizontally to be resolved. For 3 km vertical velocity anomalies, the forearc mantle and lower-trench slope crust are unresolvable at any horizontal anomaly scale (Figure 4.11b). For the forearc crust and Pacific crust and mantle only features that extend >40 km horizontally are resolved, except for features in the mid-and lower-crust of the Pacific plate, which may be resolvable if they exceed 30 km laterally. Most of the model space, including the lower-trench slope crust and forearc mantle, becomes resolvable for >4 km vertical velocity anomalies, with features larger than 30 km laterally resolvable for the forearc crust and Pacific plate (Figure 4.11c). At the largest vertical velocity anomaly size tested, 5 km, more of the model becomes resolvable, and the minimum horizontal size of resolvable velocity features is reduced further (Figure 4.11d).

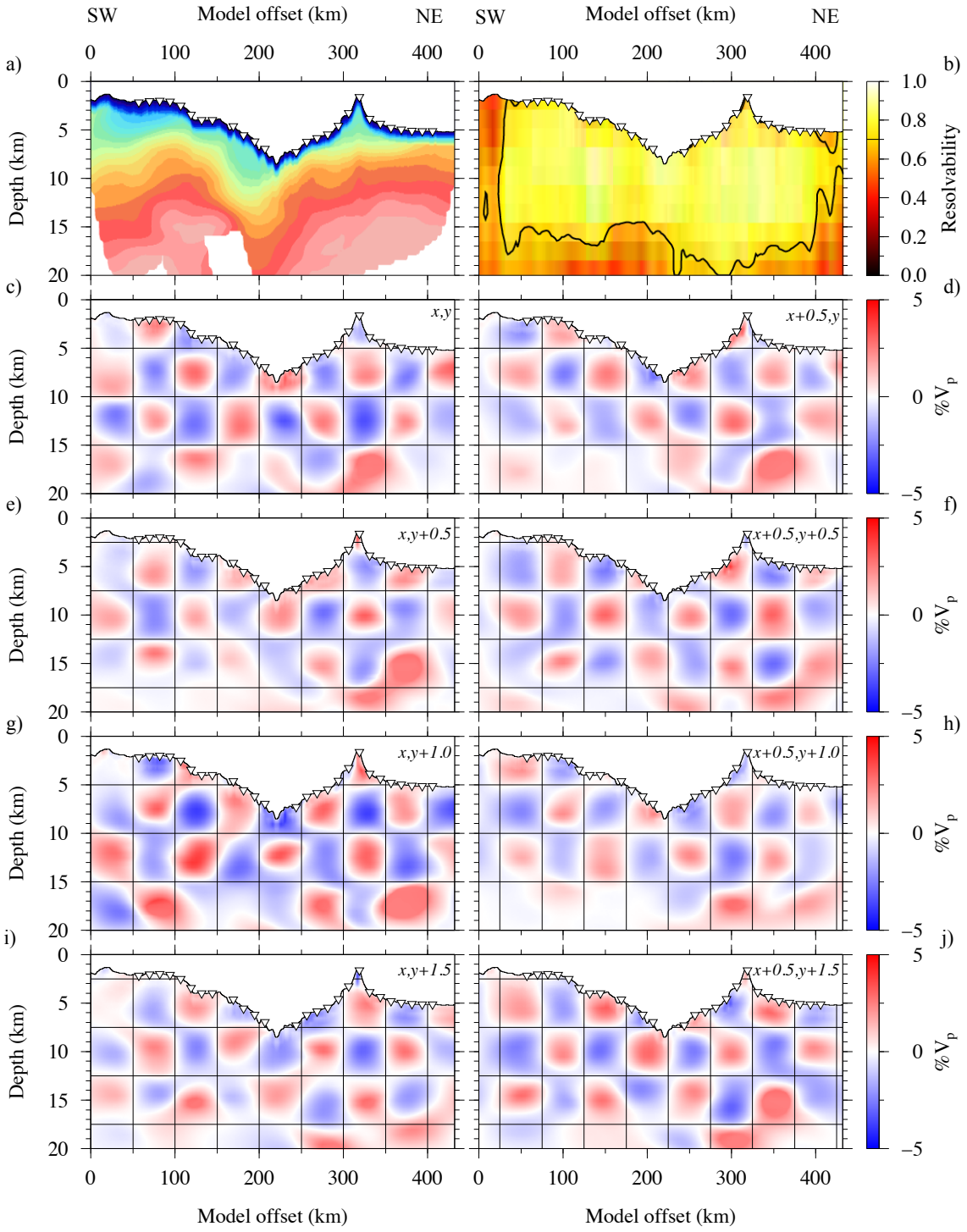

Figure 4.7: Anomaly recovery testing using 50 km x 5 km, 5% anomaly, offset checkerboards. a) Final inversion velocity model. b) Average resolvability with regions exceeding the 0.7 threshold outlined by a contour if applicable. c)-j) Recovered checkerboards. Lateral and vertical checkerboard offsets, in checkerboard wavelengths, are indicated in the top righthand corner of each panel. Note that the grid overlay for c)-j) indicates the expected boundary of individual checkers within each test board.

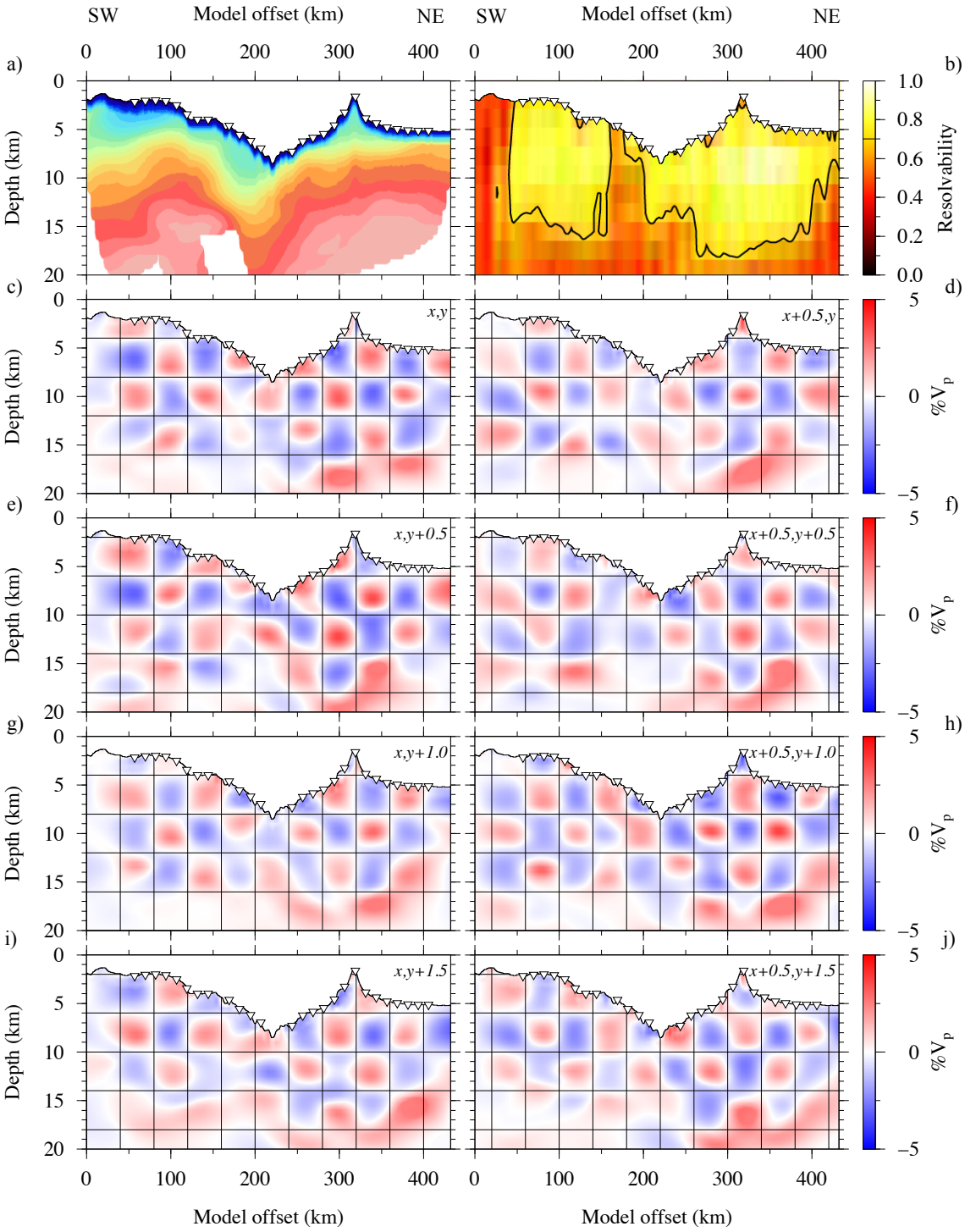

Figure 4.8: Anomaly recovery testing using 40 km x 4 km, 5% anomaly, offset checkerboards. a) Final inversion velocity model. b) Average resolvability with regions exceeding the 0.7 threshold outlined by a contour if applicable. c)-j) Recovered checkerboards. Lateral and vertical checkerboard offsets, in checkerboard wavelengths, are indicated in the top righthand corner of each panel. Note that the grid overlay for c)-j) indicates the expected boundary of individual checkers within each test board.

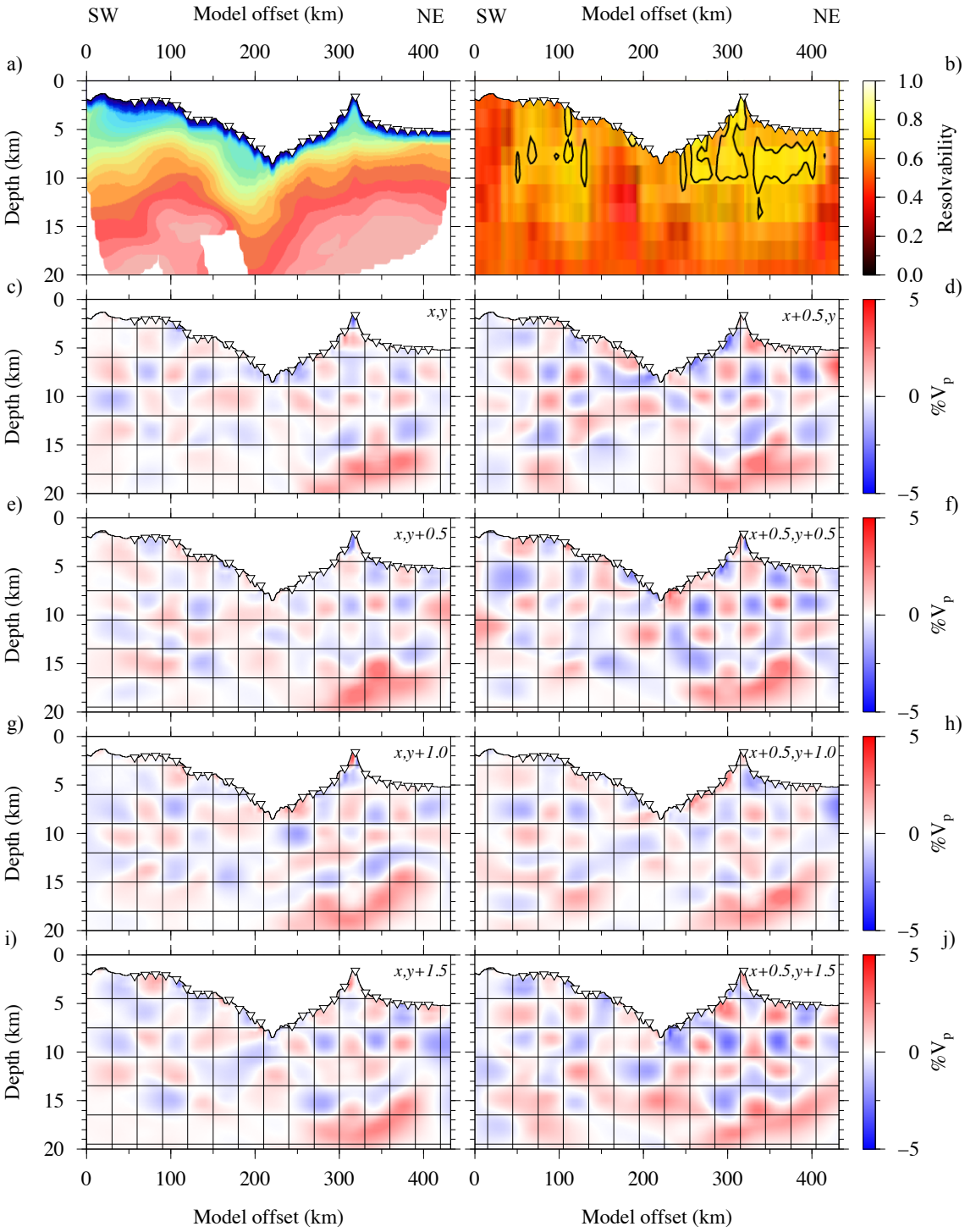

Figure 4.9: Anomaly recovery testing using 30 km x 3 km, 5% anomaly, offset checkerboards. a) Final inversion velocity model. b) Average resolvability with regions exceeding the 0.7 threshold outlined by a contour if applicable. c)-j) Recovered checkerboards. Lateral and vertical checkerboard offsets, in checkerboard wavelengths, are indicated in the top righthand corner of each panel. Note that the grid overlay for c)-j) indicates the expected boundary of individual checkers within each test board.

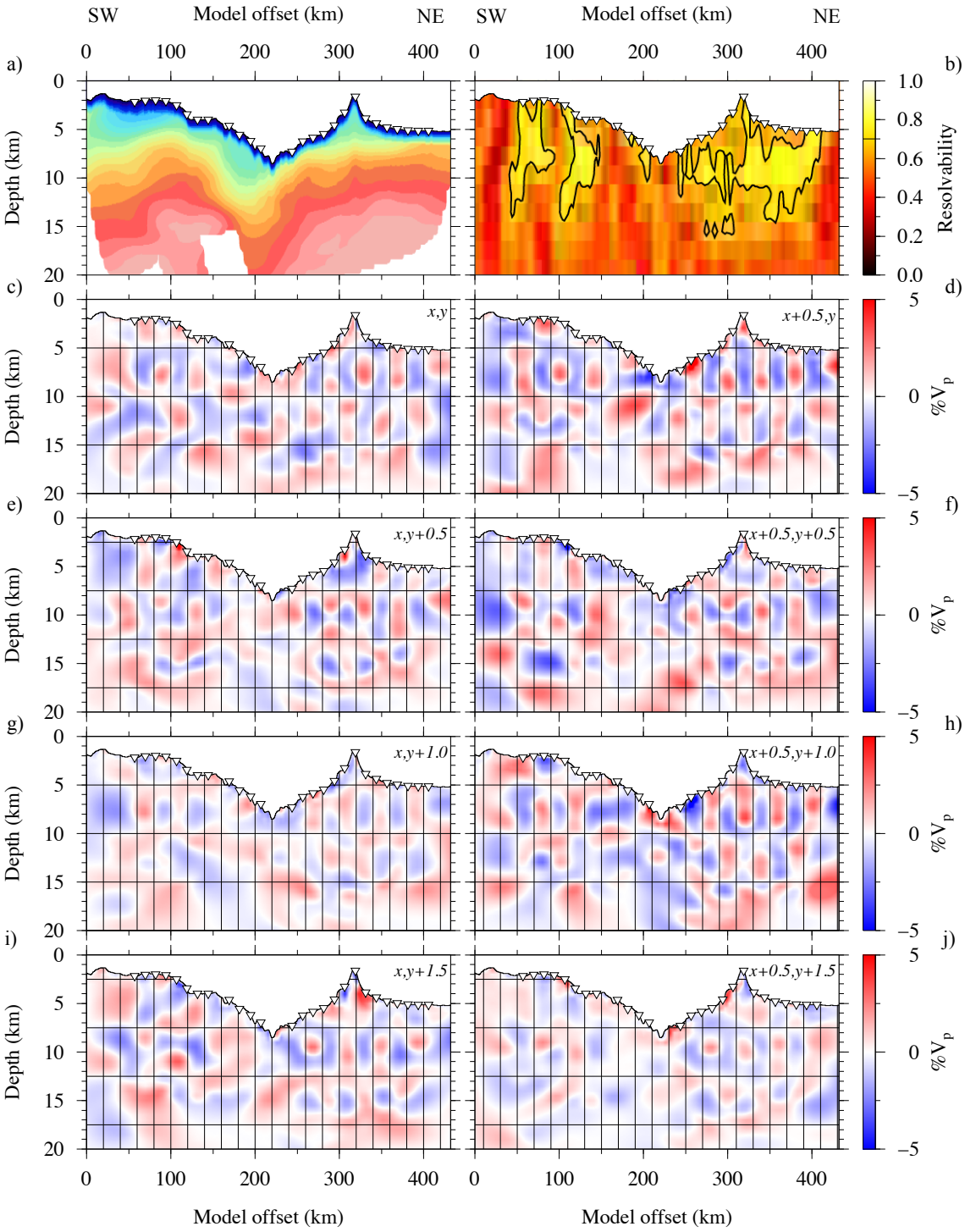

Figure 4.10: Anomaly recovery testing using 20 km x 5 km, 5% anomaly, offset checkerboards. a) Final inversion velocity model. b) Average resolvability with regions exceeding the 0.7 threshold outlined by a contour if applicable. c)-j) Recovered checkerboards. Lateral and vertical checkerboard offsets, in checkerboard wavelengths, are indicated in the top righthand corner of each panel. Note that the grid overlay for c)-j) indicates the expected boundary of individual checkers within each test board.

Throughout the Pacific lower- and mid-crust, velocity structures as small as 20 km laterally may be resolvable (as shown in Figure 4.10).

4.3.4 Checkerboard testing summary

The checkerboard testing method enables the qualitative assessment of the minimum sized velocity anomalies that may be recovered through inversion modelling, using the same set of parameters and traveltime picks that were used to generate the final inversion velocity model (Section 4.2.2). For each checkerboard size, different offset patterns were tested to determine the effect of velocity anomaly location within the model space on its potential to be resolved. These are summarised by the calculation of the average resolvability value for each checkerboard (Zelt, 1998). Along Profile B, velocity anomalies larger than 50 km x 4 km may be recoverable throughout the model space. In regions of relatively high ray coverage, such as throughout the Pacific oceanic crust, smaller features may be recovered, either down to 40 km x 3 km or 20 km x 5 km. This result is summarised in Figure 4.11, which demonstrates the minimum resolvability of the model space determined as the smallest size velocity anomaly (considering a 5% input checkerboard) that can be recovered at a given point in the model space. The minimum resolvability of the inversion velocity model matches the results of the forward velocity model sensitivity testing, whereby the Pacific crust and upper mantle tend to be better constrained than the forearc crust and upper mantle; the lower-trench slope is poorly constrained at all but the largest of scales.

Following the development and testing of the inversion velocity model (Section 4.2 and 4.3, respectively), the final forward velocity model has been shown to be robust with well documented controls on model sensitivity and resolvability. The inversion model iterated to a comparable broad-scale velocity-depth structure as the forward model (Figure 4.5), suggesting that the imaged structure is free from significant modeller and dataset bias in the forward model. Furthermore, checkerboard testing indicated that the range of anomaly dimensions and offsets may be recoverable with the first arrival traveltime picks available (Section 4.3.3).

4.4 Gravity data and modelling

A final test of the forward velocity-depth model uniqueness can be carried out using independently acquired data to assess the preferred model sub-surface structure. The gravity data acquired throughout cruise SO215 (Peirce & Watts, 2011) are dependent on instrumentation errors and uncertainties that are largely independent of

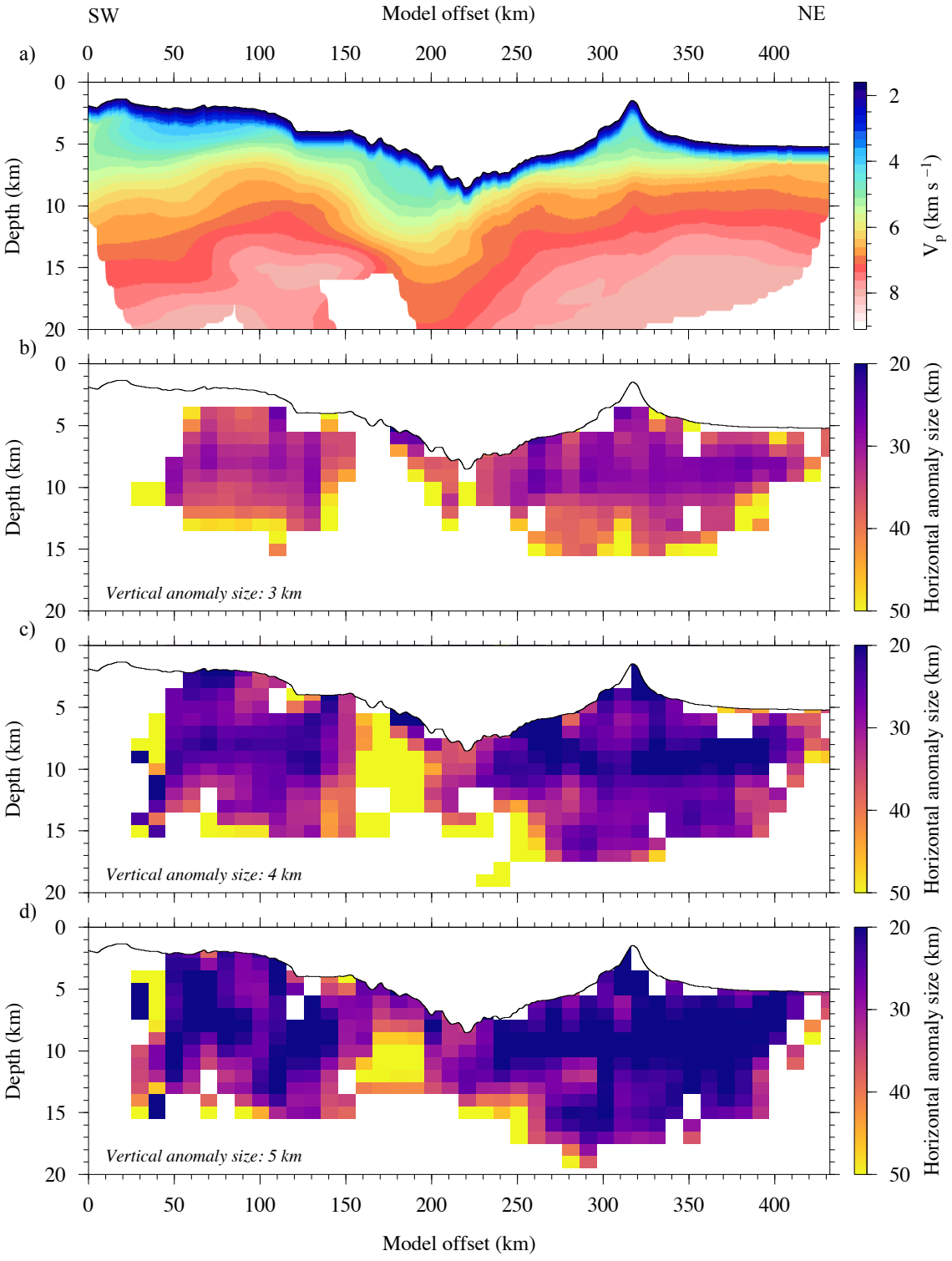

Figure 4.11: Summary of inversion model resolution. a) Final inversion velocity model. b) Minimum horizontal model resolvability for anomalies of 3 km vertical checkerboard size, with a 5% velocity anomaly. Only relatively large horizontal checkerboards (>30 km) are resolvable. c) Minimum horizontal model resolvability for anomalies of 4 km vertically. Only 50 km-wide velocity structures may be observable on the lower-trench slope. d) Minimum horizontal model resolvability for anomalies of 5 km vertically. Small horizontal velocity anomalies (∼20 km) may be resolvable through the Pacific crust.

those present in the seismic dataset. Furthermore, gravity modelling relies on different assumptions to those necessary for forward and inversion velocity modelling. Therefore, the modelling of the gravity field generated by the final forward velocity model is an important and independent test of the validity and uniqueness of the proposed sub-surface structure, and may provide further constraint on the nature of specific features.

4.4.1 Regional gravity field

The Tonga-Kermadec subduction system is defined by a typical regional gravity signature comprising a FAA low across the trench and a high across the forearc and arc (Figure 4.12). On the Pacific plate, the LRSC is expressed as a series of pseudo-circular FAA (>200 mGal) and positive vertical gravity gradient (VGG) highs, surrounded by a broad low FAA (∼0 mGal) and negative VGG indicative of the flexural moat. Capricorn seamount (at ∼18.5°S 172.0°W), is observed as a similar gravity feature to the LRSC volcanic cones. A linear, east-west trending FAA low and negative VGG at ∼26°S on the Pacific plate, clearly delineates the location of the extinct Osbourn spreading centre, which is not as clearly defined in the bathymetry data (e.g. Figure 1.3).

The linear FAA low (<-200 mGal) that defines the Tonga-Kermadec trench becomes less negative (to -100 mGal) at the intersection with the LRSC around 26°S. Coincident with the bathymetric low of Horizon Deep Bight and the westward step in the trench axis north of the LRSC-trench intersection point, the trench demonstrates the lowest observed FAA of the region (<-300 mGal) and increases significantly in width. Along the forearc a broad high FAA (>150 mGal) and positive VGG that follows the strike of the trench, decreases in amplitude from north to south (Figure 4.12). Further west, the arc volcanoes are clearly indicated by a series of small FAA circular highs along the northern segment although, through the centre, these features become less prominent. In the southern segment of the Kermadec arc (south of 31°S), the arc is split into a linear ridge with small circular FAA highs immediately to its west in the backarc. The Lau Basin is wider and exhibits a lower FAA (0-50 mGal north of 20°S) in the north than in the south (50-100 mGal at 25°S). Finally, the Lau-Colville backarc is expressed as a linear FAA high (∼100 mGal) with point highs (<150 mGal) representing extinct volcanic centres.

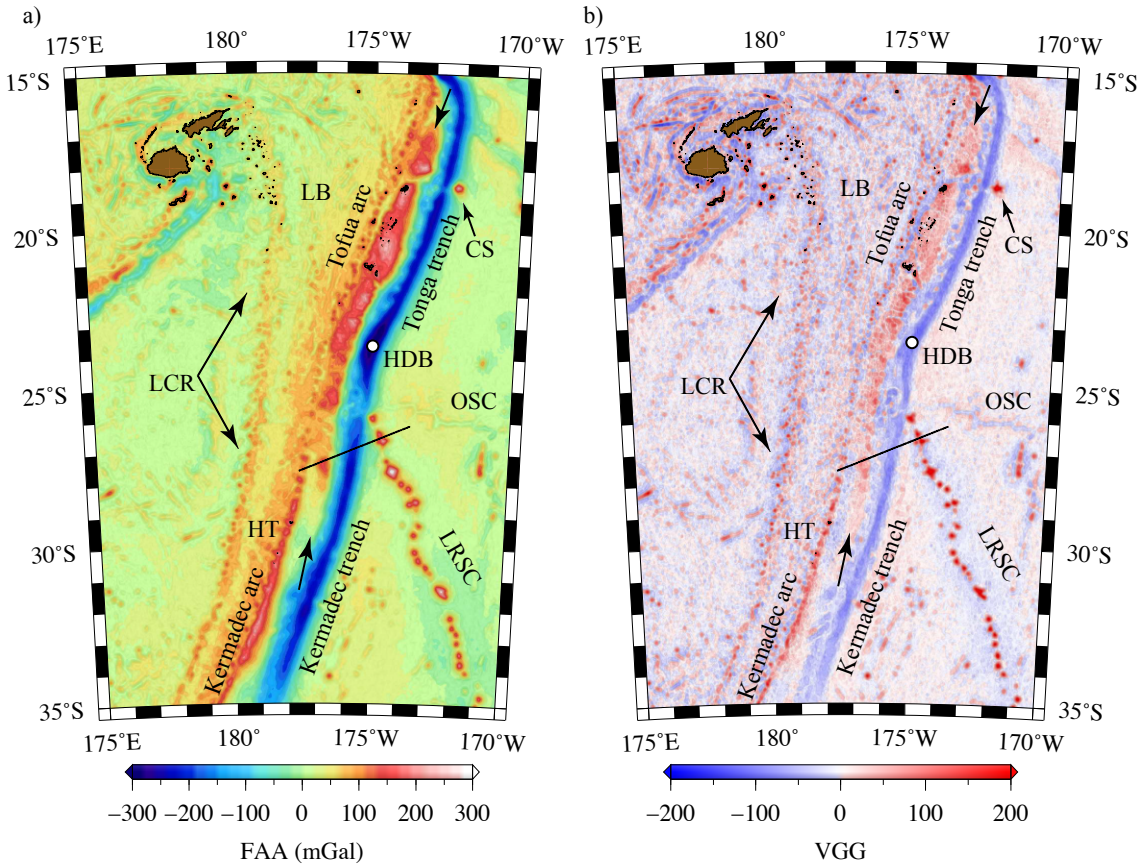

Figure 4.12: Satellite-derived regional gravity maps over the Tonga-Kermadec subduction system and LRSC. a) Satellite-derived FAA data (Sandwell *et al.*, 2014), with annotation highlighting the Tonga forearc high (between black arrows), Osbourn spreading centre (OSC), and Capricorn seamount (CS), Horizon Deep Bight (HDB), Lau Basin (LB), Havre Trough (HT), and Lau-Colville Ridge (LCR). b) VGG over the same region, highlighting features defined by rapid lateral variations in gravity such as the LRSC, Osbourn spreading centre, and the Tonga-Kermadec trench-arc-backarc system. The black line indicates the location of Profile B in a) and b).

4.4.2 Acquisition

Shipboard gravity data were acquired, port-to-port, using a Lacoste & Romberg Air-Sea gravimeter. Absolute gravity base station ties were made in Auckland (New Zealand), and Townsville (Australia), to determine and correct for long-period instrument drift, which was calculated to be just 4.73 mGal over the 47 day cruise ($\sim$ 0.1 mGal per day; Peirce & Watts, 2011). As well as correcting for drift, the absolute station base ties enabled the conversion of the relative gravity measurements obtained by the shipboard gravimeter to absolute values.

The instrument has a reported accuracy of 0.1 mGal, however, cross-over analysis with >2,000 readings gave a RMS misfit of $\sim$10.0 mGal (Peirce & Watts, 2011).

This high cross-over RMS misfit may be expected because of the high gravity gradients observed in the region of the Tonga-Kermadec subduction system generated by the rough and steep gradients of the seabed topography, and the heavy sea state throughout the cruise SO215. The crossover error of 10.0 mGal is most likely the worst case error, and is thus taken to represent the dataset uncertainty for modelling purposes because the value is an objective quantification of the combined instrumentation errors and uncertainties.

4.4.3 FAA gravity analysis

The ship-derived FAA data displays a strong noise component for short wavelength features that was effectively removed through the application of a gaussian-weighted filter over an 8 km rolling window (Figure 4.13). Following filtering, the along-profile ship-derived FAA closely matches the satellite-derived FAA (Sandwell *et al.*, 2014), and highlights the significant bathymetric features (Figure 4.13). On the Pacific plate, Canopus seamount is observed as a FAA high of ∼200 mGal surrounded by a low representing the flexural moat. The Kermadec trench exhibits a typical low of <-200 mGal, that rises sharply through the trench slope into the forearc high. Despite being >0.5 km further below sea level than the volcanic arc, the forearc high is represented by a >30 mGal higher FAA of ∼150 mGal. While the seabed topography predominantly controls the shape of the FAA, the forearc FAA may also be influenced by a significant sub-seabed density anomaly.

4.4.4 Two-dimensional gravity modelling

Two-dimensional gravity modelling was undertaken to independently test the forward velocity-depth model, and provide additional constraint on the composition and nature of the sub-surface structures. This modelling was achieved by converting the forward velocity-depth model into a representative density-depth model using standard velocity-density relationship equations (e.g. Nafe & Drake, 1957; Ludwig *et al.*, 1970; Carlson & Raskin, 1984; Christensen & Mooney, 1995), and comparing the gravity anomaly calculated over the model space with the observed FAA. The fit between the observed and calculated gravity anomalies is dependent on:

- errors and uncertainties in the observed dataset;
- suitability of the definition of the 2-D polygonal bodies;
- suitability of the seismic velocity-density relationship used to represent the material described by each polygon; and

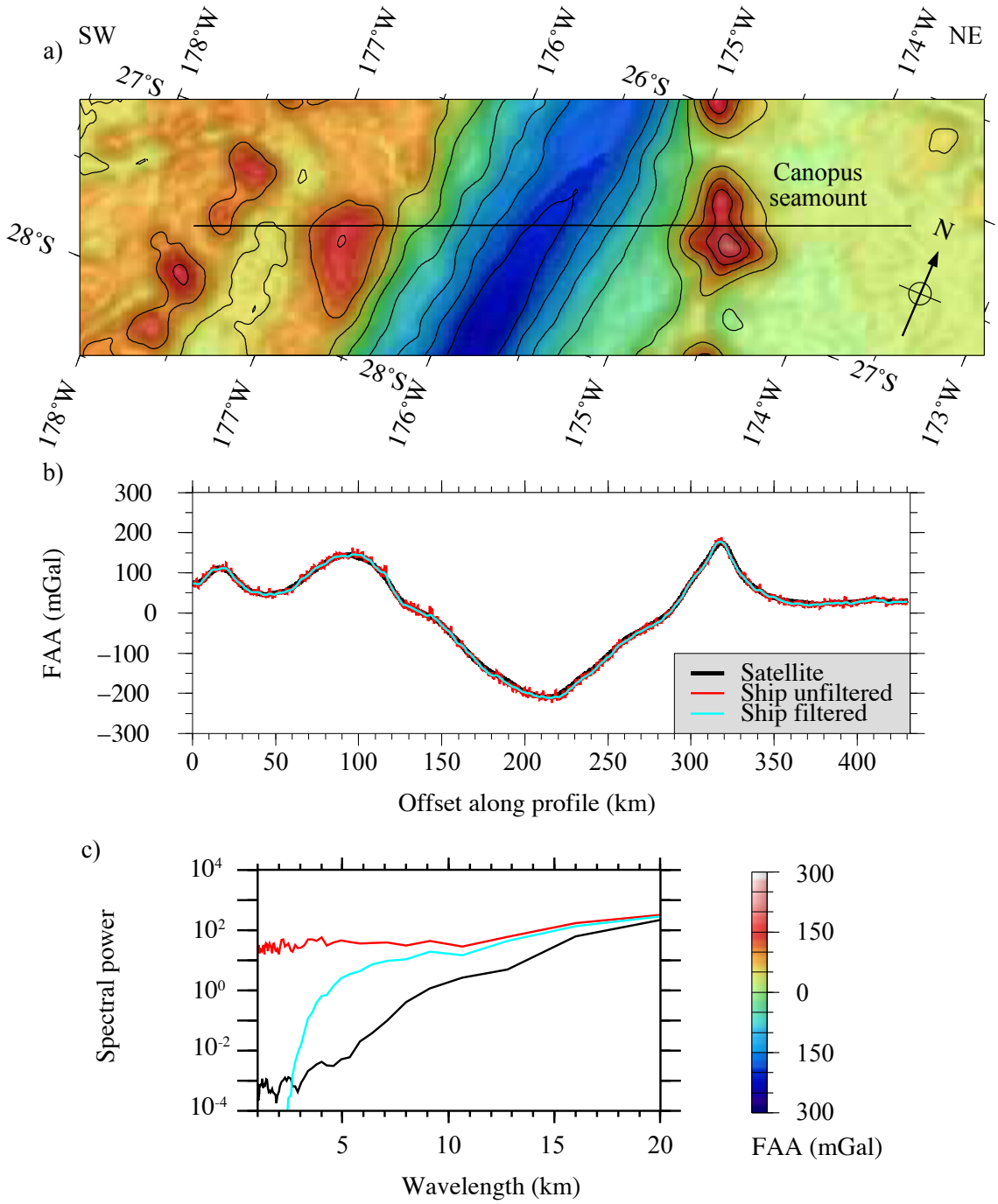

Figure 4.13: Summary of Profile B FAA data. a) Map of the satellite-derived FAA (Sandwell *et al.*, 2014) in the vicinity of Profile B. The black line indicates the location of the profile. b) Comparison of ship and satellite FAAs along the profile, highlighting that the shipboard-acquired data matches the satellite-derived data well at the longer wavelengths. The unfiltered shipboard data exhibits a strong noise component that is removed by filtering. c) Spectral power of the different wavelength components of the FAAs that demonstrates the short-wavelength noise component in the raw shipboard dataset, but that a Gaussian-weighted filter over an 8 km rolling window effectively removes this to reveal a shorter wavelength component that is not resolved by the satellite FAA.

- assumptions and limitations of the gravity modelling program.

4.4.4.1 *grav2d*

grav2d is a program, written by J.H. Leutgart, following the algorithm of Talwani *et al.* (1959), that calculates the two-dimensional gravity anomaly generated by a series of user defined polygons, each represented by a single density value. Two-dimensional gravity modelling assumes that the density structure is uniform over an infinite distance perpendicular to the model. While profiles taken across a region with minimal out-of-plane structural variability will not introduce large errors into modelling, regions with strong three-dimensionality may be poorly modelled. The method of Talwani *et al.* (1959) is widely used because the two-dimensional limitation is considered negligible for large-scale structures such as continental margins and subduction systems that exhibit minimal along-strike variability. However, for smaller and laterally limited features, such as seamounts, this modelling technique can introduce significant errors so 3D gravity modelling techniques are preferred (e.g. Hwang & Kim, 2016).

4.4.4.2 Model construction

To fully test the forward velocity model, a range of different density models with varying detail were tested. The models were constructed following the same underlying method:

- the boundary nodes for juxtaposing layers from the rayinvr *v.in* file (Appendix D) were combined to form polygons defining each layer;
- a representative density was calculated for each of the model polygons by applying one of the standard velocity-density relationships to the median velocity value of the respective block defined in the forward model space;
- the model was extended laterally to ±1000 km from each edge (i.e. spanning -1000 to 1432 km model offset). For later models, this included draping the extended model edge structure beneath corresponding actual bathymetry extracted from the GEBCO dataset.
- for later models, the model depth was increased from 35 to 100 km and the subducting slab added from the Slab1.0 model (Section 3.7.3.3; Hayes *et al.*, 2012).

The models were developed iteratively, with a focus on improving the model regions that did not satisfy the observed FAA.

4.4.4.3 Velocity-density conversion

To ensure that each of the model polygons were represented by an appropriate density, different velocity-density relationships were applied to each of the forward velocity model layer median velocities as appropriate.

The sediment layer was represented by the empirical relationship of Ludwig *et al.* (1970), following Nafe & Drake (1957), which is based on measurements of velocity and density in sediments (Equation 4.2; Figure 4.14a):

$$\rho = -0.00283V_p^4 + 0.07V_p^3 - 0.598V_p^2 + 2.23V_p - 0.7 \tag{4.2}$$

where ρ is the density in g cm^{-3}, and V_p is the P-wave velocity in km s^{-1}. This relationship may result in an underestimate of the density of the velocity model sediment layer because the relationship is empirically based upon the average of all sediment types, of which the volcaniclastics expected along Profile B are most likely an upper end-member component. The velocity-density relationship used for the oceanic crust (Figure 4.14b) was taken from Carlson & Raskin (1984), where the crust is divided into layer 2 (Equation 4.3) and layer 3 (Equation 4.4). Carlson & Raskin (1984) note that Equation 4.4 is also suitable to describe the bulk oceanic crust (i.e. layers 2 and 3 combined).

$$\rho = 3.50 - \frac{3.79}{V_p} \tag{4.3}$$

$$\rho = 3.81 - \frac{5.99}{V_p} \tag{4.4}$$

The forearc crust was tested with both of the standard oceanic crust relationships of Carlson & Raskin (1984), and also the standard continental crust relationship presented by Christensen & Mooney (1995) (Equation 4.5; Figure 4.14b), because although the intra-oceanic arc setting of the Tonga-Kermadec system is considered the opposite end-member to continental subduction (Uyeda, 1982), a number of studies propose that these systems may be sites where continental crust is generated (Takahashi *et al.*, 2008; 2009; Kodaira *et al.*, 2010).

$$\rho = 5.055 - \frac{14.094}{V_p} \tag{4.5}$$

The water column was assigned a fixed density of 1.03 g cm^{-3} for each of the models as the density variations within the layer are significantly below the resolution of the observed gravity data. The mantle density for both the subducting and overriding plates was set to 3.30 g cm^{-3} as an initial value. Model densities

are quoted in g cm^{-3}, rather than the S.I. units, kg m^{-3}, for brevity and clarity of annotation on the figures.

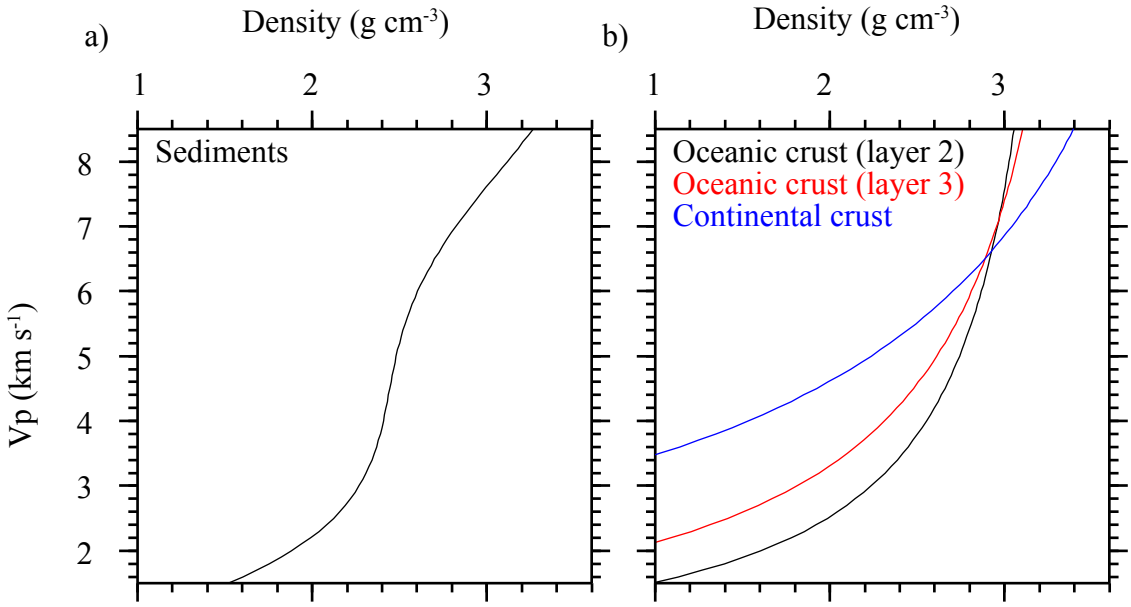

Figure 4.14: Velocity-density relationships tested and applied to the polygons defined in density modelling. a) Sediment relationship from Ludwig *et al.* (1970) after Nafe & Drake (1957). b) Crustal relationships for oceanic crust layers 2 and 3 (Carlson & Raskin, 1984) as well as continental crust (Christensen & Mooney, 1995).

4.4.5 Coarse polygon model

The coarse polygon model was developed first to calculate the gravity anomaly generated by the simplest density model capable of describing the Profile B forward model. This model comprised the water column, sediment layer, and single polygons representing the crust and mantle for both the overriding and subducting plates. Each polygon was built directly from the forward model layers and extended laterally to ±1000 km from the Profile B model space with densities determined for the sediments using the sedimentary relationship (Equation 4.2; Ludwig *et al.*, 1970), and for the subducting crust, the bulk oceanic crustal relationship was applied (Equation 4.4; Carlson & Raskin, 1984).

This coarse polygon density model (Figure 4.15) generates a FAA that is broadly similar to the observed data with either oceanic and continental crustal relationships applied to the overriding plate crust. The calculated anomaly replicates the FAA high around Canopus seamount, and the low around the Kermadec trench. Across the forearc the fit is less good as, although the anomalies match in the lower-trench

slope regions, they begin to diverge over the forearc basin and arc. For an overriding plate crust with oceanic composition (Equation 4.4), the RMS misfit is 39.2 mGal, whereas with a continental composition (Equation 4.5), the RMS misfit is 32.5 mGal. While there is a slight improvement in the misfit with the use of the continental crust velocity-density relationship, both relationships applied fail to capture the shorter wavelength component of the forearc FAA, and appear to exhibit a very long wavelength misfit. Although the misfit between the calculated and observed anomalies is of the same order of magnitude as the dataset uncertainty (10.0 mGal), there are a number of features of the model that may be contributing to the model misfit, including:

- model resolution - the model is only defined by the large-scale sedimentary, crustal, and mantle polygons, which is most likely not sufficiently detailed to effectively recreate the observed FAA;
- velocity-density conversion - the empirically-derived velocity-density conversion equations may be an incorrect representation of the relationship for the defined model polygons;
- edge effects - the simple extension of the sub-surface structure at the model edges to $\pm$1000 km may introduce long-wavelength edge effects into the calculated FAA. The most significant factor in this mismatch may be large bathymetric variations at short distances from the southwest end of Profile B;
- model depth - the density model extends only to the 35 km depth of the forward model. This may be inadequate for modelling the entire FAA associated with the subducting slab, which is likely to contribute to the long-wavelength misfit towards the southwestern end of the profile; and
- degree of three-dimensionality - the Tonga-Kermadec subduction system is not entirely two-dimensional along-strike and in addition the LRSC and Canopus seamount are isolated bathymetric features (Section 4.4.1).

To account for some of these possible sources of model misfit, a more detailed model was developed by breaking up the main polygons of the coarse model, adding more detailed bathymetry to the lateral extensions of the model space, and extending the slab to greater depth using the Slab1.0 model.

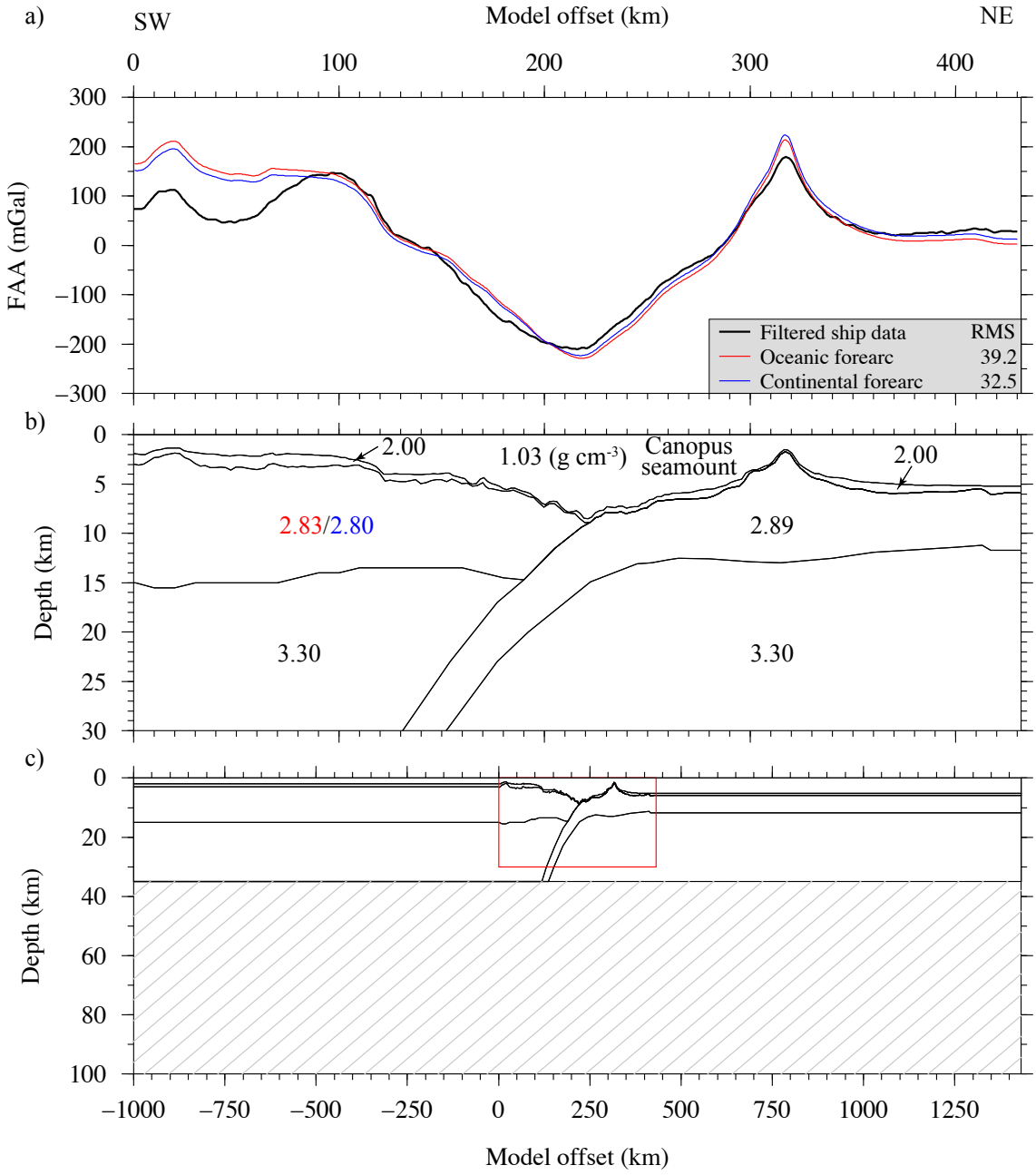

Figure 4.15: Coarse polygon model and associated calculated gravity anomaly. a) Comparison of the calculated and observed FAAs for the coarse polygon model shown in b). b) Coarse polygon density model, comprising a continuous sediment unit, and distinct whole-crust and mantle polygons for the Pacific and overriding plates. Overriding plate crustal density is either determined with oceanic (red) or continental (blue) velocity-density relationships. c) Entire gravity model extended laterally to ±1000 km, using the structure at the forward model edges. The cross-hatched region is not included in the FAA calculation, and the red box indicates the model space shown in b).

4.4.6 Layered polygon model

The layered polygon model was constructed by subdividing the crustal polygons into their distinct forward model layers (three for both the overriding and subducting plate crust). The layer polygons were extended beyond the Profile B model space by applying the GEBCO bathymetry to the seabed for 300 km on either side, and draping the 1D sub-surface structure at the model edge beneath it. Beyond the ±300 km extension, the density model was extended to ±1000 km without any further extrapolation or data input, because of the negligible effect of the bathymetry on the Profile B FAA at these offsets. For the additional polygons, as a starting point, the upper two crustal polygons of the forearc and Pacific crust were represented by the oceanic crustal relationship for layer 2, and the lower crustal polygon by the relationship for layer 3 (Equations 4.3 and 4.4 respectively; Carlson & Raskin, 1984).

The initial result from the layered polygon model (Figure 4.16; 'no crustal anomaly, no slab' model) indicated a slight improvement in the total RMS misfit (32.8 mGal), although the long-wavelength misfit at the southwestern end of the model (model offset <100 km) remained. To investigate the cause of this, the model space was extended from 35 km to 100 km in depth, with the bottom of the subducting plate projected to the new base of the model using the Slab1.0 model (Section 3.7.3.3; Hayes *et al.*, 2012). Maintaining the same crustal and mantle densities throughout the model space, and extending the slab in this way effectively removed the long-wavelength misfit at the southwestern end of the model. The removal of the long-wavelength residual misfit highlighted a short-wavelength misfit across the forearc morphological high caused by a significantly lower calculated than observed FAA and resulted in a total RMS misfit of 33.6 mGal (Figure 4.16; 'no crustal anomaly, slab' model). To account for this apparently high FAA over the forearc morphological ridge, a polygon of higher density (3.30 ± 0.10 g cm^{-3}) was required at the base of the forearc crust (Figure 4.16b). The higher density polygon was defined by the region of abnormally high velocity at the base of the crust in the forward model (7.0-7.4 km s^{-1}, 70-160 km model offset; Figure 3.17). This feature will be discussed in more detail, in the context of the other geophysical datasets along Profile B and globally, in the next chapter (Section 5.3.4). When combined with the oceanic crustal velocity-density relationship for the forearc crust, this density-depth model produced the lowest RMS misfit of 13.1 mGal (Figure 4.16; 'crustal anomaly, slab' model).

The fit for Canopus seamount is remarkably good for each of these model cases. This is surprising given that the seamount is laterally limited, and so violates the

2D assumption of modelling, although the models do slightly over-calculate the anomaly by ∼20 mGal. The observed FAA for Canopus seamount may be higher than expected for the structure modelled along Profile B because the profile crosses the topographic saddle between two bathymetrically prominent volcanic cones. Although not supported by evidence from Profile B, these volcanoes are proposed to have high velocity intrusive cores (Richards *et al.*, 2013), that have been successfully modelled with unusually high densities (2.80 g cm^{-3}) less than 1 km below the seabed (Contreras-Reyes *et al.*, 2010; Hwang & Kim, 2016), and so might significantly increase the FAA observed along a profile adjacent to them. In short, although the 2D FAA calculated along Profile B is based on the bathymetry through the topographic saddle of Canopus seamount, the observed FAA is actually a function of the longer-wavelength 3D seamount structure, comprising two shallower morphological edifices and a possibly higher density core.

4.4.7 Gravity modelling summary

Modelling of the gravity anomaly using the density-converted forward velocity model was undertaken as the final independent test of the sub-surface seismic velocity structure and to better understand the possible composition of the different model components. The Tonga-Kermadec subduction system exhibits typical FAA features, including extreme lows (<-200 mGal) across the trench and highs (>150 mGal) across the forearc ridge and volcanic arc. The observed FAA was initially not well matched by the anomaly generated by the simpler coarse polygon model, indicating that this whole-crustal model failed to account for vertical and lateral density variations in the crust. An effective fit of the FAA along Profile B was only achieved when multiple crustal polygons were included to match the vertical layering and lateral variation of the forward velocity model, and appropriate steps were taken to accommodate the significant model edge effect, primarily due to seabed topography immediately off the profile ends, and a long-wavelength misfit, due to the projection of the subducting slab at depth.

Both the subducting and overriding plates generate the best fit to the observed data if oceanic velocity-density empirical relationships are used to convert the forward velocity model. Despite being the most laterally isolated feature imaged along Profile B, and thus violating the assumption of minimal out-of-plane structure required by the Talwani *et al.* (1959) algorithm, the FAA modelled for Canopus seamount fits remarkably well to the observed data. Across the Kermadec forearc ridge, a significant misfit between the calculated and observed FAA was found to be most effectively minimised by adding an anomalously high density polygon

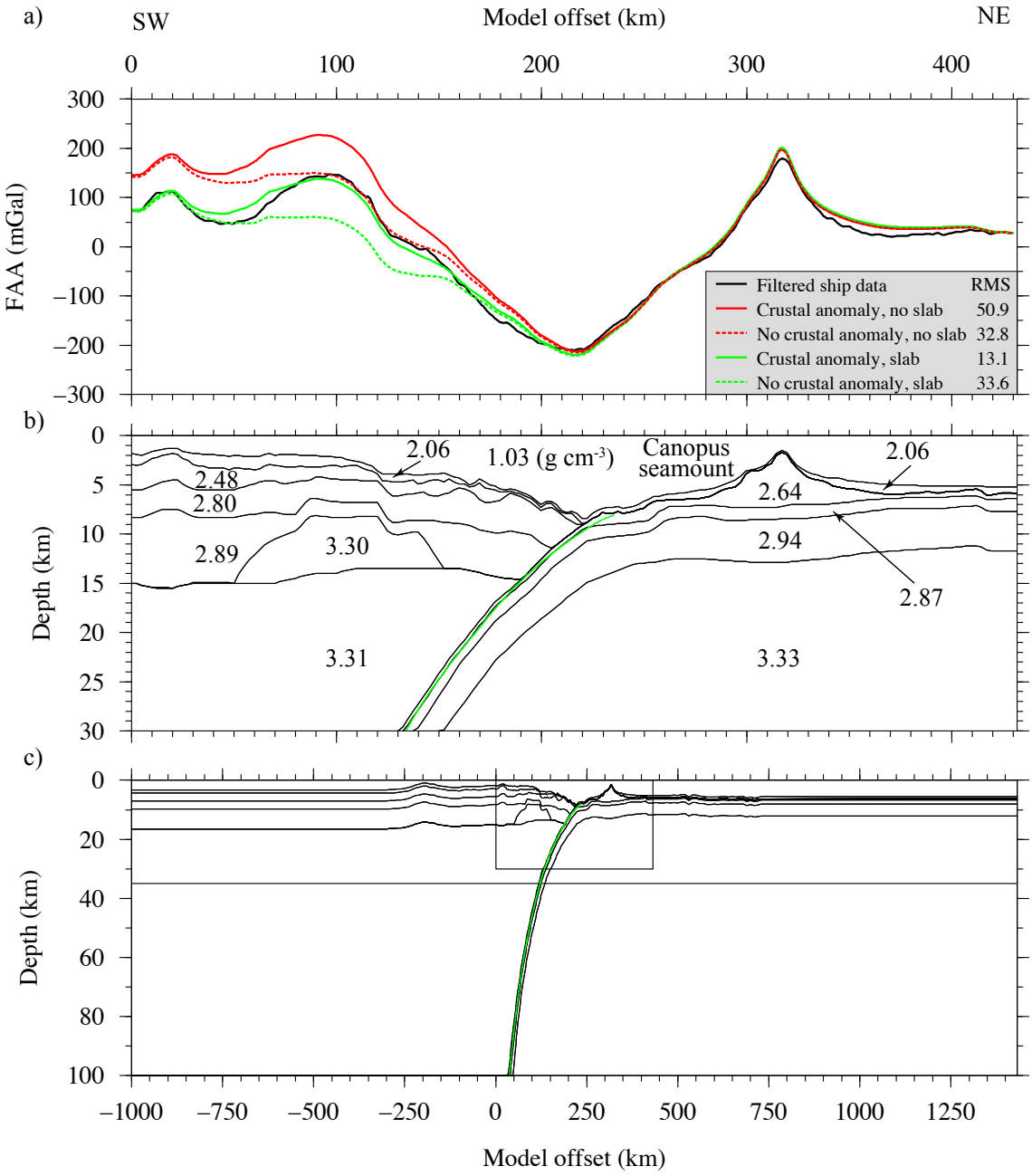

Figure 4.16: Layered polygon model and associated calculated gravity anomaly. a) Comparison of the calculated and observed FAAs for different layered polygon models summarised in b). b) Layered polygon density model, comprising a continuous sediment unit, three distinct blocks for both the overriding and subducting plate crust and separate mantle blocks for the Pacific and overriding plates. c) Extension of the model to ±1000 km, including GEBCO-derived bathymetry to ±300 km, with the layer structure at the model edge draped beneath, and the bottom of the density-depth velocity model at 35 km or extended to 100 km. The red box indicates the model space shown in b). For the 'no slab' models in a), the FAA is calculated for a mantle that only extends to 35-km depth, whereas for 'slab' models, the full 100 km-depth mantle structure is included. Similarly, the 'crustal anomaly' and 'no crustal anomaly' FAAs in a) are calculated from models that include and exclude the lower crustal anomaly polygon with a density of 3.30 g cm^{-3} respectively. Green line in b) and c) is the Slab1.0 model top-slab (Hayes *et al.*, 2012).

(3.30 ± 0.10 g cm^{-3}) at the base of the crust. While this feature is not expressed as a distinct layer in the forward velocity-depth model, it was included to coincide with the region of anomalously high velocity in the forward model. This high velocity region was corroborated through inversion modelling, which suggests that it is a real sub-surface feature independent of modeller and dataset bias. Consequently, the forward model can be considered as a robust model that satisfies the independent approaches of inversion and gravity modelling with only minor modifications required to produce a good fit.

4.5 Summary

In this chapter the final forward model presented in Chapter 3 has been tested by independent inversion and gravity modelling to test model resolvability, non-uniqueness, and modelling bias. Inversion modelling was undertaken to: i) determine whether a modeller independent inversion yields a comparable velocity-depth model to the results of forward modelling; ii) determine what scale of velocity features are resolvable throughout the model space with the acquired data; and, iii) which regions of the model are not well constrained by the WA dataset. The inversion velocity-depth model iterated to remarkably similar broad-scale velocity structure as the forward model, but failed to resolve sharp velocity discontinuities in the shallow sub-surface and at the Moho due to model smoothing and the removal of reflected phase arrivals (P_mP) from modelling. Checkerboard testing indicated that, despite this, the inversion velocity model resolvability generally correlated with the forward model sensitivity test results, showing that no large-scale features of the final forward model were below the minimum possible resolvability for a given point in the model space. The Pacific crust and upper mantle were best constrained and the most resolvable across the model, but the lower-trench slope of the forearc was poorly resolved and only the largest velocity features (>40 km x 5 km) were capable of being recovered here.

Gravity modelling was undertaken to test the validity and uniqueness of the final forward model structure with an independent dataset capable of providing further constraint on the likely composition of the sub-surface. The best-fit gravity model was a direct conversion of the forward velocity-depth model layers to density using standard velocity-density relationships on the median velocity of each layer. Following the extension of the bathymetry to 300 km beyond the model edges and the addition of the subducting slab structure to 100 km depth, a long-wavelength FAA misfit was removed. Although the only additional feature required to generate

the best-fit FAA that was not present in the forward model was a high density anomaly at the base of the forearc crust, this coincides with a region of remarkably high velocity in the forward and inversion models, and so is consistent with forward model structure.

In Chapter 5, the results and implications of the different modelling techniques and datasets will be discussed and combined to create a structural model for the crust and upper mantle along Profile B. This model will then be discussed and compared in the context of other datasets from the Tonga-Kermadec subduction system in Chapter 6 to develop a regional model of structural variability for the downgoing and overriding plates along the margin.

Chapter 5

Results and interpretation

5.1 Introduction

In Chapters 2, 3, and 4 the processing, modelling, and testing of geophysical data along Profile B were described and discussed. In Chapter 2, the acquisition and processing of the MCS data were documented, and the initial interpretation of the imaged sedimentary structures along-profile was presented. The sediment column thickness and seismic velocities from the MCS processing informed the initial WA seismic velocity-depth model presented in Chapter 3. This model was improved using the OBS WA seismic dataset, and was directly tested to determine model sensitivity and reliability. Further assessment of the preferred forward velocity-depth model was undertaken in Chapter 4, in which inversion modelling tested the forward model robustness, maximum resolvability, and degree of modeller bias. A series of density models were tested against the observed gravity anomaly to determine the likely crustal compositions and the extent of model non-uniqueness.

In this chapter, the different datasets and models presented thus far are combined to inform the results and interpretation of the crust and upper mantle structure along Profile B. The results are presented, ordered from northeast to southwest along the profile, starting with the background Pacific plate, crossing Canopus seamount and the Kermadec trench, and ending with the Kermadec forearc and active arc (Section 5.2). Specific features from the models that are either interesting or particularly complex are discussed in more detail in Section 5.3 to establish the most appropriate and geologically realistic interpretation given the range of data available. Finally, these results and interpretations are integrated to inform the combined model for Profile B (Section 5.4).

5.2 Results

The purpose of this study was to develop an improved understanding of structural variability along the Tonga-Kermadec subduction system through the robust imaging of the crust and upper mantle of the background Pacific plate, Canopus seamount, and the Kermadec trench and forearc. Before the results of this study can be discussed in the regional and global context, the different datasets and models need to be synthesised to form a combined best-fit model of the sub-surface structure along Profile B. Independently, each of the datasets and models provide information on specific properties of the sub-surface features. When combined, the models have the potential to robustly constrain sub-surface structures, determine the nature of crustal compositions and, importantly, understand the level of control and certainty on the combined model resulting from all the different datasets together.

In this section the results from the different datasets and models will be compared and integrated to develop an interpretation of the basic structures imaged along the profile. Interesting or more complex sub-surface features that are highlighted here will be discussed in more detail in Section 5.3 to develop and establish a coherent best-fit model. For ease of interpretation, the results are presented from northeast to southwest, following the model subdivisions:

- background Pacific plate (Section 5.2.1);
- Canopus seamount (LRSC) (Section 5.2.2);
- trench-outer rise region (Section 5.2.3);
- inner-trench slopes (Section 5.2.4); and
- Kermadec forearc and arc (Section 5.2.5).

The results will be considered, first and foremost, through analysis of the preferred, forward velocity-depth model (Figure 5.1b). Other quantitative and qualitative information provided by the MCS data (see Section 2.4) as well as the inversion and density models (Figure 5.1c, d, and e) independently enables the assessment of the forward model robustness and geological feasibility. Where suitable, existing regional or global feature-specific understanding will be incorporated to supplement the data and models from Profile B to provide additional constraint on the combined model interpretation.

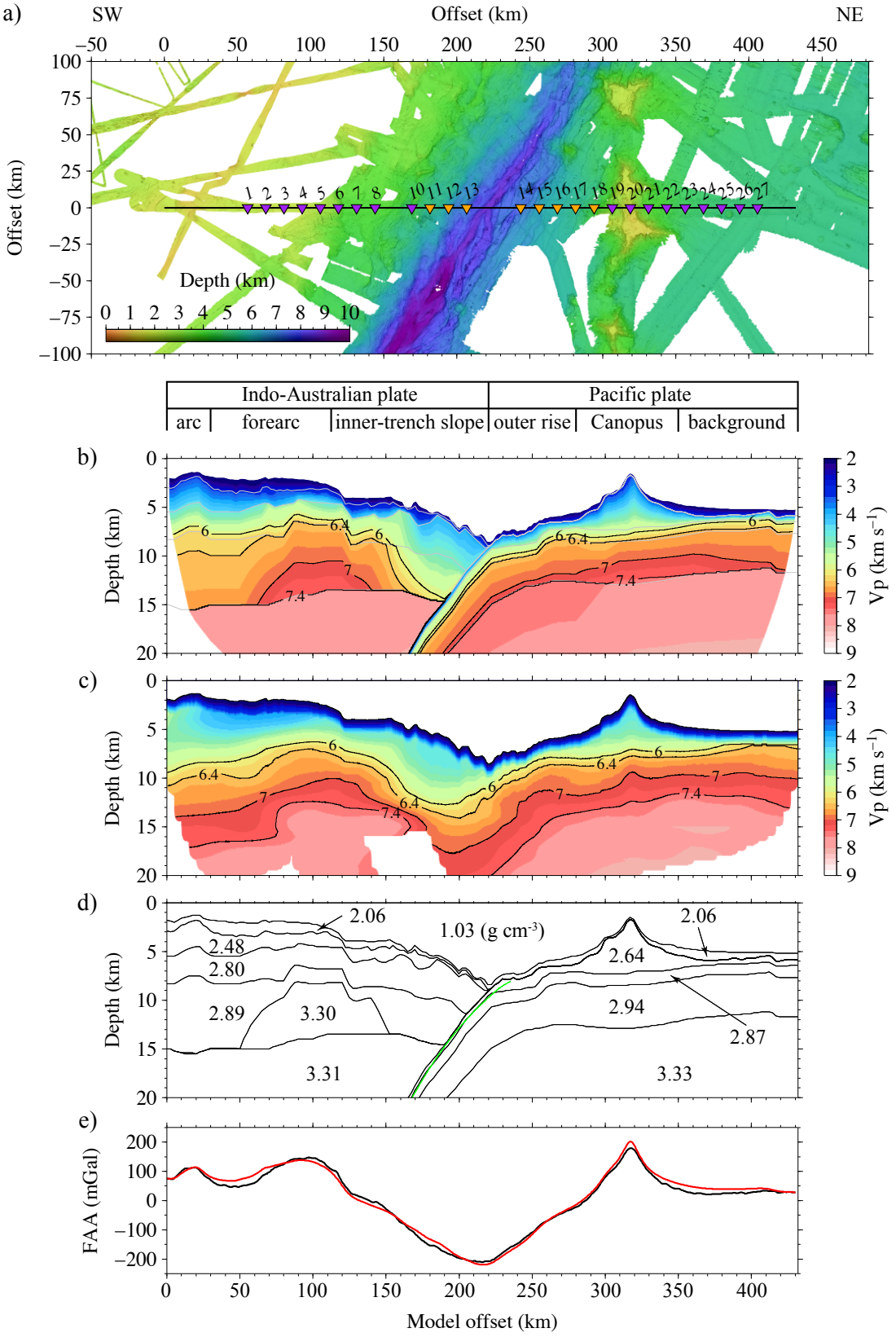

Figure 5.1: Caption next page.

Figure 5.1: (Previous page) Summary of the final forward and inversion velocity-depth models, as well as density models for Profile B. a) Swath bathymetry data surrounding Profile B, with OBSs numbered (purple triangles are LC-type, orange triangles are KUM-type). b) Forward velocity-depth model presented in Section 3.7.4. Model layers (grey lines) indicate the major sub-surface structures. Above b) the banner indicates major tectonic structural regions. c) Inversion velocity-depth model (Section 4.3). Note that for b) and c), black annotated lines represent velocity contours for comparison (in km s^{-1}). d) Density-depth model (Section 4.4.6), with the top-slab from Slab1.0 indicated by the green line (Hayes *et al.*, 2012). Densities are presented in g cm^{-3} for brevity. e) Observed (black line) and calculated FAA (red line) for the density-depth model presented in d), with an RMS residual misfit of 13.1 mGal.

5.2.1 Background Pacific plate

Across the Pacific plate, the sediment thickness varies from <0.1 to 1.3 km thick (Figure 5.1). Sediment thicknesses typical for the region (<0.2 km; Raitt *et al.*, 1955; Burns & Andrews, 1973; Funnell *et al.*, 2014) are only observed at 410 km offset along profile (Figure 5.1) atop the footwall of a large normal fault scarp. This large scarp is not evident in the bathymetry due to the significant sediment fill (up to 0.5 s TWTT; Section 2.4), but was also observed in the MCS data at the eastern end of Profile A (Stratford *et al.*, 2015). The significant sediment fill (0.5 s TWTT) and cover (∼0.2 s TWTT) of the fault suggests that the feature was most likely primarily active before the emplacement of the LRSC, which acted as a major source of sediment for the region after ∼80 Ma (Koppers *et al.*, 2004; 2011; Vanderkluysen *et al.*, 2014). This feature may be the remnant expression of a transform fault generated at the Osbourn spreading centre, <20 km to the north, which exhibits an offset in the axial valley in line with this feature, and was active until 86-93 Ma (Worthington *et al.*, 2006; Downey *et al.*, 2007). Although the sedimentary structures are similar to other examples of fracture zones (e.g. Minshull *et al.*, 1991), the fracture zone appears not to be completely traversed by the profile (i.e. is >20 km-wide). Further, the typical thinned or serpentinised crust of a fracture zone (e.g. Sinha & Louden, 1983; Minshull *et al.*, 1991) is not observed along Profile B (>415 km model offset; Figure 5.1) or Profile A (Stratford *et al.*, 2015), but poor ray coverage at the model ends most likely makes such a feature unresolvable.

The sampled Pacific crust displays fairly typical seismic velocities, with the oceanic crust being ∼6.0 ± 0.3 km-thick, consisting of an ∼1.5 ± 0.3 km-thick upper- and middle-crust (oceanic layers 2a/b and 2c, respectively; 3.5-6.5 ± 0.2 km s^{-1}), and a 4.5 ± 0.3 km-thick lower crust (oceanic layer 3) that reaches 7.1 ± 0.3 km s^{-1} at the base of the crust. The inversion model corroborates the velocity structure

determined in the forward velocity model, except at sharp boundaries such as the base of the sediment and Moho. Checkerboard testing suggests velocity features as small as 20 km laterally or 3 km vertically may be resolvable at this depth (Section 4.3). This broad structure is comparable to other documented examples from the region (Crawford *et al.*, 2003; Stratford *et al.*, 2015), and also compilation studies (i.e. Spudich & Orcutt, 1980; White *et al.*, 1992), suggesting that the crust imaged is typical of the Pacific oceanic crust. Interestingly, the upper mantle seismic velocity is consistently low throughout the forward and inversion velocity-depth models, ~7.6 ± 0.3 km s^{-1}, compared to typical Pacific plate mantle velocity of ~8.2 km s^{-1} (Spudich & Orcutt, 1980; White *et al.*, 1992). This low observed upper mantle seismic velocity will be discussed in more detail in Section 5.3.1.

5.2.2 Canopus seamount (LRSC)

Canopus seamount is the site of the greatest sedimentary and crustal structure change across the Pacific plate imaged along the profile (280-350 km model offset). The sediments on the summit and steep slopes (310-325 km model offset; Figure 5.1) are only a thin veneer, 0.1 ± 0.1 km-thick, but in the moat to the northeast of the seamount, sediments reach 1.3 ± 0.1 km-thick (Figure 5.1). Such thin sediment cover prevented the observation or modelling of sediment turning rays, so their internal velocity, from 1.8 ± 0.5 km s^{-1} to 3.1 ± 0.3 km s^{-1}, was mainly derived from the MCS velocity analysis (Section 2.3.4.1) and only adjusted slightly to fit the shallow crustal refractions (Section 3.7). The inversion velocity model struggled to resolve the sediment basement boundary because of the absence of these phases and the use of strong smoothing parameters, so the forward model is considered to be more geologically realistic. The forward velocity-depth model basal sediment boundary fits the equivalent reflections in the WA-restacked MCS record section to <0.1 s TWTT (Figure 3.19) which is within the expected layer depth uncertainty of ± 0.1 km. These seismic velocities are consistent with observations at other seamounts (e.g. P03 and Profile A; Contreras-Reyes *et al.*, 2010; Stratford *et al.*, 2015), and the expected lithologies of volcaniclastic basalts and glass associated with LRSC-seamount emplacement (Koppers *et al.*, 2011; Vanderkluysen *et al.*, 2014).

Beneath Canopus seamount the background Pacific crustal velocity structure changes, with the upper crustal unit thickening by ~6 km (Figure 5.1). The mid-crustal layer velocity and thickness remains consistent with the background structure, but the lower crustal layer exhibits a slight increase in seismic velocity, reaching 7.4 ± 0.1 km s^{-1} at the base of the crust up to 50 km from the seamount summit,

instead of the typical 7.1 ± 0.1 km s^{-1}. Comparable elevated velocities are imaged over similar distances at the base of the crust beneath the adjacent seamounts (Contreras-Reyes *et al.*, 2010; Stratford *et al.*, 2015), which suggests that the LRSC seamounts are supported by broad lower-crustal intrusions extending over 50 km from the edifice summits (Richards *et al.*, 2013).

Comparable crustal seismic velocities are also observed throughout the crust of the Canopus seamount edifice in the inversion model, suggesting that it is a relatively robust and bias-free result. These low upper-crustal velocities internal to the seamount edifice, and the remarkably good fit between the modelled and observed FAA profiles, suggests that the shallow seamount structure imaged comprises highly porous extrusive and intrusive basaltic rocks typical of the upper oceanic crust (White *et al.*, 1992; Vanderkluysen *et al.*, 2014). This is remarkably different to the internal LRSC structures determined by other studies (Contreras-Reyes *et al.*, 2010; Stratford *et al.*, 2015; Robinson, 2017), and so will be discussed in Section 5.3.2.

5.2.3 Trench-outer rise region

Between Canopus seamount and the Kermadec trench (220-280 km model offset), the Pacific crust is pervasively faulted. These normal faults predominantly dip trenchward and are manifest as seabed offsets of <0.1-0.3 km, preserving a subhorizontal seabed (e.g. Ranero *et al.*, 2003; Funnell *et al.*, 2014). Coincident with this region of faulting, between 0-55 km perpendicular distance from the trench, the velocities of the forward model are reduced with respect to the 'background' Pacific crust (Section 5.2.1). In the upper- and mid-crustal layers, the velocities are reduced by ∼0.3 ± 0.3 km s^{-1}, from 3.5-6.5 km s^{-1} at 400 km model offset to 3.3-6.2 km s^{-1} at 200 km model offset. When combined with an increase in the upper-crustal layer thickness of 1 km, the velocity of the oceanic crust is effectively 1 km s^{-1} slower at a given depth below seabed in the trench-outer rise than in regions of background crustal structure (Figure 5.1). The increased thickness of the upper-crustal layer and maintenance of the whole-crustal thickness is effectively accommodated by a reduction in the lower crustal layer thickness by 1 km. Further to the reductions in the crustal seismic velocity, the upper mantle velocity appears to decrease by ∼0.3 km s^{-1}, from 7.7 ± 0.3 to 7.4 ± 0.3 km s^{-1}. These reductions in velocity are at the limit of the forward model sensitivity (Section 3.8.1), and similar changes in the inversion velocity model are below the anomaly size required for it to be reliably recovered.

5.2.4 Inner-trench slopes

Large fault blocks, a rough seabed, and an opaque seismic reflection response define the lower-trench slope of the overriding plate (170-220 km model offset; Section 2.4; Figure 5.1). These observations are commonly reported for the lower-trench slope along the length of the Tonga-Kermadec subduction system (Karig, 1970; Ballance *et al.*, 1999; Wright *et al.*, 2000; Funnell *et al.*, 2014; Bassett *et al.*, 2016). The sediment accumulations are limited to <0.1 s TWTT-thick and are, for the most part, absent due to the ∼10° angle of slope. Crustal velocities over this region are the lowest and most poorly constrained in the model, reaching just over 6.0 ± 0.6 km s^{-1} at the base of the ∼9.0 ± 0.7 km-thick crust. This remarkably low velocity is also observed in the inversion model; however, resolution testing found that only the largest of velocity structures (>50 km x 4 km) could be resolved in this region due to the extremely low ray coverage (Section 4.3). This is an interesting result as, although a seamount is not expected to be observed along Profile B, the typical seamount bathymetric expression is smaller than the resolvability of this model region, and so one may not be imaged with any degree of confidence with a similar acquisition geometry across other regions of the lower-trench slope.

The calculated gravity anomaly for the lower-trench slope displays a good fit to the observed FAA across the region (Figure 5.1). Such a good fit is unexpected, as this region of extremely low seismic velocity is being accurately represented by a density more typical of normal crustal velocities, so will be discussed in Section 5.3.3.

Further west, between 120-170 km offset, an up to ∼1.0 ± 0.1 km (∼1 s TWTT; Figure 3.21) thick mid-slope basin is observed. The basin is separated from the lower-trench slope to the northeast by a large (0.75 km-high) horst and graben structure, and is bound to the southwest by a <2 km-high scarp, similar to other basins observed along the Tonga-Kermadec subduction system (Wright *et al.*, 2000; Funnell *et al.*, 2014). More typical crustal structure is observed beneath this basin, with the velocity increasing to >6.0 ± 0.3 km s^{-1} just 4 km below the basement, and reaching typical lower crustal range of 6.8-7.2 ± 0.3 km s^{-1} (e.g. Holbrook *et al.*, 1999; Contreras-Reyes *et al.*, 2011).

5.2.5 Kermadec forearc and arc

The Kermadec forearc at ∼27.5°S (30-120 km model offset; Figure 5.1) is defined by an ∼50 km-wide ridge and 40 km-wide basin, juxtaposing the active volcanic arc. Sediments beneath the ridge are modelled as 1.2 ± 0.1 km-thick, and sediments

within the basin are 1.6 ± 0.1 km-thick (although are most likely underestimated as discussed in Section 3.8.2). Beneath the forearc ridge and basin, the crustal thickness ranges from 10.0-12.0 ± 0.7 km-thick, and there is significant lateral variation in the velocity structure. Upper- and mid-crustal velocities under the forearc basin increase from ∼3.0 to 6.2 ± 0.3 km s^{-1} over 5 km in depth and reach 6.8 ± 0.2 km s^{-1} at the base of the crust. Under the forearc morphological ridge, the velocity gradient is much steeper, resulting in the observation of mid-crustal velocities ∼2 km shallower than beneath the basin to the west. The velocity beneath the forearc ridge increases to reach 7.4 ± 0.2 km s^{-1} just above the Moho, the fastest crustal velocity in the model. Throughout the forearc mantle, velocity remains relatively consistent at ∼7.8 ± 0.8 km s^{-1}, although this model region is very poorly constrained due to the limited ray coverage (Section 3.8.1).

The inversion process also converged on high velocity gradients throughout the forearc ridge crust and reached the high lower crustal velocity (>7.1 km s^{-1}) ∼0.4 km shallower than the surrounding forearc. Beneath the forearc ridge, a mantle velocity of >7.6 km s^{-1} is observed ∼2 km shallower in the inversion model than the forward model. Although this discrepancy is significant, the agreement on the depth of upper mantle velocities between the forward and inversion models is better beneath the forearc ridge than the rest of the forearc (Section 4.2), most likely due to the more gentle velocity gradient introduced by the anomalously high velocity at the base of the crust. In addition to the mismatch between the forward and inversion models, the density model poorly represented this region of the gravity profile even after the removal of the long-wavelength mismatch introduced by the subducting slab (Section 4.4). This important but complex feature of the model is discussed in more detail in Section 5.3.4.

5.3 Model features

The results from Profile B highlight the general structure of the regions of sediment column, crust, and upper mantle imaged. There are typical and expected structures, such as the background Pacific crust, but also a number of features that are either particularly interesting or not easily explained by the different datasets. Before the implications of the sub-surface structure determined along Profile B can be considered and applied to the regional and global context, a better understanding needs to be gained of the key model features. These include the:

- Pacific plate mantle (Section 5.3.1);

- Canopus seamount internal structure (Section 5.3.2);
- lower-trench slope structure (Section 5.3.3); and
- forearc lower crustal anomaly (Section 5.3.4);

and will be discussed in more detail to inform the Profile B best-fit combined model.

As with the presentation of the results, these features are presented from the northeastern to the southwestern end of the profile.

5.3.1 Pacific plate mantle

Analysis of the upper Pacific mantle along Profile B (Section 5.2.1) indicated that the seismic velocity is consistently low (<7.6 ± 0.3 km s^{-1}) relative to other studies in the region (>8.2 km s^{-1}; Contreras-Reyes *et al.*, 2010) and typical observations throughout the Pacific plate (∼8.2 km s^{-1}; White *et al.*, 1992). There are a number of potential causes of the observed low mantle velocity, introduced by the proximity of the profile to large geological features including the Kermadec trench, LRSC, and Osbourn spreading centre (Figure 5.2). Profile B was acquired at ∼65° to the palaeo-spreading, or fast seismic wave propagation direction, of the now extinct Osbourn spreading centre (Billen & Stock, 2000; Worthington *et al.*, 2006; Downey *et al.*, 2007). The remnant preferential olivine crystal alignment could introduce anisotropic seismic wave propagation with the fast direction parallel to palaeo-spreading and slow propagation perpendicular to it. Interestingly, the observed reduction in seismic velocity between Profile P03 (∼8.2 km s^{-1}; Contreras-Reyes *et al.*, 2010) and the northeastern 'background' Profile B Pacific mantle (<7.6 ± 0.3 km s^{-1}) gives a mantle anisotropy of 7% (Figure 5.2b), which is similar to previous observations (Hess, 1964; Shimamura *et al.*, 1983). Neither Profile B nor P03 were acquired directly along the expected directions of maximum anisotropy, and so the true value for mantle anisotropy may be larger (e.g. Kodaira *et al.*, 2014).

There is a further reduction in the observed seismic velocity throughout the mantle along Profile B (to 7.4 ± 0.3 km s^{-1}) that occurs as the Pacific plate becomes more proximal (<60 km) to the Kermadec trench (Figures 5.1 and 5.2). This velocity reduction coincides with the pervasively bend-faulted region of the Pacific plate, and would increase the mantle anisotropy to >10%, which is greater than most documented cases (Kodaira *et al.*, 2014). As such, this low seismic velocity most likely originates from the faulting and hydration of the upper mantle as the Pacific plate is deformed through subduction-related bending (e.g. Moscoso & Grevemeyer, 2015;

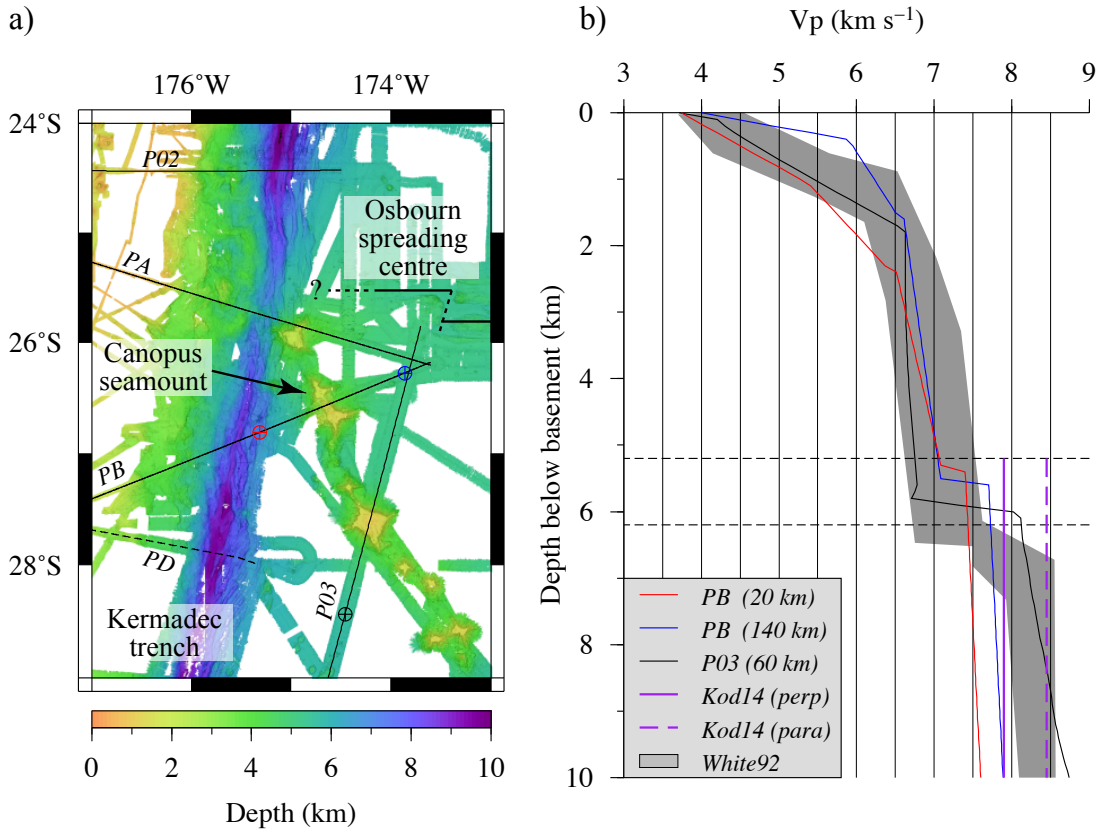

Figure 5.2: Analysis of variations in the structural characteristics throughout the Pacific crust and upper mantle along Profile B. a) Bathymetric map of the region surrounding the present-day Tonga-Kermadec trench-LRSC intersection point. Relevant geophysical profiles are indicated by black lines and annotated with their designated names (PB refers to Profile B, etc.). Circle and cross markers indicate the locations of the velocity profiles presented in b). b) Velocity-depth profiles for the Pacific crust and upper mantle. Profiles are displayed over the typical seismic velocity range envelope for Pacific crust (White *et al.*, 1992). The two purple lines are the seismic velocities through the uppermost oceanic mantle perpendicular (solid line) and parallel (dashed line) to the spreading direction, highlighting the largest Pacific plate mantle anisotropy observed (Kodaira *et al.*, 2014).

Korenaga, 2017) rather than remnant anisotropic effects. This variation in upper mantle seismic velocity along Profile B (0.2 km s^{-1}) is below the limit of forward model sensitivity (0.3 km s^{-1}), so this result cannot be considered as conclusive.

5.3.2 Canopus seamount internal structure

The seismic velocity imaged within the Canopus seamount edifice along Profile B (Section 5.2.2) is much lower than that reported in previous studies (Contreras-Reyes *et al.*, 2010; Stratford *et al.*, 2015; Robinson, 2017). It is important to deter-

mine whether the internal seamount structure imaged in this study is a geologically feasible and accurate representation of the sub-surface, or a function of modelling limitations and scale of errors.

The extruded volcanic edifices vary along the 4,300 km-long LRSC, with the seamounts usually exceeding 3 km in height above the seafloor and ranging between 5-40 km in summit diameter (Figure 5.3; Hawkins *et al.*, 1987; Lonsdale, 1988). Further, the internal seismic velocity structure of these seamounts varies, as imaged by profiles crossing different seamounts in a range of orientations, and modelled using different methods. At the northwestern end of the LRSC, where surveying of the seamounts has been focussed (Figure 5.3), four distinct profiles sample the internal structure of different seamounts. Profile B observes the lowest internal seismic velocity of the volcanic edifices (Figure 5.3d), reaching ∼6.0 km s^{-1}, 6.0 km beneath the seabed in both the forward and modeller-independent inversion models. This internal structure is considered to be well constrained by both the forward model sensitivity testing (± 0.3 km s^{-1}; Section 3.8.1), and the inversion model resolution testing, which suggested features larger than 30 x 3 km may be resolvable (Section 4.3). Similar internal velocity structures, albeit slightly seismically faster (∼6.0 km s^{-1} at <5.0 km below seabed), are imaged by Profile A (Figure 5.3c; Stratford *et al.*, 2015), and by Profile C where the profiles cross the seamount flanks (Figure 5.3b; Robinson, 2017). Where profiles directly traverse the seamount summit (e.g. Osbourn and 27.6°S by Profile C, and 27.6°S by Profile P03; Figure 5.3), fast seismic velocities (>6.0 km s^{-1}) are observed <1 km below the seabed at the seamount edifice (Contreras-Reyes *et al.*, 2010; Robinson, 2017). While the steepest sub-basement velocity gradient is observed by Contreras-Reyes *et al.* (2010) beneath 27.6°S seamount, using only the inversion modelling technique of Korenaga *et al.* (2000) and Korenaga *et al.* (2001), Robinson (2017) also found a similar internal seismic velocity using the modelling techniques of Zelt & Smith (1992) along an intersecting profile. That these remarkably high velocity features in the shallow sub-surface beneath the LRSC seamount summits are observed independent of the modelling method and acquisition array used indicates that they are, most likely, real geological features and not an artefact of these experimental variables.

This direct correlation between the sampling location and the internal structure of the seamount edifice (Figure 5.3f), indicates that the highly intrusive mafic-ultramafic core proposed by Contreras-Reyes *et al.* (2010) and Richards *et al.* (2013) is either laterally limited within the edifice, or may be absent in some seamounts. Where the high velocity material is absent, seismic velocity is more indicative of porous extrusive and intrusive basaltic rocks typical of the upper layer of the oceanic

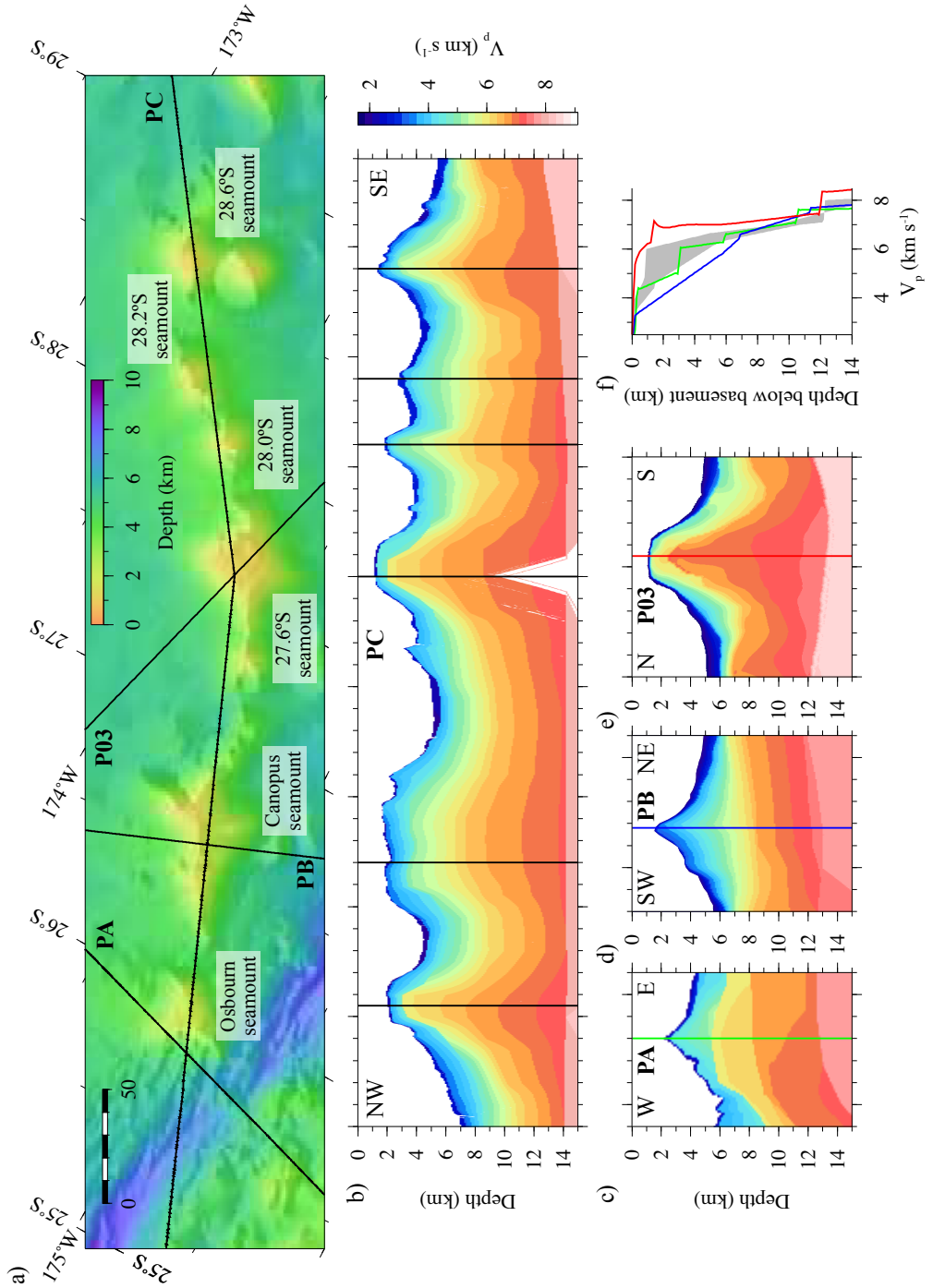

Figure 5.3: Caption next page.

Figure 5.3: Variation in seamount morphology and internal velocity structure at the northwestern end of the LRSC. a) Bathymetry map over the oldest extant region of the LRSC, with seamounts labelled. Profiles presented in b)-f) are plotted and annotated. b) Profile C forward model, which traverses the LRSC (Robinson, 2017). c) Profile A forward velocity-depth model over the northern flank of Osbourn seamount (Stratford *et al.*, 2015). d) Profile B forward model through the saddle between the two volcanic cones of Canopus seamount (Funnell *et al.*, 2017). e) Profile P03 inversion model across 27.6°S seamount (Contreras-Reyes *et al.*, 2010), following the method of Korenaga *et al.* (2000). Models presented in b)-d) were developed using the method of Zelt & Smith (1992). f) Velocity-depth profiles colour-coded for the seamounts presented in c)-e), overlain on the velocity envelope for the seamounts imaged by Profile C, shown in b).

crust (White *et al.*, 1992), that have been directly sampled along the LRSC (Koppers *et al.*, 2012; Vanderkluysen *et al.*, 2014). Modelling of the Canopus seamount internal density as that of standard oceanic crust (e.g. Carlson & Raskin, 1984) yielded a remarkably good fit between the calculated and observed FAAs (Section 4.4.6). This fit is most likely improved by the unusual sampling location of the profile. Instead of steep slopes juxtaposing the profile across the seamount, two larger volcanic edifices are present, potentially introducing a more positive FAA through their shallower morphology and possible high-density core (Contreras-Reyes *et al.*, 2010). As a result, the well-constrained low seismic velocity and density observed internal to Canopus seamount along Profile B are most likely geologically accurate, but indicative of the extrusive and intrusive basaltic material generated during seamount formation, and not a highly intrusive mafic-ultramafic core. The profile does not image a high seismic velocity core, although this does not preclude its presence within the dual Canopus seamount edifices, but imposes a limit on the possible lateral extent of the feature (<15 km from the centre of the summit). A more detailed understanding of these features and certainty over the presence, and lateral limit, of the highly-intrusive high-density cores may be achieved by 3D gravity modelling in a future study.

5.3.3 Lower-trench slope structure

The lower-trench slope of the overriding plate is an interesting model feature because although a low seismic velocity is observed throughout the crust (<6.0 km s^{-1} at the base of the 9 km-thick crust; Figure 5.4), the FAA over the model region was accurately calculated using densities that represent typical higher velocity materials. An optimum fit between the observed and calculated FAA (RMS misfit of 13.1 mGal; Figure 5.1) was obtained by modelling the sub-surface as a series of typical crustal layers that were each represented by a single density (Section 4.4). This, in effect,

neglected the observed changes in velocity along each layer, and thus the possibility that there may also be localised density variations. For the lower-trench slope, the use of the standard oceanic crustal velocity-density relationships of Carlson & Raskin (1984) on the median layer velocity should have resulted in the over-calculation of the FAA because the seismic velocity is remarkably low in this region. However, the good observed fit indicates that the standard oceanic crustal velocity-density relationship fails or is not applicable in this region of the model.

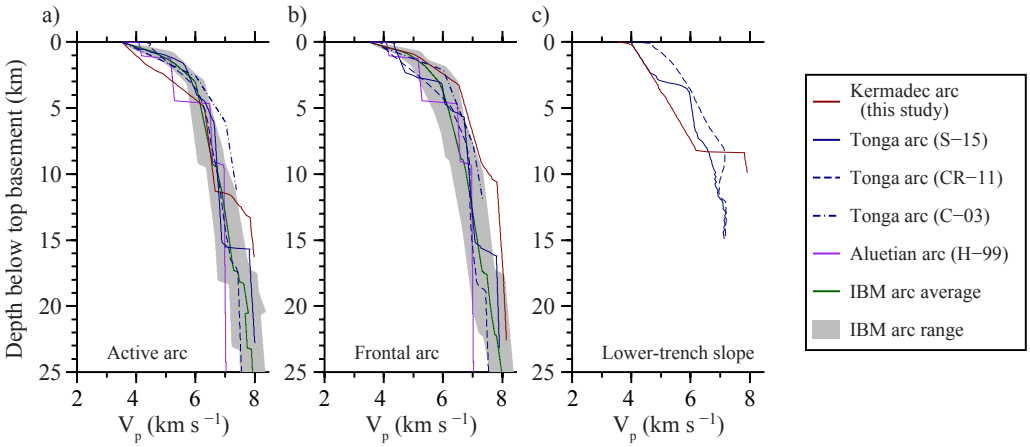

Figure 5.4: Seismic velocity profiles through the overriding crust and upper mantle. Velocities from along the Tonga-Kermadec subduction system are plotted against results from the IBM and Aleutian margins. a), b), and c) show seismic velocity through the active arc, frontal arc, and lower-trench slopes of the respective overriding plates. The 1D profiles presented are, S-15, from Stratford *et al.* (2015), CR-11, from Contreras-Reyes *et al.* (2011), C-03, from Crawford *et al.* (2003), and H-99 from Holbrook *et al.* (1999). The IBM range and 1D-seismic velocity average profiles are derived from a range of published results including: Takahashi *et al.* (2007), Calvert *et al.* (2008), Takahashi *et al.* (2009), and Kodaira *et al.* (2010).

Similar seismic wavespeeds and poor reflectivity are observed by Contreras-Reyes *et al.* (2011) and Sallarès & Ranero (2005) at the Tonga and North Chile margins respectively (Figure 5.4c). These characteristics are attributed to the pervasive faulting, disaggregation, and hydration of the overriding crust in response to subduction erosion (Clift *et al.*, 1998; Clift & Vannucchi, 2004) and, in the case of the IBM forearc, the presence of serpentinite seamounts (Suyehiro *et al.*, 1996; Oakley *et al.*, 2007; Fryer, 2012). Serpentinite seamounts are not only of a lower seismic velocity but also a lower bulk density than typical oceanic crust, so the observed FAA across the lower-trench slope would be expected to be lower than is presented

here. There is no morphological evidence of serpentinite seamounts along the Tonga-Kermadec subduction system (Wright *et al.*, 2000) as observed at other margins (e.g. Suyehiro *et al.*, 1996; Bassett & Watts, 2015b). It is, therefore, most likely that the low seismic velocity is primarily caused by the faulting and disaggregation of the lower-trench slope as the overriding crust undergoes significant tectonic erosion, but importantly, this process has a less significant effect on the bulk density of the rock than it does on the velocity characteristics.

5.3.4 Forearc lower crustal anomaly

Through forward modelling, high seismic velocities (7.1-7.4 km s^{-1}) were observed at the base of the crust beneath the forearc morphological ridge. These high velocities were found to result not from modeller bias because the inversion model converged to a similar velocity structure. Slight discrepancies between these models were found in the depth to typical upper mantle velocity (>7.6 km s^{-1}) by ∼2 km, and further, the unusually high FAA observed over this feature, ∼150 mGal, was significantly undercalculated by the simple layered density model using typical velocity-density relationships (Carlson & Raskin, 1984; Christensen & Mooney, 1995). Density modelling of a 2 km-thinner forearc crust beneath the morphological ridge (i.e. a shallower mantle) reduced the misfit between the observed and calculated datasets, although an RMS residual misfit of ∼30 mGal remained. Adjusting the forward model to match this layer depth no longer produced an acceptable fit to the observed Moho-reflections and upper mantle refractions to within their assigned uncertainty values. A better fit was achieved for this model region by maintaining the forward model structure for the forearc crust, and incorporating an ∼5 km-high lower-crustal density anomaly, over the same region as the high seismic velocity at the base of the forearc crust. A range of representative densities was tested for this anomaly, from 3.10-3.50 g cm^{-3}, with 3.30 g cm^{-3} found to produce the smallest RMS residual misfit of 13.1 mGal (Figure 5.5). Despite this, a range of density values tested produced suitably low average RMS residual misfits, so this density is considered to have an uncertainty of ± 0.10 g cm^{-3}. Thus, the forward velocity and density models are satisfied across the forearc by the addition of minimal structure at the base of the model. The 2 km discrepancy between the forward and inversion velocity model Moho depths is most likely the result of the inversion method being unable to model P_mP arrivals or generate sharp velocity discontinuities due to spatial smoothing. The misfit remains within the inversion model resolvability for the region (Section 4.3).

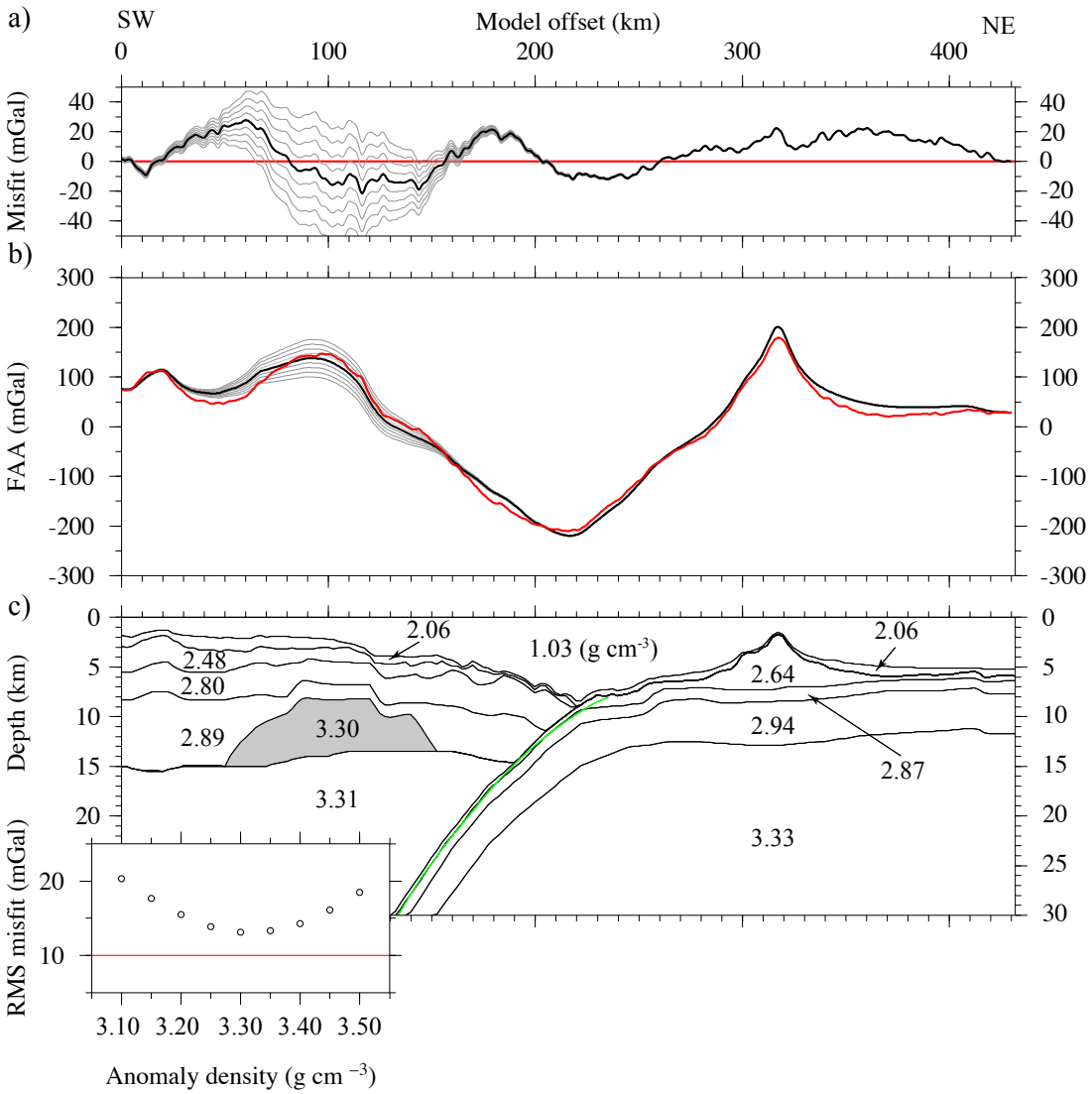

Figure 5.5: Modelling of the optimum density for the forearc morphological ridge lower crustal anomaly. a) Misfit between the calculated (grey lines) and observed (red line) FAA for different densities applied to the anomalous lower crustal forearc feature. b) Observed (red line) and modelled FAAs (grey and black lines) along Profile B. The grey lines demonstrate the range of FAAs generated through testing different densities of the lower crustal high density anomalous feature. The black lines in a) and b) show the best fitting FAA, generated by the optimum anomalous feature density (3.30 g cm^{-3}). c) Preferred density model used to generate the range of FAAs presented in a) and b), following the modelling procedure presented in Section 4.4. The model extends to ±1000 km from the edges of the displayed model space, with the bathymetry extended to ±300 km, and the depth of the subducting slab incorporated to 100 km depth (using slab1.0; Hayes *et al.*, 2012). Inset graph shows the variation in RMS misfit between the observed and modelled FAA for different lower crustal anomaly densities.

Compared to previous results from the Tonga-Kermadec (Contreras-Reyes *et al.*, 2011; Stratford *et al.*, 2015), Izu-Bonin-Mariana (Suyehiro *et al.*, 1996; Takahashi *et al.*, 2008; 2009), Aluetian (Grow, 1973; Holbrook *et al.*, 1999), and South Sandwich subduction system (Larter *et al.*, 2003), the forward model along Profile B describes a relatively thin forearc crust (10-12 km thick; Figure 5.4). Despite this, Kodaira *et al.* (2010) imaged <10 km-thick forearc crust at the Bonin margin, which is another type-example of the intra-oceanic subduction zone setting, so this result is not unusual (Figure 5.4). The forearc morphological high imaged by Profile B is located towards the most southern extent of the bathymetrically expressed Tonga Ridge (Karig, 1970; Lonsdale, 1986; Contreras-Reyes *et al.*, 2011; Stratford *et al.*, 2015) that was initially interpreted from the MCS dataset to have formed prior to the deposition of most sediments along the system. Although this morphological ridge is commonly associated with being the site of initial volcanism at the onset of west-dipping subduction along the subduction system (48-51 Ma Meffre *et al.*, 2012; Michibayashi *et al.*, 2016), there is no direct sampling of the forearc basement at Profile B (∼27.5°S) to corroborate this dating (Clift *et al.*, 1998). The 48-51 Ma ridge origin (Meffre *et al.*, 2012; Michibayashi *et al.*, 2016) coincides with the onset of subduction at other margins that display similar forearc morphological ridges, e.g. the Izu-Bonin-Marianna (Stern *et al.*, 2012; Reagan *et al.*, 2013). Both sets of forearc ridges are proposed to have been directly formed by, or developed from, tholeiitic and boninitic volcanism associated with subduction initiation (Clift *et al.*, 1994; Meffre *et al.*, 2012; Reagan *et al.*, 2013). Given the origin of this region of the forearc crust, the lower-crustal anomalous structure may comprise high density pyroxenitic restites that are left as a residual lower crustal material following initial subduction volcanism that can reach up to ∼3.90 g cm^{-3} (Nakajima & Arima, 1998; Meffre *et al.*, 2012). Henceforth, the forearc morphological ridge, with its high density and high seismic velocity lower crust, will be referred to as the extinct Eocene frontal arc.

5.4 Final combined model

The comparison and synthesis of results from the different Profile B datasets and models enabled the discussion and comprehensive interpretation of the sub-surface structure and model features. Together, these combined features are capable of explaining each of the observed datasets within the assigned uncertainties and modelling limitations to give the final combined model shown in Figure 5.6.

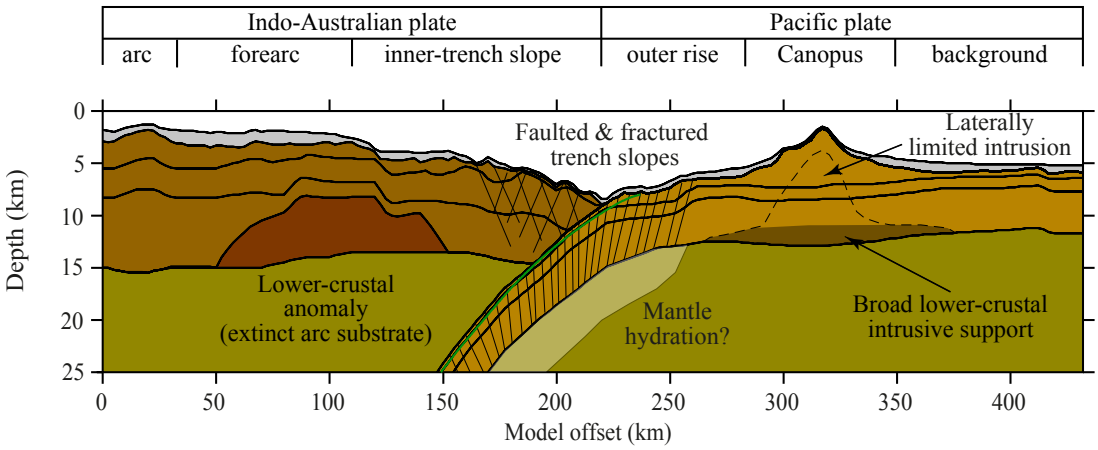

Figure 5.6: Final best fit schematic model for Profile B. The model is annotated with the important model features highlighted through the results and interpretation of the different geophysical datasets presented in this chapter. The schematic is formed primarily from the forward model layer boundaries (Section 3.7.4), except for the inclusion of the forearc lower crustal density anomaly, which was required to fit the FAA data along the profile (Figure 5.5).

At the northeastern end of the profile, the Pacific crust is of a typical velocity and density structure, with minimal sediment cover (0.2 ± 0.1 km) except in the vicinity of a fracture zone (>0.7 ± 0.1 km at >415 km offset along profile). Sediment fill increases into the moat of Canopus seamount (>1.3 ± 0.1 km), but is almost absent from the slopes and summit due to steep slopes that promote sediment transportation into the moat. Internal to the volcanic edifice along the profile, Canopus seamont displays relatively low seismic velocities and representative densities that are indicative of porous extrusive and intrusive basalts. This is unexpected because high seismic velocities (>6.0 km s^{-1} at 1 km below basement) indicative of an intrusive mafic-ultramafic core (Contreras-Reyes *et al.*, 2010) are typically observed. This difference in imaged interior structure is most likely a result of sampling location, and indicates the intrusive cores are laterally limited to <15 km from the summit centre. Profile B crosses the saddle through the two volcanic edifices of Canopus seamount, and so does not directly sample the intrusive cores within each of the seamount summits. A slight downward deflection of the Moho (>1 km), and increased velocity at the base of the crust around the seamount (to ∼7.4 km^{-1}), indicates there is a broad lower crustal intrusion that is observed to greater offsets from the summits, possibly providing structural support. Between Canopus seamount and the trench, crustal velocities are reduced and significant normal faulting is displayed throughout the sediments. Upper mantle seismic velocity is low, ∼7.6 km s^{-1},

across the sampled Pacific plate, most likely due to the profile being acquired at 65° to the spreading direction of the Osbourn spreading centre and, hence, more aligned with the slow seismic anisotropic direction (e.g. Hess, 1964; Kodaira *et al.*, 2014). Seismic velocity throughout the upper mantle reduces beneath the trench-outer rise, to 7.4 km s^{-1}, possibly as a result of the faulting and hydration of the mantle as the plate bends (Moscoso & Grevemeyer, 2015; Korenaga, 2017), although this velocity variation is below the sensitivity of the model (± 0.3 km s^{-1}).

The lower-trench slope of the overriding plate is heavily faulted and fractured, characterised by limited sedimentation (<0.1 km), a rough seabed, and low crustal seismic velocity (3.0-6.0 km s^{-1}). Despite this, the modelled densities for this region suggest that the composition is that of standard oceanic crust that has not been significantly affected by the extensive alteration. A mid-slope basin to the west of the lower-trench slope acts as a sediment pond that has undergone pervasive minor extensional faulting. The Kermadec forearc is characterised by a ridge and basin morphology that was most likely generated during the inception of west-dipping subduction along the margin, and has subsequently experienced significant episodes of sedimentation. This region broadly demonstrates typical forearc velocity and a density structure best represented by an oceanic crust velocity-density relationship. At the base of the forearc morphological ridge crust, high seismic velocity (up to 7.4 km s^{-1}) and a high FAA (>150 mGal) are indicative of an anomalous lower crustal structure that requires densities of 3.30 ± 0.10 g cm^{-3} to match the gravity anomaly accurately. This could be a high density residual pyroxenitic restite (e.g. Nakajima & Arima, 1998) formed during subduction initiation that still exists, despite the overall tectonically erosive subduction regime, because it is inherently dense and structurally robust (Funnell *et al.*, 2014). The forearc basin and arc display more typical oceanic forearc structure without the unusually high velocity and density lower crust, and sediment cover that reaches up to 2 km-thick. Upper mantle velocity across the forearc is invariable at 7.6 km s^{-1}, but are poorly constrained (± 0.7 km s^{-1}), so cannot be considered further.

5.5 Summary

In this chapter the results from the initial MCS data interpretation were synthesised with the forward and inversion velocity models as well as the density model to develop the combined best-fit model for the sub-surface structure beneath Profile B. Together these datasets and models provide strong constraint on the crustal and upper mantle structure as well as a quantifiable understanding of model certainty,

enabling the robust interpretation of sub-seabed geological features and the nature and extent of structural evolution and deformation.

The combined model shows typical oceanic crust and upper mantle structure throughout the Pacific plate, an extrusive and intrusive basaltic seamount edifice sampled away from the highly intrusive core, and extensive deformation of the subducting plate throughout the trench-outer rise. Across the overriding plate the lower-trench slope is also highly deformed, but poorly resolved, and is bound on the arcward side by a long-lived mid-slope basin. The forearc exhibits a basin and ridge morphology with both a high density and high velocity anomaly at the base of the ridge crust that most likely formed during subduction initiation along the system.

In Chapter 6 the results and interpretation of the combined model along Profile B will be discussed in the context of the Tonga-Kermadec subduction system as a whole, and other intra-oceanic arcs, to develop a model of along-arc structural variation.

Chapter 6

Discussion

6.1 Introduction

Chapter 5 presented the processed datasets and models along Profile B, combining the results and independent testing methods to develop the most geologically feasible and robust structural model. This model is considered the combined 'best fit' for the processed MCS data, forward and inversion velocity-depth models, and the density-depth model. Interesting and more structurally complex features were discussed in detail, drawing on previous research from along the Tonga-Kermadec and other erosive intra-oceanic subduction systems.

In this chapter, the combined model will be considered in the context of the regional structure of the subduction system, and synthesised with previously published datasets to robustly constrain and characterise variations along the Tonga-Kermadec margin. Variations in the subducting oceanic crust will be considered first, with a focus on the region surrounding the LRSC-trench intersection, to determine whether the presence of seamounts causes any change to the background subduction processes (Section 6.2). Following this, the forearc crustal structure and its variability along the margin will be discussed, starting with the structure inherited by the overriding crust during its evolution from a single-arc system, from ∼51 Ma until the present day (Sections 6.3-6.5). The characterisation of the along-arc crustal structure is then used to differentiate between inherited forearc features and deformation generated by the subduction of the LRSC, to develop a well constrained model for the effects of seamount subduction on the forearc along the margin (Section 6.6).

6.2 Variations in subducting crust and upper mantle structure

Along the Tonga-Kermadec subduction system, subduction-induced bending of the downgoing Pacific plate generates pervasive normal faulting that is observed as significant seabed offsets of up to 2 km (Ballance *et al.*, 1989; Crawford *et al.*, 2003), and as downthrown sedimentary units in seismic reflection data (Pelletier & Dupont, 1990; Funnell *et al.*, 2014). This broad region of deformation (up to ∼60 km trench-perpendicular offset) coincides with a reduction in the seismic velocity of the upper 2 km of the subducting oceanic crust and the uppermost mantle by ∼1.0 and 0.2 ± 0.3 km s^{-1}, respectively, along Profile B (Section 5.2.3). Considered in isolation, the velocity change in the upper mantle along the profile is not statistically significant because it is within the sensitivity of the model region (Section 3.8.1); however, when compared to velocities determined by other profiles a consistent result is obtained (Figure 6.1). Average upper mantle velocity observed within the trench-outer rise is ∼5% slower than that found in background regions of the Pacific plate (from 7.4 to 7.8 km s^{-1}), for profiles acquired perpendicular to the palaeo-spreading direction of the Osbourn spreading centre (Downey *et al.*, 2007). Along Profile C, there is no observed variability in upper mantle velocity with increasing proximity to the trench (Robinson, 2017). This suggests that either any velocity change is below model sensitivity, or that the presence of the LRSC masks or limits it. Seismic velocity throughout the upper mantle parallel to the palaeo-spreading direction of the Osbourn spreading centre (Downey *et al.*, 2007) is ∼6% faster than that perpendicular and acquired away from the trench-outer rise (from 8.3 to 7.8 km s^{-1}; Figure 6.1), which is a typical value for upper mantle anisotropy (Hess, 1964; Shimamura *et al.*, 1983).

Bend faulting similar to that at the Tonga-Kermadec subduction system is observed in the mantle of the Costa Rican margin (Ranero *et al.*, 2003), and along the Chilean trench-outer rise (Ranero *et al.*, 2005; Contreras-reyes *et al.*, 2008). At the Chilean margin, the bend-faulted region coincides with reduced crustal and upper mantle seismic velocity, by 0.4-0.7 km s^{-1} and up to 0.5 km s^{-1} respectively (Sallarès & Ranero, 2005; Contreras-reyes *et al.*, 2008; Moscoso *et al.*, 2011; Moscoso & Grevemeyer, 2015). Such faulting patterns and reductions in seismic velocity are widely proposed, together with reduced heat flow (Grevemeyer *et al.*, 2005), to be the physical manifestations of hydration and upper mantle serpentinisation (i.e. offshore Costa Rica and Nicaragua - Ranero *et al.*, 2005; Ivandic *et al.*, 2010). The combined effects of structural weakening, through the physical and geochemical

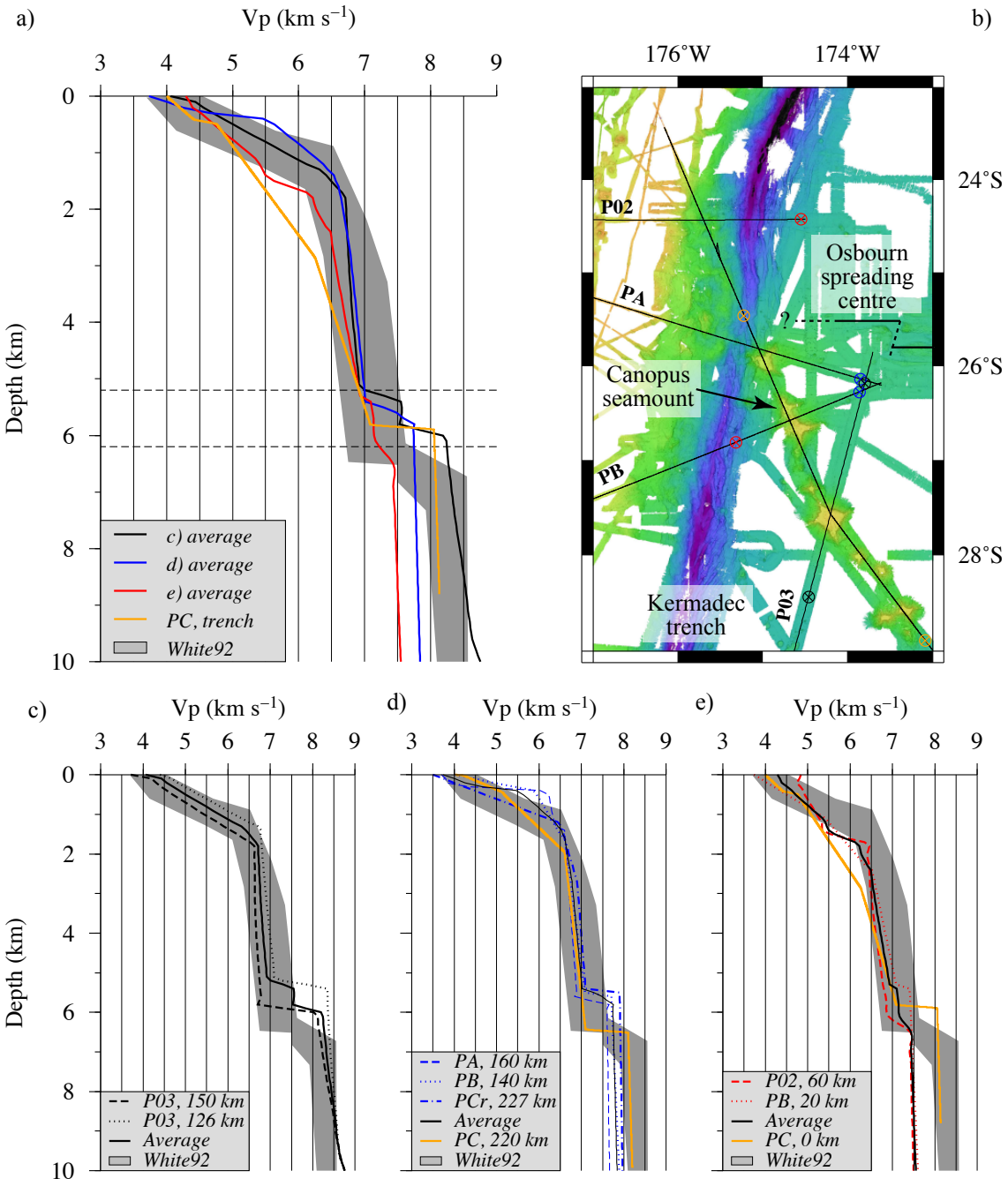

Figure 6.1: Pacific plate velocity-depth profiles around the trench-LRSC intersection. a) Comparison of average velocity-depth profiles parallel and perpendicular to the palaeo-spreading direction, as well as proximal to the trench and perpendicular to palaeo-spreading. b) Swath bathymetry map of the trench-LRSC intersection with the relevant WA seismic profiles, and the locations of velocity-depth profiles indicated (circles). c) Profiles acquired parallel to palaeo-spreading direction through the background Pacific plate (P03; Contreras-Reyes *et al.*, 2010). d) Profiles acquired perpendicular to palaeo-spreading direction through the background Pacific plate (PCr, PA, PB; Crawford *et al.*, 2003; Stratford *et al.*, 2015; this study). e) Profiles acquired perpendicular to palaeo-spreading direction through the bend-faulted Pacific plate (P02, PB; Contreras-Reyes *et al.*, 2011; this study). Profile C (orientated 25-40° to the palaeo-spreading direction) is included where relevant to indicate velocity in the upper mantle beneath the LRSC.

modification of bend-faulted oceanic crust, is attributed with directly reducing the flexural rigidity and yield strength of the subducting plate by up to three orders of magnitude over the trench-outer rise region (Billen & Gurnis, 2005; Arredondo & Billen, 2012).

The nature and magnitude of bend faulting varies significantly along the Tonga-Kermadec subduction system. Pelletier & Dupont (1990) and Ballance *et al.* (1999) note that normal faults north of ∼32°S exhibit scarps up to 1.5 km high, and to the south fault scarps reach 0.1-0.2 km in height, and suggest that this disparity results from a relic tectonic boundary. Where typical Pacific oceanic crust is subducted along the margin, large normal faults with 1.5 km vertical throw form, evenly distributed between trenchward and seaward dipping, and with sediments tilted ∼5° towards the trench over a 70 km area (Crawford *et al.*, 2003; Contreras-Reyes *et al.*, 2011; Funnell *et al.*, 2014). This background trench-outer rise faulting structure is exemplified by Profile D (Figure 6.2d; Funnell *et al.*, 2014), which was acquired ∼220 km south of the present day LRSC-trench intersection. Faults that are closer to the LRSC-trench intersection, such as those imaged along Profile B (Figure 6.2c; Funnell *et al.*, 2017; this study), predominantly form trenchward-dipping half graben with significantly reduced throw (<0.3 km vertical offset), resulting in a plate that remains relatively sub-horizontal (<1° dip). The axial depth of the Tonga-Kermadec trench, which is typically 10 km, shallows by ∼4 km over 150 km towards the LRSC-trench intersection (Figure 6.3). The coincident reduction in axial trench depth and change in the nature and magnitude of outer-rise bend-faulting suggests that the LRSC imposes a strong control on the style and extent of the subducting oceanic crust deformation. North of the LRSC-trench intersection, the trench reaches its deepest at Horizon Deep Bight, 23.3°S (10.87 km below sea surface; Fisher, 1974; Lonsdale, 1986), and the trench-outer rise bend-faulted region covers a larger trench-perpendicular area (∼100 km instead of 60 km; Figure 6.3). This change in the trench axis and subducting plate structure north of the LRSC-trench intersection is widely thought to be the result of increased subduction erosion as seamounts actively remove material from the overriding plate (Ballance *et al.*, 1989; Contreras-Reyes *et al.*, 2011; Stratford *et al.*, 2015). Overall the bend-faulting is limited and the trench axis shallows over a region covering up to 120 km from the seamounts (Figure 6.3), which is significantly larger than the 50 km-wide bathymetric swell and region of lower crustal support imaged by WA seismic data modelling (Ballance *et al.*, 1989; Contreras-Reyes *et al.*, 2010; Stratford *et al.*, 2015; Funnell *et al.*, 2017; this study). Although some larger faults are found on the flanks of Osbourn seamount (Figure 6.2a; Stratford *et al.*, 2015), the general reduction in

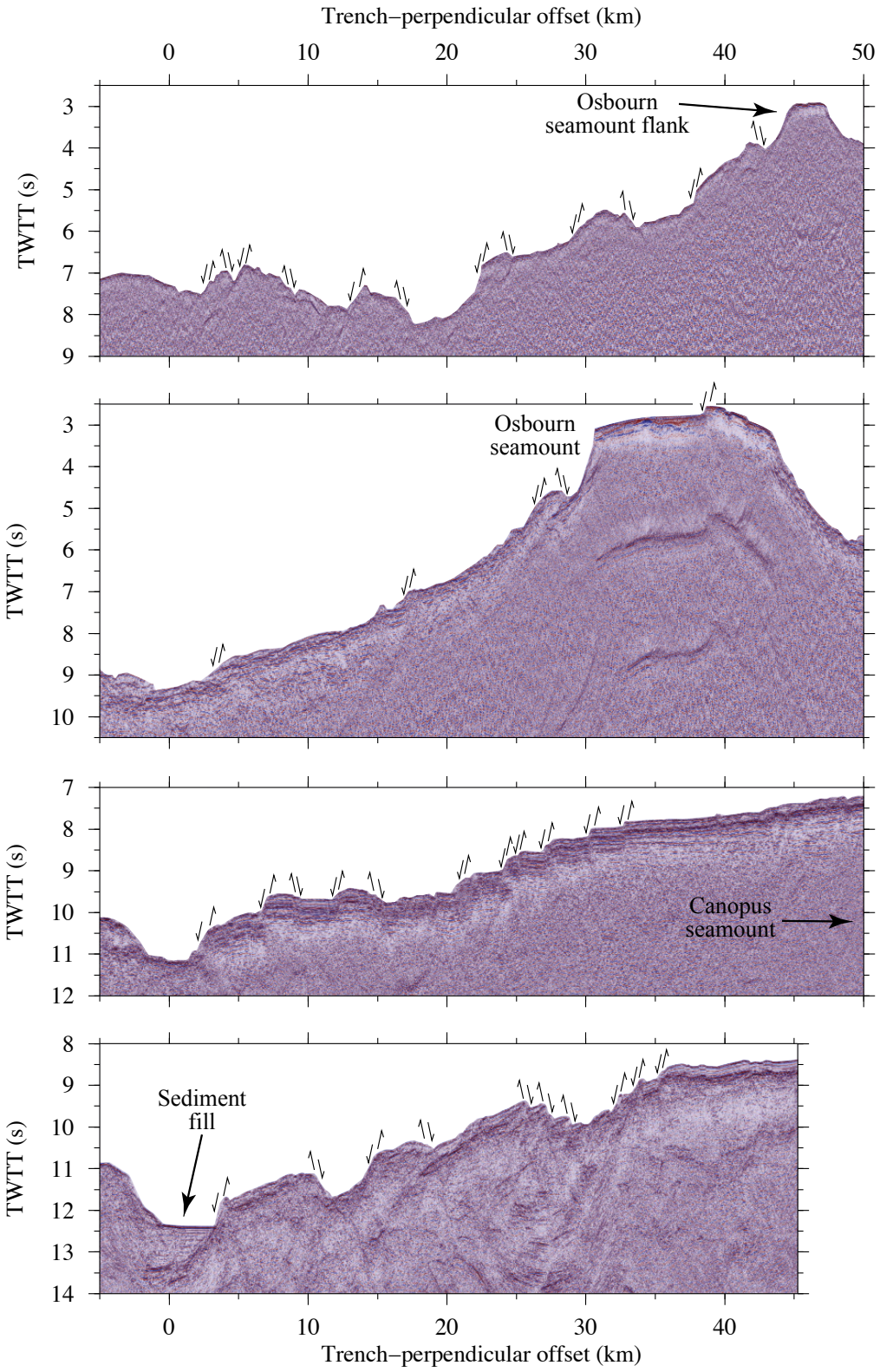

Figure 6.2: Caption next page.

Figure 6.2: (Previous page) MCS reflection sections, translated to trench-perpendicular offset, from different locations across the trench-outer rise region of the Tonga-Kermadec subduction system. a) Profile A (Stratford *et al.*, 2015), crossing the northern flank of Osbourn seamount. b) Profile C (Robinson, 2017), imaging a fault across the summit of Canopus seamount. c) Profile B (this study; Funnell *et al.*, 2017), indicating pervasive small offset (<0.3 s TWTT) faults. d) Profile D (Funnell, 2013; Funnell *et al.*, 2014), exhibiting large offset (1.5 s TWTT) bend-faults, typical of background Pacific plate subduction along the Tonga-Kermadec margin.

subducting plate dip, fault offset, and trench axial depth (Figure 6.3), suggests that the presence of the LRSC and the crustal thickening associated with it moderates deformation of the subducting plate by providing structural and buoyancy-driven support (Funnell *et al.*, 2017).

This hypothesis is consistent with analogue and numerical models that predict the subduction of buoyant and structurally robust (aseismic) ridges locally reduces the dip of the subducting slab (Martinod *et al.*, 2005; 2013; Zeumann & Hampel, 2015; 2016). Similar observations of reduced slab dip, and variable bend-faulting patterns, are made at the Cocos and Carnegie ridges, which subduct to the east along the Central- and South-American subduction systems (Walther, 2003; Ranero *et al.*, 2005). The Cocos ridge is >250 km across but, despite this difference in scale, comparable changes in subducting plate deformation are observed around the Tonga-Kermadec trench-LRSC intersection, supporting the notion that the seamount edifices are underlain by a structurally robust and buoyant ridge. These observations contradict the Ballance *et al.* (1989) model of seamount subduction, which is based on spatially limited MCS data. Although Ballance *et al.* (1989) correctly notes that the trench shallows, fault offsets do not increase but instead reduce within the region proximal to the subducting seamount relative to background regions (Figure 6.3; Funnell *et al.*, 2017) As a result, the observations of reduced plate dip indicated by trench shallowing, limited trench-outer rise deformation, and the possible retention of typical background upper mantle seismic velocity (Figure 6.1), implies that the presence of the LRSC moderates the subducting plate deformation (Martinod *et al.*, 2013; Zeumann & Hampel, 2015), effectively decreasing the amount by which the flexural rigidity of the subducting plate reduces (Billen & Gurnis, 2005; Arredondo & Billen, 2012).

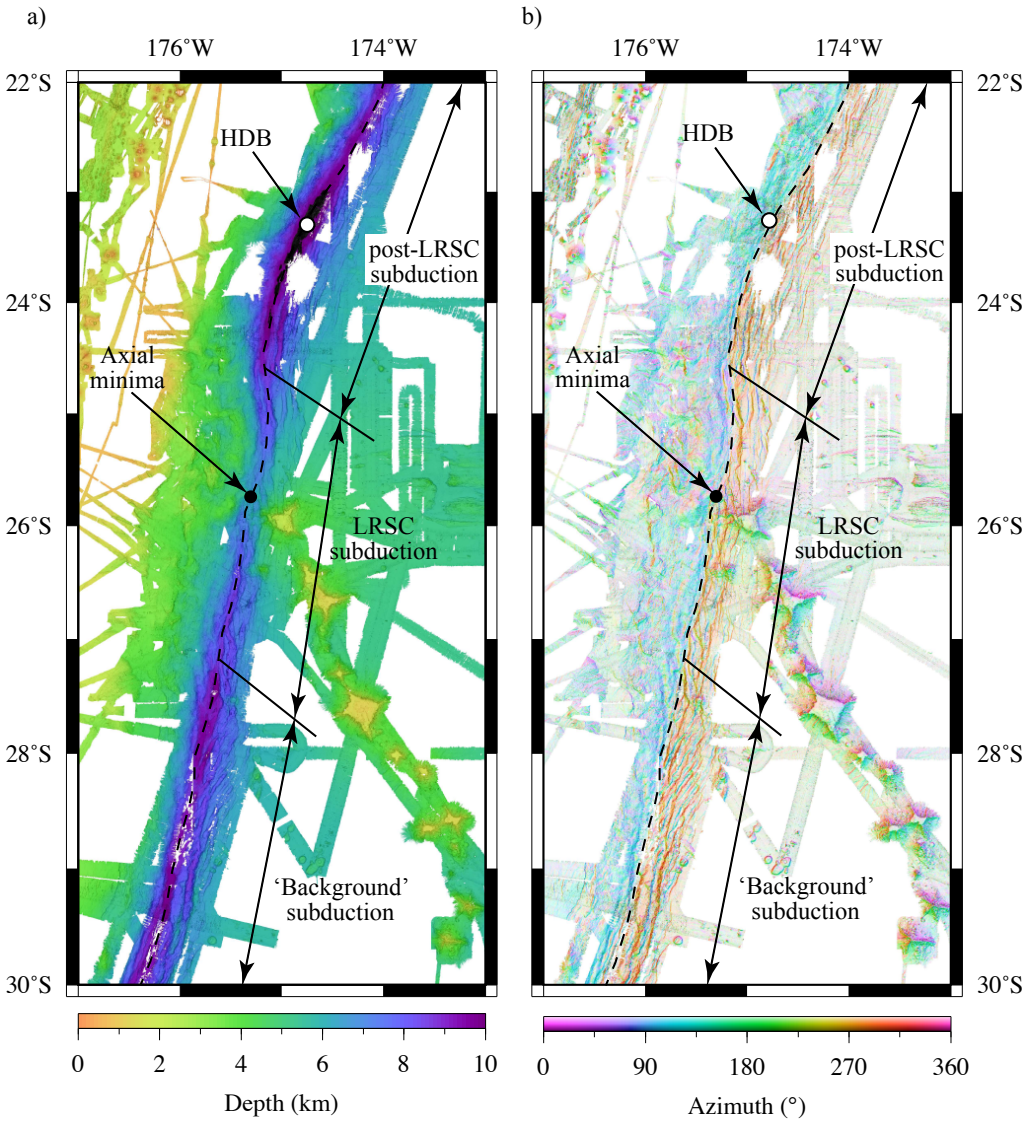

Figure 6.3: Swath bathymetry and azimuth-dip maps of the region surrounding the Tonga-Kermadec trench-LRSC intersection. a) Swath bathymetry map. b) Azimuth-dip map, with the colour determined by the slope azimuth at a given point, and the strength of the colour determined by the angle of slope. Regions with the greatest angles of slope show the strongest azimuthal colours; relatively flat regions appear lighter. This approach effectively highlights the flanks of the LRSC seamounts, the Osbourn spreading centre axial valley, and the trench-outer rise bend faults of the subducting Pacific plate. The location of Horizon Deep Bight (HDB), the deepest point of the Tonga trench (10.87 km-deep) is indicated.

6.3 Characterising the along-strike variability of the Tonga-Kermadec forearc

The forearc-arc crust imaged along Profile B is found to be thin, at 12.0-13.0 ± 0.7 km-thick, relative to previous regional and global observations of the overriding crust at intra-oceanic erosive subduction zones (Section 5.2.5). This crustal thickness appears not to be unique to ∼27°S along the Kermadec forearc, but part of a broader trend of varying crustal thickness along the entire subduction system (Figure 6.4). To the north, Profile A (Stratford *et al.*, 2015) and P02 (Contreras-Reyes *et al.*, 2011) image a crustal thickness of >18 km, while Robinson (2017) determines a crustal thickness that reaches 15 km at the eastern edge of the forearc along Profile C, although the profile does not cross a sufficient length of the forearc to provide more than an indicative estimate. In addition, Crawford *et al.* (2003) present crustal models along PCr where the crust is >15 km thick, but the mantle and Moho were not sampled so the depth of the Moho was not directly constrained. Consequently, no direct crustal thickness measurements are available north of P02. South of Profile B, Profiles M4, M3, and M2 image Kermadec forearc crust ∼12 km in thickness, with minimal variability in the depth of the Moho below sea surface (Bassett *et al.*, 2016).

To assess this along-arc crustal variability more qualitatively, the area of crust determined by modelling (i.e. between the 2.9-7.4 km s^{-1} contours) was calculated for each of the published models along the subduction system (Appendix F). This crustal area is widely reported as a volume per unit length along the subduction system, with the units of km^3/km (Clift *et al.*, 1998; Holbrook *et al.*, 1999; Takahashi *et al.*, 2008; Calvert *et al.*, 2008; Takahashi *et al.*, 2009), so quoted values will be presented in these units for consistency. In the regions of the forearc sampled, the local crustal volume is inversely proportional to the seabed depth (Figure 6.4). Along the Tonga forearc (north of 26°S) the crustal volume is on average >3000 km^3/km, which is similar to observations at the IBM subduction system (∼2500-2700 km^3/km, Appendix F; Takahashi *et al.*, 2008; 2009). South of Profile A, there is a rapid reduction in crustal volume to ∼2300 km^3/km at Profile B and 2000 km^3/km at M4 (Figure 6.4). South of 32°S, the crustal volume does not appear to significantly vary, averaging 1800 km^3/km.

The increase in crustal thickness and volume north of Profile B, by ∼6 km and >700 km^3/km respectively, over 300 km along the strike of the forearc appears to be mainly facilitated by an increase in the depth of the forearc Moho from 15 to 20 km depth below sea surface, and also an ∼2 km shallower seabed. This crustal

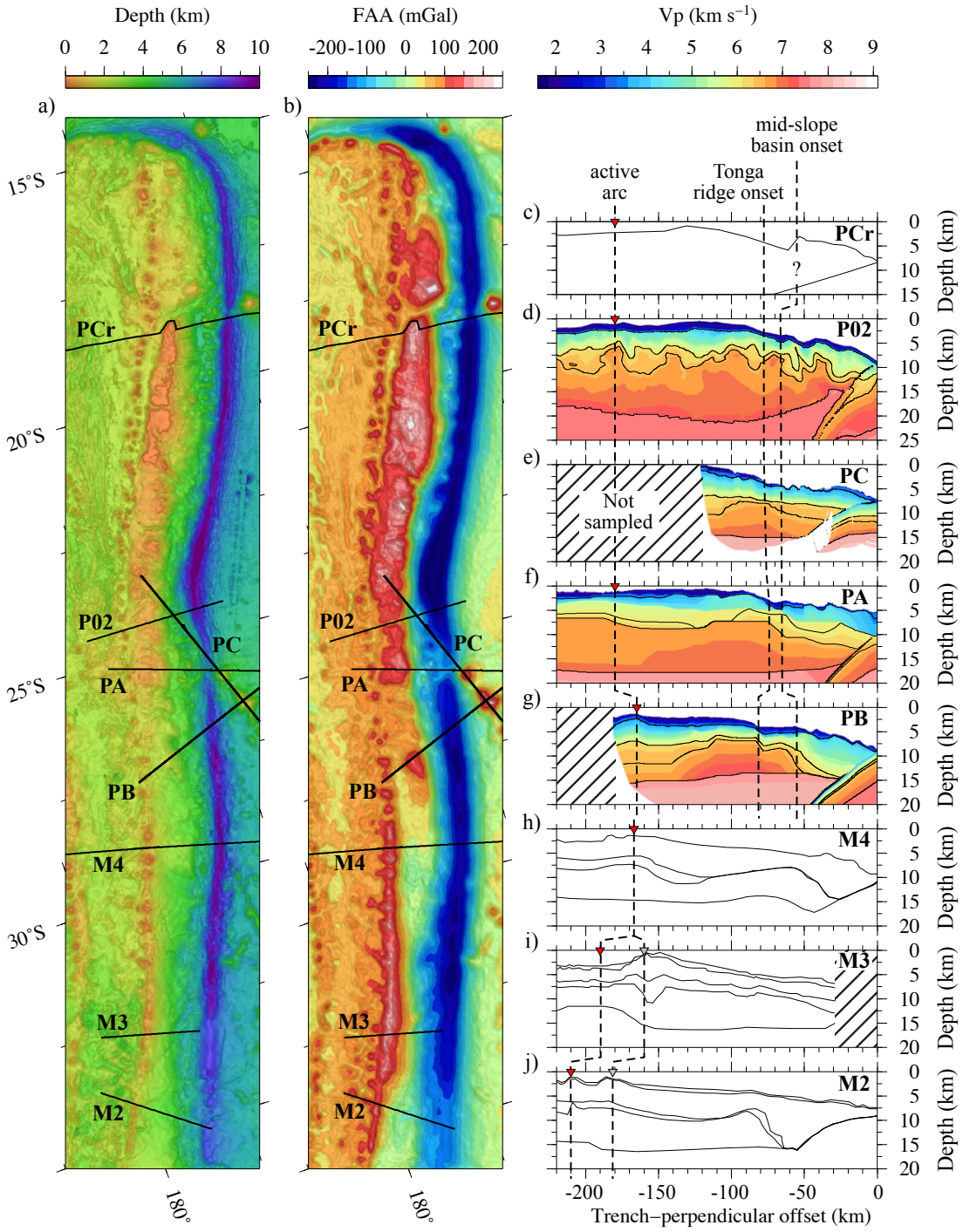

Figure 6.4: Caption next page.

Figure 6.4: (Previous page) Comparison of velocity-depth models through the forearc of the Tonga-Kermadec subduction system. a) Regional bathymetry map, rotated to highlight the bathymetric morphological variability along the trench. Relevant profiles, presented in c)-j) are annotated. b) Regional FAA (Sandwell *et al.*, 2014), demonstrating the along-strike variability in FAA. c) PCr with the major crustal units digitised from Crawford *et al.* (2003). d) P03 from Contreras-Reyes *et al.* (2011). e) PC from Robinson (2017), note that the profile does not cross much of the forearc due to is oblique approach angle. f) PA from Stratford *et al.* (2015). g) PB from Funnell *et al.* (2017) and this study. h), i), and j) are M4, M3, and M2, respectively from Bassett *et al.* (2016) with major crustal layers digitised. Regions of the velocity-depth models that are cross-hatched were not sampled, and so indicate where no velocity data are present. From south to north along the Tonga-Kermadec forearc, the bathymetry generally shallows and the FAA as well as crustal thickness and volume (where sampled; see Appendix F) increases.

thickness increase appears to be primarily focussed in the region of higher seismic velocity found in the lower crust (6.8-7.4 km s^{-1}). Beneath the forearc morphological high of Profile B, the base of the lower crust, defined by >6.8 km s^{-1}, reaches 4 km-thick. Further north at Profile A and P02, this lower crustal region is 7 and 11 km thick respectively (Figure 6.4; Contreras-Reyes *et al.*, 2011; Stratford *et al.*, 2015). Although there is no morphological ridge on the forearc at Profile M4, the high velocity anomaly is ∼5 km-thick, whereas further south at Profiles M2 and M3, neither a forearc morphological ridge or base-crustal high velocity structure is observed (Bassett *et al.*, 2016). Interestingly, the signature of the FAA (Sandwell *et al.*, 2014) over the Tonga-Kermadec forearc is consistently <0 mGal south of Profile M4, but increases gradually northward to ∼150 mGal by Profile B (27°S). North of Profile B there is a reduction in the FAA, to 100 mGal, although the forearc seabed remains at a comparable depth until Profile A (26°S), where another increase in FAA (to 150 mGal) continues north to the Tongan island group, reaching >250 mGal just south of 18°S. Over the extent of the forearc along the Tonga-Kermadec subduction system, the bathymetry clearly exhibits a primary control over the amplitude of the FAA; however, further variations in the FAA where no significant bathymetric change is observed suggest that the quantity of lower crustal material also exerts a control on the observed gravity anomaly. The apparent importance of the lower crustal velocity anomaly on the along-forearc FAA variability is perhaps unsurprising following the requirement of such a high-density anomaly (3.30 ± 0.10 g cm^{-3}) to explain the FAA across the Profile B forearc (Section 5.3.4).

Where sampled, the morphology of the forearc crust indicates that its broad structure predates the majority of sedimentation at the margin (e.g. Section 2.4; Herzer & Exon, 1985; Funnell *et al.*, 2014; 2017). The presence of a small morphological ridge ∼20 km across on Profile D, with significant basement faulting and

slight sediment cover coincident with a high FAA, led Funnell *et al.* (2014) to interpret the region of the forearc to be underlain by a high density, structurally robust crustal anomaly that was more resistant to subduction erosive processes. Although it is not directly imaged north of Profile P02, the morphological prominence and the northward increasing FAA of the extinct Eocene frontal arc appears to continue north and south of the region imaged by Profiles B and A, and Profile P02 (Figure 6.4). These observations suggest that the trend in forearc crustal thickness along the margin is controlled by systematic variations in material generation or erosion following formation (∼51 Ma; Meffre *et al.*, 2012), but prior to significant sedimentation and seamount subduction (Funnell *et al.*, 2017). This would fit with the proposed tectonic model of Meffre *et al.* (2012) which, despite only sampling along the northern end of the Tonga arc, infers subduction initiation propagated southward along the Tonga arc, enabling more volcanic material to be generated in the north where subduction had been active for longer.

6.4 Southern extent of the extinct Eocene frontal arc

The extinct Eocene frontal arc is speculated to terminate between 26°S (e.g. Ballance *et al.*, 1999) and 37°S (e.g. Collot & Davy, 1998b). Collot & Davy (1998b) suggests that although the regional FAA signature of the Tonga forearc terminates near 31°S (Figure 6.5; Sandwell *et al.*, 2014), the extinct arc once extended to 37°S but was eroded between 31-35°S, leaving an isolated sliver currently beneath the Raukumara Basin at 36-37°S. In contrast, Ballance *et al.* (1999) proposes that the southern extent of the Tongan forearc is at 26°S, because microfossil evidence usually associated with the ridge is absent south of this point and there is a significant increase in depth of the forearc (Figure 6.5).

The Tonga arc, which now forms the forearc ridge, is clearly observed over 2000 km along the subduction system in bathymetry and backscatter images (Lonsdale, 1986; MacLeod & Lothian, 1994; Clift *et al.*, 1998), and becomes less morphologically prominent south of ∼26°S (Figure 6.5). The width of the forearc ridge decreases and water depth increases until ∼28°S, just south of Profile D, where all seabed morphological evidence of the ridge disappears, and the forearc becomes a gentle concave-up basin (Funnell *et al.*, 2014). The forearc ridge is characterised by high seismic velocity and density at the base of the lower crust, representative of residual pyroxenites from the initiation of subduction (Section 5.3.4), which is observed to decrease in volume between 24-28°S (Figure 6.4). The observation of the high

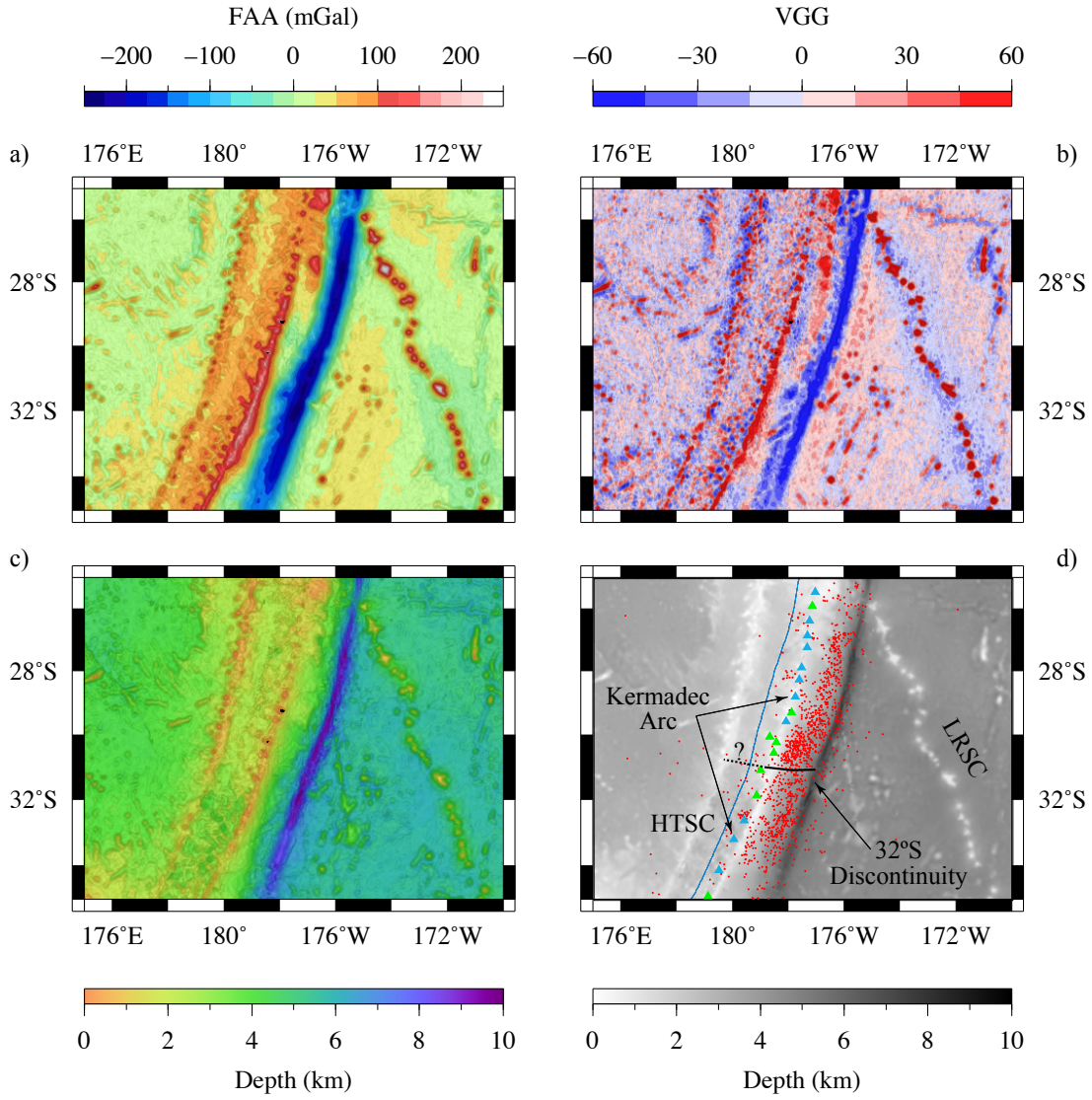

Figure 6.5: Summary of regional data demonstrating the southern termination of the extinct Tonga arc at the 32°S Discontinuity. a) FAA map showing the gradual reduction in FAA south along the Kermadec forearc from >100 mGal at 26°S to <0 mGal at 32°S. b) VGG highlighting the clear termination of the positive FAA at the 32°S Discontinuity, and the strong variation in backarc basin structure across the boundary. c) Bathymetry showing the morphological expression of the extinct Tonga arc terminates at ∼28°S. d) Summary schematic of the 32°S Discontinuity. Green triangles indicate active volcanoes (Venzke, 2013), while blue triangles are volcanic edifices evident in the bathymetry that are not included in the Venzke (2013) volcano dataset. Red dots are the locations of shallow earthquakes (<50 km depth), and significant tectonic features are labelled, including the Havre Trough spreading centre (HTSC) and the LRSC. Note that the figure shows the seismic quiescence thought to be caused by LRSC-subduction (<27°S), and shows the greatest density of earthquakes just north of the 32°S Discontinuity.

velocity structure at the base of Profile M4, at 29°S, and the extension of the associated high FAA to 31°S (Figure 6.5a) suggests that the extinct Eocene arc is present at these latitudes, but is not bathymetrically expressed, existing only in the subsurface. Bassett & Watts (2015b) and Bassett *et al.* (2016) present de-trended FAA data that highlight residual features following the removal of a spectrally-averaged profile across the subduction system, that clearly suggests the presence of the extinct Eocene arc to 31.5°S. A similar, but more locally sensitive technique, is to consider the regional vertical gravity gradient (VGG; Sandwell *et al.*, 2014), which reveals that the positive VGG associated with the Tonga ridge extends to 31.5°S. South of the 32°S tectonic boundary the high velocity lower crust of the forearc is not observed (velocity-depth profiles M3 and M4; Bassett *et al.*, 2016), and the high FAA associated with the extinct Tonga arc is absent.

Pelletier & Dupont (1990) were the first to observe the local structural variability around the 32°S Discontinuity, finding that the Kermadec trench axis reaches >10 km water depth just north of boundary with large-offset (>1.5 km) normal faults and trenchward-dipping subducting sediments. South of the boundary the trench axis shallows and steps eastward, and the subducting plate is defined by smaller offset faults (100-200 m). These observations led Pelletier & Dupont (1990) to propose that this boundary was caused by a change in regime from subduction erosion north of 32°S to accretion further south. They proposed that this change is caused by a shift in the maximum depth of the subducting slab from 550 km north of the boundary to 250-300 km in the south (see Figure 3.16; Hayes *et al.*, 2012). Collot & Davy (1998a) alternatively propose this to be the site of initial Hikurangi plateau subduction, which is currently subducting ∼36°S. Ballance *et al.* (1999) note that geophysical evidence suggests the plateau is not observed far enough north beneath the overriding plate for this to be the case, although do not propose an alternative origin for the 32°S boundary. These structural variations are not limited to the subducting plate and forearc as, south of 32°S, the active arc migrates westward into the backarc basin, which is 1.5 km deeper (from 2.5 to 4.0 km below sea surface) and more asymmetric (Figure 6.5; Ballance *et al.*, 1999)

A southern tectonic boundary along the Tonga-Kermadec subduction system is implied in the evolutionary history of the South Fiji Basin prior to the merging of the Tonga-Kermadec-Hikurangi trenches <15 Ma (Herzer *et al.*, 2011). The 32°S boundary may originate from this tectonic history, effectively demarcating the southern extent of the subduction system before it migrated eastward after 34 Ma (Bassett *et al.*, 2016). South of the boundary, the overriding plate material most likely only formed at some point during the opening of the South Fiji Basin (34-15 Ma; Herzer

et al., 2011), as there is no evidence of the initial Tonga Ridge, but the Kermadec arc-Havre Trough-Colville Ridge are observed (Figure 6.5). This later formation of the overriding plate south of the 32°S tectonic boundary, which was not built upon the extinct Tonga arc substrate, suitably explains the variable structure across it, including the less prominent backarc, deeper backarc basin, and the migration of the active arc further south (Bassett *et al.*, 2016; Funnell *et al.*, 2017).

6.5 Northern extent of the extinct Eocene frontal arc

North of 26°S the Tonga forearc widens (from 60 to 100 km across) and shallows, coinciding with an increase in the amplitude of the FAA (from 100 to >200 mGal) towards the Tongan islands at 21°S. Just beyond the northern tip of this island group, at ∼18.5°S, a 20 km-wide and 2 km-deep bathymetric canyon and a sharp reduction in FAA (to <100 mGal) generates a negative VGG that separates the Tonga platform from a broader and deeper forearc in the north (Figure 6.6). Bonnardot *et al.* (2006; 2007), observing a slight reduction in seismicity, refer to this feature as the Fonualei Discontinuity. Although there is a continuous presence of morphological volcanic edifices across the boundary, the active volcanism at the Tofua arc appears to terminate at the Fonualei Discontinuity, but this may be a limitation of the active volcano dataset (Venzke, 2013). The Fonualei Discontinuity also coincides with a variation in the age of dredged rock samples, which are between 51-39 Ma south of the boundary and from 35-28 Ma to the north (Meffre *et al.*, 2012); however, the limited nature of dredge sampling may result in the true age of the forearc crust not being accurately represented. Structural variations are not limited to the forearc and arc, as the Fonualei Rift extends from ∼15 to 18°S, just behind the volcanic arc north of the boundary (Figure 6.6).

The pronounced nature of the ∼150 km-long canyon led Wright *et al.* (2000) to propose that the feature was the result of forearc uplift and fracturing during subduction of the LRSC. Bonnardot *et al.* (2006; 2007), highlighted the presence of Capricorn seamount, currently proximal to the trench, noting that it was unlikely to be currently affecting the forearc and independently proposed a link to LRSC subduction. Seamount subduction is commonly documented to increase the rate of subduction erosion and remove significant quantities of material from the overriding plate (Dominguez *et al.*, 1998b; 2000; Vannucchi *et al.*, 2006; Wang & Bilek, 2011). Despite this, the canyon associated with the Fonualei Discontinuity is sharper and extends much further arcward (>150 km) than is typical for seamount subduction.

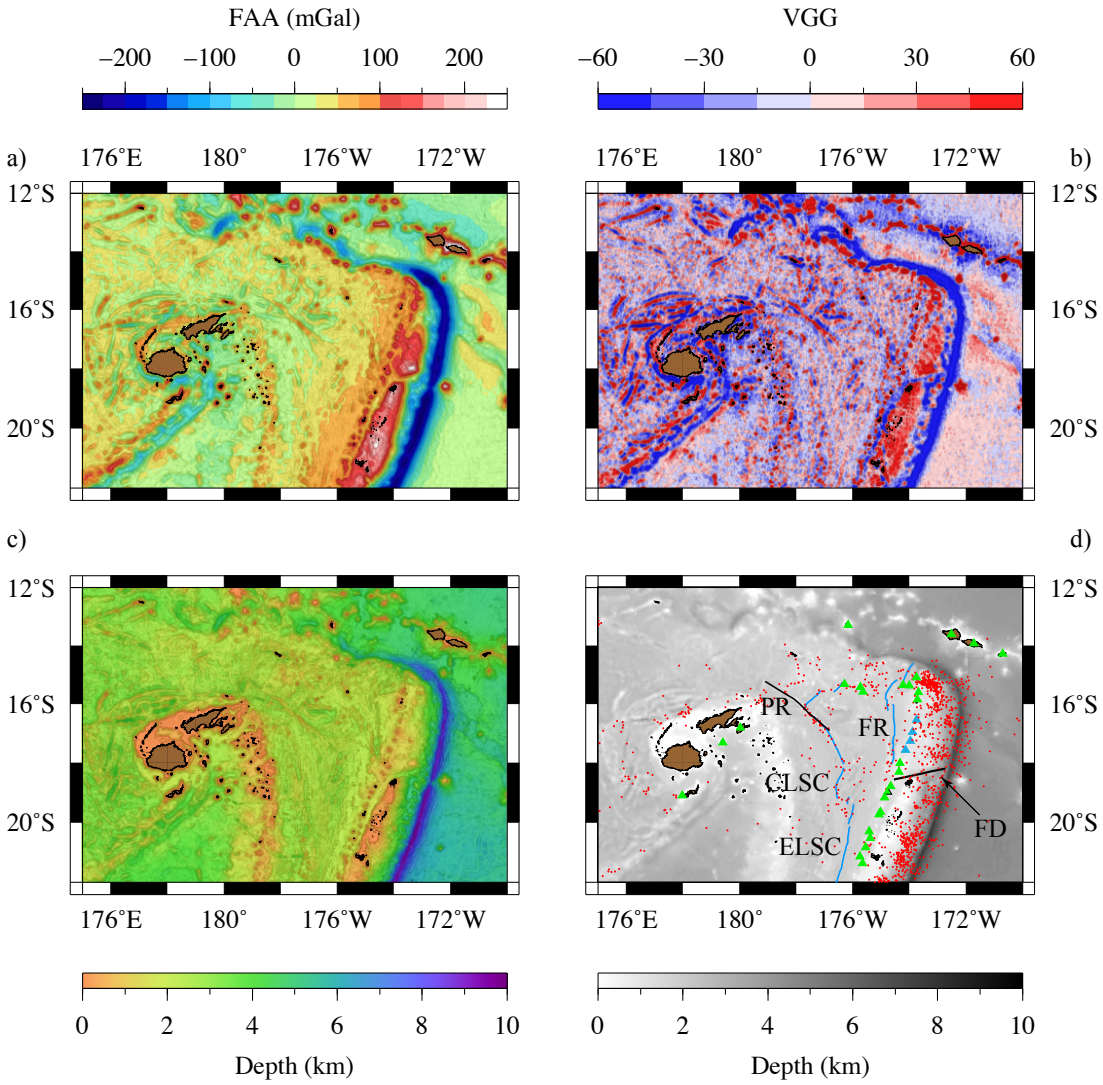

Figure 6.6: Summary of regional data demonstrating the northern termination of the extinct Tonga arc at the Fonualei Discontinuity (FD). a) FAA with a pronounced reduction at 18°S, from ∼250 to <100 mGal. b) VGG highlighting the change in FAA in a), and the structure of the backarc Lau Basin. c) Bathymetry showing the 2 km-deep, 150 km-long canyon at the northern end of the Tonga arc. d) Summary schematic of the Fonualei Discontinuity. Green triangles indicate active volcanoes (Venzke, 2013), while blue triangles are volcanic edifices evident in the bathymetry that are not included in the Venzke (2013) volcano dataset. Red dots are the locations of shallow earthquakes (<50 km depth), and significant backarc basin spreading centres are labelled: Central Lau spreading centre (CLSC), East Lau spreading centre (ELSC), Peggy Ridge (PR), and the Fonualei Rift (FR). Note that the greatest density of earthquakes shown, around <16°S, is associated with the tearing of the Pacific plate at the northern end of the subduction system (Isacks *et al.*, 1969; Bonnardot *et al.*, 2007).

For example, ∼50 km of sediment deformation and slumping is observed at the accretionary Costa Rica margin (Dominguez *et al.*, 1998b), and ∼80 km of frontal erosion is attributed to the subduction of the LRSC just north of the present day ridge-trench intersection (Clift & MacLeod, 1999). The theory that seamount subduction caused the Fonualei Discontinuity also fails to explain other observations, such as the variation in the age of dredged forearc rocks across the boundary, as well as the apparent absence of volcanism for more than 200 km to the north.

The variation in most of the observable characteristics of the overriding plate across the Fonualei Discontinuity indicates that it may be a significant tectonic boundary (Figure 6.6), rather than a consequence of the more spatially and temporally limited subduction of a seamount. South of 18°S, the predominant forearc crustal structure is the inherited thick Eocene arc with a high velocity and density lower crustal anomaly that, in places, has a morphology that shallows to form island groups. North of the Fonualei Discontinuity, the forearc has not been sampled by any geophysical profile, but is immediately ∼2 km deeper and the remarkably high FAA (200-250 mGal) remains. Considering the deeper forearc seabed to the north, higher density materials are required at shallower depths beneath the seabed, perhaps indicating significantly thinner crust, or a crust with different compositional structure are influencing the gravity anomaly. Whilst the forearc north of the discontinuity is not sufficiently sampled or tested to corroborate this, such significant variability over a well defined boundary may indicate that the forearc and volcanic arc are at different stages of crustal evolution (e.g. Takahashi *et al.*, 2007; Calvert *et al.*, 2008; Kodaira *et al.*, 2010). The observed reduction in the maximum age of dredged samples north of the boundary (from 51 to 35 Ma; Meffre *et al.*, 2012) supports this hypothesis, while the slightly reduced seismicity around the discontinuity (Bonnardot *et al.*, 2007) indicates it is inherently weak, releasing stress through small-scale diffusive faults and fractures.

Such a variable forearc structure and age could be facilitated by a similar boundary to that of the 13°S Discontinuity, whereby only during the migration of the original Tonga arc does the extended arc form and evolve (Funnell *et al.*, 2017). The observed age difference across the Fonualei Discontinuity coincides with the proposed age for the opening of the South Fiji Basin (∼34 Ma; Herzer *et al.*, 2011), long before the opening of the Lau Basin ∼6 Ma (Ruellan *et al.*, 2003). The Lau Basin exhibits highly variable structural complexity (Figure 6.6; Zellmer & Taylor, 2001; Conder & Wiens, 2011), but despite features such as the Peggy Ridge and the variations in spreading style and orientation along the Central Lau spreading centre (CLSC), it is unclear whether the different arc and forearc structure imparted any

control on the formation of the backarc region, and also where the feature originates from. A lack of geophysical models through the northern region of the Lau backarc basin prevents the analysis of the crustal and upper mantle structure, and thus the determination of any structural variability. It is pertinent to note that while the origin for the Fonualei Discontinuity proposed here does not preclude the subduction of the LRSC initiating the opening of the Lau Basin (Ruellan *et al.*, 2003), it does require that the subduction of the seamount chain started further south along the subduction system. This potentially significant tectonic boundary may be an interesting target for future geological and geophysical research.

6.6 Implications for seamount subduction along the Tonga-Kermadec trench

In Sections 6.3, 6.4, and 6.5, the large-scale structural variability along the Tonga-Kermadec arc and forearc was discussed, highlighting the dominance and evolution of inherited features that were created and deformed over the ∼51 Myr history of the Tonga-Kermadec subduction system. Since the initiation of subduction along the margin the uplift and collapse events observed in drill cores, which are proposed to be caused by seamount subduction, have punctuated the otherwise steady-state erosive regime controlling the inner-trench slopes (MacLeod, 1994; Clift *et al.*, 1998). This process of regular trench-slope uplift and collapse associated with seamount subduction is widely observed to increase the rates of basal and frontal erosion of the overriding crust (Ballance *et al.*, 1989; Dominguez *et al.*, 1998b; Clift & Vannucchi, 2004). Seamount subduction has been proposed to either flex the overriding plate (Scholz & Small, 1997), scrape material from the underside of the upper plate by the intact components of the subducting seamount (Cloos, 1992; Cloos & Shreve, 1996), or deform the overriding plate through a series of ring and radial faults (Dominguez *et al.*, 1998b; Wang & Bilek, 2011; 2014). While the earlier seamount subduction models were widely applicable (Cloos, 1992; Scholz & Small, 1997) and, in the case of Cloos & Shreve (1996), varied depending on whether accretionary or erosive processes dominated a margin, the current theory of Wang & Bilek (2011) is based on observations at accretionary margins for isolated seamounts (e.g. Dominguez *et al.*, 1998b; 2000). Aseismic ridge subduction is modelled as a distinct process (Martinod *et al.*, 2005; 2013; Zeumann & Hampel, 2015; 2016), and is not considered with discrete bathymetric features on top.

The ability to determine the exact location of currently subducting seamounts along the Tonga-Kermadec forearc is limited by the morphological complexity and

data quality (Funnell *et al.*, 2017). The trench-slope juxtaposing the current Tonga-Kermadec trench-LRSC intersection point is morphologically complex and does not display clear radial faults comparable to those observed at the well-sedimented margins, or clearly defined re-entrants trenchward of a marked morphological bulge (Figure 6.7; e.g. Dominguez *et al.*, 1998b; Wang & Bilek, 2011). Published and well-tested WA seismic profiles across the Tonga-Kermadec trench-LRSC intersection fail to image a subducting seamount (Figure 6.4; Contreras-Reyes *et al.*, 2011; Stratford *et al.*, 2015; Robinson, 2017), although Bassett & Watts (2015b) present a preliminary and untested model from Profile A that suggests otherwise. The Profile A dataset was originally presented and was thoroughly tested by Stratford *et al.* (2015), but did not indicate the presence of any subducting seamount material. Testing of the Profile B forward velocity model presented in this study and by Funnell *et al.* (2017), found it is only sensitive to changes >0.5 km s^{-1} in the lower-trench slope region (Section 3.8.1), and may only reliably recover velocity anomalies that are larger than 50 km x 4 km (Section 4.3). Similar sensitivities apply to other models at the margin, as they have comparable acquisition parameters and use the same modelling techniques. This model sensitivity is of a comparable morphological size to an intact seamount (Lonsdale, 1988; Ballance *et al.*, 1999), suggesting that the current WA seismic datasets and associated modelling techniques may not be able to discriminate between the presence or absence of a seamount in the lower-trench slope, unless sampled directly over an intact high velocity core (e.g. Contreras-Reyes *et al.*, 2011). Bathymetric evidence suggests that even the structurally robust cores of the seamounts experience extensional faulting (Figure 6.2; Robinson, 2017), and so may break up completely on subduction (e.g. Staudigel & Clague, 2009). As a result, typical subduction-related hydration and alteration processes may cause the seismic velocity within the cores to be reduced (Sallarès & Ranero, 2005; Contreras-reyes *et al.*, 2008; Moscoso & Grevemeyer, 2015), and thus be less seismically distinct from the lower-trench slope crustal material. With a greater density of instruments or shots across the trench region, physically smaller features with a smaller seismic velocity difference may be more reliably constrained.

Although a single seamount cannot be directly imaged beneath the lower-trench slope with the existing seismic data (Figure 6.4), the regional effects and historical deformation of LRSC subduction on the Tonga-Kermadec forearc can be analysed. Low seismic velocity (3-6 km s^{-1}) is characteristic of lower-trench slope crust along the length of the subduction system (Section 5.3.3, Figure 6.4; Crawford *et al.*, 2003; Stratford *et al.*, 2015; Funnell *et al.*, 2017), suggesting that the region is highly faulted and fractured by the process of subduction erosion (von Huene &

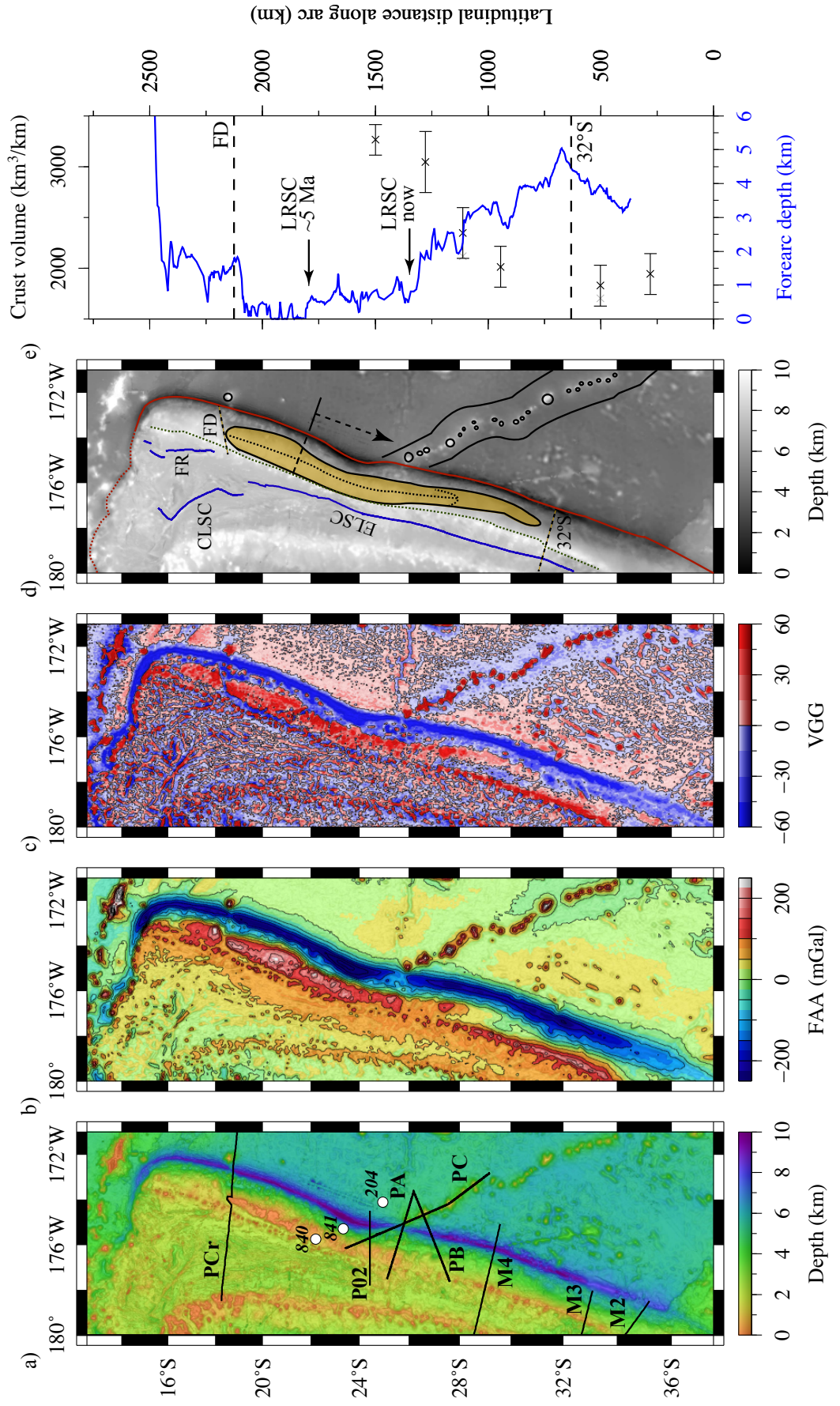

Figure 6.7: Caption next page.

Figure 6.7: (Previous page) Synthesis of along-strike structural variations, and a summary model, for the Tonga-Kermadec forearc. a) Regional bathymetry with significant geophysical profiles and drill sites from Figure 6.4 labelled. b) Regional FAA (Sandwell *et al.*, 2014) over the same region as in a). c) Regional VGG over the same region as in a). d) Schematic model of the Tonga-Kermadec overriding plate structure and variability along strike, adapted from Funnell *et al.* (2017). e) Graph of forearc seabed bathymetry and total overriding crustal volume (Appendix F) between the trench and backarc basin, plotted against latitudinal distance along the margin. Significant tectonic features are indicated.

Ranero, 2003; Sallarès & Ranero, 2005). Low sensitivity and limited resolvability of the different models in this region precludes further analysis and comparison of this region along the margin, although the deformation is consistently observed to >30 km arcward of the trench and typically as far as the eastern edge of the mid-trench slope basin. West of the lower-trench slope, a relatively flat-lying mid-slope basin is usually observed with more typical forearc velocity throughout the crust (4.0-7.0 km s^{-1}; Figure 6.4). The most well imaged example is along Profile D, which is ∼25 km across and images >2 s TWTT-thick of horizontal and planar sediments (Funnell *et al.*, 2014), and similar examples are found further south and north (e.g. Ballance *et al.*, 1999; Wright *et al.*, 2000; Funnell *et al.*, 2017; this study). In the region proximal to LRSC subduction, the mid-slope basins are smaller (∼5 km across), less well sedimented, and more heavily deformed or rotated (Contreras-Reyes *et al.*, 2011; Stratford *et al.*, 2015; Robinson, 2017). Along the Tonga-Kermadec margin the separation between the onset of the upper-trench slope and the trench varies from >80 km offset at Profile B to <70 km at Profile P02 and a minimum of 60 km at Horizon Deep Bight (Figure 6.4). The coincident reduction in mid-slope basin size and increased structural complexity north across the present-day LRSC-trench intersection demonstrates that the LRSC subduction actively enhances lower-trench slope deformation and erosion as proposed by Ballance *et al.* (1989) and Stratford *et al.* (2015). Subsequent to the subduction of the LRSC (e.g. 25-23°S) the mid-trench slopes, which are usually preserved by the steady-state subduction erosive process (Wright *et al.*, 2000; Funnell *et al.*, 2014), are absent most likely as a result of a passive gravitational re-equilibration following the extreme deformation processes caused by seamount subduction. Interestingly, these long-term deformation processes associated with LRSC subduction resemble more closely the expected response of an overriding plate to the subduction of an aseismic ridge (e.g. Lallemand *et al.*, 1992; Martinod *et al.*, 2005; 2013; Zeumann & Hampel, 2015; 2016) than the documented and proposed effects of subducting seamounts (Dominguez *et al.*, 1998b; Wang & Bilek, 2011; 2014).

These forearc crustal erosion and deformation processes define LRSC subduction against the otherwise steady-state erosive setting of the Tonga-Kermadec subduction system. North of the present-day LRSC-trench intersection point, the trench displays a broad arcuate structure. This is most pronounced at ∼23.5°S where the Tonga trench is ∼80 km west of the LRSC-trench intersection point <500 km to the south (Contreras-Reyes *et al.*, 2011), and the trench axis reaches its deepest point (10.87 km; Ballance *et al.*, 1989; MacLeod & Lothian, 1994). The trench begins to return to its typical, linear strike, at 23°S (Stratford *et al.*, 2015), although does not straighten completely until 22°S (Figure 6.7). Between 23-22°S, the mid- and lower-trench slopes appear to increase in width again, returning to typical trench-slope structure north of 22°S. Herzer & Exon (1985) observed parallel normal faulting that delimits the northern edge of pervasive faulting and doming of the Tonga forearc at 22°S, which they ascribe to extensional stresses that were active between ∼5-1 Ma based on well-tied seismic data. Coincident with this change in forearc deformation, the morphological ridge quickly shallows by 0.5 km to form the Tongan islands (Figure 6.7). This sharp change in bathymetry at 22°S, relative to the gradual crustal northward thickening, suggests that there is a significant boundary here that may relate to the onset of seamount subduction ∼5 Ma (Ruellan *et al.*, 2003). Following the initial collision and subduction of the LRSC, the deformation and erosion of the lower- and mid-trench slopes generated a steep inner-trench slope that was gravitationally unstable (Contreras-Reyes *et al.*, 2011; Stratford *et al.*, 2015). As the LRSC migrated southwards, the forearc experienced extension, forming the pervasive normal faults observed by Herzer & Exon (1985), and collapsing to re-establish the trench-slope stability (Stratford *et al.*, 2015; Funnell *et al.*, 2017). The northern limit of the extensional faulting at 22°S (Figure 6.7; Herzer & Exon, 1985) supports the proposal of Ballance *et al.* (1989), that LRSC-subduction initiated near this point along the margin and migrated southwards. Seamount subduction is documented at ODP site 841 (Figure 6.7), ∼1.5 Ma (MacLeod, 1994; Clift & MacLeod, 1999), although as discussed earlier the LRSC deforms a broad area as a ridge, so what this age marks the exact collision of is uncertain. Despite this evidence, the proposal of Ballance *et al.* (1989) is only supported by spatially limited MCS data and bathymetry data as no WA seismic data exist between 18-24°S (Crawford *et al.*, 2003; Contreras-Reyes *et al.*, 2011), and so the future acquisition of more geophysical data would provide a more robust means of testing the exact subduction history of the LRSC.

6.7 Summary

In this chapter the results and interpretations of the joint geophysical dataset acquired along Profile B were combined with existing geophysical and geological data from along the Tonga-Kermadec subduction system. Together, these revealed variations in along-arc structure in both the subducting and overriding plates. Along the subducting Pacific plate the most significant structural variability occurs around the trench-LRSC intersection point, where the presence of the seamount chain limits the deformation of the subducting plate, decreasing the expected reduction in plate rigidity. The overriding plate structure varies along-arc, with more recent deformation processes superimposed on existing features. Crustal thickness and volume generally decreases from north to south along the subduction system, largely controlled by the inherited structure of the extinct ∼51 Ma Tonga arc, which is only directly observed between 18°S and 32°S. Beyond these latitudes the Tonga-Kermadec arc, which spans 15°S to south of 36°S, formed more recently, most likely during the opening of the South Fiji Basin (34-15 Ma). Over the last 5 Myr the point of LRSC subduction has migrated from 22°S to the present day ∼26°S, progressively removing crustal material from the lower-trench slope and deforming the otherwise stable mid-slope basins. Following the subduction of the LRSC, the mid-trench basin collapses and the extinct Tonga arc appears to undergo extension, compensating for the loss of material in the trench slopes, and enabling the mid-slope basin and lower-trench slope structure to be reformed.

In the next chapter, the main conclusions from this study will be summarised, highlighting particularly significant implications for the Tonga-Kermadec region and global subduction systems. The limitations of this study, and particularly interesting questions raised by the discussion will be used to form the basis of suggestions for future research.

Chapter 7

Conclusions and future work

7.1 Conclusions

This study has investigated the along-strike variability of the Tonga-Kermadec subduction system through the synthesis of new MCS data and WA seismic and density models, with previously published data and regional gravity maps. These observations were used to characterise the inherited structure of the forearc, and determine the extent of more recent deformation caused by LRSC subduction. Starting with the subduction input and finishing with the overriding plate (i.e. from east to west across the subduction system), the primary results and conclusions from this study can be summarised as:

- Typical crustal and upper mantle velocity-depth structure is observed for the incoming Pacific plate. Variable seismic velocity in the upper mantle displayed by profiles acquired perpendicular to each other and away from the trench-outer rise region is indicative of remnant spreading-related anisotropy of ∼7%.
- Profile B fails to image high internal velocities within Canopus seamount, but crosses the saddle between two larger edifices, possibly indicating a laterally limited intrusive mafic core. Elevated seismic velocity (>7.2 km s^{-1}) is observed at offsets of up to 50 km from the seamount summits at the base of the crust, indicating their structural support likely extends beyond the physical footprint of the edifices.
- In regions of background Pacific plate subduction, such as north and south of the present-day LRSC-trench intersection point, full graben with up to 2 km vertical throw are generated, and the plate dips at ∼5°, indicating rapid structural weakening. Within the vicinity of the LRSC, deformation is reduced as

the near-horizontal subducting plate is broken by small (<200 m), predominantly trenchward-dipping, normal faults. At the present-day LRSC-trench intersection the trench shallows by 4 km, and typical reductions in the upper mantle seismic velocity (by ∼5%) are not observed, suggesting that, despite the limited bathymetric expression of the seamounts, the edifices sit on an ∼250 km-wide structurally supportive ridge.

- Low seismic velocity observed throughout the lower-trench (3.0-6.0 km s^{-1}) is primarily caused by faulting and disaggregation of the crust, but typical crustal densities modelled for this region suggest the bulk density of the rock is not significantly altered by this process. This indicates the trench slopes are persistently eroded at the front and base, resulting in the pervasive faulting, fracturing, and possible hydration of the crust that progressively collapses under gravity into the trench. Steady-state erosion removes sedimentary and crustal material from the lower-trench slope, but enables a mid-trench slope basin to be maintained along the Tonga-Kermadec margin where background Pacific oceanic crust subducts.

- The Tonga-Kermadec forearc, between 18-32°S, is dominated by a basin and ridge morphology of varying prominence that predates significant sedimentation along the margin. This ridge, which is the remnant extinct Eocene Tonga arc that formed during subduction initiation ∼51 Ma, is underlain by high seismic velocity at the base of the crust (7.0-7.4 km s^{-1}), and is most closely represented by remarkably high density (3.30 ± 0.10 g cm^{-3}). The broad-scale high FAA generated by this high density lower-crustal feature enables the analysis of along-strike variations, highlighting a general southward decrease in volume (by up to a third), and constrains the extent of the extinct Tonga arc.

- At 32°S, the high FAA associated with the extinct Tonga arc terminates, although the bathymetric expression of the forearc ridge stops at ∼28°S, suggesting that it is the southern extent of the original arc generated during subduction initiation ∼51 Ma. The forearc and arc south of the 32°S Discontinuity most likely formed during the opening of the South Fiji Basin (34-15 Ma) and has, since then, continued to develop as an extension of the main arc.

- The bathymetric morphological expression of the Tonga ridge increases north along the margin up to 18°S, where a steep-sided, >2 km-deep canyon demarcates a sudden change in forearc structure. North of this discontinuity, the

forearc is deeper and younger (34 Ma), and the backarc basin structure varies, suggesting that this boundary, and the forearc-arc to the north, also formed during South Fiji Basin opening.

- Subduction of the LRSC along the Tonga-Kermadec trench increases frontal and basal erosion of the overriding crust, shortening the lower- and mid-trench slopes. Following seamount subduction, the eastern edge of the Eocene arc most likely undergoes extension to re-equilibrate the trench-slope stability. The trench slopes are either absent or more heavily deformed and eroded as far north as 23°S along the trench, although extensional faulting of the Tonga forearc ridge is observed to 22°S. These observations suggest that LRSC subduction at the Tonga-Kermadec margin began at ∼22°S, >5 Ma, and subsequently migrated southwards.

7.2 Future work

In this study, a single joint geophysical profile was modelled and interpreted. The resulting combined best-fit model was synthesised with both a range of existing geophysical profiles from along the Tonga-Kermadec subduction system and with regional datasets, to characterise along-arc variations establishing inherited structures as well as defining features that were generated by seamount subduction. This study was able to synthesise new data with previous models from along the forearc, but it also highlighted: a paucity of geophysical data north of ∼24°S; the detrimental effects of poor velocity-depth model resolvability throughout the lower-trench slope; and the limited sampling of the LRSC volcanic edifices. Further research is thus required to resolve the uncertainties and answer remaining questions, either through further analysis of existing datasets or the acquisition of new data.

7.2.1 LRSC internal structure

Developing a more detailed model of LRSC subduction requires a better understanding of the internal structure of the volcanic edifices as well as the effect of bend-faulting on seamount structure. The four existing profiles that sample seamount structure at the northwestern end of the LRSC imply a lateral limit to the high velocity intrusive core (Contreras-Reyes *et al.*, 2010; Richards *et al.*, 2013), that has been supported by 3D gravity modelling (Hwang & Kim, 2016), but is not required within each of the edifices given the spatial limitations of the existing datasets (Section 5.3.2). A simple test of the presence of these high velocity intrusions in other

seamounts could be achieved by extending the method of Hwang & Kim (2016) from a single seamount to a selection of other seamounts along the 4300 km-length of the LRSC, focussing on those at the northwestern extent that are most likely to be structurally similar to those previously subducted. This method could be simply achieved using the existing global FAA dataset of Sandwell *et al.* (2014); however, without additional constraint from crustal models, gravity modelling is a highly non-unique approach that would require a number of assumptions based on the currently limited sampling of LRSC volcanic edifices. The acquisition of further WA seismic data, ideally as a series of high density 3D survey grids, could provide more robust constraint on the extent of the intrusive cores and reveal the internal structure of typical seamounts (e.g. L2-3D and L3-3D in Figure 7.1). The extra constraint afforded by dense 3D WA seismic surveys is also required to determine whether bend-faulting markedly alters the internal structure of the seamounts and, if so, the extent of this alteration (L1-3D; Figure 7.1).

7.2.2 Variation in overriding plate characteristics

In Section 6.3 the previously published velocity-depth models from the Tonga-Kermadec margin were synthesised to reveal along-arc variation in forearc structure. South of ∼24°S, the forearc is relatively well sampled, with WA seismic profiles typically spaced by ∼250 km, and at worst by 500 km, along-arc. North of this latitude, the only existing WA seismic profile is that presented by Crawford *et al.* (2003), which fails to image the Moho beneath the forearc and therefore is unable to constrain crustal thickness or volume. Further to this, except for dredge samples acquired at the northern end of the Tonga arc (Meffre *et al.*, 2012), the Tonga-Kermadec forearc has only been sampled by two drill sites, 840 and 841 (Clift *et al.*, 1994), located in the central region of the subduction system. As a result, discussion of structural variation at the northern end of the subduction system was based on regional bathymetry and FAA datasets (Sandwell *et al.*, 2014), as well as sparse dredge data (Meffre *et al.*, 2012).

Improved constraint on crustal structure, and crustal thickness in particular, at the northern end of the Tonga-Kermadec forearc would not only enable a better understanding of the long-term effects of seamount subduction, but also advance the regional framework of subduction system structure and evolution. Prior to the acquisition of new data at the margin, a number of preliminary gravity models may be developed for profiles across the northern section of the margin, using published models to inform the expected crustal compositions, and provide a starting point for crustal thickness. Such profiles may be preferentially located just south and north

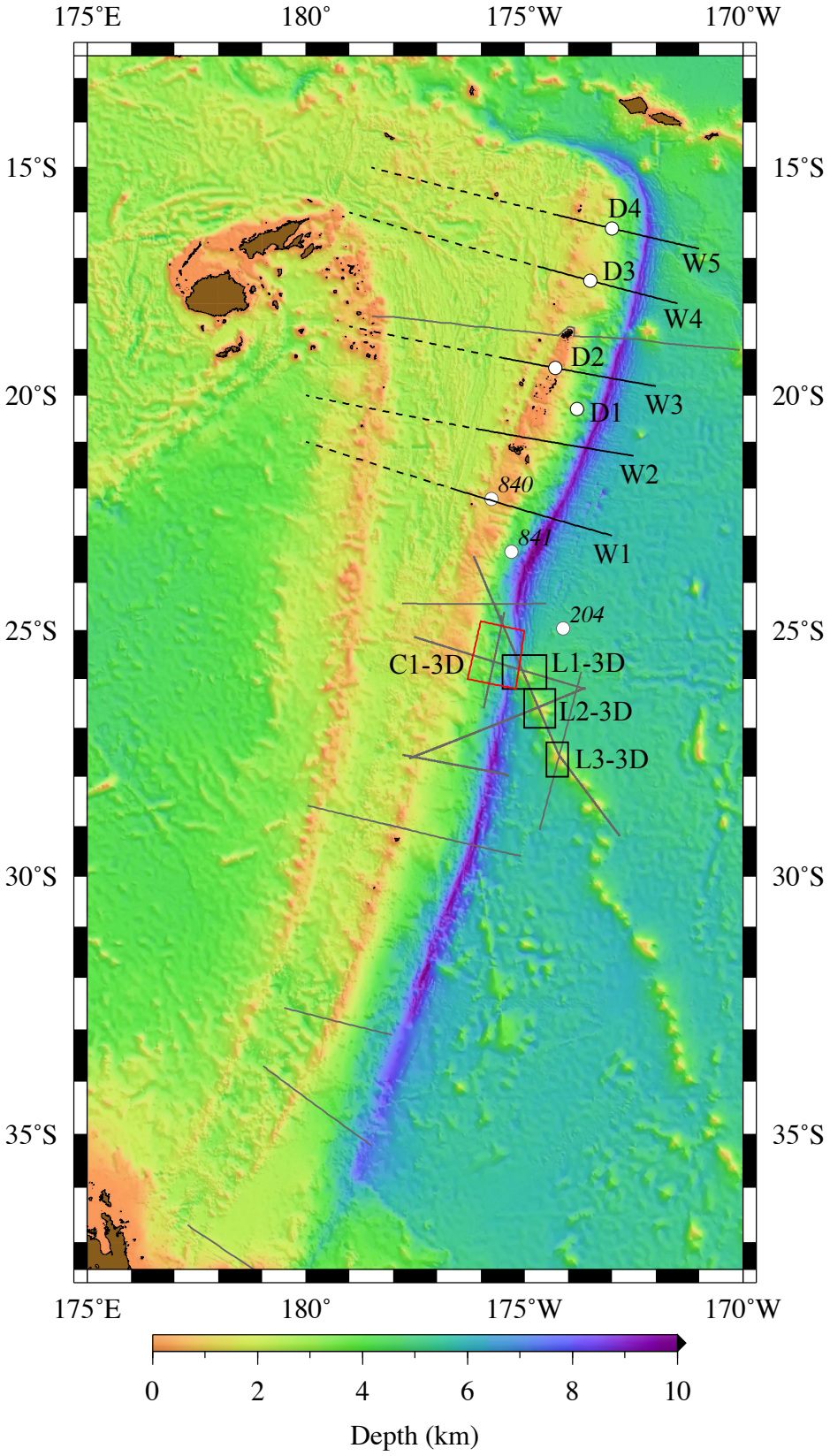

Figure 7.1: Caption next page.

Figure 7.1: (Previous page) Proposed future data acquisition along the Tonga-Kermadec subduction system. Existing geophysical profiles (grey lines) are overlain on the regional bathymetry, with existing drill sites shown as labelled white circles. A series of 3D WA seismic surveys across the northwestern-most seamounts in the chain (L1-3D, L2-3D, and L3-3D) may be able to better constrain internal edifice structure and the variations introduced as they undergo bend-faulting. Joint 2D geophysical profiles across the northern section of the Tonga subduction system, primarily acquiring WA data (W1-W5), would provide insight into the Tonga forearc background structure, not only constraining pre-LRSC subduction structure but also the origin of the Fonualei Discontinuity. Note that the dashed segments of the profiles are supplementary to the main profiles, and may only be acquired if existing datasets across the Lau Basin are found to not be suitable. Here, additional constraint on the tectonic history and composition of the overriding plate may be provided by new drill sites (D1-4). Using the 3D WA seismic grids as background studies, the present-day collision zone may be interrogated with a 3D WA seismic survey (C1-3D) to reveal the likely location of the next seamount in the chain beneath the trench-slopes of the overriding plate.

of the Fonualei Discontinuity to ascertain whether there is a significant change in crustal structure or composition across the boundary (e.g. W3 and W4 on Figure 7.1). Despite these profiles being ideally informed by existing models of overriding plate crustal structure, the models would rely heavily on assumptions of structural continuity and invariant composition, so the most robust means of assessing these structural variations is to acquire new geophysical and drill data across the forearc, ideally informed by the results from any preliminary gravity modelling.

Figure 7.1 indicates a number of WA profiles (W1-W5) that are evenly spaced to constrain forearc structure and variability over the widest possible region. Coinciding with these proposed profiles are four additional drill sites (D1-D4), that would supplement the existing samples along the margin and reveal the true ages of forearc basement, study changes in forearc subsidence and stresses, and provide geochemical analyses of crustal composition. Together, these additional datasets would enable further research into the Fonualei Discontinuity by potentially revealing major changes in crustal structure across the boundary.

7.2.3 LRSC subduction

While the proposed additional 2D WA seismic profiles would improve the model of long-term structural deformation and recovery caused by LRSC subduction, questions remain surrounding how the LRSC subducts and where the last seamount to subduct is located beneath the overriding plate. Following the acquisition of new 3D WA seismic grids over the northwestern end of the LRSC to determine the extent and variability of the intrusive core within the seamount edifices, a similar grid could

be acquired over the trench slopes on the overriding plate adjacent to the LRSC-trench intersection (e.g. C1-3D; Figure 7.1). Such a grid would seek to determine the crustal and upper mantle velocities of the subducting and overriding plates to address where the next seamount in the chain is located, its structure (i.e. whether it is whole or heavily deformed), and the extent of subducting plate faulting and hydration as a proxy for flexural rigidity. This experiment would involve the greatest risk in that it may not be able resolve the target features, as the highly fractured and faulted nature of the lower-trench slopes disperse and attenuate seismic energy (e.g. Section 5.3.3). The deployment of OBSs in a grid over this region would also enable the acquisition of a microseismicity dataset, which may reveal small active faults on the overriding plate around subducting seamounts (as predicted in Wang & Bilek, 2011; Bassett & Watts, 2015a) and may show that stress release in this area is continuous, accounting for the lack of observed large magnitude earthquakes.

7.3 Summary

This study has provided new insights into the structure and evolution of the Tonga-Kermadec forearc, revealing tectonic discontinuities and broad along-arc variability inherited over the ∼51 Myr lifespan of the subduction system. These structural variations were used to inform a regional framework of along-arc inherited structure that formed the basis of a new interpretation of LRSC subduction history along the Tonga-Kermadec margin. The seamounts were found to highly deform the lower and mid-trench slope of the overriding plate, locally increasing tectonic erosion and, following their subduction, causing the forearc to collapse under gravity to re-establish trench-slope stability.

Bibliography

Arredondo, K. M. & Billen, M. I., 2012. Rapid weakening of subducting plates from trench-parallel estimates of flexural rigidity, *Physics of the Earth and Planetary Interiors*, **196-197**, 1–13.

Aubouin, J., 1989. Some aspects of the tectonics of subduction zones, *Tectonophysics*, **160**(1-4), 1–21.

Ballance, P. F., Scholl, D. W., Vallier, T. L., Stevenson, A. J., Ryan, H., & Herzer, R. H., 1989. Subduction of a Late Cretaceous Seamount of the Louisville Ridge at the Tonga Trench: A model of normal and accelerated tectonic erosion, *Tectonics*, **8**(5), 953–962.

Ballance, P. F., Ablaev, A. G., Pushchin, I. K., Pletnec, S. P., Birylina, M. G., Itaya, T., Follas, H. A., & Gibson, G. W., 1999. Morphology and history of the Kermadec-trench-arc-backarc basin-remnant arc system at 30 to 32°S: geophysical profile, microfossil and K-Ar data, *Marine Geology*, **159**, 35–62.

Barry, K., Cavers, D., & Kneale, C., 1975. Recommended standards for digital tape formats, *Geophysics*, **40**(2), 344–352.

Bassett, D., 2014. *The Relationship Between Structure and Seismogenic Behaviour in Subduction Zones*, Ph.D. thesis, University of Oxford.

Bassett, D. & Watts, A. B., 2015a. Gravity anomalies, crustal structure, and seismicity at subduction zones: 2. Interrelationships between fore-arc structure and seismogenic behavior, *Geochemistry, Geophysics, Geosystems*, **16**(5), 1541–1576.

Bassett, D. & Watts, A. B., 2015b. Gravity anomalies, crustal structure, and seismicity at subduction zones: 1. Seafloor roughness and subducting relief, *Geochemistry, Geophysics, Geosystems*, **16**(5), 1508–1540.

Bassett, D., Kopp, H., Sutherland, R., Henrys, S., Watts, A. B., Timm, C., Scherwath, M., Grevemeyer, I., & de Ronde, C. E. J., 2016. Crustal structure of the

Kermadec arc from MANGO seismic refraction profile, *Journal of Geophysical Research: Solid Earth*, **121**.

Bell, R., Sutherland, R., Barker, D. H. N., Henrys, S., Bannister, S., Wallace, L., & Beavan, J., 2010. Seismic reflection character of the Hikurangi subduction interface, New Zealand, in the region of repeated Gisborne slow slip events, *Geophysical Journal International*, **180**, 34–48.

Billen, M. I. & Gurnis, M., 2005. Constraints on subducting plate strength within the Kermadec trench, *Journal of Geophysical Research*, **110**(B5), 1–18.

Billen, M. I. & Stock, J., 2000. Morphology and origin of the Osbourn Trough, *Journal of Geophysical Research*, **105**(B6), 481–489.

Bloomer, S. H., Taylor, B., MacLeod, C. J., Stern, R. J., Fryer, P., Hawkins, J. W., & Johnson, L., 1995. Early arc volcanism and the ophiolite problem: A perspective from drilling in the western Pacific, in *Active Margins and Marginal Basins of the Western Pacific*, vol. 88, pp. 1–30, AGU, Washington, DC.

Bonnardot, M., Regnier, M., Christova, C., Ruellan, E., & Tric, E., 2006. Stress Field in the Tonga Benioff Zone and Geodynamical Model for the First Stages of the Lau Basin Opening., *American Geophysical Union, Fall Meeting 2006, abstract #T51C-1543*.

Bonnardot, M. A., Régnier, M., Ruellan, E., Christova, C., & Tric, E., 2007. Seismicity and state of stress within the overriding plate of the Tonga-Kermadec subduction zone, *Tectonics*, **26**(5).

Brodie, J. W. & Hatherton, T., 1958. The Morphology of Kermadec and Hikurangi trenches, *Deep-Sea Research*, **5**, 18–28.

Burns, R. & Andrews, J., 1973. Initial Reports of the Deep Sea Drilling Project, 21, Tech. rep., DSDP.

Calvert, A. J., Klemperer, S. L., Takahashi, N., & Kerr, B. C., 2008. Three-dimensional crustal structure of the Mariana island arc from seismic tomography, *Journal of Geophysical Research*, **113**, 1–24.

Cande, S., 2003. Raw ship-based Multibeam Sonar Data acquired during R/V Nathaniel B. Palmer expedition NBP0304C. Interdisciplinary Earth Data Alliance., Tech. rep.

Carlson, R. L. & Herrick, C. N., 1990. Densities and porosities in the oceanic crust and their variations with depth and age, *Journal of Geophysical Research*, **95**(B6), 9153.

Carlson, R. L. & Raskin, G. S., 1984. Density of the ocean crust, *Nature*, **311**(5986), 555–558.

Castillo, P. R., Lonsdale, P. F., Moran, C. L., & Hawkins, J. W., 2009. Geochemistry of mid-Cretaceous Pacific crust being subducted along the Tonga-Kermadec Trench: Implications for the generation of arc lavas, *Lithos*, **112**(1-2), 87–102.

Christensen, N. I. & Mooney, W. D., 1995. Seismic velocity structure and composition of the continental crust: A global view, *Journal of Geophysical Research*, **100**, 9761–9788.

Clift, P. D. & MacLeod, C. J., 1999. Slow rates of subduction erosion estimated from subsidence and tilting of the Tonga forearc, *Geology*, **27**(5), 411.

Clift, P. D. & Vannucchi, P., 2004. Controls on tectonic accretion versus erosion in subduction zones: Implications for the origin and recycling of the continental crust, *Reviews of Geophysics*, **42**(2).

Clift, P. D., Bednarz, U., Boe, R., Rothwell, R. G., Hodkinson, R. A., Ledbetter, J. K. J. K., Pratt, C. E., Soakai, S., Bøe, R., Rothwell, R. G., Hodkinson, R. A., Ledbetter, J. K. J. K., Pratt, C. E., & Soakai, S., 1994. Sedimentation on the Tonga forearc related to arc rifting, subduction erosion, and ridge collision; a synthesis of results from sites 840 and 841, *Proceedings of the Ocean Drilling Program, scientific results, Lau Basin*, **135**, 843–855.

Clift, P. D., MacLeod, C. J., Tappin, D. R., Wright, D. J., & Bloomer, S. H., 1998. Tectonic controls on sedimentation and diagenesis in the Tonga Trench and forearc, southwest Pacific, *Geol. Soc. Am. Bull.*, **110**(4), 483–496.

Cloos, M., 1992. Thrust-type subduction-zone earthquakes and seamount asperities: a physical model for seismic rupture, *Geology*, **20**(7), 601–604.

Cloos, M. & Shreve, R. L., 1996. Shear-zone thickness and the seismicity of Chilean- and Marianas-type subduction zones, *Geology*, **24**(2), 107.

Collot, J.-Y. & Davy, B., 1998a. Correction to "Forearc structures and tectonic regimes at the oblique subduction zone between the Hikurangi Plateau and the southern Kermadec margin" by Jean-Yves Collot and Bryan Davy, *Journal of Geophysical Research*, **103**(B4), 7107.

Collot, J.-Y. & Davy, B., 1998b. Forearc structures and tectonic regimes at the oblique subduction zone between the Hikurangi Plateau and the southern Kermadec margin, *Journal of Geophysical Research*, **103**(B1), 623.

Conder, J. A. & Wiens, D. A., 2011. Shallow seismicity and tectonics of the central and northern Lau Basin, *Earth and Planetary Science Letters*, **304**(3-4), 538–546.

Contreras-reyes, E., Grevemeyer, I., Flueh, E. R., & Reichert, C., 2008. Upper lithospheric structure of the subduction zone offshore of southern Arauco peninsula, Chile, at ∼38°S, *Journal of Geophysical Research*, **113**, 1–19.

Contreras-Reyes, E., Grevemeyer, I., Watts, A. B., Planert, L., Flueh, E. R., & Peirce, C., 2010. Crustal intrusion beneath the Louisville hotspot track, *Earth and Planetary Science Letters*, **289**(3-4), 323–333.

Contreras-Reyes, E., Grevemeyer, I., Watts, A. B., Flueh, E. R., Peirce, C., Moeller, S., & Papenberg, C., 2011. Deep seismic structure of the Tonga subduction zone: Implications for mantle hydration, tectonic erosion, and arc magmatism, *Journal of Geophysical Research*, **116**(B10).

Crawford, W. C., Hildebrand, J. A., Dorman, L. M., Webb, S. C., & Wiens, D. A., 2003. Tonga Ridge and Lau Basin crustal structure from seismic refraction data, *Journal of Geophysical Research*, **108**(B4), 2195.

DeMets, C., Gordon, R. G., & Argus, D. F., 2010. Geologically current plate motions, *Geophysical Journal International*, **181**(1), 1–80.

Dickinson, W. R. & Seely, D. R., 1979. Structure and stratigraphy of forearc regions, *The American Association of Petroleum Geologists Bulletin*, **63**(1), 2–31.

Dix, C. H., 1955. Seismic velocities from surface measurements, *Geophysics*, **20**(1), 68–86.

Dominguez, S., Lallemand, S., Malavieille, J., & Schnürle, P., 1998a. Oblique subduction of the Gagua Ridge beneath the Ryukyu accretionary wedge system: Insights from marine observations and sandbox experiments, *Marine Geophysical Researches*, **20**(5), 383–402.

Dominguez, S., Lallemand, S. E., Malavieille, J., & Von Huene, R., 1998b. Upper plate deformation associated with seamount subduction, *Tectonophysics*, **293**(3-4), 207–224.

Dominguez, S., Malavieille, J., & Lallemand, S. E., 2000. Deformation of accretionary wedges in response to seamount subduction: Insights from sandbox experiments, *Tectonics*, **19**(1), 182–196.

Downey, N. J., Stock, J. M., Clayton, R. W., & Cande, S. C., 2007. History of the Cretaceous Osbourn spreading center, *J. Geophys. Res.*, **112**(B04102), 1–18.

Fisher, R. L., 1974. Pacific-Type Continental Margins, in *The Geology of Continental Margins*, pp. 25–41, Springer Berlin Heidelberg, Berlin, Heidelberg.

Flueh, E. R. & Kopp, H., 2007. FS Sonne SO192-1 Cruise Report: Marine Geoscientific Investigations on the Input and Output of the Kermadec Subduction Zone (MANGO), Tech. Rep. 11.

Fryer, P., 2012. Serpentinite Mud Volcanism: Observations, Processes, and Implications, *Annual Review of Marine Science*, **4**(1), 345–373.

Funnell, M. J., 2013. *Stratigraphy, structure, and deformation of the Kermadec subduction system from multichannel seismic reflection data*, Masters report, University of Durham.

Funnell, M. J., Peirce, C., Stratford, W. R., Paulatto, M., Watts, A. B., & Grevemeyer, I., 2014. Structure and deformation of the Kermadec forearc in response to subduction of the Pacific oceanic plate, *Geophysical Journal International*, **199**, 1286–1302.

Funnell, M. J., Peirce, C., & Robinson, A. H., 2017. Structural variability of the Tonga-Kermadec forearc characterised using robustly constrained geophysical data, *Geophysical Journal International*, pp. 1681–1702.

Gillies, P. N. & Davey, F., 1986. Seismic reflection and refraction studies of the Raukumara forearc basin, New Zealand, *New Zealand Journal of Geology and Geophysics*, **29**(4), 391–403.

Grevemeyer, I. & Flueh, E. R., 2008. FS Sonne SO195 Cruise Report: Tonga Thurst earthquake Asperity at Louisville Ridge (TOTAL), Tech. rep.

Grevemeyer, I., Kaul, N., Diaz-Naveas, J. L., Villinger, H. W., Ranero, C. R., & Reichert, C., 2005. Heat flow and bending-related faulting at subduction trenches: Case studies offshore of Nicaragua and Central Chile, *Earth and Planetary Science Letters*, **30**(23), 2197.

Grindlay, N. R., Mann, P., Dolan, J. F., & van Gestel, J.-P., 2005. Neotectonics and subsidence of the northern Puerto Rico-Virgin Islands margin in response to the oblique subduction of high-standing ridges, *Geological Society of America Special Paper*, **385**, 31–60.

Grow, J. A., 1973. Crustal and upper mantle structure of the central Aleutian arc, *Bulletin of the Geological Society of America*, **84**(7), 2169–2192.

Habermann, R. E., McCann, W. R., & Perin, B., 1986. Spatial seismicity variations along convergent plate boundaries, *Geophysical Journal International*, **85**(1), 43–68.

Hawkins, J. W., Lonsdale, P. F., & Batiza, R., 1987. Petrological evolution of the Louisville seamount chain, *Geophysical Monograph Series: Seamounts, Islands, and Atolls*, **43**, 235–254.

Hayes, G. P., Wald, D. J., & Johnson, R. L., 2012. Slab1.0: A three-dimensional model of global subduction zone geometries, *Journal of Geophysical Research*, **117**(B1), B01302.

Herzer, R. H. & Exon, N. F., 1985. Structure and Basin Analysis of the Southern Tonga Forearc, in *Geology and offshore resource of Pacific island arcs Tonga region, Circum-Pacific Council for Energy and Mineral Resources*, vol. 2, pp. 55–73, eds Scholl, D. W. & Vallier, T. L., Circum Pacific Council Publications, Houston, Texas.

Herzer, R. H., Barker, D. H. N., Roest, W. R., & Mortimer, N., 2011. Oligocene-Miocene spreading history of the northern South Fiji Basin and implications for the evolution of the New Zealand plate boundary, *Geochemistry, Geophysics, Geosystems*, **12**(2).

Hess, H. H., 1964. Seismic Anisotropy of the Uppermost Mantle under Oceans, *Nature*, **203**(4945), 629–631.

Hillier, J. K., 2007. Pacific seamount volcanism in space and time, *Geophysical Journal International*, **168**(2), 877–889.

Hillier, J. K. & Watts, A. B., 2007. Global distribution of seamounts from ship-track bathymetry data, *Geophysical Research Letters*, **34**(13), 1–5.

Hirano, N., Koppers, A. A. P., Takahashi, A., Fujiwara, T., & Nakanishi, M., 2008. Seamounts, knolls and petit-spot monogenetic volcanoes on the subducting Pacific Plate, *Basin Research*, **20**(4), 543–553.

Holbrook, W. S., Lizarralde, D., Bangs, N. L., & Diebold, J., 1999. Structure and composition of the Aleutian island arc and implications for continental crustal growth, *Geology*, **27**(1), 31–34.

Huhnerbach, V., Masson, D., Bohrmann, G., Bull, J. M., & Weinrebe, W., 2005. Deformation and submarine landsliding caused by seamount subduction beneath the Costa Rican margin - new insights from high-resolution sidescan sonar data, pp. 195–205.

Hwang, G. & Kim, S.-S., 2016. Flexure and gravity anomalies of the oceanic lithosphere beneath the Louisville seamount, *Tectonophysics*, **686**, 19–26.

Ide, S., 2013. The proportionality between relative plate velocity and seismicity in subduction zones, *Nature Geoscience*, **6**(9).

IOC, IHO, & BODC, 2003. "Centernary Edition of the General Bathymetric Chart of the Oceans Digital Atlas", Published on CDROM on behalf of the IOC and IHO as part of the GEBCO; BODC, Liverpool.

Isacks, B., Sykes, L. R., & Oliver, J., 1969. Focal Mechanisms of Deep and Shallow Earthquakes in the Tonga-Kermadec Region and the Tectonics of Island Arcs, *Geological Society of America Bulletin*, **80**(8), 1443.

Ishizuka, O., Tani, K., Reagan, M. K., Kanayama, K., Umino, S., Harigane, Y., Sakamoto, I., Miyajima, Y., Yuasa, M., & Dunkley, D. J., 2011. The timescales of subduction initiation and subsequent evolution of an oceanic island arc, *Earth and Planetary Science Letters*, **306**(3-4), 229–240.

Ivandic, M., Grevemeyer, I., Bialas, J., & Petersen, C. J., 2010. Serpentinization in the trench-outer rise region offshore of Nicaragua: Constraints from seismic refraction and wide-angle data, *Geophysical Journal International*, **180**(3), 1253–1264.

Kaneda, K., Kodaira, S., Nishizawa, A., Morishita, T., & Takahashi, N., 2010. Structural evolution of preexisting oceanic crust through intraplate igneous activities in the Marcus-Wake seamount chain, *Geochemistry, Geophysics, Geosystems*, **11**(10), 1–29.

Karig, D. E., 1970. Ridges and basins of the Tonga-Kermadec Island Arc System, *Journal of Geophysical Research*, **75**(2), 239–254.

Kelleher, J. & McCann, W. R., 1976. Buoyant Zones, Great Earthquakes, and Unstable Boundaries of Subduction, *Journal of Geophysical Research*, **81**(26), 4885–4896.

Kodaira, S., Noguchi, N., Takahashi, N., Ishizuka, O., & Kaneda, Y., 2010. Evolution from fore-arc oceanic crust to island arc crust: A seismic study along the Izu-Bonin fore arc, *Journal of Geophysical Research: Solid Earth*, **115**(9), 1–20.

Kodaira, S., Fujie, G., Yamashita, M., Sato, T., Takahashi, T., & Takahashi, N., 2014. Seismological evidence of mantle flow driving plate motions at a palaeo-spreading centre, *Nature Geoscience*, **7**(5), 371–375.

Koppers, A. A., Steinberger, B., & Duncan, R. A., 2004. Implications of a nonlinear 40Ar/39Ar age progression along the Louisville seamount trail for models of fixed and moving hot spots, *Geochemistry, Geophysics, Geosystems*, **5**(6), 1–22.

Koppers, A. A. P., Gowen, M. D., Colwell, L. E., Gee, J. S., Lonsdale, P. F., Mahoney, J. J., & Duncan, R. A., 2011. New 40 Ar/ 39 Ar age progression for the Louisville hot spot trail and implications for inter-hot spot motion, *Geochemistry, Geophysics, Geosystems*, **12**(12).

Koppers, A. A. P., Yamazaki, T., Geldmacher, J., Gee, J. S., Pressling, N., & Hoshi, H., 2012. Limited latitudinal mantle plume motion for the Louisville hotspot, *Nature Geoscience*, **5**, 911–918.

Korenaga, J., 2017. On the extent of mantle hydration caused by plate bending, *Earth and Planetary Science Letters*, **457**, 1–9.

Korenaga, J., Holbrook, W. S., Kent, G. M., Kelemen, P. B., Detrick, R. S., Larsen, H.-C., Hopper, J. R., & Dahl-Jensen, T., 2000. Crustal structure of the southeast Greenland margin from joint refraction and reflection seismic tomography, *Journal of Geophysical Research*, **105**(B9), 21591.

Korenaga, J., Holbrook, W. S., Detrick, R. S., & Kelemen, P. B., 2001. Gravity anomalies and crustal structure at the southeast Greenland margin, *Journal of Geophysical Research*, **106**(B5), 8853.

Lallemand, S. E., Malavieille, J., & Calassou, S., 1992. Effects of oceanic ridge subduction on accretionary wedges: experimental modeling and marine observations, *Tectonics*, **11**(6), 1301–1313.

Lallemand, S. E., Schnürle, P., & Malavieille, J., 1994. Coulomb theory applied to accretionary and nonaccretionary wedges: Possible causes for tectonic erosion and/or frontal accretion, *Journal of Geophysical Research*, **99**(B6), 12033–12055.

Langmuir, C., 2004. Vent Discovery and Petrological Sampling of the Lau Back-Arc Basin: KM0417 Cruise Report, Tech. rep.

Larter, R. D., Vanneste, L. E., Morris, P., & Smythe, D. K., 2003. Structure and tectonic evolution of the South Sandwich arc, *Geological Society, London, Special Publications*, **219**(219), 255–284.

Lonsdale, P. F., 1985. Informal report and index of navigation, depth, magnetic, and subbottom profiler data: Marathon Expedition Leg 6.

Lonsdale, P. F., 1986. A multibeam reconnaissance of the Tonga Trench axis and its intersection with the Louisville guyot chain, *Marine Geophysical Researches*, **8**(4), 295–327.

Lonsdale, P. F., 1988. Geography and history of the Louisville Hotspot Chain in the southwest Pacific, *Journal of Geophysical Research*, **93**(B4), 3078–3104.

Ludwig, W., Nafe, J. E., & Drake, C. L., 1970. Seismic refraction, in *The Sea*, pp. 53–84, ed. Maxwell, A., Wiley Interscience, New York, vol. 4 edn.

MacLeod, C. J., 1994. Structure of the outer Tonga Trench forearc at site 841, *Proceedings of the Ocean Drilling Program, Scientific Results*, **135**, 313–329.

MacLeod, C. J. & Lothian, A. M., 1994. Comparison of GLORIA sidescan sonar and core-derived structural data from site 841 (Tonga Trench), *Proceedings of the Ocean Drilling Program, Scientific Results*, **135**, 373–382.

Malahoff, A., Feden, R. H., & Fleming, H. S., 1982. Magnetic anomalies and tectonic fabric of marginal basins north of New Zealand, *Journal of Geophysical Research*, **87**(B5), 4109.

Martinod, J., Funiciello, F., Faccenna, C., Labanieh, S., & Regard, V., 2005. Dynamical effects of subducting ridges: insights from 3-D laboratory models, *Geophys. J. Int.*, **163**, 1137–1150.

Martinod, J., Guillaume, B., Espurt, N., Faccenna, C., Funiciello, F., & Regard, V., 2013. Effect of aseismic ridge subduction on slab geometry and overriding plate deformation: Insights from analogue modeling, *Tectonophysics*, **588**, 39–55.

Meffre, S., Falloon, T. J., Crawford, T. J., Duncan, R. A., Bloomer, S. H., & Wright, D. J., 2012. Basalts erupted along the Tongan fore arc during subduction initiation: Evidence from geochronology of dredged rocks from the Tonga fore arc and trench, *Geochemistry, Geophysics, Geosystems*, **13**(12), 1–17.

Michibayashi, K., Shinkai, Y., Tani, K., Uehera, S., Harigane, Y., Ishii, T., & Bloomer, S. H., 2016. Tonga trench gabbros and peridotites: A suite of temporal and spatial forearc materials, *Eos*, **91**, 1–3.

Minshull, T. A., White, R. S., Mutter, J. C., Buhl, P., Detrick, R. S., Williams, C. A., & Morris, E., 1991. Crustal Structure at the Blake Spur Fracture-Zone from Expanding Spread Profiles, *Journal of Geophysical Research*, **96**(B6), 9955–9984.

Minshull, T. A., Sinha, M. C., & Peirce, C., 2005. Multi-disciplinary, sub-seabed geophysical imaging - a new pool of 28 seafloor instruments in use by the United Kingdom Ocean Bottom Instrument Consortium, *Sea Technology*, **46**, 27–31.

Moscoso, E. & Grevemeyer, I., 2015. Bending-related faulting of the incoming oceanic plate and its effect on lithospheric hydration and seismicity: A passive and active seismological study offshore Maule, Chile, *Journal of Geodynamics*, **90**, 58–70.

Moscoso, E., Grevemeyer, I., Contreras-Reyes, E., Flueh, E. R., Dzierma, Y., Rabbel, W., & Thorwart, M., 2011. Revealing the deep structure and rupture plane of the 2010 Maule, Chile earthquake (Mw=8.8) using wide angle seismic data, *Earth and Planetary Science Letters*, **307**(1-2), 147–155.

Nafe, J. E. & Drake, C. L., 1957. Variation with Depth in Shallow and Deep Water Marine Sediments of Porosity, and the Velocities of Compressional and Shear Waves, *Geophysics*, **22**(3), 523–552.

Nakajima, N. & Arima, M., 1998. Melting experiments on hydrous low-K tholeiite: Implications for the genesis of tonalitic crust in the Izu-Bonin-Mariana arc, *The island arc*, **7**, 359–373.

Naliboff, J. B., Billen, M. I., Gerya, T., & Saunders, J., 2013. Dynamics of outer-rise faulting in oceanic-continental subduction systems, *Geochemistry, Geophysics, Geosystems*, **14**(7), 2310–2327.

Nishikawa, T. & Ide, S., 2014. Earthquake size distribution in subduction zones linked to slab buoyancy, *Nature Geoscience*, **7**, 904–908.

Oakley, A. J., Taylor, B., Fryer, P., Moore, G. F., Goodliffe, A. M., & Morgan, J. K., 2007. Emplacement, growth, and gravitational deformation of serpentinite seamounts on the Mariana forearc, *Geophysical Journal International*, **170**(2), 615–634.

Parson, L., 1992. Evolution of Backarc Basins: ODP Leg 135, Lau Basin, *Eos*, **73**(22), 241–248.

Peirce, C. & Watts, A. B., 2011. R/V Sonne SO215 Cruise Report. The Louisville Ridge - Tonga Trench collision: Implications for subduction zone dynamics, Tech. Rep. June, University of Durham.

Peirce, C., Sinha, M., & Constable, S., 1996. R/V Maurice Ewing 9512 Cruise Report: Controlled source electromagnetic and seismic investigation of the Valu Fa Ridge, Lau Basin, SW Pacific, Tech. rep.

Pelletier, B. & Dupont, J., 1990. Erosion, accretion, back-arc extension and slab length along the Kermadec subduction zone, Southwest Pacific, *C. R. Acad. Sci. Paris*, **310**(2), 1657–1664.

Raitt, R., Fisher, R., & Mason, R., 1955. Tonga Trench, *Geological Society of America*, **62**, 237–254.

Ranero, C. R., Morgan, J. P., McIntosh, K., & Reichert, C., 2003. Bending-related faulting and mantle serpentinization at the Middle America trench, *Nature*, **425**(6956), 367–73.

Ranero, C. R., Villaseñor, A., Morgan, J. P., & Weinrebe, W., 2005. Relationship between bend-faulting at trenches and intermediate-depth seismicity, *Geochemistry, Geophysics, Geosystems*, **6**(12).

Rawlinson, N. & Spakman, W., 2016. On the use of sensitivity tests in seismic tomography, *Geophysical Journal International*, **205**(2), 1221–1243.

Reagan, M. K., McClelland, W. C., Girard, G., Goff, K. R., Peate, D. W., Ohara, Y., & Stern, R. J., 2013. The geology of the southern Mariana fore-arc crust: Implications for the scale of Eocene volcanism in the western Pacific, *Earth and Planetary Science Letters*, **380**, 41–51.

Richards, M., Contreras-Reyes, E., Lithgow-bertelloni, C., Ghiorso, M., & Stixrude, L., 2013. Petrological interpretation of deep crustal intrusive bodies beneath oceanic hotspot provinces, *Geochemistry, Geophysics, Geosystems*, **14**(3), 604–619.

Robinson, A., 2017. *Seamount structure and subduction at the Louisville Ridge-Tonga-Kermadec collision*, Ph.D. thesis, University of Durham.

Rosenbaum, G. & Mo, W., 2011. Tectonic and magmatic responses to the subduction of high bathymetric relief, *Gondwana Research*, **19**(3), 571–582.

Ruellan, E., Delteil, J., Wright, I. C., & Matsumoto, T., 2003. From rifting to active spreading in the Lau Basin - Havre Trough backarc system (SW Pacific): Locking/unlocking induced by seamount chain subduction, *Geochemistry, Geophysics, Geosystems*, **4**(5).

Sallarès, V. & Ranero, C. R., 2005. Structure and tectonics of the erosional convergent margin off Antofagasta, north Chile (23°30'S), *Journal of Geophysical Research B: Solid Earth*, **110**(6), 1–19.

Sandwell, D. T., Muller, R. D., Smith, W. H. F., Garcia, E. S., & Francis, R., 2014. New global marine gravity model from CryoSat-2 and Jason-1 reveals buried tectonic structure, *Science*, **65**(6205), 1–4.

Schellart, W. P. & Rawlinson, N., 2013. Global correlations between maximum magnitudes of subduction zone interface thrust earthquakes and physical parameters of subduction zones, *Physics of the Earth and Planetary Interiors*, **225**, 41–67.

Scholz, C. H. & Campos, J., 1995. On the mechanism of seismic decoupling and back arc spreading at subduction zones, *Journal of Geophysical Research*, **100**(B11), 22103.

Scholz, C. H. & Small, C., 1997. The effect of seamount subduction on seismic coupling, *Geology*, **25**(6), 487–490.

Schwarz-Schampera, U., 2007. SONNE 192-2 Cruise report: Marine Geoscientific Research on Input and Output in the Tonga-Kermadec Subduction Zone Marine (MANGO), Tech. Rep. May.

Shimamura, H., Asada, T., Suyehiro, K., Yamada, T., & Inatani, H., 1983. Long-shot experiments to study velocity anisotropy in the oceanic lithosphere of the northwestern Pacific, *Physics of the Earth and Planetary Interiors*, **31**, 348–362.

Sinha, M. C. & Louden, K. E., 1983. The Oceanographer fracture zone - I. Crustal structure from seismic refraction studies, *Geophysical Journal of the Royal Astronomical Society*, **75**, 713–736.

Spudich, P. & Orcutt, J., 1980. A new look at the seismic velocity structure of oceanic crust, *Reviews of Geophysics and Space Physics*, **18**(3), 627–645.

Staudigel, H. & Clague, D. A., 2009. The Geological History of Deep-Sea Volcanoes, *Oceanography*, **23**(1), 58–71.

Stern, R. J., Reagan, M., Ishizuka, O., Ohara, Y., & Whattam, S., 2012. To understand subduction initiation, study forearc crust: To understand forearc crust, study ophiolites, *Lithosphere*, **4**, 469–483.

Stock, J. M. & Clayton, R., 2005. Cruise Activity Report, NBP0207, Tech. rep.

Stockwell, J. W., 1999. The CWP/SU: Seismic Un(*)x package, *Computers and Geosciences*, **25**(4), 415–419.

Stockwell, J. W., 2011. Complete Listing of CWP Free Program Self-Documentations, *CWP, Colorado School of Mines*, p. 774.

Stoffers, P., 2003. Sonne 167 Cruise Report: Louisville Ridge: Dynamics and Magmatism of a Mantle Plume and its influence on the Tonga-Kermadec subduction system, Tech. Rep. 20.

Stoffers, P. & Wright, I. C., 1999. Sonne 135 Cruise Report: Havre Trough - Taupo Volcanic Zone: Tectonic, magmatic and hydrothermal processes, Tech. rep.

Stratford, W. R., Peirce, C., Paulatto, M., Funnell, M. J. M., Watts, A. B., Grevemeyer, I., & Bassett, D., 2015. Seismic velocity structure and deformation due to the collision of the Louisville Ridge with the Tonga-Kermadec Trench, *Geophysical Journal International*, **200**(3), 1503–1522.

Suyehiro, K., Takahashi, N., Ariie, Y., Yokoi, Y., Hino, R., Shinohara, M., Kanazawa, T., Hirata, N., Tokuyama, H., & Taira, A., 1996. Continental Crust, Crustal Underplating, and Low-Q Upper Mantle Beneath an Oceanic Island Arc, *Science*, **272**, 390–392.

Taira, K., Yanagimoto, D., & Kitagawa, S., 2005. Deep CTD Casts in the Challenger Deep, Mariana Trench, *Journal of Oceanography*, **61**(3), 447–454.

Takahashi, N., Kodaira, S., Klemperer, S. L., Tatsumi, Y., Kaneda, Y., & Suyehiro, K., 2007. Crustal structure and evolution of the Mariana intra-oceanic island arc, *Geology*, **35**(3), 203–206.

Takahashi, N., Kodaira, S., Tatsumi, Y., Kaneda, Y., & Suyehiro, K., 2008. Structure and growth of the Izu-Bonin-Mariana arc crust: 1. Seismic constraint on crust and mantle structure of the Mariana arc-back-arc system, *Journal of Geophysical Research*, **113**, 1–18.

Takahashi, N., Kodaira, S., Tatsumi, Y., Yamashita, M., Sato, T., Kaiho, Y., Miura, S., No, T., Takizawa, K., & Kaneda, Y., 2009. Structural variations of arc crusts and rifted margins in the southern Izu-Ogasawara arc-back arc system, *Geochemistry, Geophysics, Geosystems*, **10**(9).

Talwani, M., 1961. Gravity Anomalies and Crustal Section across the Tonga Trench, *Journal of Geophysical Research*, **66**(4), 1265–1278.

Talwani, M., Worzel, J. L., & Landisman, M., 1959. Rapid gravity computations for two-dimensional bodies with application to the Mendocino submarine fracture zone, *Journal of Geophysical Research*, **64**(1), 49–59.

Taylor, B., Martinez, F., & Goodliffe, A., 1996. Sea-floor spreading in the Lau back-arc basin, *Earth and Planetary Science Letters*, **144**, 35–40.

Timm, C., Bassett, D., Graham, I. J., Leybourne, M. I., de Ronde, C. E. J., Woodhead, J., Layton-Matthews, D., & Watts, A. B., 2013. Louisville seamount subduction and its implication on mantle flow beneath the central Tonga-Kermadec arc, *Nature communications*, **4**, 1720.

Uyeda, S., 1982. Subduction zones: An introduction to comparative subductology, *Tectonophysics*, **81**(3-4), 133–159.

Vanderkluysen, L., Mahoney, J. J., Koppers, A. A. P., Beier, C., Regelous, M., Gee, J. S., & Lonsdale, P. F., 2014. Louisville Seamount Chain: Petrogenetic processes and geochemical evolution of the mantle source, *Geochemistry, Geophysics, Geosystems*, **15**.

Vannucchi, P., Fisher, D. M., Bier, S., & Gardner, T. W., 2006. From seamount accretion to tectonic erosion: Formation of Osa Melange and the effects of Cocos Ridge subduction in southern Costa Rica, *Tectonics*, **25**(2).

Venzke, E., 2013. Global Volcanism Program, Volcanoes of the World, v. 4.6.0., Tech. rep., Smithsonian Institution.

Vogt, P., 1973. Subduction and aseismic ridges, *Nature*, **241**, 189–191.

von Huene, R. & Ranero, C. R., 2003. Subduction erosion and basal friction along the sediment-starved convergent margin off Antofagasta, Chile, *Journal of Geophysical Research*, **108**(B2), 2079.

von Huene, R. & Scholl, D. W., 1991. Observations at convergent margins concerning sediment subduction, subduction erosion, and the growth of continental crust, *Reviews of Geophysics*, **29**(3), 279–316.

von Huene, R., Ranero, C. R., & Vannucchi, P., 2004. Generic model of subduction erosion, *Geology*, **32**(10), 913–916.

Wagner, H. J., 2007. FS Sonne SO194 Cruise Report: Bioluminescence and Biological Rhythms in the Mesopelagic Fauna, Tech. rep.

Walther, C. H. E., 2003. The crustal structure of the Cocos ridge off Costa Rica, *Journal of Geophysical Research*, **108**, 1–21.

Wang, K. & Bilek, S. L., 2011. Do subducting seamounts generate or stop large earthquakes?, *Geology*, **39**(9), 819–822.

Wang, K. & Bilek, S. L., 2014. Fault creep caused by subduction of rough seafloor relief, *Tectonophysics*, **610**, 1–24.

Watts, A. B., 1978. An analysis of isostasy in the world's oceans 1. Hawaiian-Emperor Seamount Chain, *Journal of Geophysical Research*, **83**(B12), 5989–6004.

Watts, A. B. & Talwani, M., 1974. Gravity Anomalies Seaward of Deep-Sea Trenches and their Tectonic Implications, *Geophys. J. R. astr. Soc.*, (2029), 57–90.

Watts, A. B., Weissel, J., Duncan, R. A., & Larson, R., 1988. Origin of the Louisville Ridge and its relationship to the Eltanin fracture zone system, *Journal of Geophysical Research*, **93**(B4), 3051–3077.

Watts, A. B., Peirce, C., Grevemeyer, I., Paulatto, M., Stratford, W. R., Bassett, D., Hunter, J. A., Kalnins, L. M., & de Ronde, C. E. J., 2012. Rapid rates of growth and collapse of Monowai submarine volcano in the Kermadec Arc, *Nature Geoscience*, **5**, 510–515.

Weatherall, P., Marks, K. M., Jakobsson, M., Schmitt, T., Tani, S., Arndt, J. E., Rovere, M., Chayes, D., Ferrini, V., & Wigley, R., 2015. A new digital bathymetric model of the world's oceans, *Earth and Space Science*, **2**(8), 331–345.

Wessel, P. & Smith, W. H. F., 1991. Free software helps map and display data, *EOS Trans. AGU*, **72**(41), 441–441.

Wessel, P. & Smith, W. H. F., 1995. New version of the Generic Mapping Tool released, *EOS Trans. AGU*, p. 329.

Wessel, P. & Smith, W. H. F., 1998. New, improved version of Generic Mapping Tools released, *EOS Trans. AGU*, **79**(47), 579.

White, R. S., Mckenzie, D., & O'Nions, R. K., 1992. Oceanic crustal thickness from seismic measurements and rare earth element inversions, *Journal of Geophysical Research*, **97**(B13), 683–715.

Wilson, J. T. & Burke, K., 1972. Two types of mountain building, *Nature*, **239**(5373), 448–449.

Worthington, T. J., Hekinian, R., Stoffers, P., Kuhn, T., & Hauff, F., 2006. Osbourn Trough: Structure, geochemistry and implications of a mid-Cretaceous paleospreading ridge in the South Pacific, *Earth and Planetary Science Letters*, **245**(3-4), 685–701.

Wright, D. J., Bloomer, S. H., MacLeod, C. J., Taylor, B., & Goodlife, A. M., 2000. Bathymetry of the Tonga Trench and Forearc: a map series, *Marine Geophysical Researches*, **21**(5), 489–511.

Zellmer, K. E. & Taylor, B., 2001. A three-plate kinematic model for Lau Basin opening, *Geochemistry, Geophysics, Geosystems*, **2**(5).

Zelt, C. A., 1998. Lateral velocity resolution from three-dimensional seismic refraction data, *Geophysical Journal International*, **135**(3), 1101–1112.

Zelt, C. A. & Barton, P. J., 1998. Three-dimensional seismic refraction tomography: A comparison of two methods applied to data from the Faeroe Basin, *Journal of Geophysical Research: Solid Earth*, **103**(B4), 7187–7210.

Zelt, C. A. & Smith, R. B., 1992. Seismic traveltime inversion for 2-D crustal velocity structure, *Geophysical Journal International*, **108**(1), 16–34.

Zelt, C. A., Sain, K., Naumenko, J. V., & Sawyer, D. S., 2003. Assessment of crustal velocity models using seismic refraction and reflection tomography, *Geophysical Journal International*, **153**(1), 609–626.

Zeumann, S. & Hampel, A., 2015. Deformation of erosive and accretive forearcs during subduction of migrating and non-migrating aseismic ridges: Results from 3-D finite element models and application to the Central American, Peruvian, and Ryukyu margins, *Tectonics*, **34**, 1769–1791.

Zeumann, S. & Hampel, A., 2016. Tectonophysics Three-dimensional finite-element models on the deformation of forearcs caused by aseismic ridge subduction: The role of ridge shape, friction coefficient of the plate interface and mechanical properties of the forearc, *Tectonophysics*, **684**, 76–91.

Appendices

Appendix A

Summary of cruises with publicly available swath bathymetry data in the Tonga-Kermadec subduction zone study region. The swath bathymetry data from these cruises were combined, as described in Section 1.6, to create a detailed map of the small-scale variations in seabed structure along the subduction system.

Cruise identifier	Year	Research Vessel	Reference
MRTN06WT	1984	Thomas Washington	Lonsdale (1985)
PPTU04WT	1986	Thomas Washington	Unpublished
PPTU05WT	1986	Thomas Washington	Unpublished
RNDB15WT	1989	Thomas Washington	Unpublished
WEST06MV	1994	R/V Melville	Unpublished
WEST12MV	1995	R/V Melville	Unpublished
EW9512	1995	R/V Maurice Ewing	Peirce *et al.* (1996)
SO135	1998	R/V Sonne	Stoffers & Wright (1999)
NBP9806A	1998	Nathaniel B. Palmer	Unpublished
KIWI11RR	1998	R/V Roger Revelle	Unpublished
COOK14MV	2001	R/V Melville	Unpublished
DRFT09RR	2002	R/V Roger Revelle	Unpublished
SO167	2002	R/V Sonne	Stoffers (2003)
NBP0207	2002	Nathaniel B. Palmer	Stock & Clayton (2005)
NBP0304A	2003	Nathaniel B. Palmer	Unpublished
NBP0304C	2003	Nathaniel B. Palmer	Cande (2003)
KM0417	2004	R/V Kilo Moana	Langmuir (2004)
AMAT02RR	2006	R/V Roger Revelle	Unpublished
SO192-1	2007	R/V Sonne	Flueh & Kopp (2007)
SO192-2	2007	R/V Sonne	Schwarz-Schampera (2007)
SO194	2007	R/V Sonne	Wagner (2007)
SO195	2008	R/V Sonne	Grevemeyer & Flueh (2008)
BMRG08MV	2008	R/V Melville	Unpublished
TN236	2009	Thomas G. Thompson	Unpublished
SO215	2011	R/V Sonne	Peirce & Watts (2011)

Table A.1: List, in chronological order, of all cruises prior to 2017 in the study region around the Tonga-Kermadec subduction zone with swath bathymetry data available from the US National Geophysical Data Centre (https://maps.ngdc.noaa.gov/). Each of these datasets, which have variable coverage and quality, were incorporated into the regional swath bathymetry map (Figure 1.5).

Appendix B

Summary of OBS deployment and recovery locations along Profile B. LC-type OBSs were provided by the UK Ocean-Bottom Instrumentation Consortium (Minshull *et al.*, 2005), and KUM-type OBSs were provided by GEOMAR. OBS 09 does not have a relocated position because no usable data were recovered from that instrument (Peirce & Watts, 2011).

Table B.1: (Next page) Summary of OBS deployment and recovery locations along Profile B. Relocated OBS positions were determined as described in Section 3.3.1.

OBS	Type	Sample rate	Deployment		Recovery		Relocated		Offset	Depth
		(Hz)	Long.	Lat.	Long.	Lat.	Long.	Lat.	(m)	(m)
01	LC2000	250	-177.093	-27.442	-177.096	-27.447	-177.095	-27.443	56.935	2.17
02	LC4x4	250	-176.975	-27.401	-176.977	-27.405	-176.976	-27.402	69.500	2.04
03	LC2000	250	-176.858	-27.360	-176.858	-27.366	-176.860	-27.361	81.817	2.00
04	LC4x4	250	-176.740	-27.319	-176.747	-27.325	-176.742	-27.320	94.299	2.11
05	LC2000	250	-176.623	-27.278	-176.631	-27.287	-176.625	-27.280	106.714	2.50
06	LC4x4	250	-176.506	-27.237	-176.515	-27.246	-176.509	-27.239	119.029	3.45
07	LC2000	250	-176.388	-27.195	-176.396	-27.206	-176.392	-27.198	131.545	3.99
08	LC4x4	250	-176.272	-27.154	-176.280	-27.169	-176.274	-27.156	144.116	3.99
09	LC2000	250	-176.156	-27.113	-176.164	-27.123	-	-	-	-
10	LC4x4	250	-176.039	-27.071	-176.041	-27.075	-176.039	-27.073	169.149	4.62
11	KUM	200	-175.922	-27.029	-175.922	-27.029	-175.922	-27.031	181.625	5.56
12	KUM	200	-175.805	-26.988	-175.809	-26.985	-175.802	-26.988	194.374	6.19
13	KUM	200	-175.687	-26.946	-175.690	-26.945	-175.686	-26.947	206.816	6.98
14	KUM	200	-175.337	-26.820	-175.344	-26.820	-175.340	-26.822	243.786	7.29
15	KUM	200	-175.220	-26.777	-175.232	-26.776	-175.222	-26.779	256.444	6.26
16	KUM	200	-175.104	-26.735	-175.109	-26.735	-175.106	-26.737	268.889	5.86
17	KUM	200	-174.982	-26.691	-174.994	-26.693	-174.989	-26.695	281.397	5.49
18	KUM	200	-174.872	-26.650	-174.876	-26.650	-174.872	-26.652	293.938	4.60
19	LC4x4	250	-174.755	-26.607	-174.759	-26.608	-174.757	-26.610	306.345	3.28
20	LC4x4	250	-174.640	-26.565	-174.644	-26.564	-174.640	-26.567	318.923	1.61
21	LC4x4	250	-174.524	-26.523	-174.529	-26.523	-174.526	-26.524	331.228	3.89
22	LC4x4	250	-174.408	-26.480	-174.411	-26.482	-174.409	-26.481	343.832	4.36
23	LC4x4	250	-174.291	-26.436	-174.294	-26.439	-174.292	-26.438	356.334	4.79
24	LC4x4	250	-174.175	-26.393	-174.179	-26.396	-174.177	-26.395	368.745	4.96
25	LC4x4	250	-174.060	-26.351	-174.064	-26.355	-174.062	-26.352	381.190	5.09
26	LC4x4	250	-173.944	-26.308	-173.947	-26.311	-173.947	-26.309	393.648	5.13
27	LC2000	250	-173.830	-26.265	-173.833	-26.270	-173.833	-26.266	405.914	5.15

Appendix C

WA seismic record sections are presented in Figures C.1-C.23, with picked and modelled arrivals annotated. The phase identification and arrival picking approach is described in Sections 3.3 and 3.4. These figures also show the modelled rays traced through the relevant sections of the velocity-depth model.

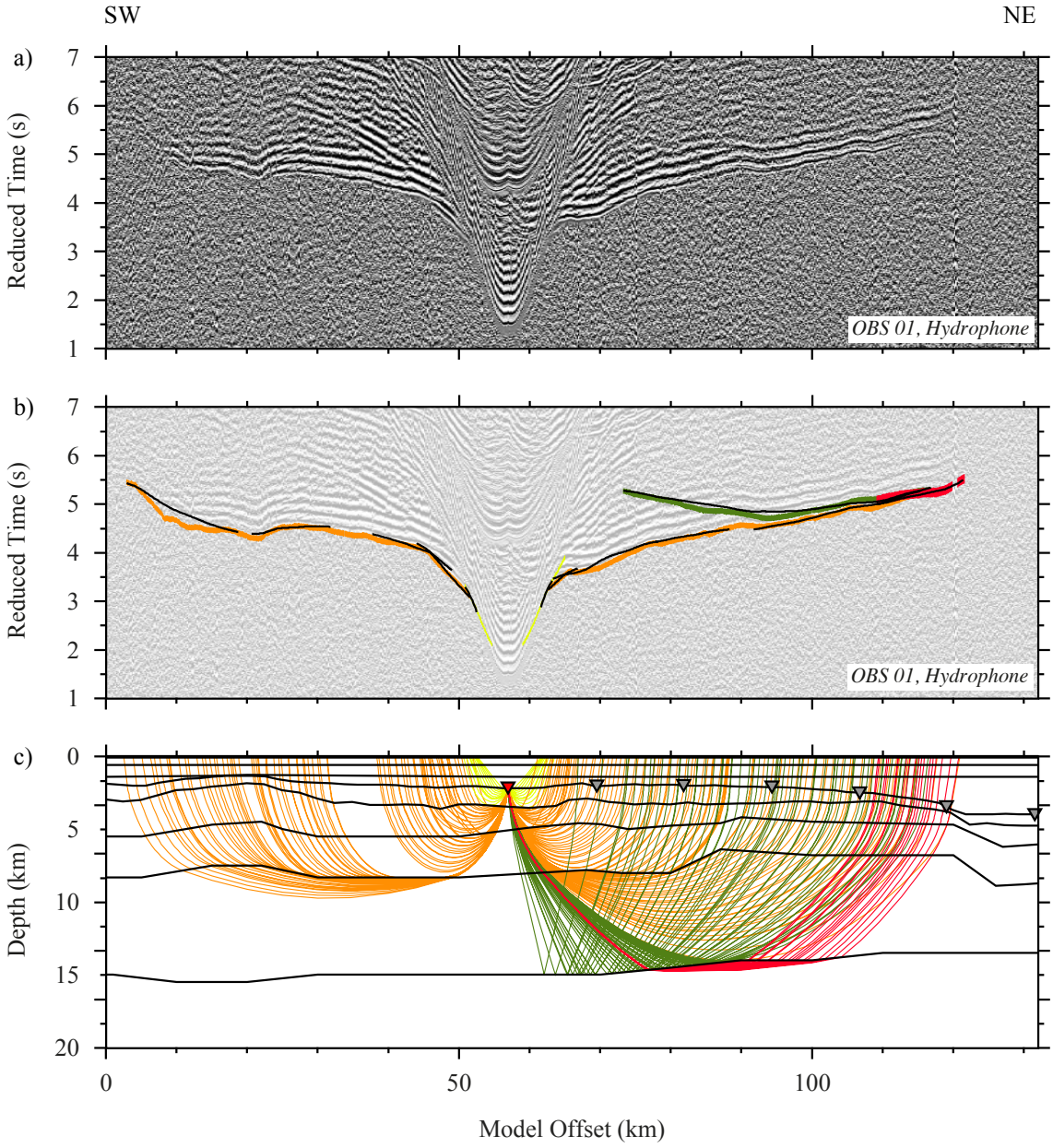

Figure C.1: WA seismic data and modelled arrival comparison for OBS 01. a) Filtered hydrophone data from OBS 01 reduced at 8 km s^{-1}, phase identifications are as indicated in b). b) Picked phases are indicated by vertical coloured bars (P_s - yellow; P_g - orange; P_n - red; P_mP - green). The height of the coloured bar represents the pick uncertainty, the black lines on top are the modelled arrival times. c) Calculated refracted and reflected rays traced through the velocity-depth model (layer boundaries indicated by the black lines). Ray colours match the assigned pick phases (in b), the location of OBS 01 is indicated by an inverted red triangle, and other OBSs are depicted as inverted grey triangles.

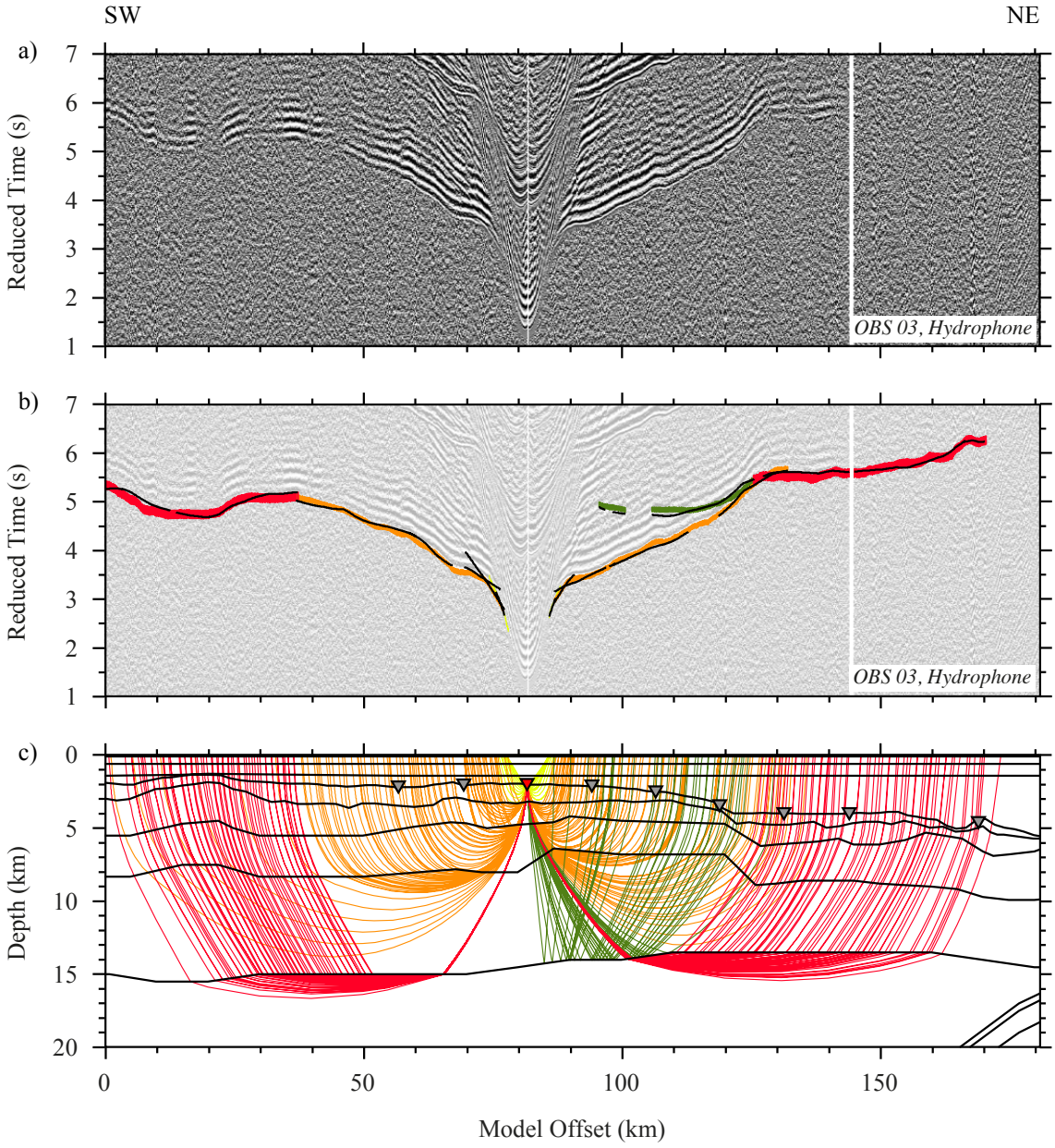

Figure C.2: WA seismic data and modelled arrival comparison for OBS 03. a) Filtered hydrophone data from OBS 03 reduced at 8 km s^{-1}, phase identifications are as indicated in b). b) Picked phases are indicated by vertical coloured bars (P_s - yellow; P_g - orange; P_n - red; P_mP - green). The height of the coloured bar represents the pick uncertainty, the black lines on top are the modelled arrival times. c) Calculated refracted and reflected rays traced through the velocity-depth model (layer boundaries indicated by the black lines). Ray colours match the assigned pick phases (in b), the location of OBS 03 is indicated by an inverted red triangle, and other OBSs are depicted as inverted grey triangles.

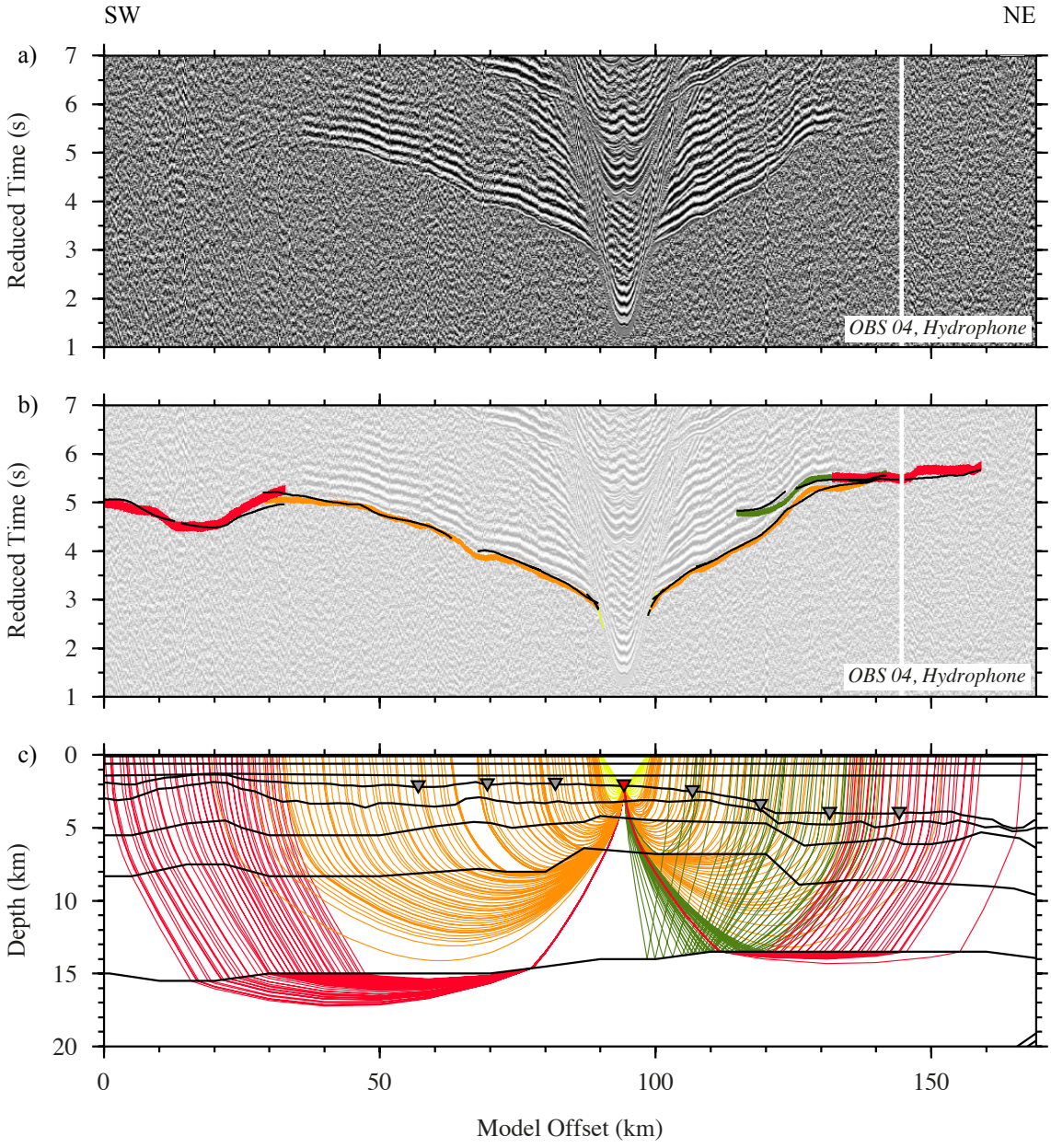

Figure C.3: WA seismic data and modelled arrival comparison for OBS 04. a) Filtered hydrophone data from OBS 04 reduced at 8 km s^{-1}, phase identifications are as indicated in b). b) Picked phases are indicated by vertical coloured bars (P_s - yellow; P_g - orange; P_n - red; P_mP - green). The height of the coloured bar represents the pick uncertainty, the black lines on top are the modelled arrival times. c) Calculated refracted and reflected rays traced through the velocity-depth model (layer boundaries indicated by the black lines). Ray colours match the assigned pick phases (in b), the location of OBS 04 is indicated by an inverted red triangle, and other OBSs are depicted as inverted grey triangles.

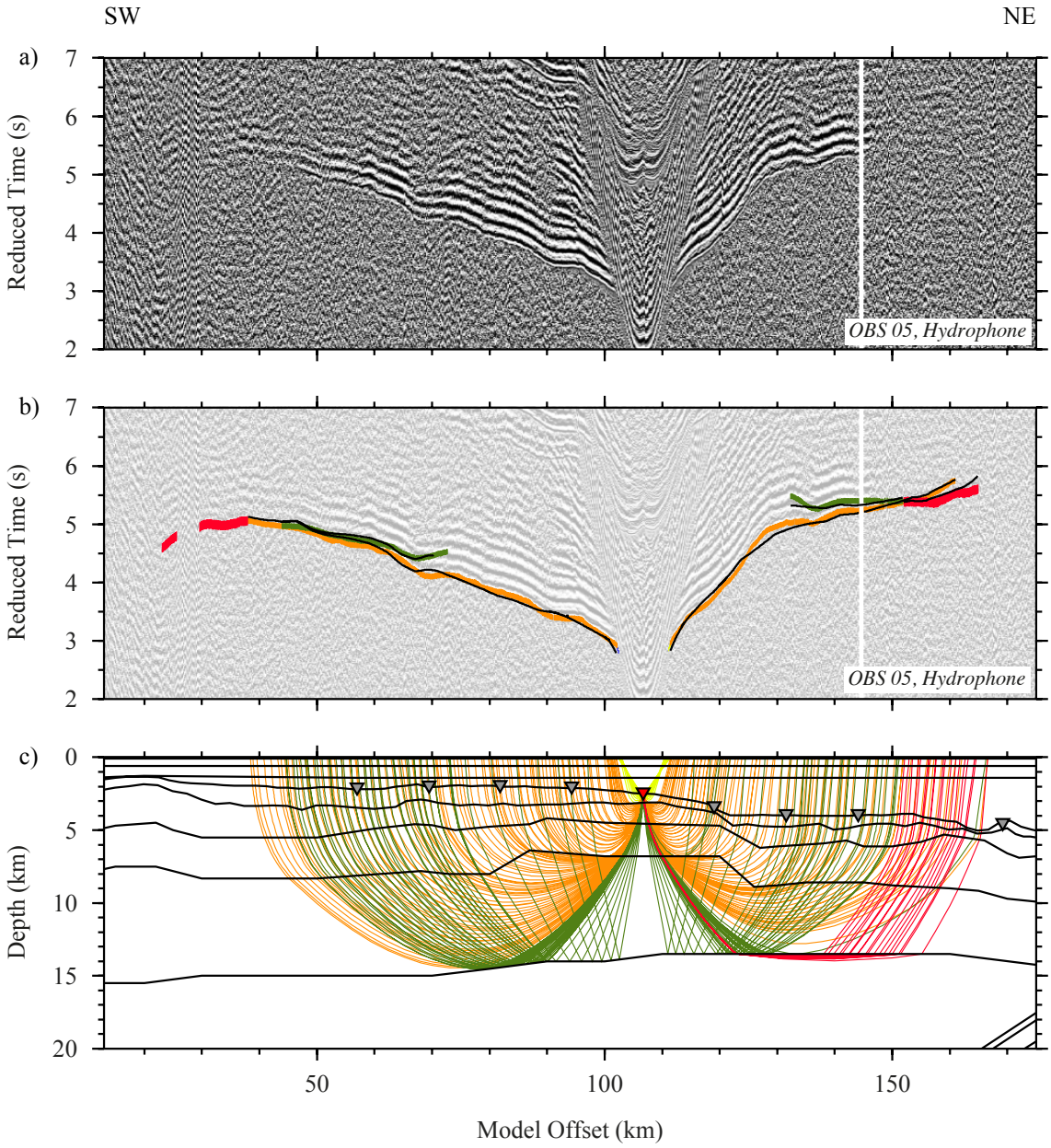

Figure C.4: WA seismic data and modelled arrival comparison for OBS 05. a) Filtered hydrophone data from OBS 05 reduced at 8 km s^{-1}, phase identifications are as indicated in b). b) Picked phases are indicated by vertical coloured bars (P_s - yellow; P_g - orange; P_n - red; P_mP - green). The height of the coloured bar represents the pick uncertainty, the black lines on top are the modelled arrival times. c) Calculated refracted and reflected rays traced through the velocity-depth model (layer boundaries indicated by the black lines). Ray colours match the assigned pick phases (in b), the location of OBS 05 is indicated by an inverted red triangle, and other OBSs are depicted as inverted grey triangles.

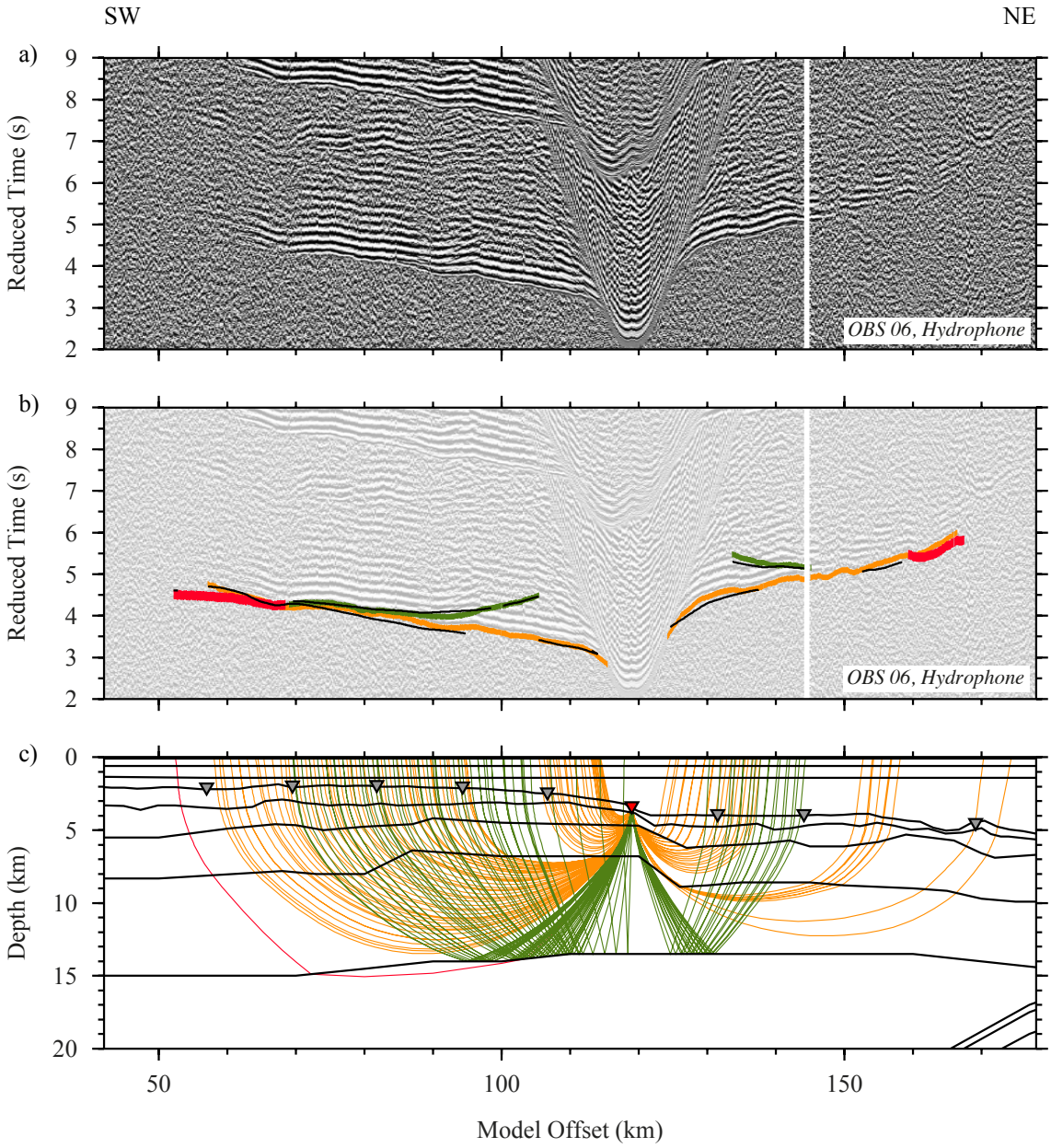

Figure C.5: WA seismic data and modelled arrival comparison for OBS 06. a) Filtered hydrophone data from OBS 06 reduced at 8 km s^{-1}, phase identifications are as indicated in b). b) Picked phases are indicated by vertical coloured bars (P_s - yellow; P_g - orange; P_n - red; P_mP - green). The height of the coloured bar represents the pick uncertainty, the black lines on top are the modelled arrival times. c) Calculated refracted and reflected rays traced through the velocity-depth model (layer boundaries indicated by the black lines). Ray colours match the assigned pick phases (in b), the location of OBS 06 is indicated by an inverted red triangle, and other OBSs are depicted as inverted grey triangles.

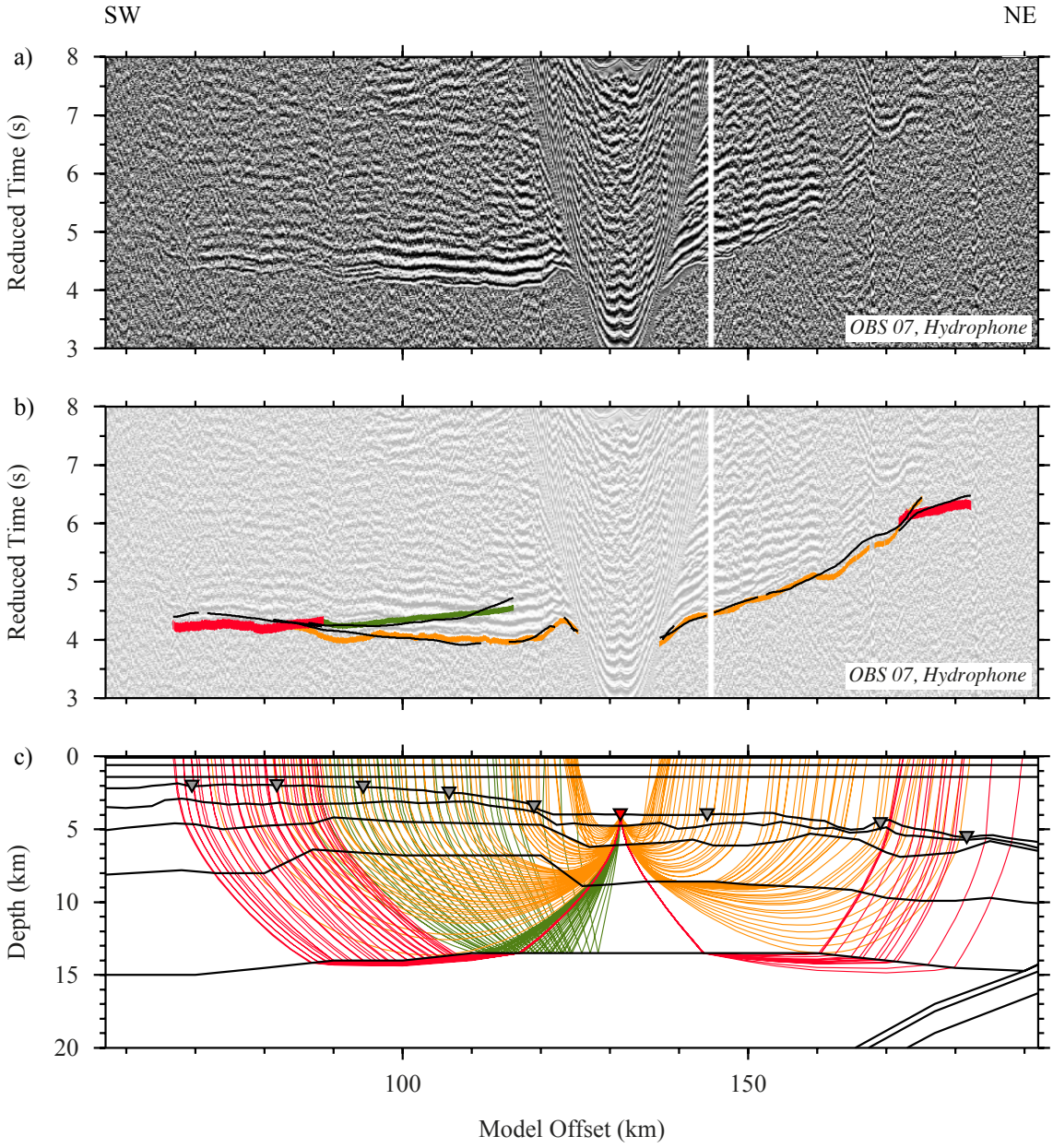

Figure C.6: WA seismic data and modelled arrival comparison for OBS 07. a) Filtered hydrophone data from OBS 07 reduced at 8 km s^{-1}, phase identifications are as indicated in b). b) Picked phases are indicated by vertical coloured bars (P_s - yellow; P_g - orange; P_n - red; P_mP - green). The height of the coloured bar represents the pick uncertainty, the black lines on top are the modelled arrival times. c) Calculated refracted and reflected rays traced through the velocity-depth model (layer boundaries indicated by the black lines). Ray colours match the assigned pick phases (in b), the location of OBS 07 is indicated by an inverted red triangle, and other OBSs are depicted as inverted grey triangles.

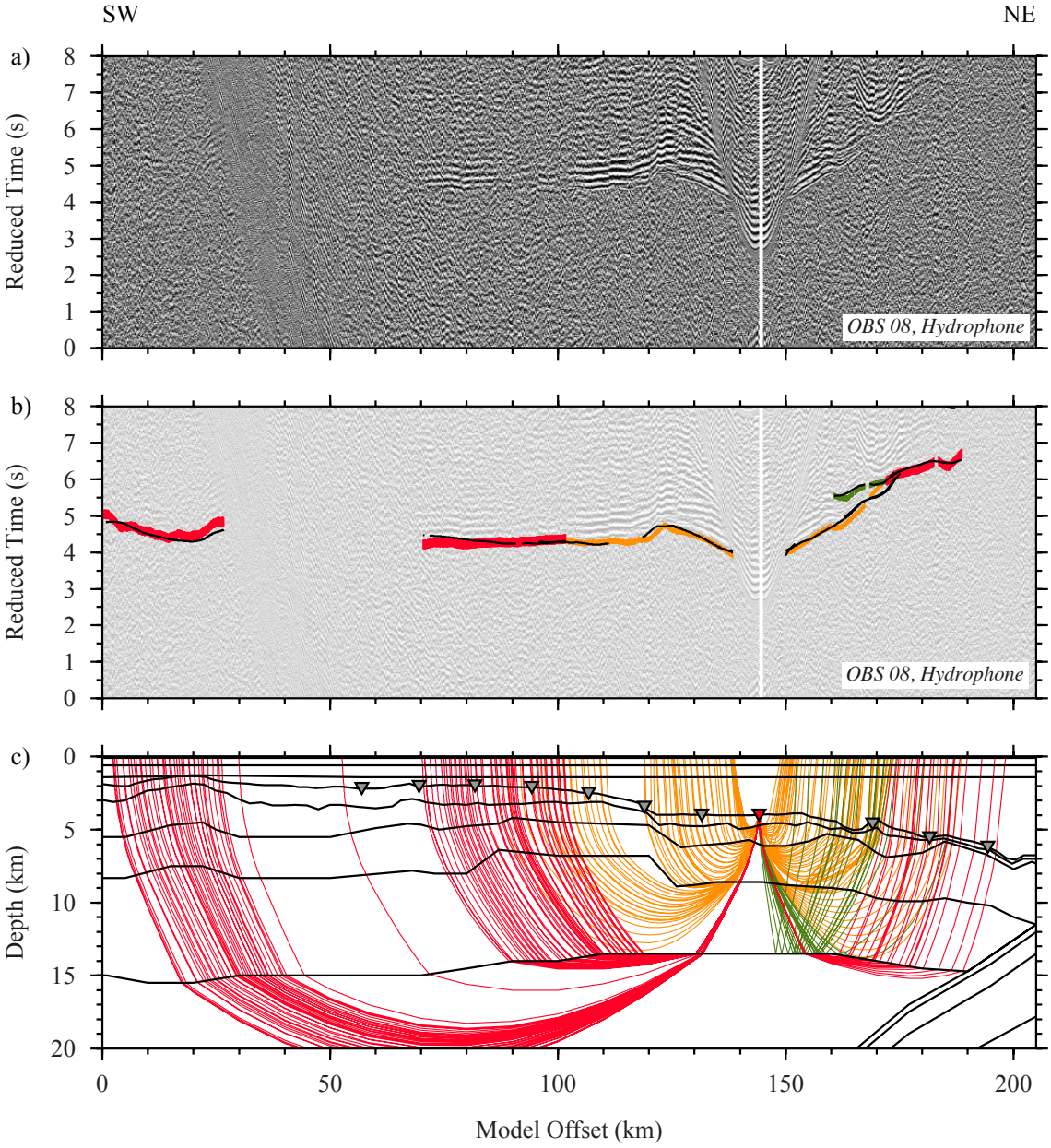

Figure C.7: WA seismic data and modelled arrival comparison for OBS 08. a) Filtered hydrophone data from OBS 08 reduced at 8 km s^{-1}, phase identifications are as indicated in b). b) Picked phases are indicated by vertical coloured bars (P_s - yellow; P_g - orange; P_n - red; P_mP - green). The height of the coloured bar represents the pick uncertainty, the black lines on top are the modelled arrival times. c) Calculated refracted and reflected rays traced through the velocity-depth model (layer boundaries indicated by the black lines). Ray colours match the assigned pick phases (in b), the location of OBS 08 is indicated by an inverted red triangle, and other OBSs are depicted as inverted grey triangles.

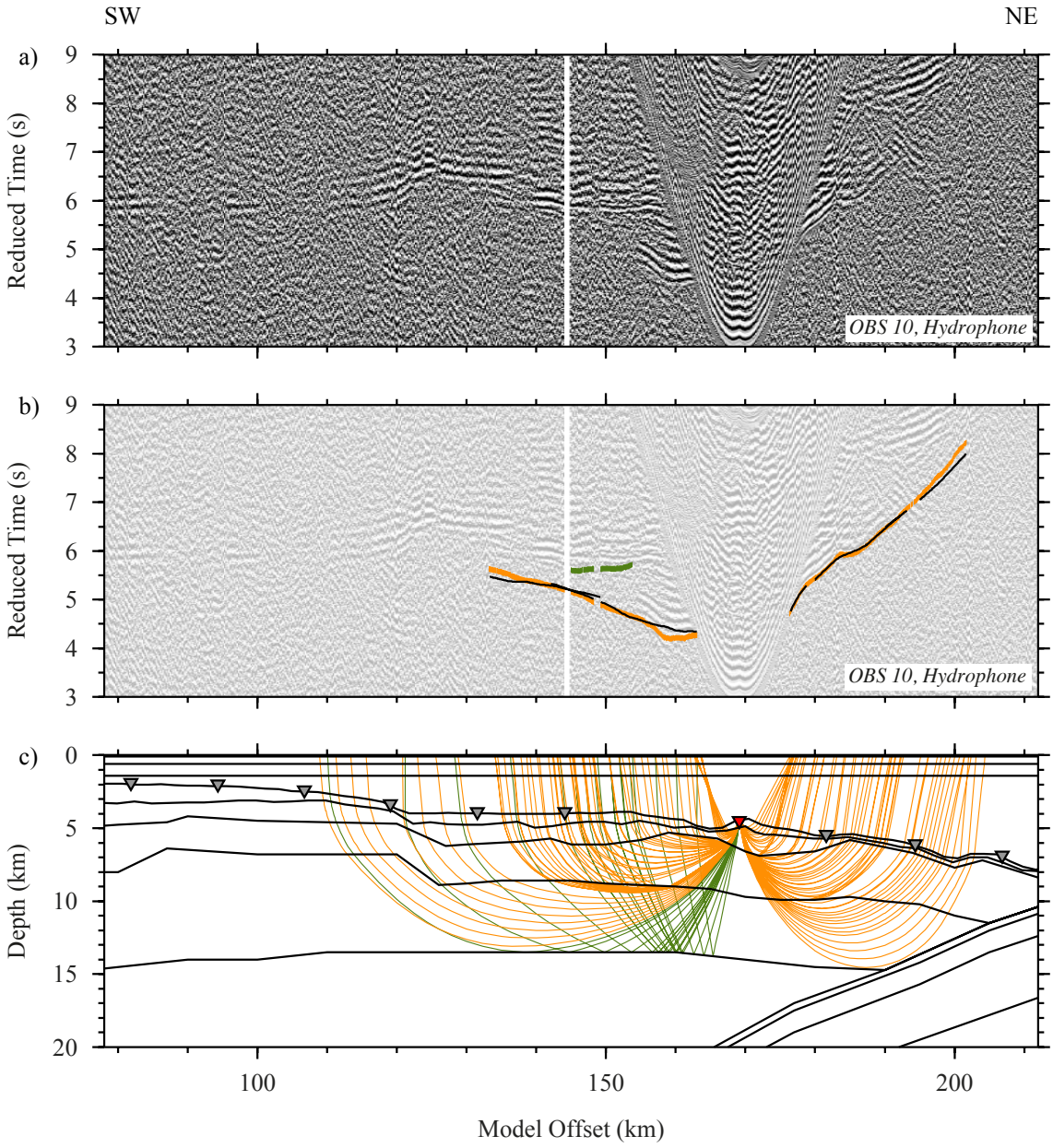

Figure C.8: WA seismic data and modelled arrival comparison for OBS 10. a) Filtered hydrophone data from OBS 10 reduced at 8 km s^{-1}, phase identifications are as indicated in b). b) Picked phases are indicated by vertical coloured bars (P_s - yellow; P_g - orange; P_n - red; P_mP - green). The height of the coloured bar represents the pick uncertainty, the black lines on top are the modelled arrival times. c) Calculated refracted and reflected rays traced through the velocity-depth model (layer boundaries indicated by the black lines). Ray colours match the assigned pick phases (in b), the location of OBS 10 is indicated by an inverted red triangle, and other OBSs are depicted as inverted grey triangles.

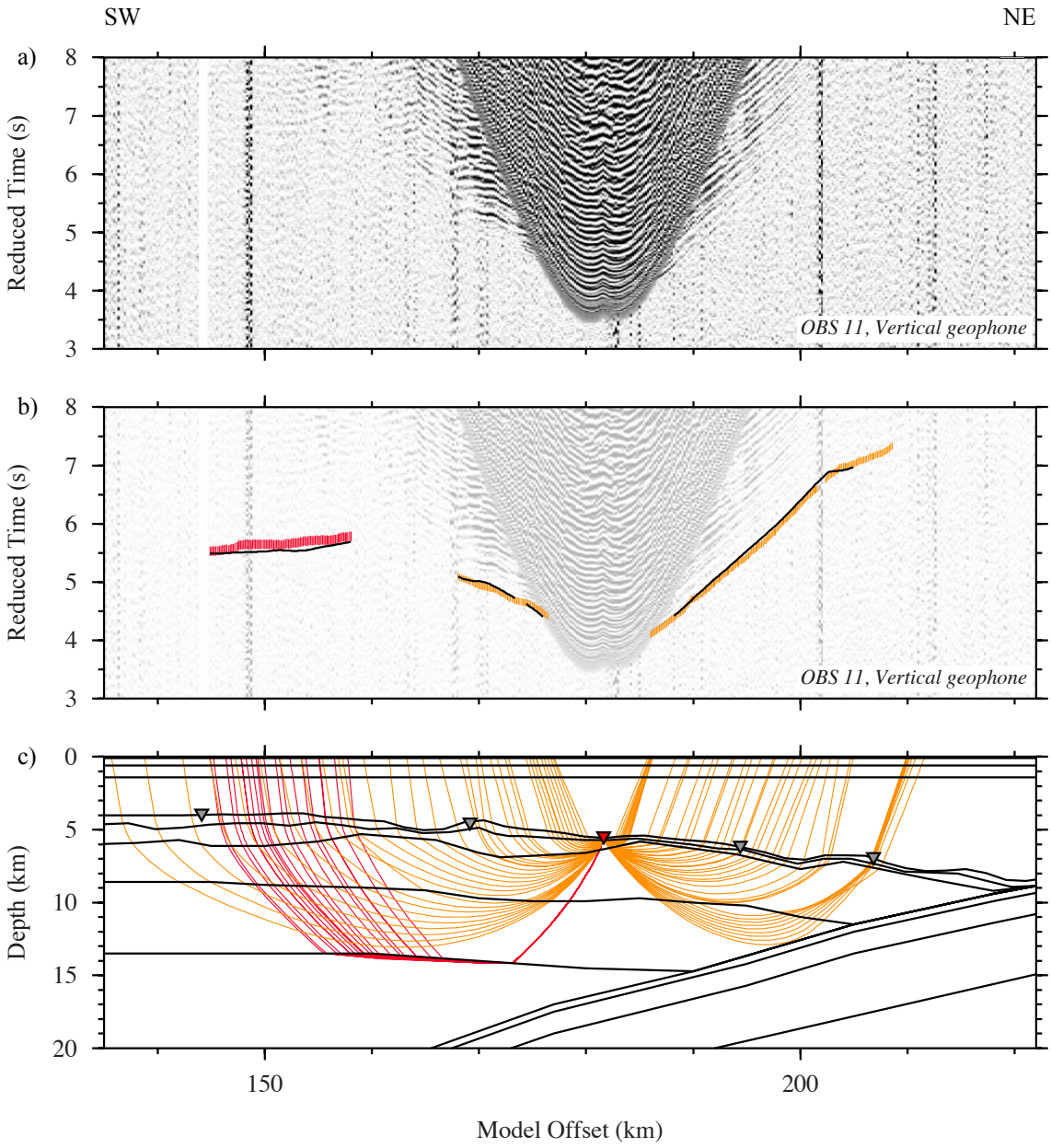

Figure C.9: WA seismic data and modelled arrival comparison for OBS 11. a) Filtered vertical geophone data from OBS 11 reduced at 8 km s^{-1}, phase identifications are as indicated in b). b) Picked phases are indicated by vertical coloured bars (P_s - yellow; P_g - orange; P_n - red; P_mP - green). The height of the coloured bar represents the pick uncertainty, the black lines on top are the modelled arrival times. c) Calculated refracted and reflected rays traced through the velocity-depth model (layer boundaries indicated by the black lines). Ray colours match the assigned pick phases (in b), the location of OBS 11 is indicated by an inverted red triangle, and other OBSs are depicted as inverted grey triangles.

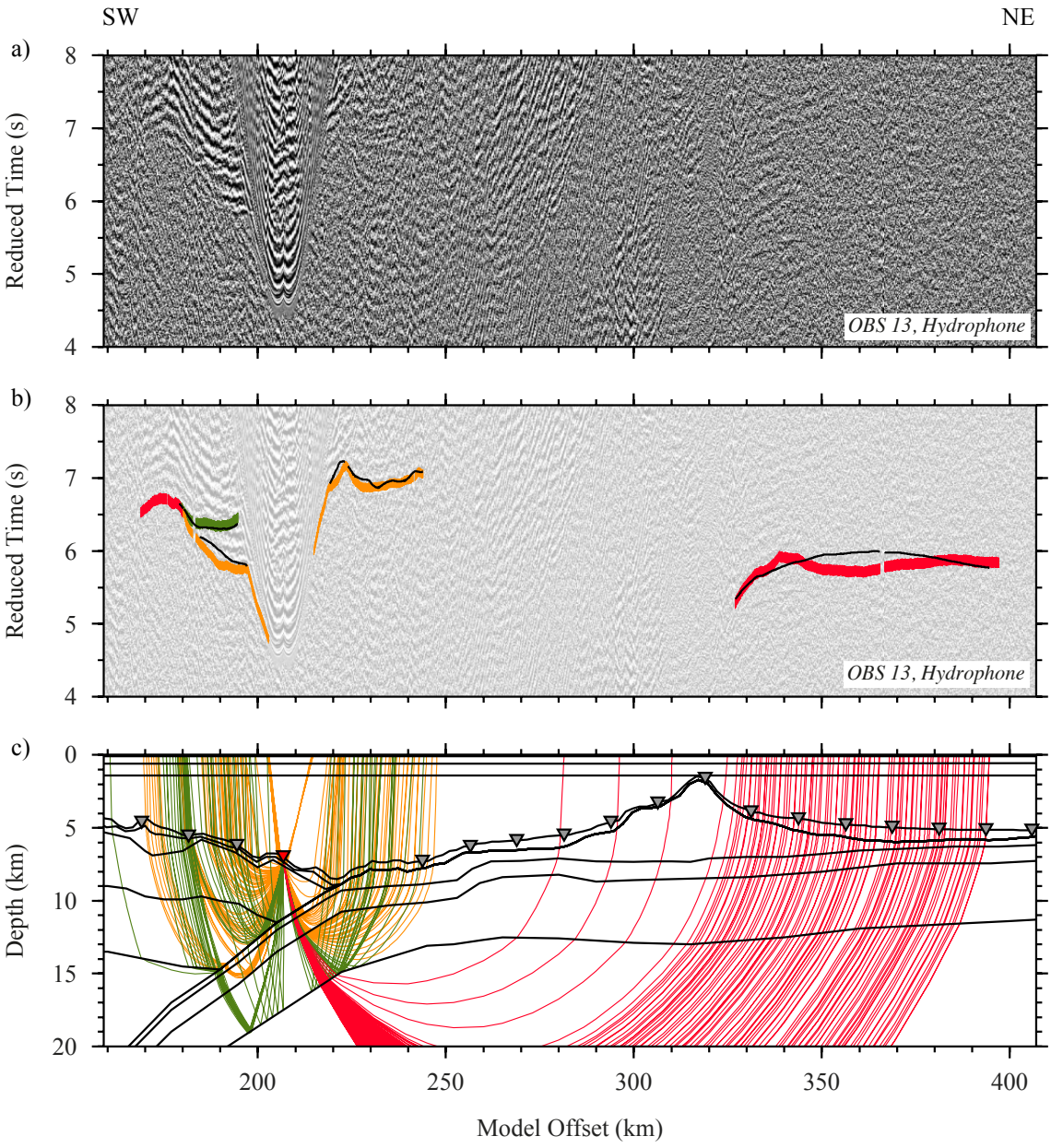

Figure C.10: WA seismic data and modelled arrival comparison for OBS 13. a) Filtered hydrophone data from OBS 13 reduced at 8 km s^{-1}, phase identifications are as indicated in b). b) Picked phases are indicated by vertical coloured bars (P_s - yellow; P_g - orange; P_n - red; P_mP - green). The height of the coloured bar represents the pick uncertainty, the black lines on top are the modelled arrival times. c) Calculated refracted and reflected rays traced through the velocity-depth model (layer boundaries indicated by the black lines). Ray colours match the assigned pick phases (in b), the location of OBS 13 is indicated by an inverted red triangle, and other OBSs are depicted as inverted grey triangles.

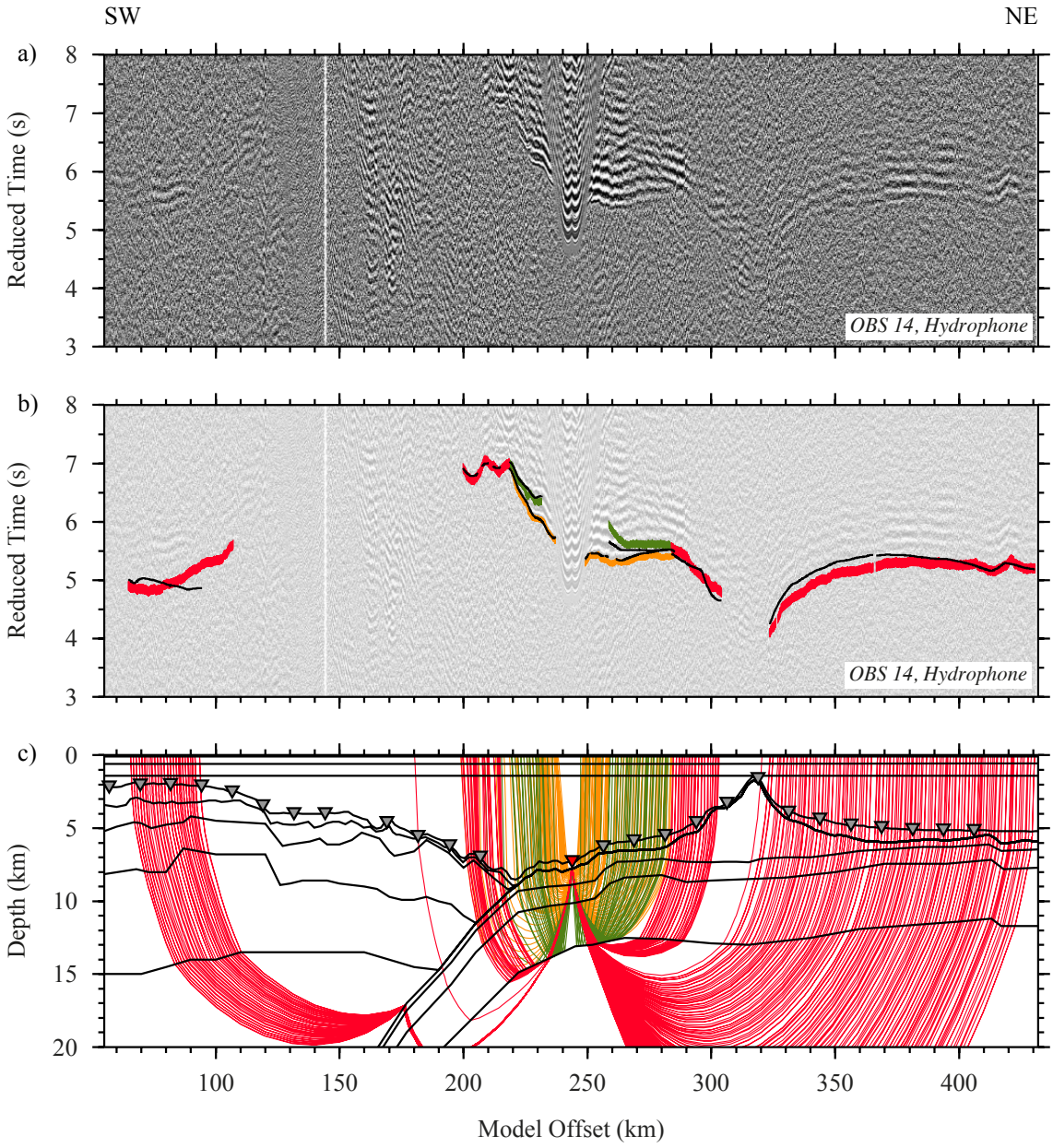

Figure C.11: WA seismic data and modelled arrival comparison for OBS 14. a) Filtered hydrophone data from OBS 14 reduced at 8 km s^{-1}, phase identifications are as indicated in b). b) Picked phases are indicated by vertical coloured bars (P_s - yellow; P_g - orange; P_n - red; P_mP - green). The height of the coloured bar represents the pick uncertainty, the black lines on top are the modelled arrival times. c) Calculated refracted and reflected rays traced through the velocity-depth model (layer boundaries indicated by the black lines). Ray colours match the assigned pick phases (in b), the location of OBS 14 is indicated by an inverted red triangle, and other OBSs are depicted as inverted grey triangles.

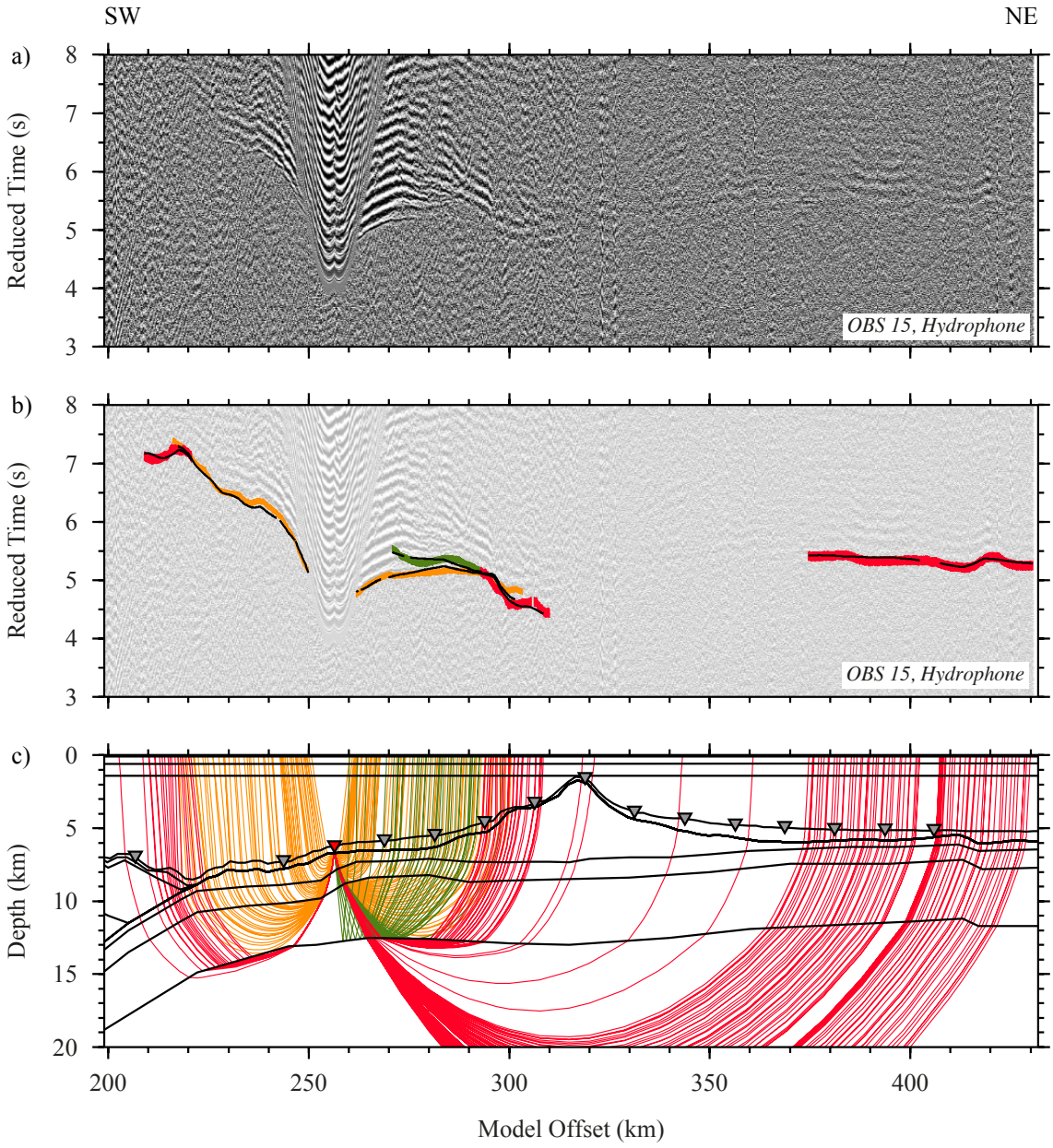

Figure C.12: WA seismic data and modelled arrival comparison for OBS 15. a) Filtered hydrophone data from OBS 15 reduced at 8 km s^{-1}, phase identifications are as indicated in b). b) Picked phases are indicated by vertical coloured bars (P_s - yellow; P_g - orange; P_n - red; P_mP - green). The height of the coloured bar represents the pick uncertainty, the black lines on top are the modelled arrival times. c) Calculated refracted and reflected rays traced through the velocity-depth model (layer boundaries indicated by the black lines). Ray colours match the assigned pick phases (in b), the location of OBS 15 is indicated by an inverted red triangle, and other OBSs are depicted as inverted grey triangles.

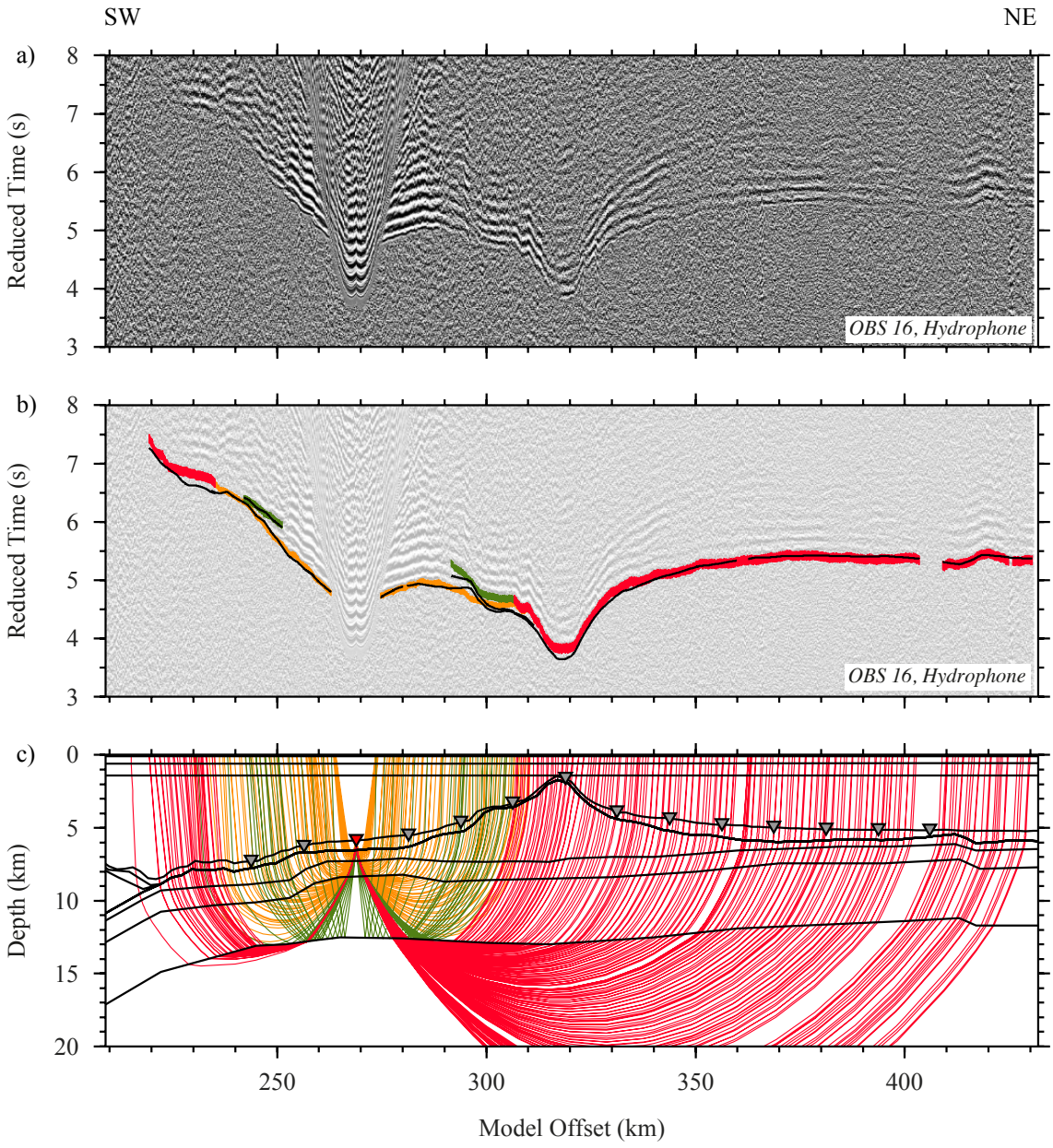

Figure C.13: WA seismic data and modelled arrival comparison for OBS 16. a) Filtered hydrophone data from OBS 16 reduced at 8 km s^{-1}, phase identifications are as indicated in b). b) Picked phases are indicated by vertical coloured bars (P_s - yellow; P_g - orange; P_n - red; P_mP - green). The height of the coloured bar represents the pick uncertainty, the black lines on top are the modelled arrival times. c) Calculated refracted and reflected rays traced through the velocity-depth model (layer boundaries indicated by the black lines). Ray colours match the assigned pick phases (in b), the location of OBS 16 is indicated by an inverted red triangle, and other OBSs are depicted as inverted grey triangles.

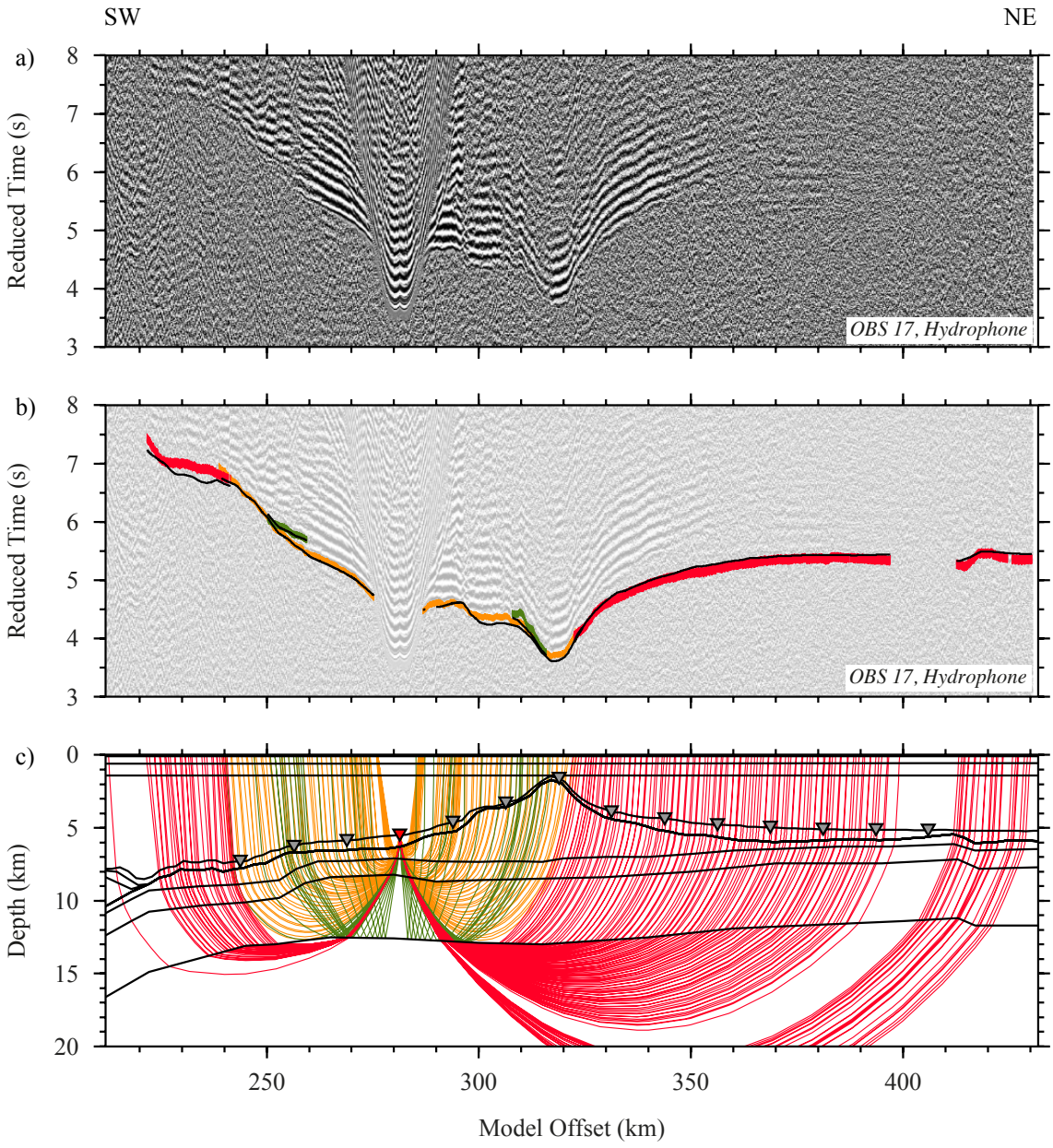

Figure C.14: WA seismic data and modelled arrival comparison for OBS 17. a) Filtered hydrophone data from OBS 17 reduced at 8 km s^{-1}, phase identifications are as indicated in b). b) Picked phases are indicated by vertical coloured bars (P_s - yellow; P_g - orange; P_n - red; P_mP - green). The height of the coloured bar represents the pick uncertainty, the black lines on top are the modelled arrival times. c) Calculated refracted and reflected rays traced through the velocity-depth model (layer boundaries indicated by the black lines). Ray colours match the assigned pick phases (in b), the location of OBS 17 is indicated by an inverted red triangle, and other OBSs are depicted as inverted grey triangles.

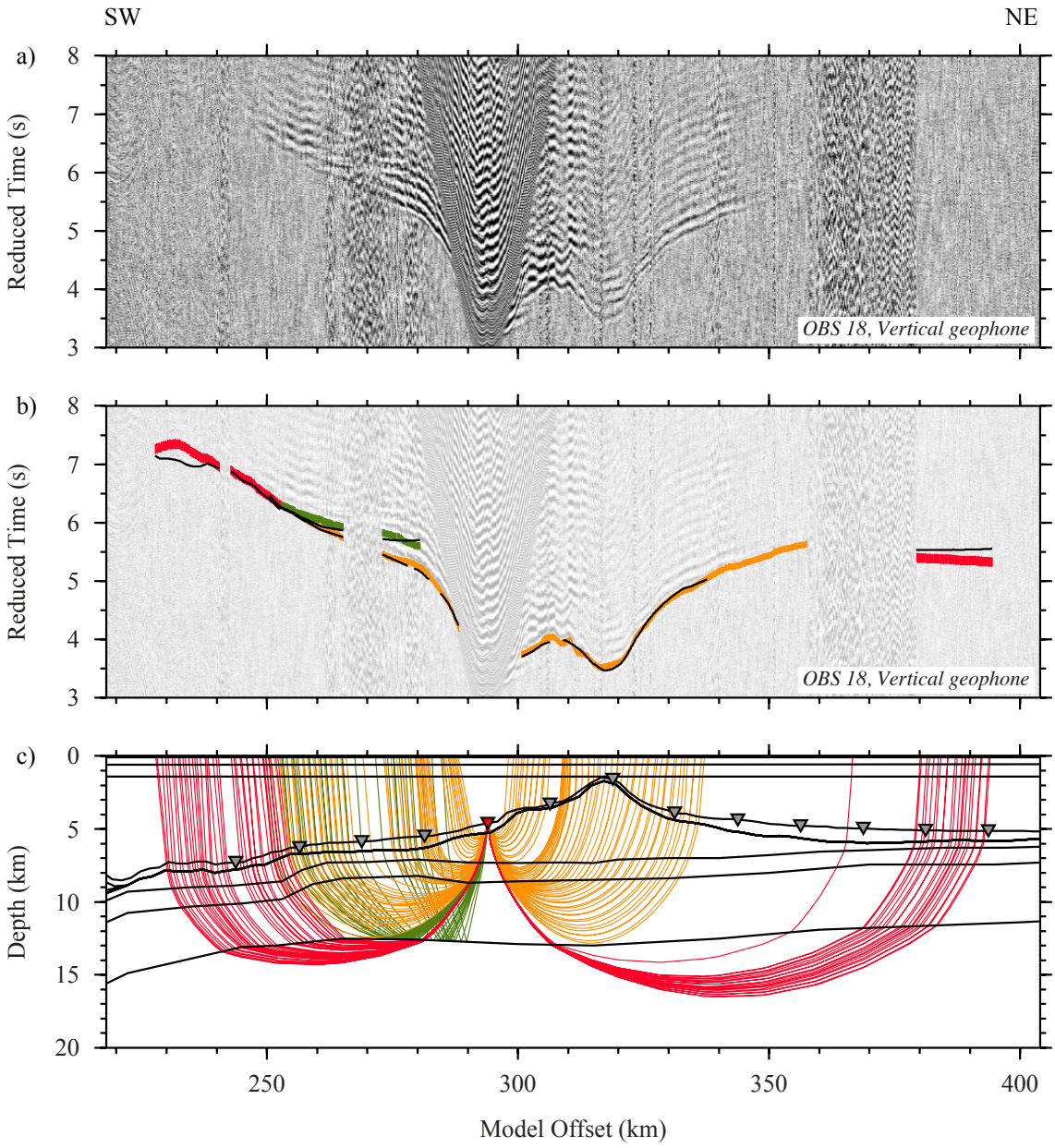

Figure C.15: WA seismic data and modelled arrival comparison for OBS 18. a) Filtered vertical geophone data from OBS 18 reduced at 8 km s^{-1}, phase identifications are as indicated in b). b) Picked phases are indicated by vertical coloured bars (P_s - yellow; P_g - orange; P_n - red; P_mP - green). The height of the coloured bar represents the pick uncertainty, the black lines on top are the modelled arrival times. c) Calculated refracted and reflected rays traced through the velocity-depth model (layer boundaries indicated by the black lines). Ray colours match the assigned pick phases (in b), the location of OBS 18 is indicated by an inverted red triangle, and other OBSs are depicted as inverted grey triangles.

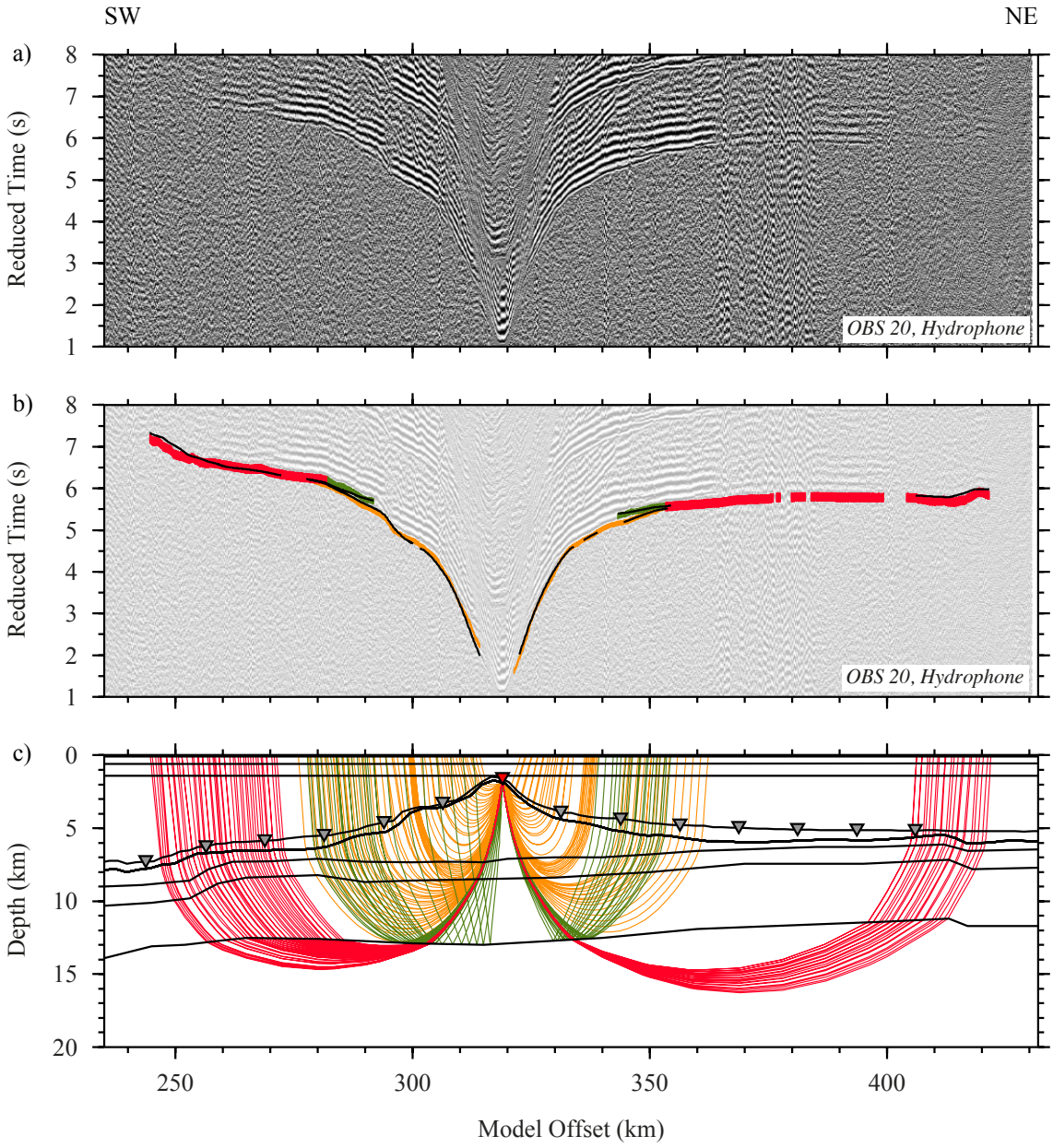

Figure C.16: WA seismic data and modelled arrival comparison for OBS 20. a) Filtered hydrophone data from OBS 20 reduced at 8 km s^{-1}, phase identifications are as indicated in b). b) Picked phases are indicated by vertical coloured bars (P_s - yellow; P_g - orange; P_n - red; P_mP - green). The height of the coloured bar represents the pick uncertainty, the black lines on top are the modelled arrival times. c) Calculated refracted and reflected rays traced through the velocity-depth model (layer boundaries indicated by the black lines). Ray colours match the assigned pick phases (in b), the location of OBS 20 is indicated by an inverted red triangle, and other OBSs are depicted as inverted grey triangles.

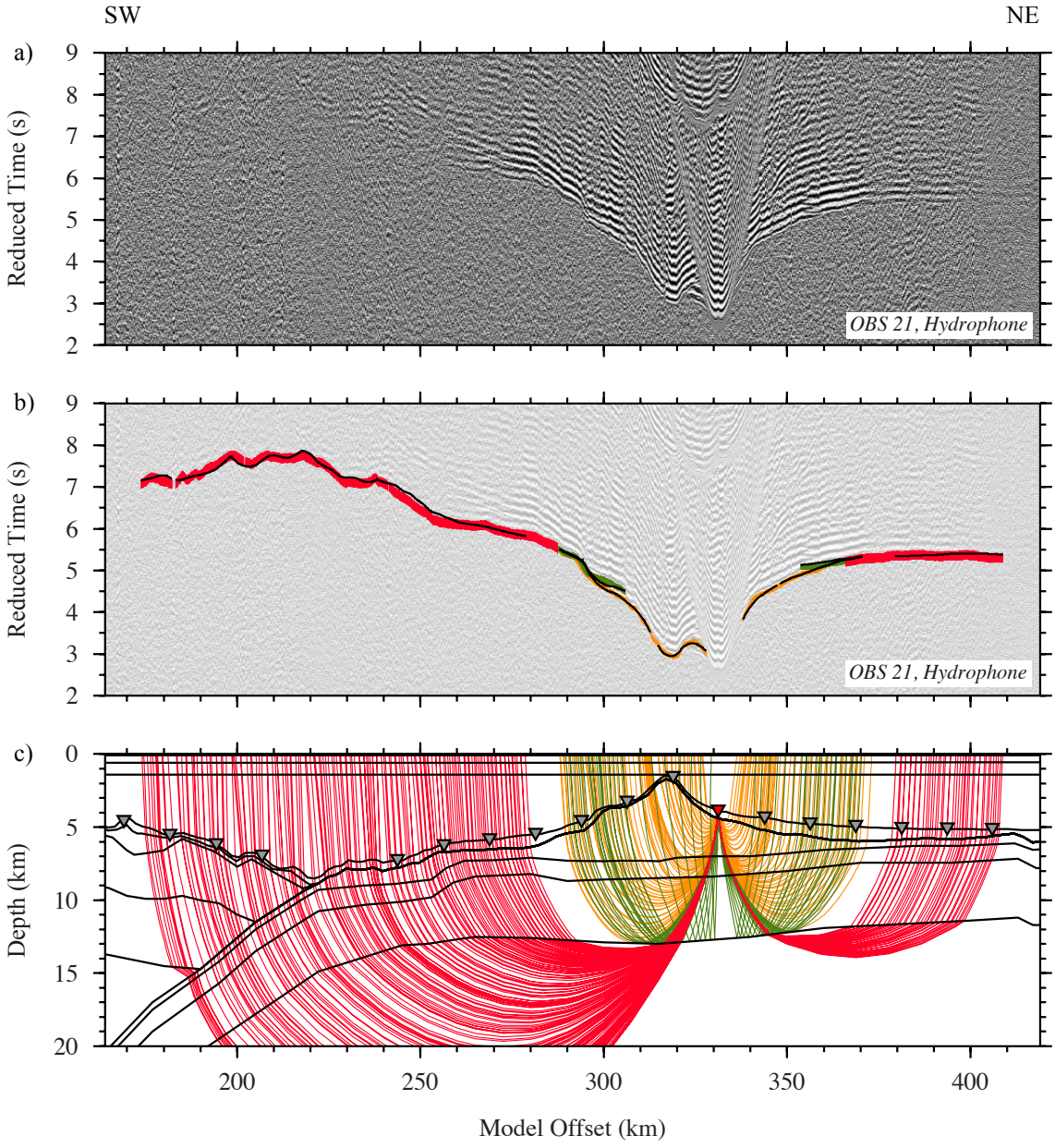

Figure C.17: WA seismic data and modelled arrival comparison for OBS 21. a) Filtered hydrophone data from OBS 21 reduced at 8 km s^{-1}, phase identifications are as indicated in b). b) Picked phases are indicated by vertical coloured bars (P_s - yellow; P_g - orange; P_n - red; P_mP - green). The height of the coloured bar represents the pick uncertainty, the black lines on top are the modelled arrival times. c) Calculated refracted and reflected rays traced through the velocity-depth model (layer boundaries indicated by the black lines). Ray colours match the assigned pick phases (in b), the location of OBS 21 is indicated by an inverted red triangle, and other OBSs are depicted as inverted grey triangles.

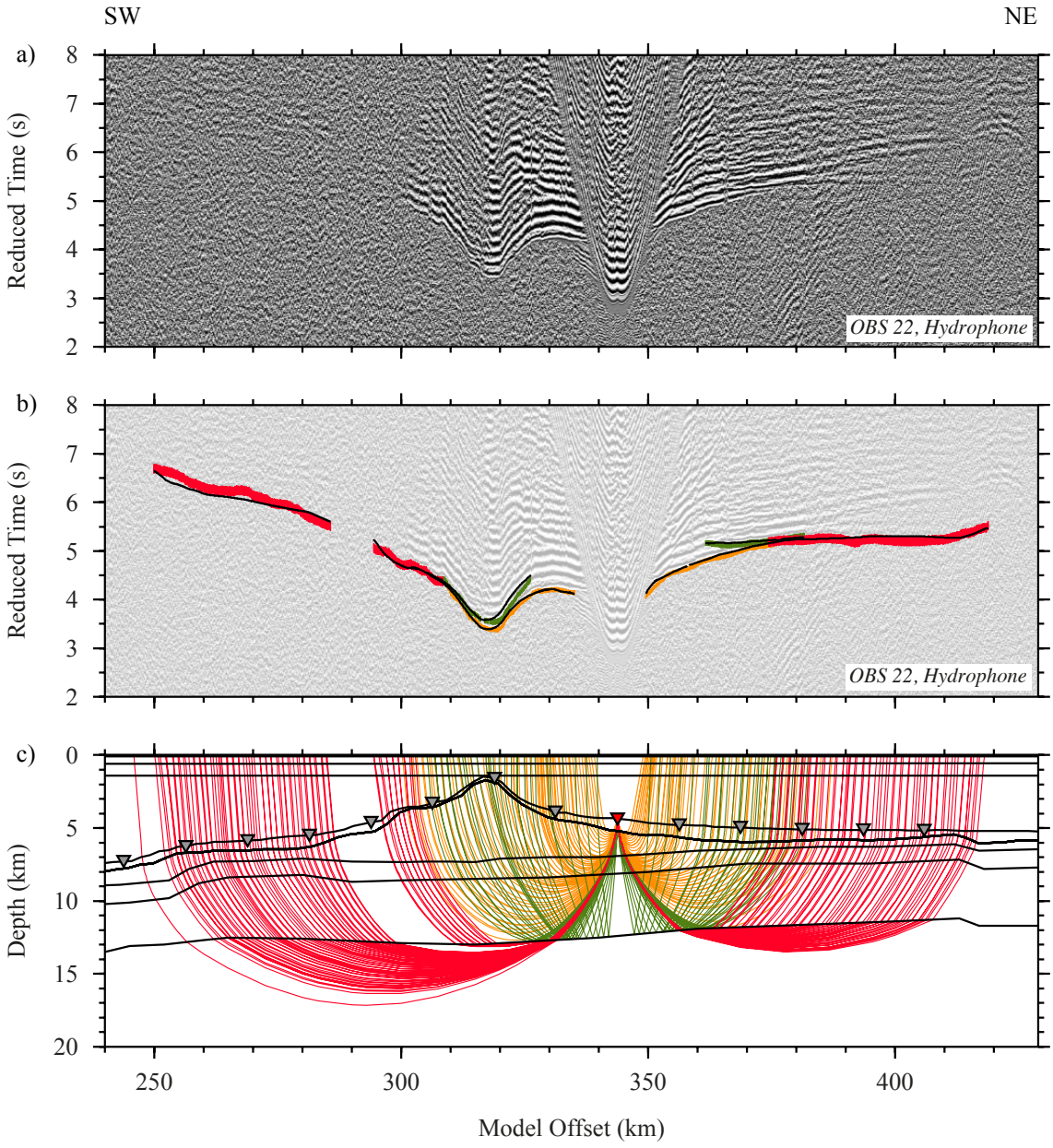

Figure C.18: WA seismic data and modelled arrival comparison for OBS 22. a) Filtered hydrophone data from OBS 22 reduced at 8 km s^{-1}, phase identifications are as indicated in b). b) Picked phases are indicated by vertical coloured bars (P_s - yellow; P_g - orange; P_n - red; P_mP - green). The height of the coloured bar represents the pick uncertainty, the black lines on top are the modelled arrival times. c) Calculated refracted and reflected rays traced through the velocity-depth model (layer boundaries indicated by the black lines). Ray colours match the assigned pick phases (in b), the location of OBS 22 is indicated by an inverted red triangle, and other OBSs are depicted as inverted grey triangles.

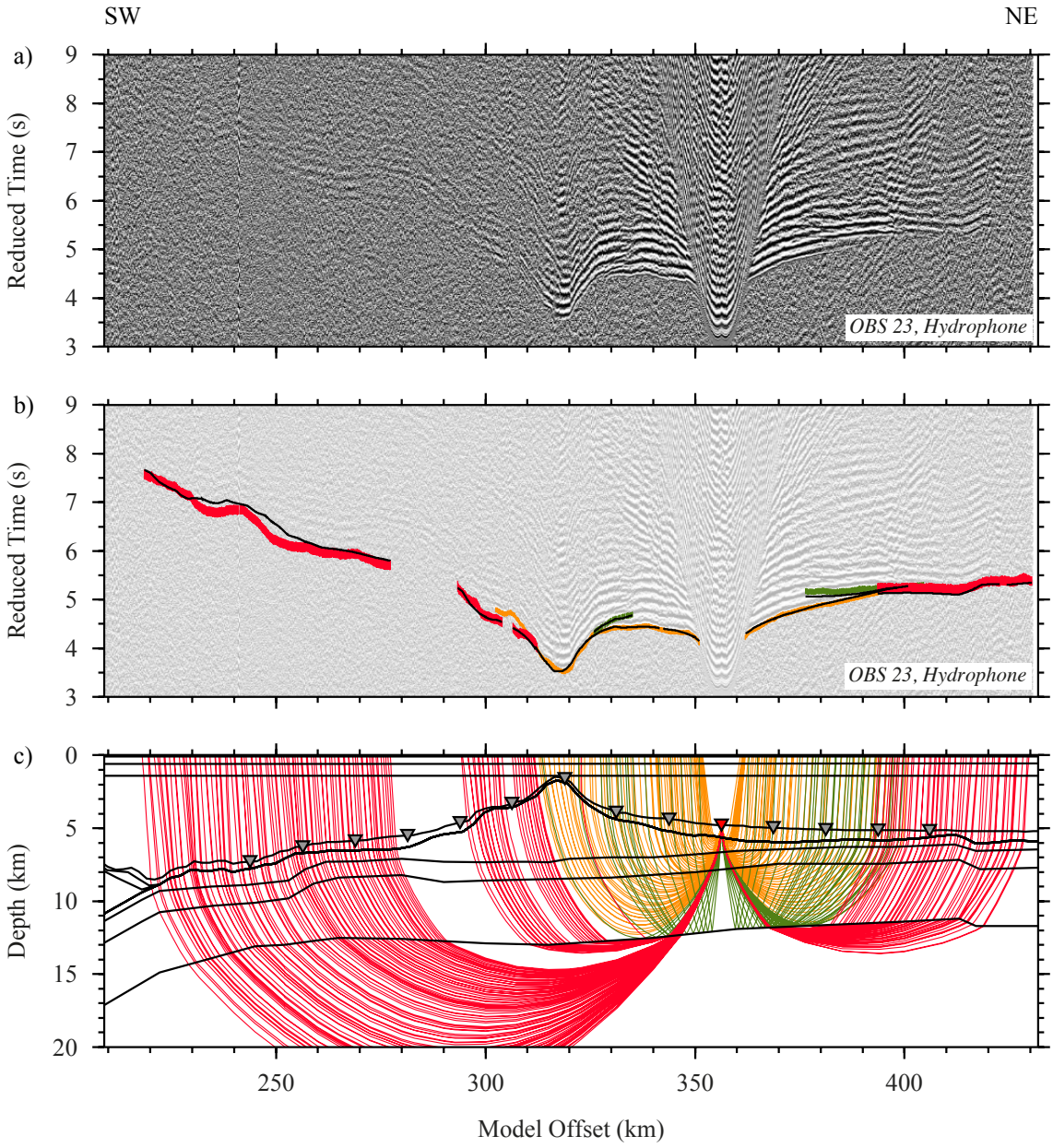

Figure C.19: WA seismic data and modelled arrival comparison for OBS 23. a) Filtered hydrophone data from OBS 23 reduced at 8 km s^{-1}, phase identifications are as indicated in b). b) Picked phases are indicated by vertical coloured bars (P_s - yellow; P_g - orange; P_n - red; P_mP - green). The height of the coloured bar represents the pick uncertainty, the black lines on top are the modelled arrival times. c) Calculated refracted and reflected rays traced through the velocity-depth model (layer boundaries indicated by the black lines). Ray colours match the assigned pick phases (in b), the location of OBS 23 is indicated by an inverted red triangle, and other OBSs are depicted as inverted grey triangles.

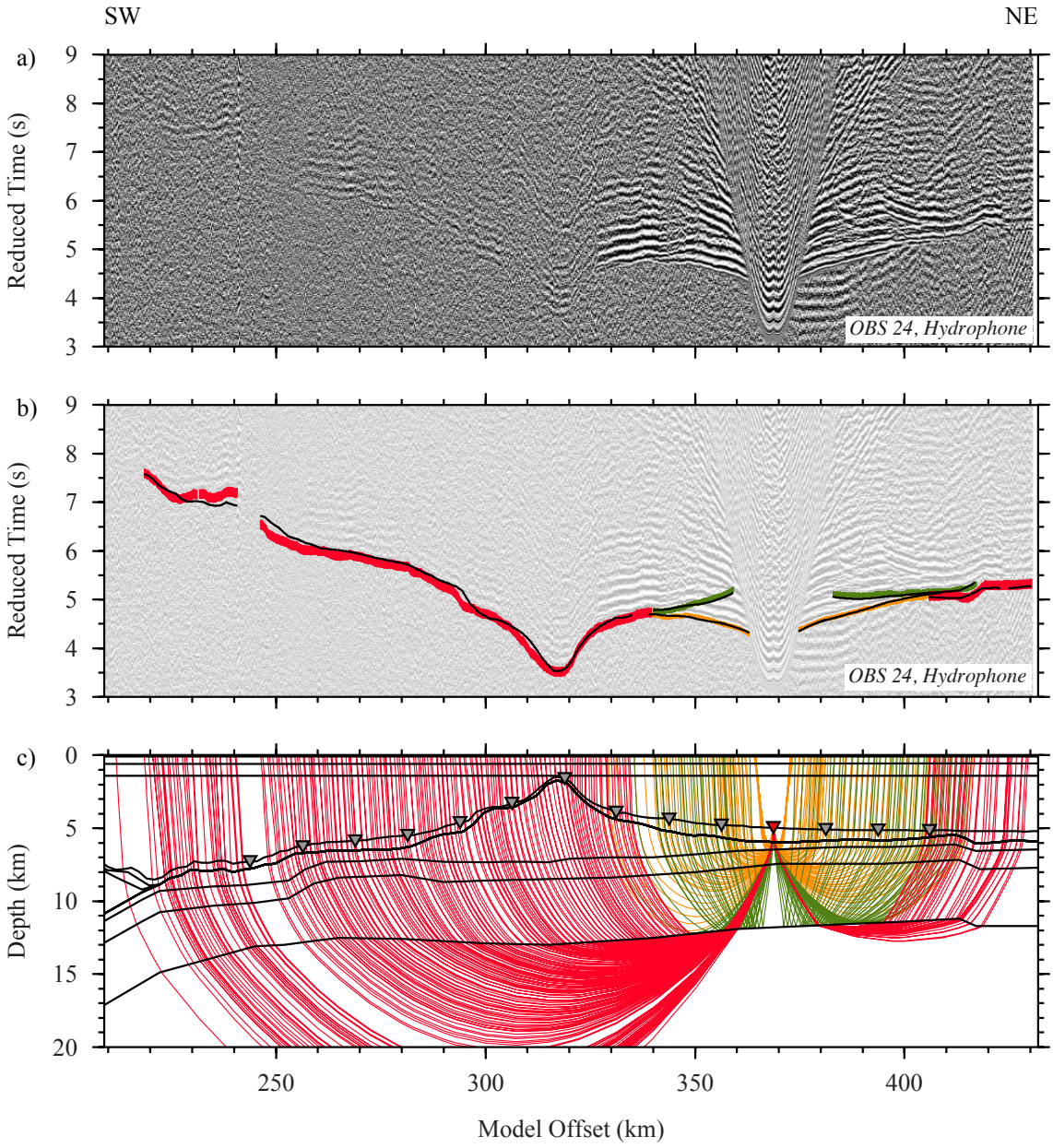

Figure C.20: WA seismic data and modelled arrival comparison for OBS 24. a) Filtered hydrophone data from OBS 24 reduced at 8 km s^{-1}, phase identifications are as indicated in b). b) Picked phases are indicated by vertical coloured bars (P_s - yellow; P_g - orange; P_n - red; P_mP - green). The height of the coloured bar represents the pick uncertainty, the black lines on top are the modelled arrival times. c) Calculated refracted and reflected rays traced through the velocity-depth model (layer boundaries indicated by the black lines). Ray colours match the assigned pick phases (in b), the location of OBS 24 is indicated by an inverted red triangle, and other OBSs are depicted as inverted grey triangles.

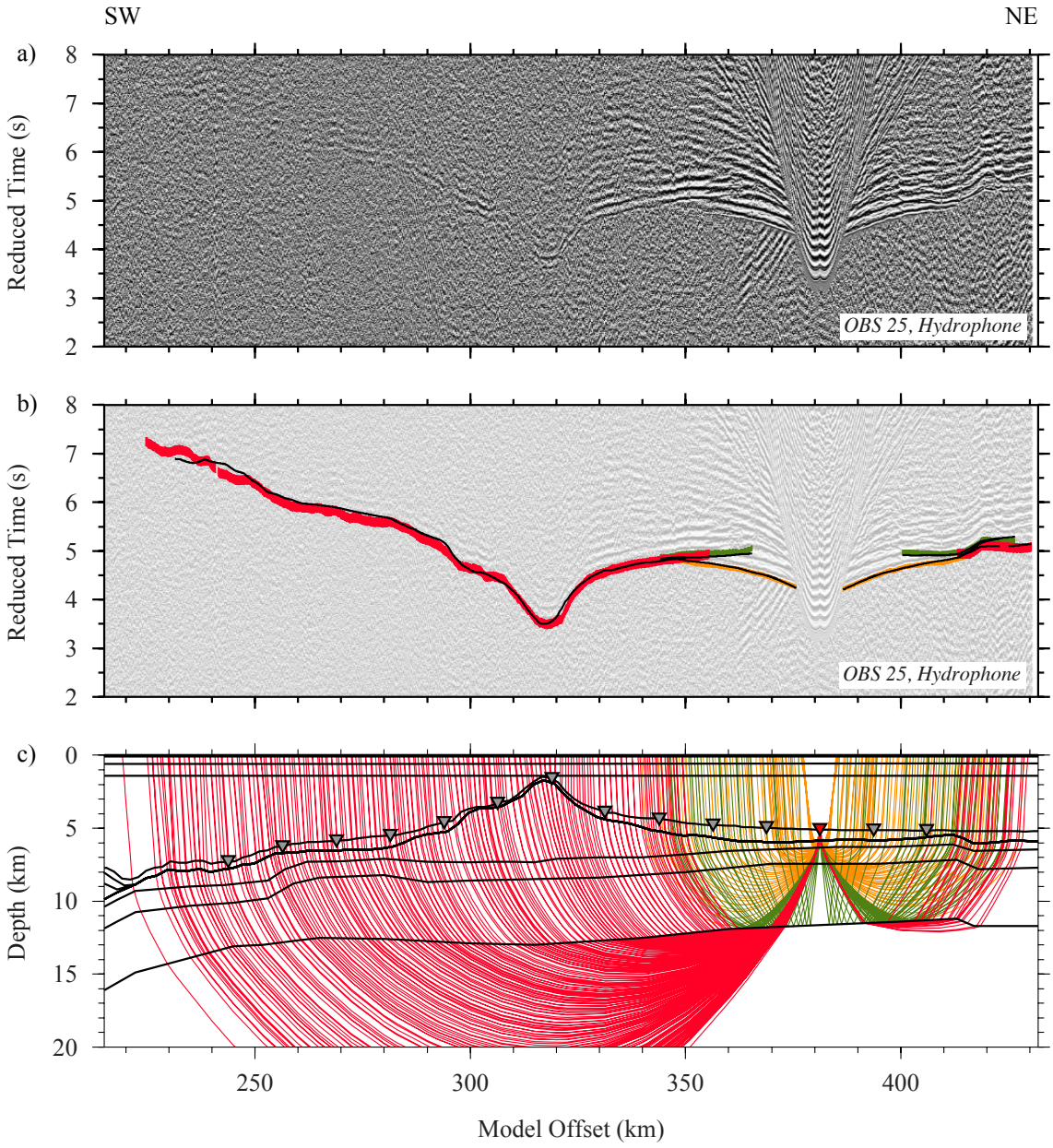

Figure C.21: WA seismic data and modelled arrival comparison for OBS 25. a) Filtered hydrophone data from OBS 25 reduced at 8 km s^{-1}, phase identifications are as indicated in b). b) Picked phases are indicated by vertical coloured bars (P_s - yellow; P_g - orange; P_n - red; P_mP - green). The height of the coloured bar represents the pick uncertainty, the black lines on top are the modelled arrival times. c) Calculated refracted and reflected rays traced through the velocity-depth model (layer boundaries indicated by the black lines). Ray colours match the assigned pick phases (in b), the location of OBS 25 is indicated by an inverted red triangle, and other OBSs are depicted as inverted grey triangles.

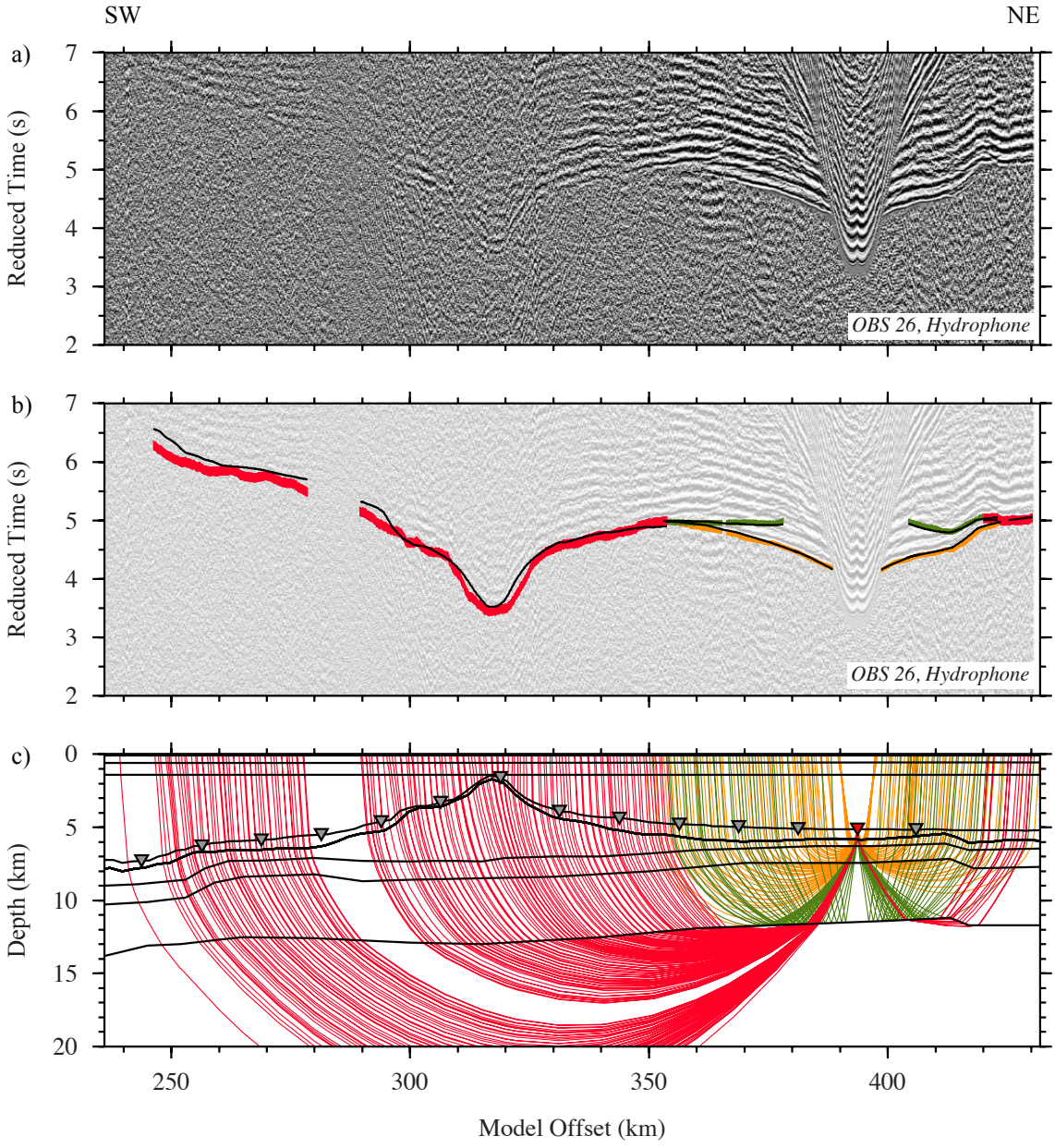

Figure C.22: WA seismic data and modelled arrival comparison for OBS 26. a) Filtered hydrophone data from OBS 26 reduced at 8 km s^{-1}, phase identifications are as indicated in b). b) Picked phases are indicated by vertical coloured bars (P_s - yellow; P_g - orange; P_n - red; P_mP - green). The height of the coloured bar represents the pick uncertainty, the black lines on top are the modelled arrival times. c) Calculated refracted and reflected rays traced through the velocity-depth model (layer boundaries indicated by the black lines). Ray colours match the assigned pick phases (in b), the location of OBS 26 is indicated by an inverted red triangle, and other OBSs are depicted as inverted grey triangles.

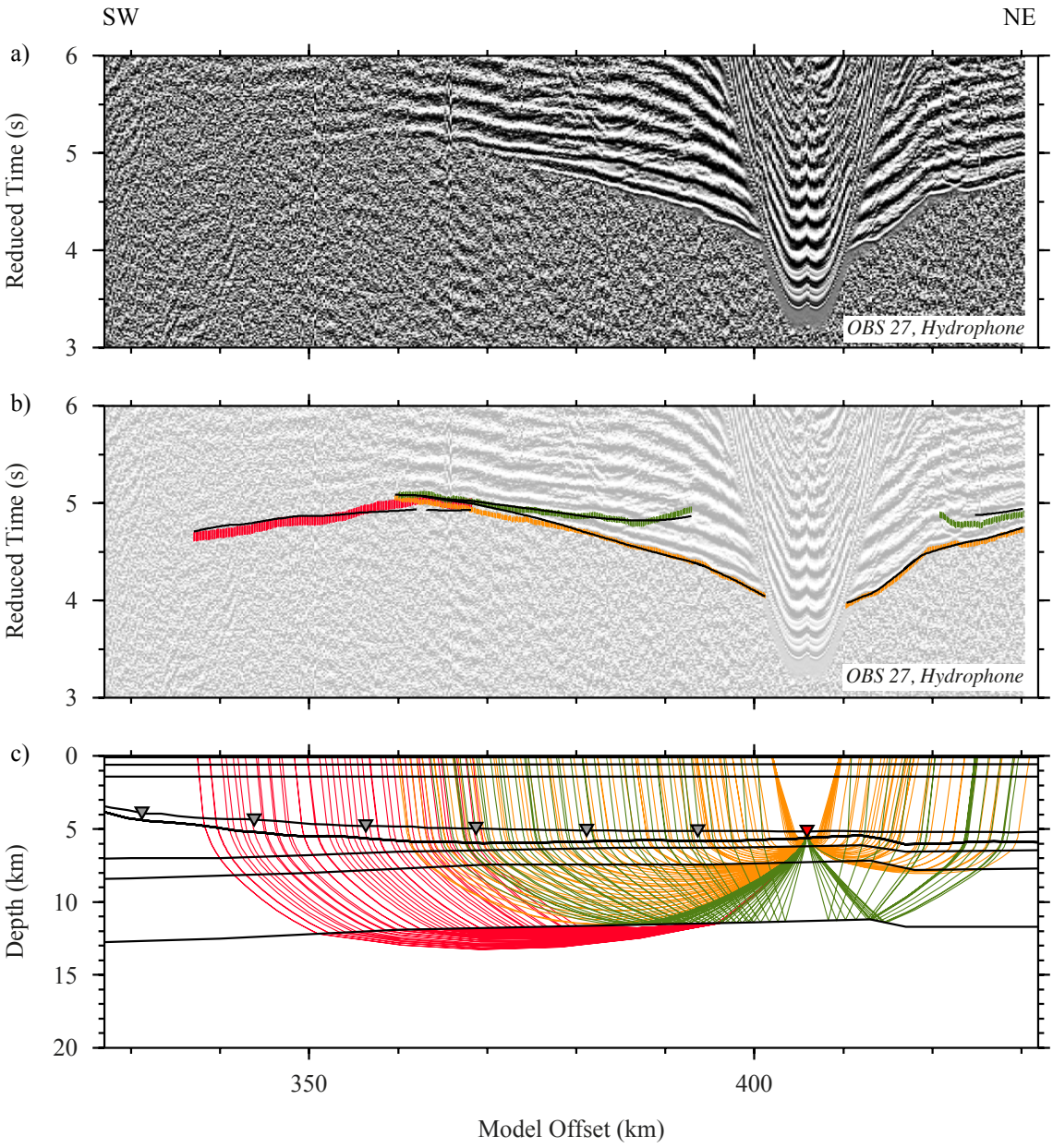

Figure C.23: WA seismic data and modelled arrival comparison for OBS 27. a) Filtered hydrophone data from OBS 27 reduced at 8 km s^{-1}, phase identifications are as indicated in b). b) Picked phases are indicated by vertical coloured bars (P_s - yellow; P_g - orange; P_n - red; P_mP - green). The height of the coloured bar represents the pick uncertainty, the black lines on top are the modelled arrival times. c) Calculated refracted and reflected rays traced through the velocity-depth model (layer boundaries indicated by the black lines). Ray colours match the assigned pick phases (in b), the location of OBS 27 is indicated by an inverted red triangle, and other OBSs are depicted as inverted grey triangles.

Appendix D

The final forward velocity-depth model is presented below in the *rayinvr* v.in file format (Zelt & Smith, 1992). Note that the velocity model is annotated with comment lines (beginning with a #) to inform the reader what each model section represents within the model space. These comment lines should be removed before the model is input into *rayinvr*.

```
# -------------------------- Water column 1 -------------------------- #
# -> Layer depths
 1    0.00  57.14 169.28 294.04 406.28 431.88
 0   0.000  0.000  0.000  0.000  0.000  0.000
         1      1      1      1      1      1
# -> Upper layer velocities
 1    0.00  57.14 169.28 210.00 294.04 406.28 431.88
 0   1.516  1.515  1.524  1.526  1.525  1.524  1.525
         1      1      1      1      1      1      1
# -> Lower layer velocities
 1    0.00  57.14 169.28 210.00 294.04 406.28 431.88
 0   1.519  1.519  1.524  1.529  1.527  1.524  1.525
         1      1      1      1      1      1      1

# -------------------------- Water column 2 -------------------------- #
# -> Layer depths
 2    0.00  57.14 169.28 294.04 406.28 431.88
 0   0.100  0.100  0.100  0.100  0.100  0.100
         1      1      1      1      1      1
# -> Upper layer velocities
 2  431.88
 0    0.00
         1
# -> Lower layer velocities
 2    0.00  57.14 169.28 210.00 294.04 406.28 431.88
 0   1.483  1.481  1.492  1.496  1.490  1.492  1.493
         1      1      1      1      1      1      1

# -------------------------- Water column 3 -------------------------- #
# -> Layer depths
 3    0.00  57.14 169.28 210.00 294.04 406.28 431.88
 0   0.600  0.600  0.600  0.600  0.600  0.550  0.550
         1      1      1      1      1      1      1
# -> Upper layer velocities
```

```
 3  431.88
 0    0.00
         1
# -> Lower layer velocities
 3    0.00  57.14 169.28 210.00 294.04 406.28 431.88
 0   1.485  1.485  1.486  1.486  1.485  1.492  1.492
         1      1      1      1      1      1      1

# ------------------------- Water column 4 -------------------------- #
# -> Layer depths
 4    0.00  14.99  19.98  57.14 169.28 294.04 406.28 431.88
 0   1.400  1.354  1.256  1.400  1.400  1.400  1.400  1.400
         1      1      1      1      1      1      1      1
# -> Upper layer velocities
 4  431.88
 0    0.00
         1
# -> Lower layer velocities
 4    0.00   9.99  19.98  29.98  39.96  49.95  59.94  69.93  79.92  89.91
 1   1.489  1.487  1.484  1.486  1.486  1.486  1.488  1.488  1.489  1.488
         1      1      1      1      1      1      1      1      1      1
 4   99.90 109.89 119.89 129.88 139.87 149.86 159.85 169.84 179.84 189.83
 1   1.492  1.496  1.503  1.510  1.513  1.513  1.515  1.516  1.532  1.535
         1      1      1      1      1      1      1      1      1      1
 4  199.82 209.81 219.80 229.79 239.78 249.77 259.76 269.75 279.73 289.72
 1   1.566  1.582  1.595  1.565  1.568  1.557  1.542  1.538  1.533  1.524
         1      1      1      1      1      1      1      1      1      1
 4  299.71 309.69 319.68 329.67 339.65 349.64 359.62 369.61 379.59 389.57
 1   1.507  1.503  1.487  1.510  1.515  1.519  1.522  1.524  1.526  1.527
         1      1      1      1      1      1      1      1      1      1
 4  399.55 409.52 419.51 429.49 431.88
 0   1.527  1.527  1.528  1.528  1.528
         1      1      1      1      1

# ------------------------ Sediment column -------------------------- #
# -> Layer depths
 5    0.00   1.87   3.75   5.62   7.49   9.37  11.24  13.11  14.99  16.86
 1   1.888  1.952  2.014  2.022  1.815  1.669  1.544  1.493  1.404  1.349
         0      0      0      0      0      0      0      0      0      0
 5   18.73  20.61  22.48  24.35  26.23  28.10  29.98  31.85  33.72  35.60
 1   1.356  1.327  1.370  1.581  1.703  1.771  1.814  1.851  1.905  1.934
```

```
      0      0      0      0      0      0      0      0      0      0
5  37.47  39.34  41.21  43.09  44.96  46.83  48.70  50.57  52.45  54.32
1  1.937  1.940  1.998  2.099  2.097  2.152  2.125  2.038  2.053  2.108
      0      0      0      0      0      0      0      0      0      0
5  56.19  58.07  59.94  61.81  63.68  65.55  67.43  69.30  71.17  73.05
1  2.173  2.186  2.183  2.139  2.031  1.945  1.838  2.051  2.016  1.933
      0      0      0      0      0      0      0      0      0      0
5  74.92  76.80  78.67  80.54  82.42  84.29  86.16  88.04  89.91  91.78
1  1.932  1.970  1.940  1.956  2.023  2.001  1.998  2.036  2.075  2.098
      0      0      0      0      0      0      0      0      0      0
5  93.66  95.53  97.40  99.28 101.15 103.03 104.90 106.77 108.65 110.52
1  2.113  2.117  2.159  2.231  2.289  2.306  2.474  2.504  2.514  2.663
      0      0      0      0      0      0      0      0      0      0
5 112.39 114.27 116.14 118.01 119.89 121.76 123.64 125.51 127.38 129.26
1  2.779  2.884  3.039  3.205  3.660  3.970  3.982  3.989  3.958  3.988
      0      0      0      0      0      0      0      0      0      0
5 131.13 133.00 134.88 136.75 138.62 140.50 142.37 144.24 146.12 147.99
1  3.993  3.983  3.998  4.022  4.018  4.017  4.010  3.988  3.952  3.978
      0      0      0      0      0      0      0      0      0      0
5 149.86 151.74 153.61 155.48 157.36 159.23 161.10 162.97 164.85 166.72
1  3.934  3.867  3.892  4.125  4.235  4.348  4.435  4.832  5.020  4.957
      0      0      0      0      0      0      0      0      0      0
5 168.60 170.47 172.34 174.22 176.09 177.96 179.84 181.71 183.58 185.46
1  4.500  4.350  4.750  4.970  5.080  5.225  5.462  5.564  5.434  5.399
      0      0      0      0      0      0      0      0      0      0
5 187.33 189.20 191.08 192.95 194.82 196.70 198.57 200.44 202.32 204.19
1  5.569  5.725  5.804  5.966  6.264  6.548  6.956  7.070  6.773  6.746
      0      0      0      0      0      0      0      0      0      0
5 206.06 207.94 209.81 211.68 213.56 215.43 217.30 219.18 221.05 222.92
1  6.784  7.279  7.626  7.830  7.795  7.714  7.966  8.466  8.512  8.356
      0      0      0      0      0      0      0      0      0      0
5 224.80 226.67 228.54 230.41 232.29 234.16 236.03 237.91 239.78 241.65
1  7.911  7.701  7.650  7.280  7.364  7.369  7.220  7.223  7.429  7.325
      0      0      0      0      0      0      0      0      0      0
5 243.52 245.40 247.27 249.14 251.02 252.89 254.76 256.64 258.51 260.38
1  7.301  7.279  6.981  6.876  6.587  6.518  6.279  6.266  6.093  6.052
      0      0      0      0      0      0      0      0      0      0
5 262.25 264.13 266.00 267.87 269.75 271.62 273.49 275.36 277.24 279.11
1  5.942  5.929  5.917  5.881  5.847  5.796  5.707  5.625  5.574  5.525
      0      0      0      0      0      0      0      0      0      0
5 280.98 282.85 284.73 286.60 288.47 290.34 292.21 294.09 295.96 297.83
```

```
 1   5.501  5.487  5.324  5.219  5.105  4.864  4.725  4.590  4.484  3.870
        0      0      0      0      0      0      0      0      0      0
 5  299.71 301.58 303.45 305.32 307.20 309.07 310.94 312.81 314.69 316.56
 1   3.667  3.550  3.540  3.398  3.191  3.091  2.724  2.264  1.815  1.489
        0      0      0      0      0      0      0      0      0      0
 5  318.43 320.31 322.18 324.05 325.92 327.80 329.67 331.54 333.41 335.28
 1   1.557  1.846  2.483  2.956  3.298  3.551  3.721  3.932  3.950  4.111
        0      0      0      0      0      0      0      0      0      0
 5  337.16 339.03 340.90 342.77 344.65 346.52 348.39 350.26 352.13 354.01
 1   4.221  4.300  4.327  4.324  4.395  4.463  4.543  4.642  4.689  4.764
        0      0      0      0      0      0      0      0      0      0
 5  355.88 357.75 359.62 361.50 363.37 365.24 367.11 368.98 370.86 372.73
 1   4.784  4.805  4.831  4.837  4.926  4.928  4.947  4.966  5.001  5.024
        0      0      0      0      0      0      0      0      0      0
 5  374.60 376.47 378.34 380.22 382.09 383.96 385.83 387.70 389.57 391.45
 1   5.035  5.072  5.080  5.094  5.089  5.103  5.137  5.142  5.132  5.127
        0      0      0      0      0      0      0      0      0      0
 5  393.32 395.19 397.06 398.93 400.80 402.67 404.54 406.41 408.28 410.15
 1   5.131  5.131  5.128  5.135  5.143  5.156  5.156  5.153  5.147  5.148
        0      0      0      0      0      0      0      0      0      0
 5  412.02 413.89 415.76 417.63 419.51 421.38 423.25 425.12 426.99 428.86
 1   5.167  5.188  5.204  5.214  5.208  5.205  5.199  5.205  5.214  5.219
        0      0      0      0      0      0      0      0      0      0
 5  430.73 431.88
 0   5.204  5.201
        0      0
# -> Upper layer velocities
 5   0.000  40.00  50.00  60.00  70.00  80.00  90.00 100.00 110.00 120.00
 1   1.750  1.750  1.700  1.650  1.770  1.650  1.700  1.700  1.700  1.800
        0      0      0      0      0      0      0      0      0      0
 5  140.00 160.00 180.00 220.00 315.00 431.88
 0   1.750  1.725  1.725  1.800  1.800  1.800
        0      0      0      0      0      0
# -> Lower layer velocities
 5   0.000  40.00  50.00  60.00  70.00  80.00  90.00 100.00 125.00 140.00
 1   2.800  2.800  2.730  2.750  2.850  2.900  2.920  2.850  2.850  2.850
        0      0      0      0      0      0      0      0      0      0
 5  160.00 180.00 210.00 220.00 315.00 431.88
 0   2.400  2.800  2.800  3.100  3.100  3.100
        0      0      0      0      0      0
```

```
# ------------------------ Overriding crust 1 ------------------------- #
# -> Layer depths
 6    0.00   2.40   4.90   7.39   9.89  12.39  14.89  17.39  19.88  22.38
 1   2.971  3.087  2.991  2.665  2.322  2.246  2.085  1.968  1.849  1.902
       1      1      1      1      1      1      1      1      1      1
 6   24.88  27.38  29.88  32.37  34.87  37.37  39.86  42.36  44.86  47.36
 1   2.322  2.500  2.900  3.200  3.150  3.350  3.350  3.300  3.350  3.600
       1      1      1      1      1      1      1      1      1      1
 6   49.85  52.35  56.19  59.94  63.68  65.55  68.00  69.30  71.17  73.05
 1   3.300  3.300  3.450  3.550  3.400  3.000  2.900  2.950  3.150  3.200
       1      1      1      1      1      1      1      1      1      1
 6   74.82  77.32  79.82  82.32  84.81  87.31  89.81  92.31  94.81  97.30
 1   3.300  3.250  3.300  3.182  3.300  3.275  3.230  3.233  3.178  3.097
       1      1      1      1      1      1      1      1      1      1
 6   99.80 102.30 104.80 107.30 109.80 112.50 114.79 117.29 119.50 122.29
 1   3.089  3.211  3.174  3.095  3.091  3.377  3.500  3.650  3.860  4.682
       1      1      1      1      1      1      1      1      1      1
 6  124.78 127.28 129.78 132.28 134.78 137.27 139.77 142.27 144.77 147.26
 1   4.600  4.720  4.750  4.750  4.650  4.550  4.950  4.850  4.6500  4.550
       1      1      1      1      1      1      1      1      1      1
 6  149.76 152.26 154.76 157.26 159.75 162.25 164.75 167.25 170.00 171.40
 1   4.550  4.733  4.474  4.704  4.950  4.900  5.220  5.150  4.870  5.260
       1      1      1      1      1      1      1      1      1      1
 6  172.80 174.00 179.74 182.24 184.73 187.23 189.73 192.23 194.72 197.22
 1   5.450  5.450  5.700  5.700  5.600  5.800  6.000  6.300  6.400  6.900
       1      1      1      1      1      1      1      1      1      1
 6  199.72 202.22 204.72 207.21 209.71 212.21 214.71 217.20 219.70 222.20
 1   7.320  6.997  6.987  7.403  7.861  7.951  7.996  8.497  8.940  8.848
       1      1      1      1      1      1      1      1      1      1
 6  224.70 227.19 229.69 232.19 234.69 237.18 239.68 242.18 244.67 247.17
 1   8.412  8.234  7.847  7.916  7.902  7.789  8.000  7.850  7.750  7.500
       1      1      1      1      1      1      1      1      1      1
 6  249.67 252.17 254.66 257.16 259.66 262.15 264.65 267.15 269.65 272.14
 1   7.421  7.049  6.720  6.698  6.657  6.559  6.551  6.541  6.525  6.470
       1      1      1      1      1      1      1      1      1      1
 6  274.64 277.14 279.63 282.13 284.62 287.12 289.62 292.12 294.61 297.11
 1   6.460  6.453  6.388  6.246  5.983  5.637  5.435  5.327  5.220  4.715
       1      1      1      1      1      1      1      1      1      1
 6  299.61 302.10 304.60 307.10 309.59 312.09 314.59 317.08 319.58 322.08
 1   3.950  3.650  3.650  3.500  3.150  2.800  2.000  1.700  1.950  2.771
       1      1      1      1      1      1      1      1      1      1
```

```
 6  324.57 327.07 329.57 332.06 334.56 337.06 339.55 342.05 344.55 347.04
 1   3.396  3.832  4.237  4.468  4.557  4.683  4.886  5.119  5.223  5.396
        1      1      1      1      1      1      1      1      1      1
 6  349.54 352.04 354.53 357.03 359.52 362.02 364.52 367.01 369.51 372.00
 1   5.489  5.481  5.526  5.686  5.777  5.885  5.889  5.908  5.974  5.933
        1      1      1      1      1      1      1      1      1      1
 6  374.50 377.00 379.49 381.99 384.48 386.98 389.48 391.97 394.46 396.96
 1   5.937  5.908  5.887  5.854  5.821  5.763  5.780  5.808  5.843  5.798
        1      1      1      1      1      1      1      1      1      1
 6  399.45 401.95 404.44 406.93 409.43 411.92 414.42 416.91 419.41 421.90
 1   5.768  5.709  5.663  5.587  5.511  5.444  5.671  6.035  6.021  5.965
        1      1      1      1      1      1      1      1      1      1
 6  424.40 426.89 429.39 431.88
 0   5.868  5.858  5.886  5.909
        1      1      1      1
# -> Upper layer velocities
 6    0.00  50.00  60.00  70.00  75.00  85.00 100.00 120.00 125.00 130.00
 1   3.300  3.300  3.300  2.800  3.300  3.300  2.800  2.800  2.600  2.800
        0      0      0      0      0      0      0      0      0
 6  160.00 170.00 180.00 185.00 200.00 205.00 210.00 431.88
 0   2.800  2.600  2.800  2.800  2.800  2.800  2.800  2.800
        0      0      0      0      0      0      0      0
# -> Lower layer velocities
 6    0.00  40.00  60.00  75.00  80.00 100.00 110.00 120.00 127.00 130.00
 1   4.500  4.500  4.200  4.100  4.100  4.800  4.600  4.200  4.200  4.200
        0      0      0      0      0      0      0      0      0      0
 6  140.00 160.00 170.00 175.00 180.00 185.00 200.00 205.00 210.00 431.88
 0   4.400  4.500  4.000  3.800  3.800  3.800  3.700  3.700  3.700  3.700
        0      0      0      0      0      0      0      0      0      0


# ------------------------ Overriding crust 2 ------------------------- #
# -> Layer depths
 7    0.00   5.00  15.00  22.00  25.00  30.00  40.00  50.00  55.00  60.00
 1   5.500  5.500  4.700  4.500  5.000  5.500  5.500  5.500  5.200  4.900
        1      1      1      1      1      1      1      1      1      1
 7   67.00  70.00  74.00  80.00  87.00  90.00 100.00 110.00 120.00 127.00
 1   4.600  4.650  5.000  4.750  4.600  4.200  4.500  4.600  4.700  6.200
        1      1      1      1      1      1      1      1      1      1
 7  130.00 138.00 142.00 145.00 150.00 155.00 159.00 166.00 170.00 172.00
 1   6.100  5.900  5.700  6.100  6.100  5.800  5.300  5.700  6.600  6.900
```

```
        1      1      1      1      1      1      1      1      1      1
 7  175.00 180.00 182.00 185.00 194.00 200.00 204.00 212.00 218.00 222.20
 1   6.800  6.600  6.300  5.800  6.700  7.700  7.200  8.400  9.200  8.848
        1      1      1      1      1      1      1      1      1      1
 7  224.70 227.19 229.69 232.19 234.69 237.18 239.68 242.18 244.67 247.17
 1   8.412  8.234  7.847  7.916  7.902  7.789  8.000  7.850  7.750  7.500
        1      1      1      1      1      1      1      1      1      1
 7  249.67 252.17 254.66 257.16 259.66 262.15 264.65 267.15 269.65 272.14
 1   7.421  7.049  6.720  6.698  6.657  6.559  6.551  6.541  6.525  6.470
        1      1      1      1      1      1      1      1      1      1
 7  274.64 277.14 279.63 282.13 284.62 287.12 289.62 292.12 294.61 297.11
 1   6.460  6.453  6.388  6.246  5.983  5.637  5.435  5.327  5.220  4.715
        1      1      1      1      1      1      1      1      1      1
 7  299.61 302.10 304.60 307.10 309.59 312.09 314.59 317.08 319.58 322.08
 1   3.950  3.650  3.650  3.500  3.150  2.800  2.000  1.700  1.950  2.771
        1      1      1      1      1      1      1      1      1      1
 7  324.57 327.07 329.57 332.06 334.56 337.06 339.55 342.05 344.55 347.04
 1   3.396  3.832  4.237  4.468  4.557  4.683  4.886  5.119  5.223  5.396
        1      1      1      1      1      1      1      1      1      1
 7  349.54 352.04 354.53 357.03 359.52 362.02 364.52 367.01 369.51 372.00
 1   5.489  5.481  5.526  5.686  5.777  5.885  5.889  5.908  5.974  5.933
        1      1      1      1      1      1      1      1      1      1
 7  374.50 377.00 379.49 381.99 384.48 386.98 389.48 391.97 394.46 396.96
 1   5.937  5.908  5.887  5.854  5.821  5.763  5.780  5.808  5.843  5.798
        1      1      1      1      1      1      1      1      1      1
 7  399.45 401.95 404.44 406.93 409.43 411.92 414.42 416.91 419.41 421.90
 1   5.768  5.709  5.663  5.587  5.511  5.444  5.671  6.035  6.021  5.965
        1      1      1      1      1      1      1      1      1      1
 7  424.40 426.89 429.39 431.88
 0   5.868  5.858  5.886  5.909
        1      1      1      1
# -> Upper layer velocities
 7    0.00  65.00  70.00  90.00 110.00 115.00 125.00 130.00 140.00 160.00
 1   4.700  4.700  5.300  5.300  4.700  4.700  5.300  5.300  5.300  5.200
        0      0      0      0      0      0      0      0      0      0
 7  170.00 175.00 180.00 200.00 210.00 431.88
 0   4.500  4.000  4.000  4.000  3.900  3.900
        0      0      0      0      0      0
# -> Lower layer velocities
 7    0.00  50.00 130.00 140.00 150.00 165.00 180.00 200.00 210.00 431.88
 0   6.300  6.300  6.400  6.600  6.200  5.300  5.000  5.000  4.600  4.600
```

```
         0      0      0      0      0      0      0      0      0      0

# ------------------------ Overriding crust 3 ------------------------- #
# -> Layer depths
 8    0.00   5.00  15.00  22.00  30.00  50.00  68.00  73.00  80.00  87.00
 1   8.300  8.300  7.500  7.500  8.300  8.300  7.800  8.000  8.000  6.400
         1      1      1      1      1      1      1      1      1      1
 8  100.00 120.00 126.00 130.00 135.00 145.00 150.00 155.00 160.00 165.00
 1   6.800  6.800  8.900  8.800  8.600  8.600  8.800  8.900  9.000  9.150
         1      1      1      1      1      1      1      1      1      1
 8  170.00 175.00 180.00 185.00 190.00 195.00 200.00 205.00 218.00 222.20
 1   9.700  9.900  9.900  9.700 10.000 10.200 11.000 11.500  9.400  8.848
         1      1      1      1      1      1      1      1      1      1
 8  224.70 227.19 229.69 232.19 234.69 237.18 239.68 242.18 244.67 247.17
 1   8.412  8.234  7.847  7.916  7.902  7.789  8.000  7.850  7.750  7.500
         1      1      1      1      1      1      1      1      1      1
 8  249.67 252.17 254.66 257.16 259.66 262.15 264.65 267.15 269.65 272.14
 1   7.421  7.049  6.720  6.698  6.657  6.559  6.551  6.541  6.525  6.470
         1      1      1      1      1      1      1      1      1      1
 8  274.64 277.14 279.63 282.13 284.62 287.12 289.62 292.12 294.61 297.11
 1   6.460  6.453  6.388  6.246  5.983  5.637  5.435  5.327  5.220  4.715
         1      1      1      1      1      1      1      1      1      1
 8  299.61 302.10 304.60 307.10 309.59 312.09 314.59 317.08 319.58 322.08
 1   3.950  3.650  3.650  3.500  3.150  2.800  2.000  1.700  1.950  2.771
         1      1      1      1      1      1      1      1      1      1
 8  324.57 327.07 329.57 332.06 334.56 337.06 339.55 342.05 344.55 347.04
 1   3.396  3.832  4.237  4.468  4.557  4.683  4.886  5.119  5.223  5.396
         1      1      1      1      1      1      1      1      1      1
 8  349.54 352.04 354.53 357.03 359.52 362.02 364.52 367.01 369.51 372.00
 1   5.489  5.481  5.526  5.686  5.777  5.885  5.889  5.908  5.974  5.933
         1      1      1      1      1      1      1      1      1      1
 8  374.50 377.00 379.49 381.99 384.48 386.98 389.48 391.97 394.46 396.96
 1   5.937  5.908  5.887  5.854  5.821  5.763  5.780  5.808  5.843  5.798
         1      1      1      1      1      1      1      1      1      1
 8  399.45 401.95 404.44 406.93 409.43 411.92 414.42 416.91 419.41 421.90
 1   5.768  5.709  5.663  5.587  5.511  5.444  5.671  6.035  6.021  5.965
         1      1      1      1      1      1      1      1      1      1
 8  424.40 426.89 429.39 431.88
 0   5.868  5.858  5.886  5.909
         1      1      1      1
# -> Upper layer velocities
```

```
 8    0.00  50.00  90.00 130.00 140.00 150.00 160.00 180.00 210.00 431.88
 0   6.300  6.300  6.500  6.500  6.600  6.400  5.800  5.000  4.600  4.600
        0      0      0      0      0      0      0      0      0      0
# -> Lower layer velocities
 8    0.00  50.00  70.00  80.00 120.00 130.00 140.00 160.00 195.00 431.88
 0   6.700  6.700  7.200  7.400  7.400  7.200  7.000  6.500  6.000  6.000
        0      0      0      0      0      0      0      0      0      0

# ------------------------ Overriding mantle -------------------------- #
# -> Layer depths
 9    0.00  01.00  10.00  20.00  30.00  40.00  50.00  70.00  80.00  90.00
 1  15.000 15.000 15.500 15.500 15.000 15.000 15.000 15.000 14.500 14.000
        1      1      1      1      1      1      1      1      1      1
 9  100.00 110.00 120.00 140.00 160.00 180.00 190.00 205.00 218.00 222.20
 1  14.000 13.500 13.500 13.500 13.500 14.500 14.700 11.500  9.400  8.848
        1      1      1      1      1      1      1      1      1      1
 9  224.70 227.19 229.69 232.19 234.69 237.18 239.68 242.18 244.67 247.17
 1   8.412  8.234  7.847  7.916  7.902  7.789  8.000  7.850  7.750  7.500
        1      1      1      1      1      1      1      1      1      1
 9  249.67 252.17 254.66 257.16 259.66 262.15 264.65 267.15 269.65 272.14
 1   7.421  7.049  6.720  6.698  6.657  6.559  6.551  6.541  6.525  6.470
        1      1      1      1      1      1      1      1      1      1
 9  274.64 277.14 279.63 282.13 284.62 287.12 289.62 292.12 294.61 297.11
 1   6.460  6.453  6.388  6.246  5.983  5.637  5.435  5.327  5.220  4.715
        1      1      1      1      1      1      1      1      1      1
 9  299.61 302.10 304.60 307.10 309.59 312.09 314.59 317.08 319.58 322.08
 1   3.950  3.650  3.650  3.500  3.150  2.800  2.000  1.700  1.950  2.771
        1      1      1      1      1      1      1      1      1      1
 9  324.57 327.07 329.57 332.06 334.56 337.06 339.55 342.05 344.55 347.04
 1   3.396  3.832  4.237  4.468  4.557  4.683  4.886  5.119  5.223  5.396
        1      1      1      1      1      1      1      1      1      1
 9  349.54 352.04 354.53 357.03 359.52 362.02 364.52 367.01 369.51 372.00
 1   5.489  5.481  5.526  5.686  5.777  5.885  5.889  5.908  5.974  5.933
        1      1      1      1      1      1      1      1      1      1
 9  374.50 377.00 379.49 381.99 384.48 386.98 389.48 391.97 394.46 396.96
 1   5.937  5.908  5.887  5.854  5.821  5.763  5.780  5.808  5.843  5.798
        1      1      1      1      1      1      1      1      1      1
 9  399.45 401.95 404.44 406.93 409.43 411.92 414.42 416.91 419.41 421.90
 1   5.768  5.709  5.663  5.587  5.511  5.444  5.671  6.035  6.021  5.965
        1      1      1      1      1      1      1      1      1      1
 9  424.40 426.89 429.39 431.88
```

```
 0   5.868  5.858  5.886  5.909
         1      1      1      1
# -> Upper layer velocities
 9    0.00  50.00  70.00 100.00 200.00 431.88
 0   7.800  7.800  7.800  7.800  7.800  7.800
         0      0      0      0      0
# -> Lower layer velocities
 9    0.00 100.00 150.00 170.00 205.00 431.88
 0   8.500  8.500  8.100  8.000  7.800  7.800
         0      0      0      0      0      0

# -------------------------- Pacific crust 1 -------------------------- #
# -> Layer depths
10  000.00  20.00 119.00 131.00 154.00 177.00 190.00 205.00 218.00 222.20
 1  35.000 35.000 35.000 30.000 23.000 17.000 14.700 11.500  9.400  8.848
         1      1      1      1      1      1      1      1      1      1
10  224.70 227.19 229.69 232.19 234.69 237.18 239.68 242.18 244.67 247.17
 1   8.412  8.234  7.847  7.916  7.902  7.789  8.000  7.850  7.750  7.500
         1      1      1      1      1      1      1      1      1      1
10  249.67 252.17 254.66 257.16 259.66 262.15 264.65 267.15 269.65 272.14
 1   7.421  7.049  6.720  6.698  6.657  6.559  6.551  6.541  6.525  6.470
         1      1      1      1      1      1      1      1      1      1
10  274.64 277.14 279.63 282.13 284.62 287.12 289.62 292.12 294.61 297.11
 1   6.460  6.453  6.388  6.246  5.983  5.637  5.435  5.327  5.220  4.715
         1      1      1      1      1      1      1      1      1      1
10  299.61 302.10 304.60 307.10 309.59 312.09 314.59 317.08 319.58 322.08
 1   3.950  3.650  3.650  3.500  3.150  2.800  2.000  1.700  1.950  2.771
         1      1      1      1      1      1      1      1      1      1
10  324.57 327.07 329.57 332.06 334.56 337.06 339.55 342.05 344.55 347.04
 1   3.396  3.832  4.237  4.468  4.557  4.683  4.886  5.119  5.223  5.396
         1      1      1      1      1      1      1      1      1      1
10  349.54 352.04 354.53 357.03 359.52 362.02 364.52 367.01 369.51 372.00
 1   5.489  5.481  5.526  5.686  5.777  5.885  5.889  5.908  5.974  5.933
         1      1      1      1      1      1      1      1      1      1
10  374.50 377.00 379.49 381.99 384.48 386.98 389.48 391.97 394.46 396.96
 1   5.937  5.908  5.887  5.854  5.821  5.763  5.780  5.808  5.843  5.798
         1      1      1      1      1      1      1      1      1      1
10  399.45 401.95 404.44 406.93 409.43 411.92 414.42 416.91 419.41 421.90
 1   5.768  5.709  5.663  5.587  5.511  5.444  5.671  6.035  6.021  5.965
         1      1      1      1      1      1      1      1      1      1
10  424.40 426.89 429.39 431.88
```

```
 0   5.868  5.858  5.886  5.909
         1      1      1      1
# -> Upper layer velocities
10    0.00  20.00  40.00  60.00  80.00 100.00 120.00 140.00 160.00 180.00
 1   3.300  3.300  3.300  3.300  3.300  3.300  3.300  3.300  3.300  3.300
         0      0      0      0      0      0      0      0      0      0
10  200.00 220.00 240.00 270.00 280.00 290.00 310.00 315.00 320.00 350.00
 1   3.500  3.500  3.500  3.400  3.400  3.200  3.200  3.000  3.500  3.500
         0      0      0      0      0      0      0      0      0      0
10  370.00 431.88
 0   3.400  3.400
         0      0
# -> Lower layer velocities
10    0.00  20.00  40.00  60.00  80.00 100.00 120.00 140.00 160.00 180.00
 1   4.200  4.200  4.200  4.300  4.300  4.300  4.300  4.300  4.300  4.300
         0      0      0      0      0      0      0      0      0      0
10  240.00 250.00 260.00 280.00 305.00 315.00 320.00 360.00 370.00 431.88
 0   5.400  5.400  5.400  5.500  5.700  5.700  5.800  5.700  5.900  5.900
         0      0      0      0      0      0      0      0      0      0

# -------------------------- Pacific crust 2 -------------------------- #
# -> Layer depths
11  000.00  20.00 121.00 133.00 156.00 177.00 195.00 205.00 218.00 222.20
 1  35.000 35.000 35.000 30.000 23.000 17.500 14.200 12.000  9.900  9.300
         1      1      1      1      1      1      1      1      1      1
11  234.70 234.80 234.90 235.00 243.00 253.00 257.00 262.00 270.00 280.00
 1   9.000  9.000  9.000  9.000  8.900  8.600  7.800  7.300  7.250  7.100
         0      0      0      0      0      0      0      0      0      0
11  290.00 300.00 305.00 310.00 315.00 320.00 330.00 340.00 350.00 360.00
 1   7.300  7.350  7.300  7.300  7.350  7.100  7.000  7.000  6.800  6.550
         0      0      0      0      0      0      0      0      0      0
11  370.00 385.00 397.00 412.00 417.00 431.88
 0   6.450  6.300  6.300  6.100  6.550  6.450
         0      0      0      0      0      0
# -> Upper layer velocities
11  000.00 220.00 260.00 280.00 300.00 320.00 350.00 370.00 380.00 431.88
 0   5.400  5.400  5.400  5.500  5.500  5.750  5.800  5.900  5.900  5.900
         0      0      0      0      0      0      0      0      0      0
# -> Lower layer velocities
11    0.00 200.00 240.00 290.00 350.00 370.00 431.88
 0   6.200  6.200  6.400  6.350  6.600  6.500  6.500
```

```
        0      0      0      0      0      0      0

# -------------------------- Pacific crust 3 -------------------------- #
# -> Layer depths
12    0.00 127.00 139.00 161.00 177.00 195.00 205.00 218.00 222.20 235.00
 1  35.000 35.000 30.000 23.000 19.000 15.700 13.500 11.400 10.750 10.300
        0      0      0      0      0      0      0      0      0      0
12  245.00 253.00 259.00 265.00 280.00 290.00 300.00 330.00 350.00 370.00
 1  10.100  9.800  8.800  8.400  8.200  8.700  8.600  8.400  8.000  7.450
        0      0      0      0      0      0      0      0      0      0
12  395.00 413.00 418.00 431.88
 0   7.450  7.150  7.800  7.700
        0      0      0      0
# -> Upper layer velocities
12    0.00 200.00 260.00 280.00 300.00 310.00 330.00 431.88
 0   6.500  6.500  6.500  6.500  6.400  6.600  6.600  6.600
        0      0      0      0      0      0      0      0
# -> Lower layer velocities
12    0.00 280.00 290.00 300.00 310.00 330.00 360.00 380.00 400.00 431.88
 0   7.100  7.100  7.300  7.400  7.500  7.500  7.400  7.200  7.100  7.000
        0      0      0      0      0      0      0      0      0      0

# ----------------------- Pacific plate mantle ----------------------- #
# -> Layer depths
13    0.00   5.00  10.00  20.00  30.00  40.00 137.00 152.00 177.00 192.00
 1  35.000 35.000 35.000 35.000 35.000 35.000 35.000 30.000 23.000 20.000
        0      0      0      0      0      0      0      0      0      0
13  222.20 245.00 252.00 260.00 265.00 280.00 300.00 315.00 340.00 360.00
 1  14.900 13.100 13.000 12.700 12.500 12.600 12.900 13.000 12.500 11.900
        0      0      0      0      0      0      0      0      0      0
13  400.00 413.00 417.00 431.88
 0  11.400 11.200 11.700 11.700
        0      0      0      0
# -> Upper layer velocities
13    0.00 240.00 280.00 290.00 300.00 320.00 350.00 360.00 431.88
 0   7.500  7.400  7.400  7.500  7.600  7.700  7.700  7.700  7.700
        0      0      0      0      0      0      0      0      0
# -> Lower layer velocities
13    0.00 140.00 180.00 315.00 431.88
 0   7.400  7.400  8.000  8.700  8.700
        0      0      0      0      0
```

```
# ---------------------------- Model bottom ----------------------------- #
# -> Layer depths
14    0.00 100.00 200.00 260.00 431.88
 0    35.0   35.0   35.0   35.0   35.0
```

Appendix E

Figures E.1-E.12 show checkerboard test results, complementing those in Section 4.3.2. The checkerboard testing method is described in Section 4.3.

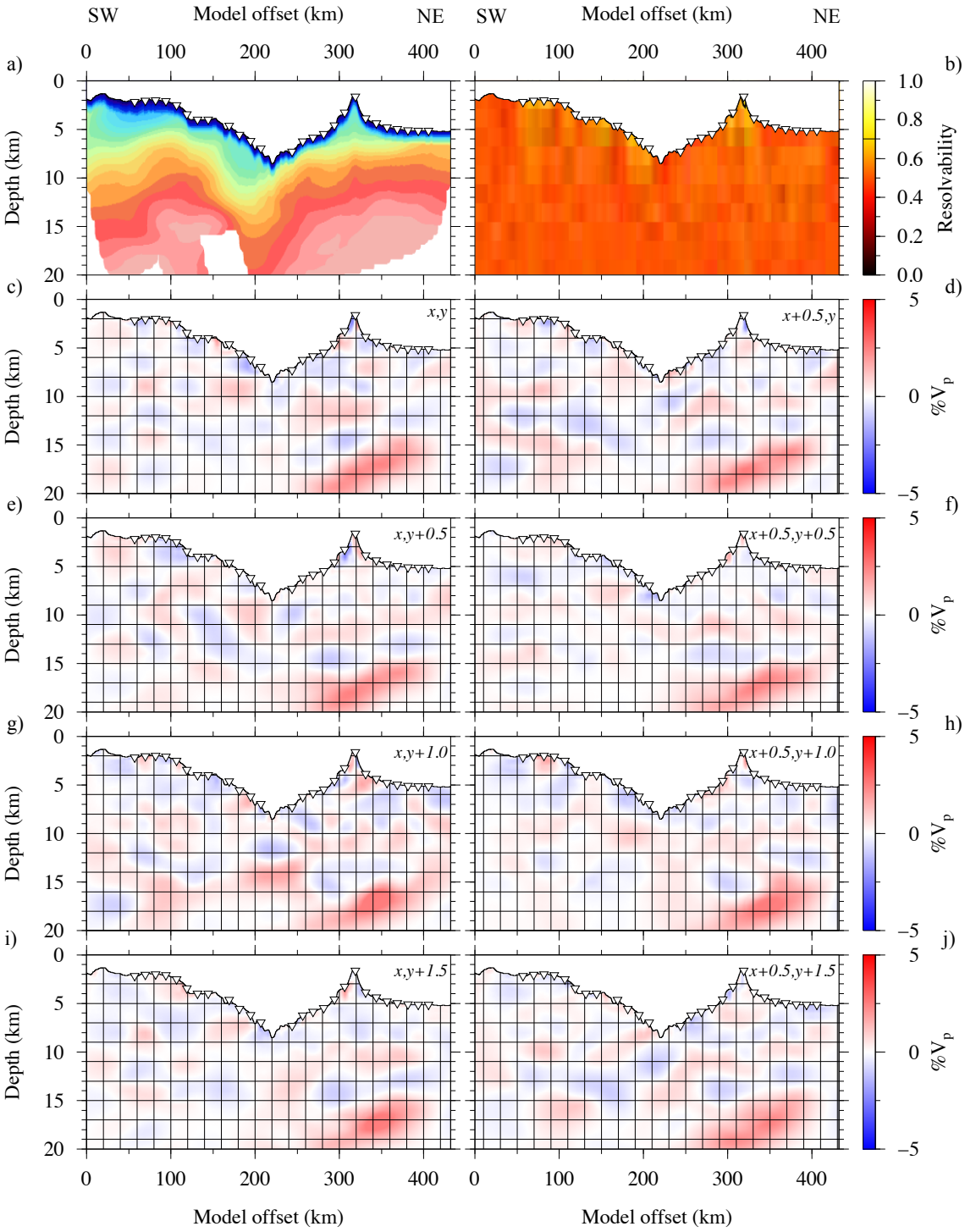

Figure E.1: Anomaly recovery testing using 20 km x 2 km, 5% anomaly, offset checkerboards. a) Final inversion velocity model. b) Average resolvability with regions exceeding the 0.7 threshold outlined by a contour if applicable. c)-j) Recovered checkerboards. Lateral and vertical checkerboard offsets, in checkerboard wavelengths, are indicated in the top righthand corner of each panel. Note that the grid overlay for c)-j) indicates the expected boundary of individual checkers within each test board.

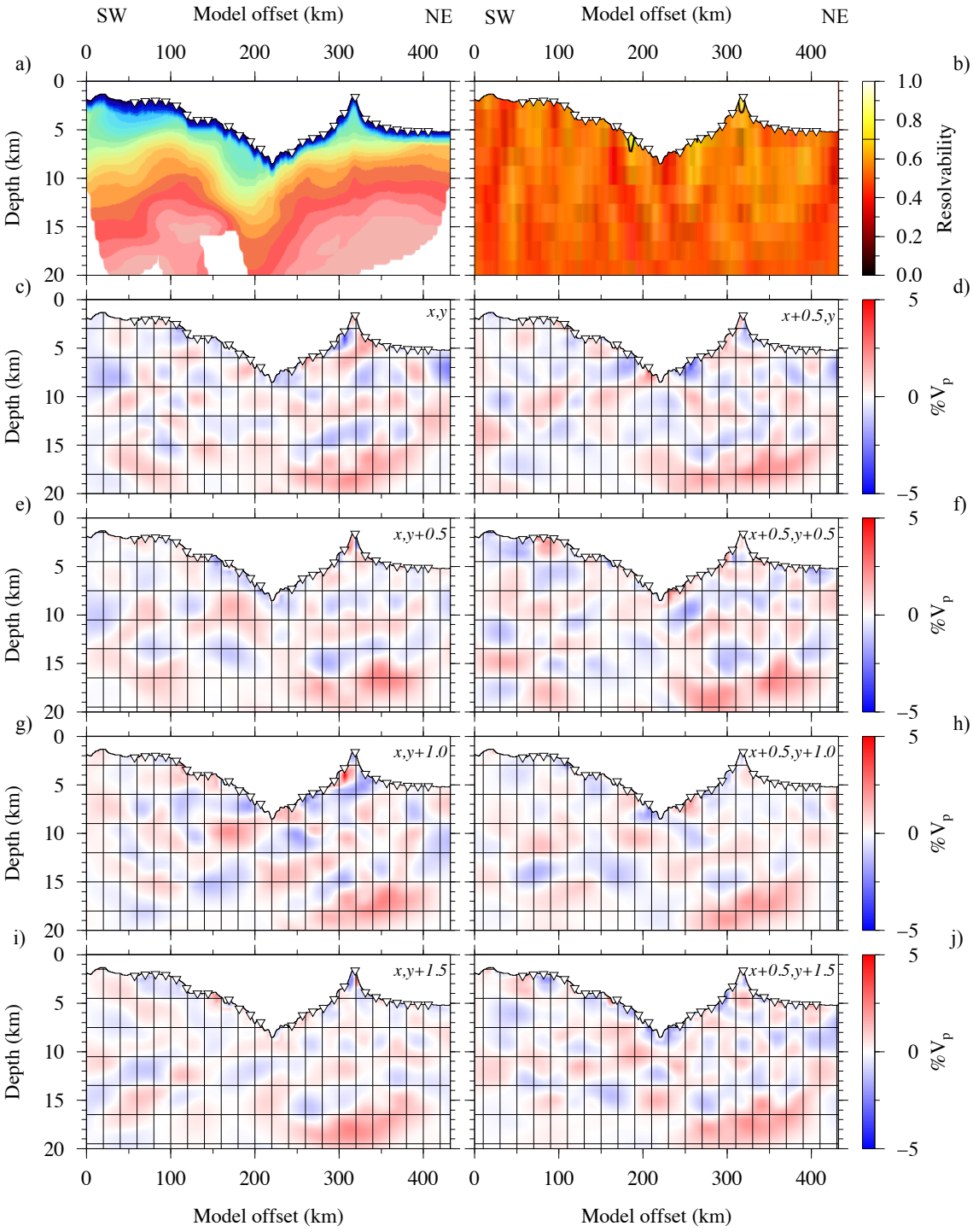

Figure E.2: Anomaly recovery testing using 20 km x 3 km, 5% anomaly, offset checkerboards. a) Final inversion velocity model. b) Average resolvability with regions exceeding the 0.7 threshold outlined by a contour if applicable. c)-j) Recovered checkerboards. Lateral and vertical checkerboard offsets, in checkerboard wavelengths, are indicated in the top righthand corner of each panel. Note that the grid overlay for c)-j) indicates the expected boundary of individual checkers within each test board.

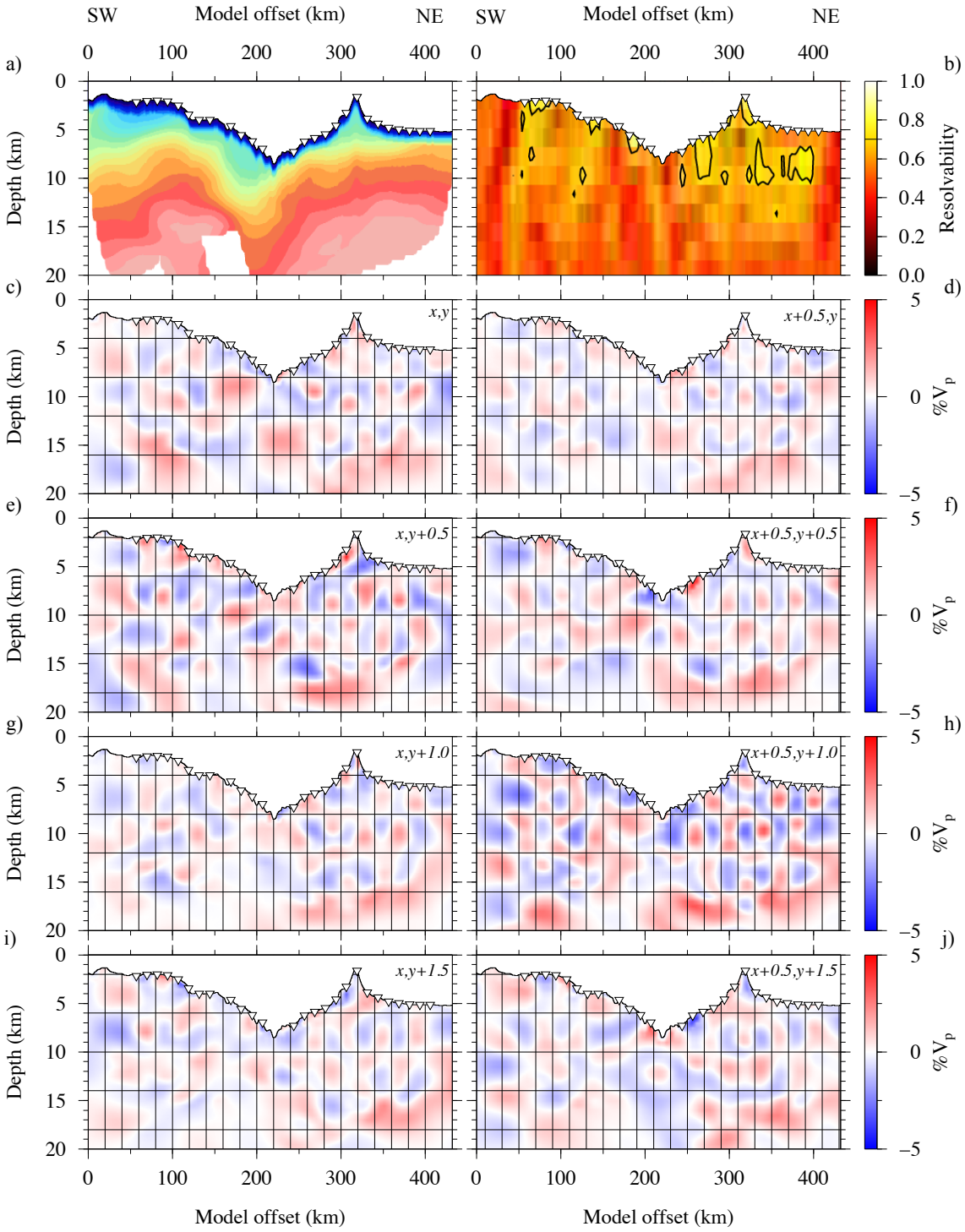

Figure E.3: Anomaly recovery testing using 20 km x 4 km, 5% anomaly, offset checkerboards. a) Final inversion velocity model. b) Average resolvability with regions exceeding the 0.7 threshold outlined by a contour if applicable. c)-j) Recovered checkerboards. Lateral and vertical checkerboard offsets, in checkerboard wavelengths, are indicated in the top righthand corner of each panel. Note that the grid overlay for c)-j) indicates the expected boundary of individual checkers within each test board.

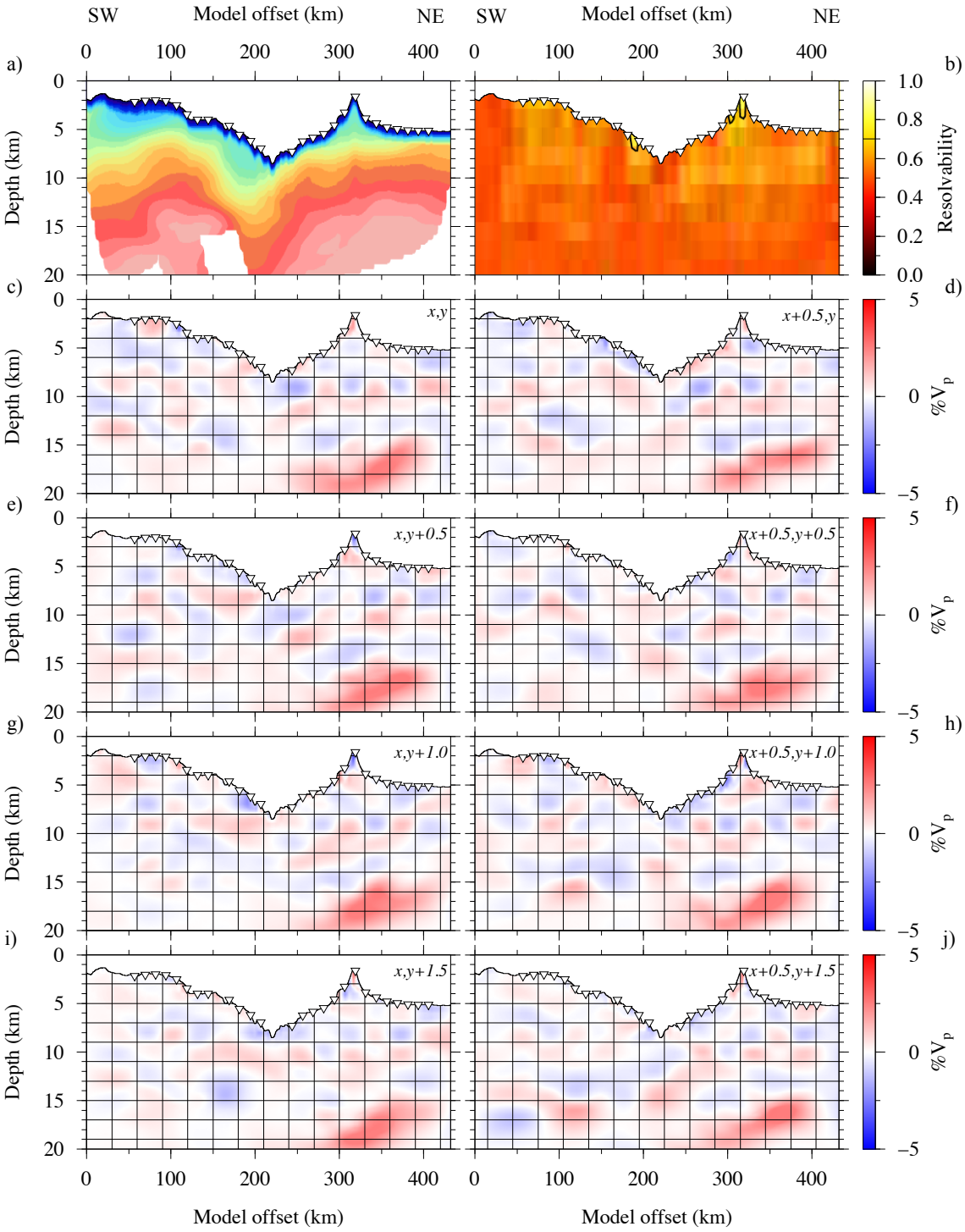

Figure E.4: Anomaly recovery testing using 30 km x 2 km, 5% anomaly, offset checkerboards. a) Final inversion velocity model. b) Average resolvability with regions exceeding the 0.7 threshold outlined by a contour if applicable. c)-j) Recovered checkerboards. Lateral and vertical checkerboard offsets, in checkerboard wavelengths, are indicated in the top righthand corner of each panel. Note that the grid overlay for c)-j) indicates the expected boundary of individual checkers within each test board.

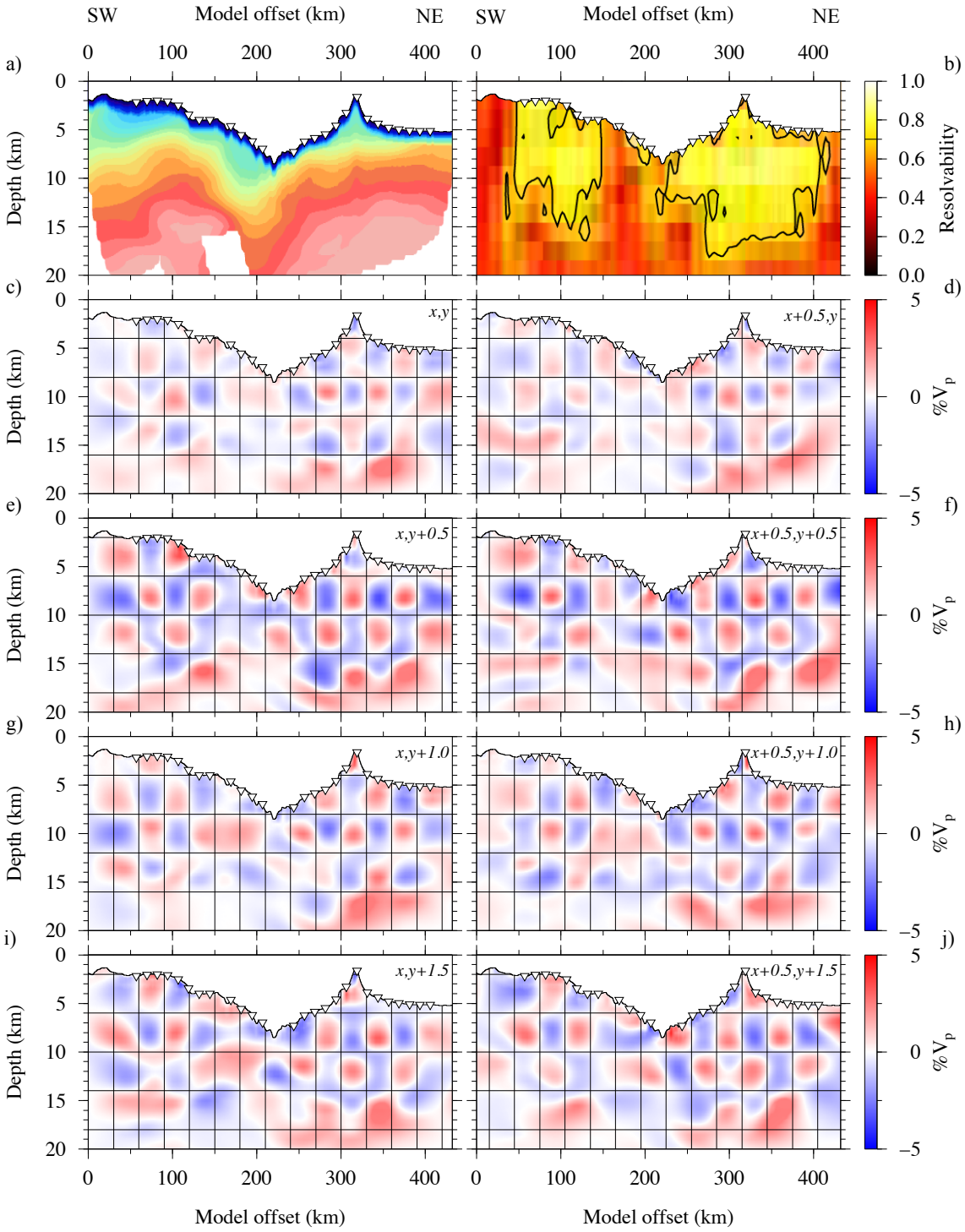

Figure E.5: Anomaly recovery testing using 30 km x 4 km, 5% anomaly, offset checkerboards. a) Final inversion velocity model. b) Average resolvability with regions exceeding the 0.7 threshold outlined by a contour if applicable. c)-j) Recovered checkerboards. Lateral and vertical checkerboard offsets, in checkerboard wavelengths, are indicated in the top righthand corner of each panel. Note that the grid overlay for c)-j) indicates the expected boundary of individual checkers within each test board.

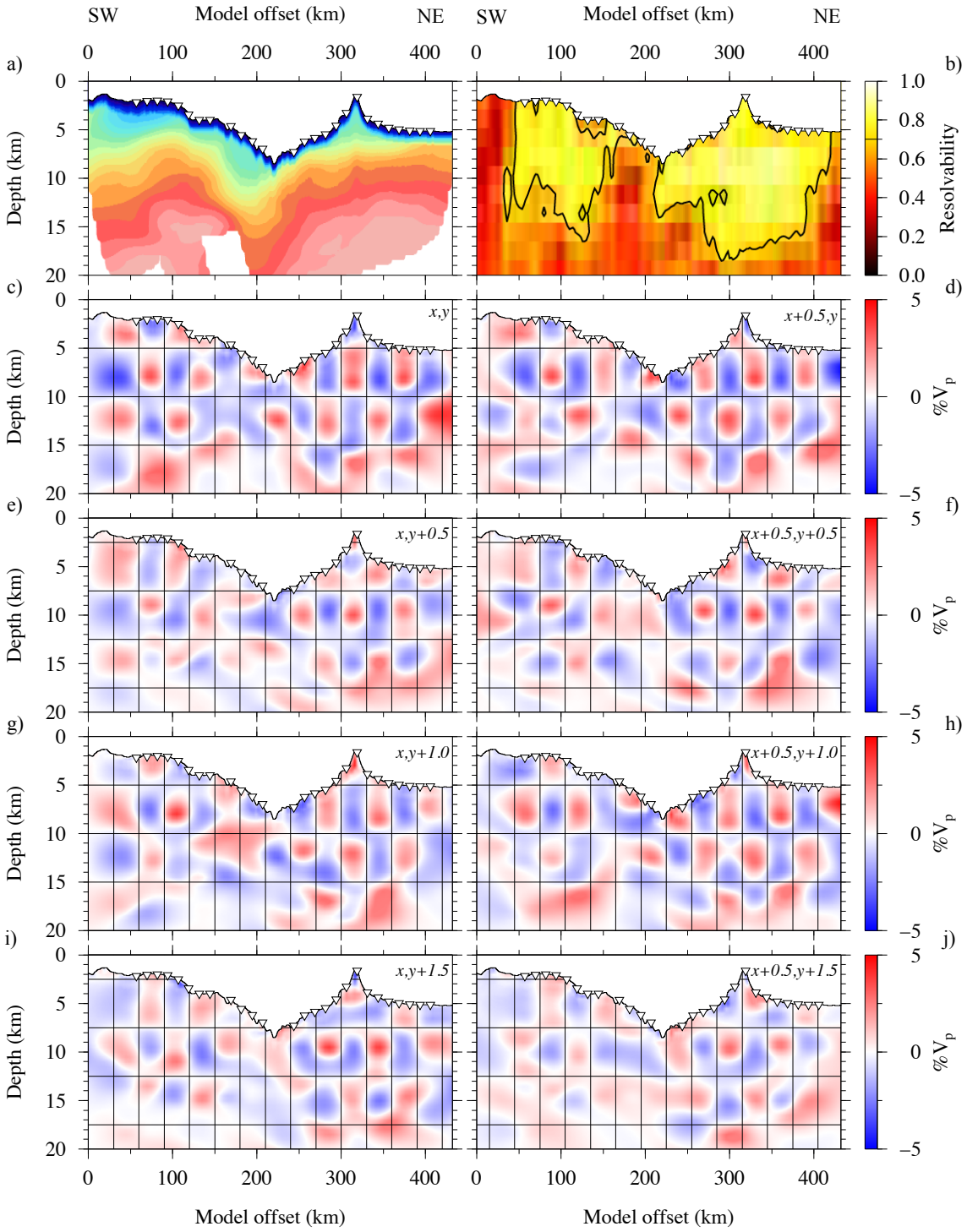

Figure E.6: Anomaly recovery testing using 30 km x 5 km, 5% anomaly, offset checkerboards. a) Final inversion velocity model. b) Average resolvability with regions exceeding the 0.7 threshold outlined by a contour if applicable. c)-j) Recovered checkerboards. Lateral and vertical checkerboard offsets, in checkerboard wavelengths, are indicated in the top righthand corner of each panel. Note that the grid overlay for c)-j) indicates the expected boundary of individual checkers within each test board.

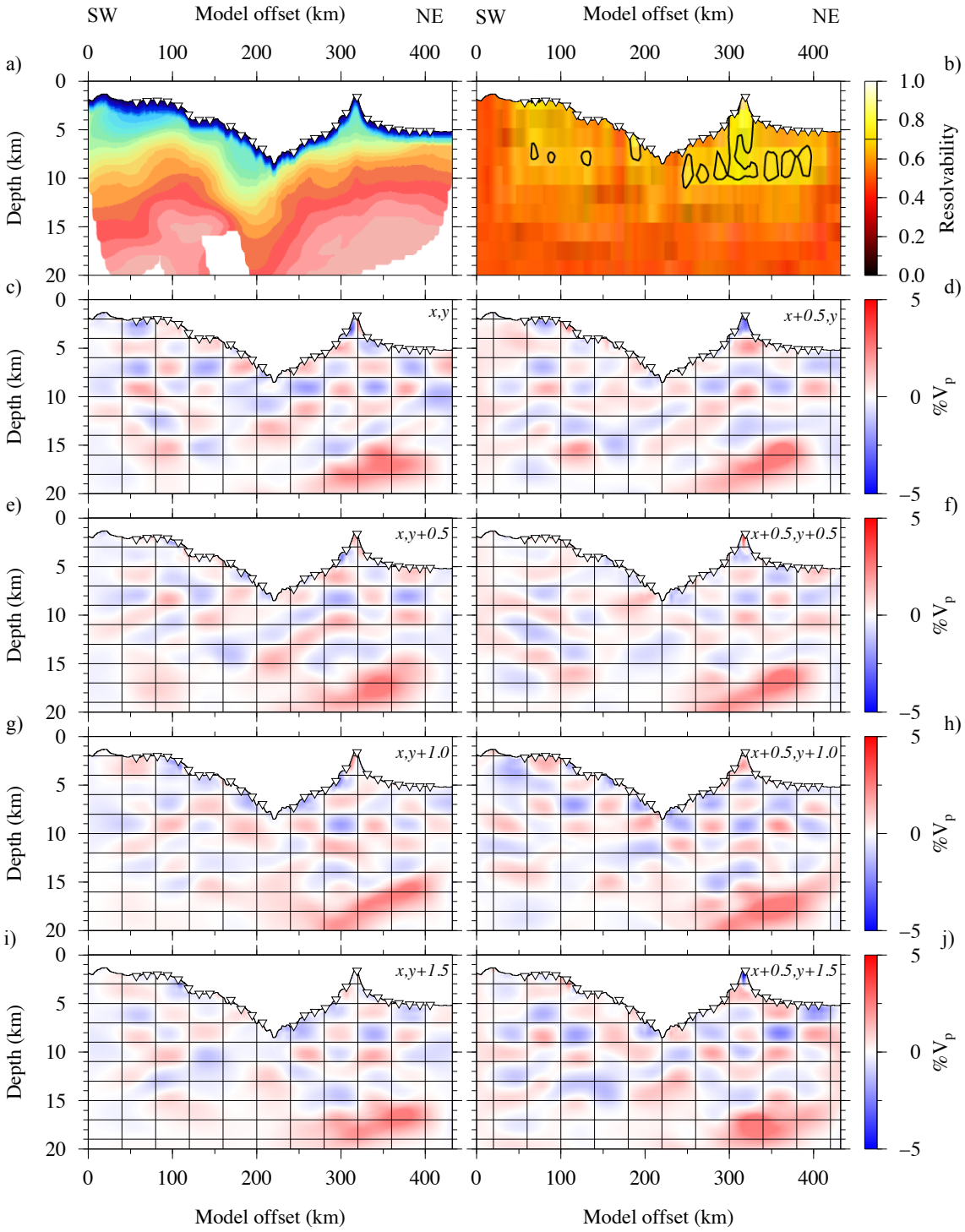

Figure E.7: Anomaly recovery testing using 40 km x 2 km, 5% anomaly, offset checkerboards. a) Final inversion velocity model. b) Average resolvability with regions exceeding the 0.7 threshold outlined by a contour if applicable. c)-j) Recovered checkerboards. Lateral and vertical checkerboard offsets, in checkerboard wavelengths, are indicated in the top righthand corner of each panel. Note that the grid overlay for c)-j) indicates the expected boundary of individual checkers within each test board.

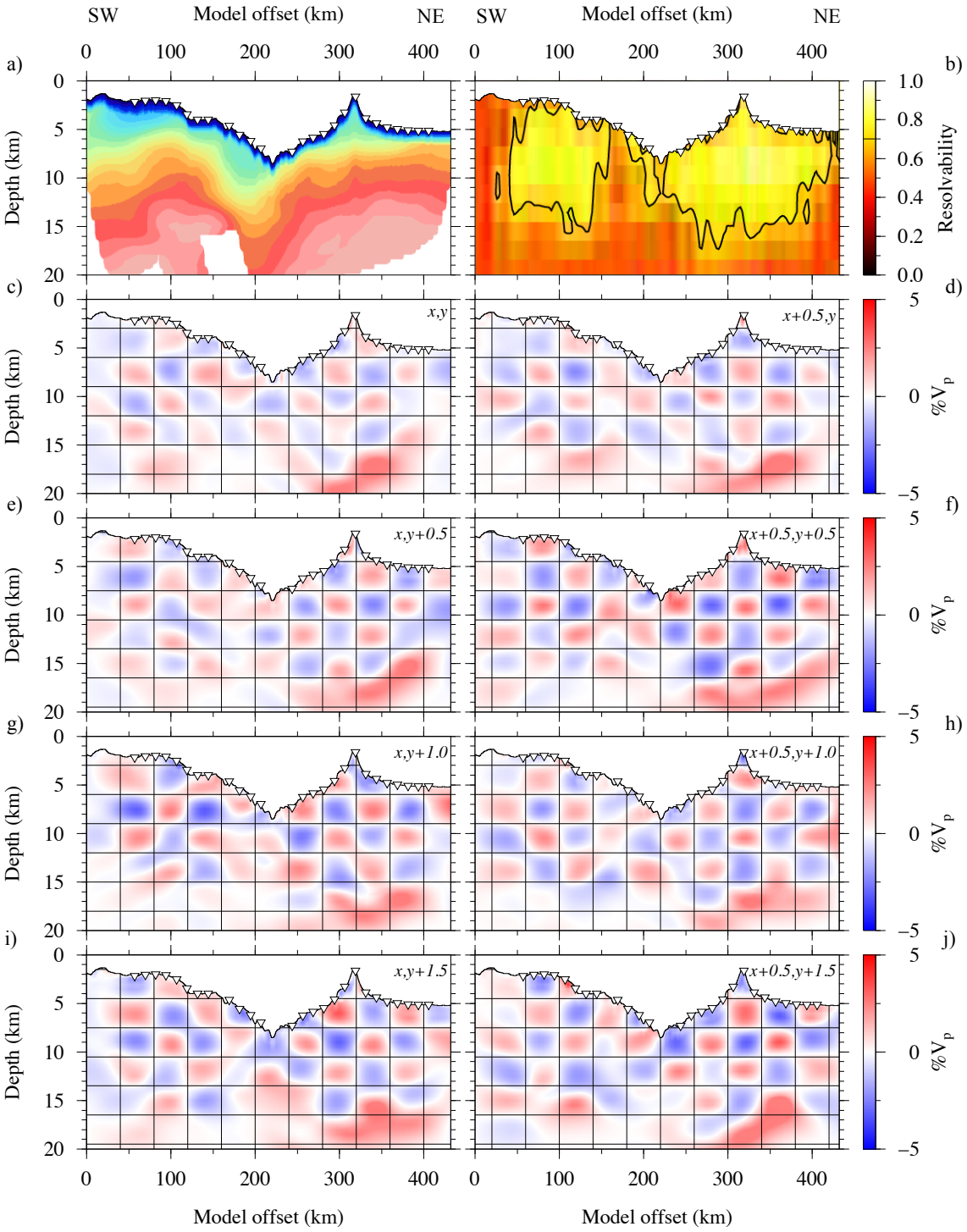

Figure E.8: Anomaly recovery testing using 40 km x 3 km, 5% anomaly, offset checkerboards. a) Final inversion velocity model. b) Average resolvability with regions exceeding the 0.7 threshold outlined by a contour if applicable. c)-j) Recovered checkerboards. Lateral and vertical checkerboard offsets, in checkerboard wavelengths, are indicated in the top righthand corner of each panel. Note that the grid overlay for c)-j) indicates the expected boundary of individual checkers within each test board.

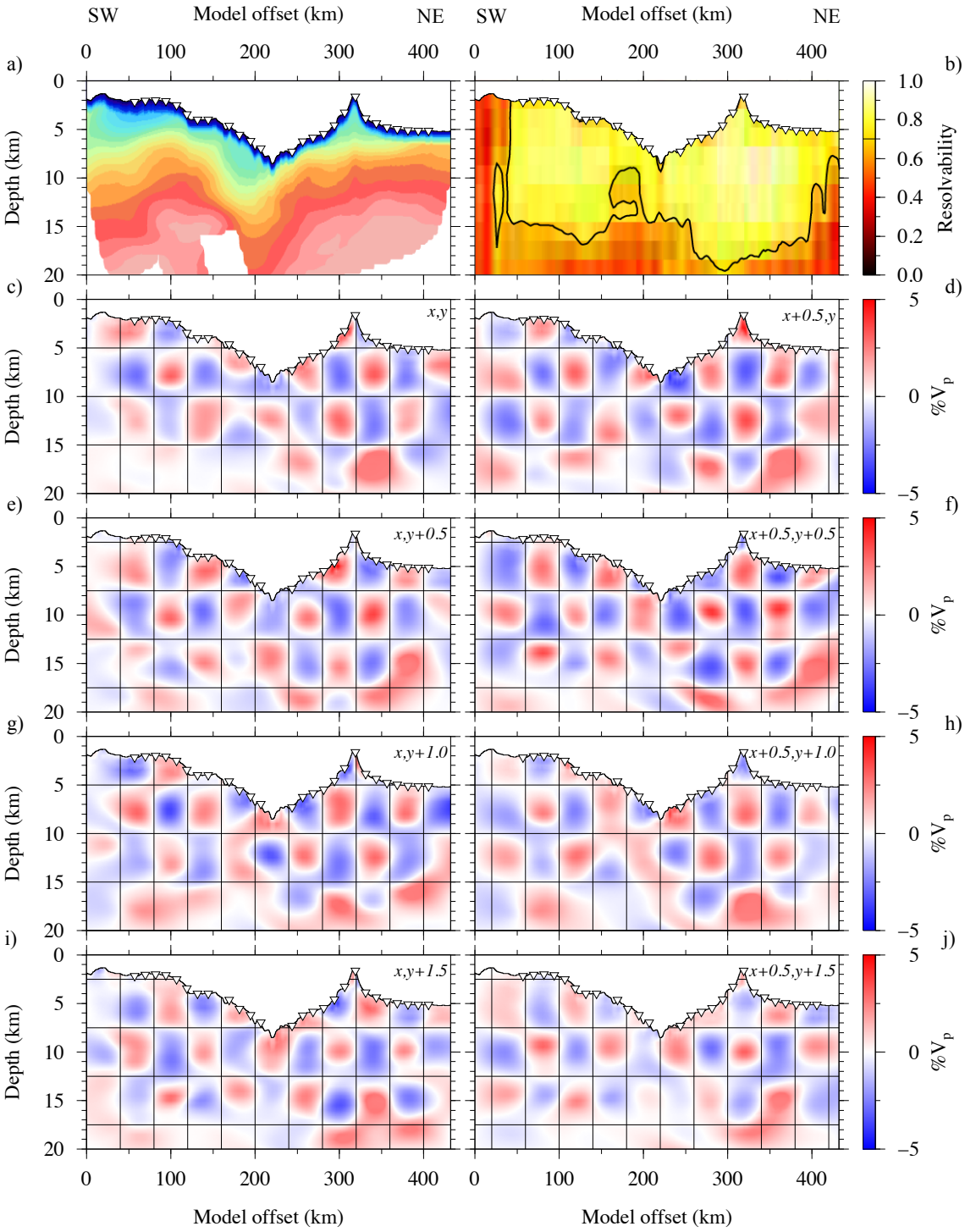

Figure E.9: Anomaly recovery testing using 40 km x 5 km, 5% anomaly, offset checkerboards. a) Final inversion velocity model. b) Average resolvability with regions exceeding the 0.7 threshold outlined by a contour if applicable. c)-j) Recovered checkerboards. Lateral and vertical checkerboard offsets, in checkerboard wavelengths, are indicated in the top righthand corner of each panel. Note that the grid overlay for c)-j) indicates the expected boundary of individual checkers within each test board.

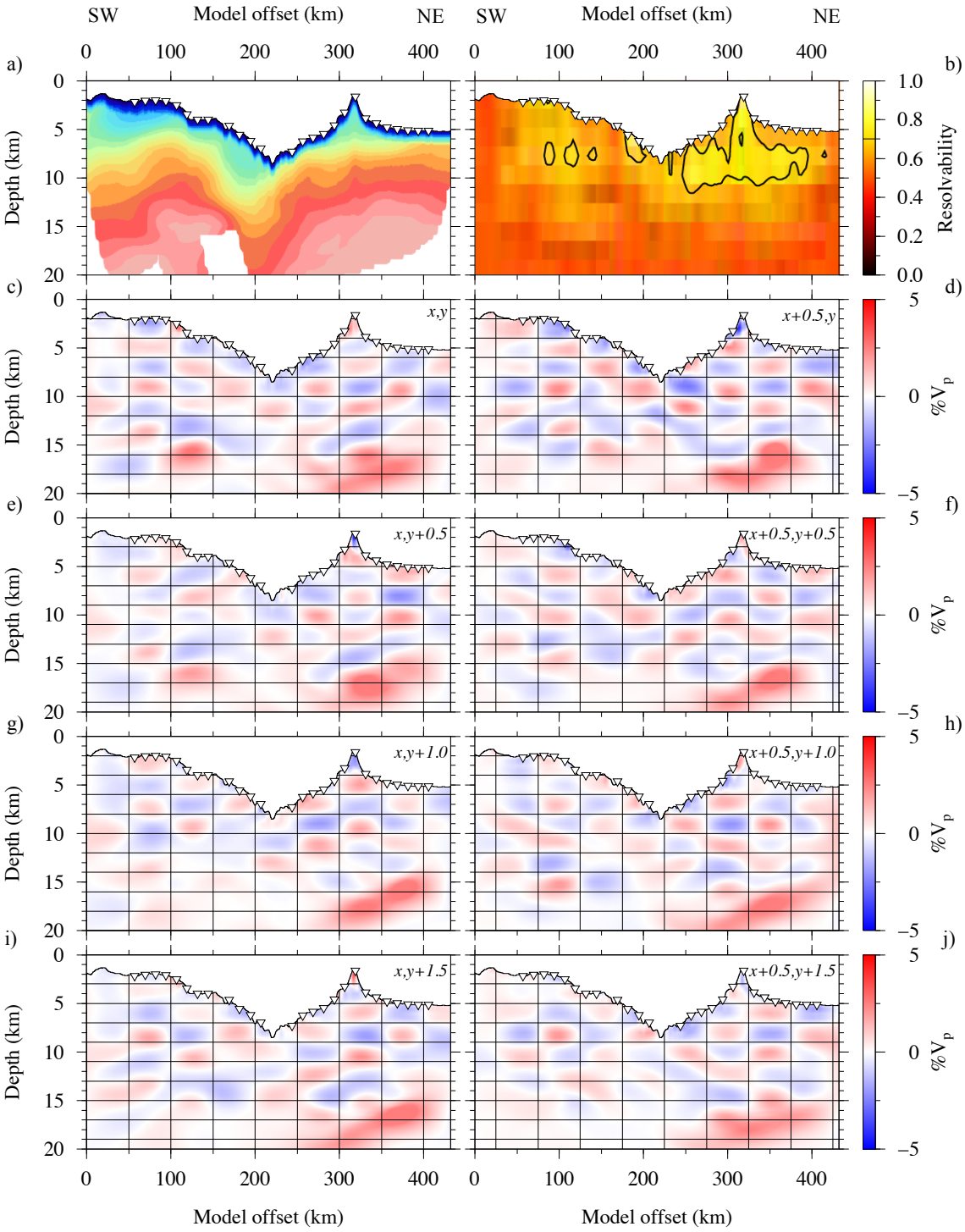

Figure E.10: Anomaly recovery testing using 50 km x 2 km, 5% anomaly, offset checkerboards. a) Final inversion velocity model. b) Average resolvability with regions exceeding the 0.7 threshold outlined by a contour if applicable. c)-j) Recovered checkerboards. Lateral and vertical checkerboard offsets, in checkerboard wavelengths, are indicated in the top righthand corner of each panel. Note that the grid overlay for c)-j) indicates the expected boundary of individual checkers within each test board.

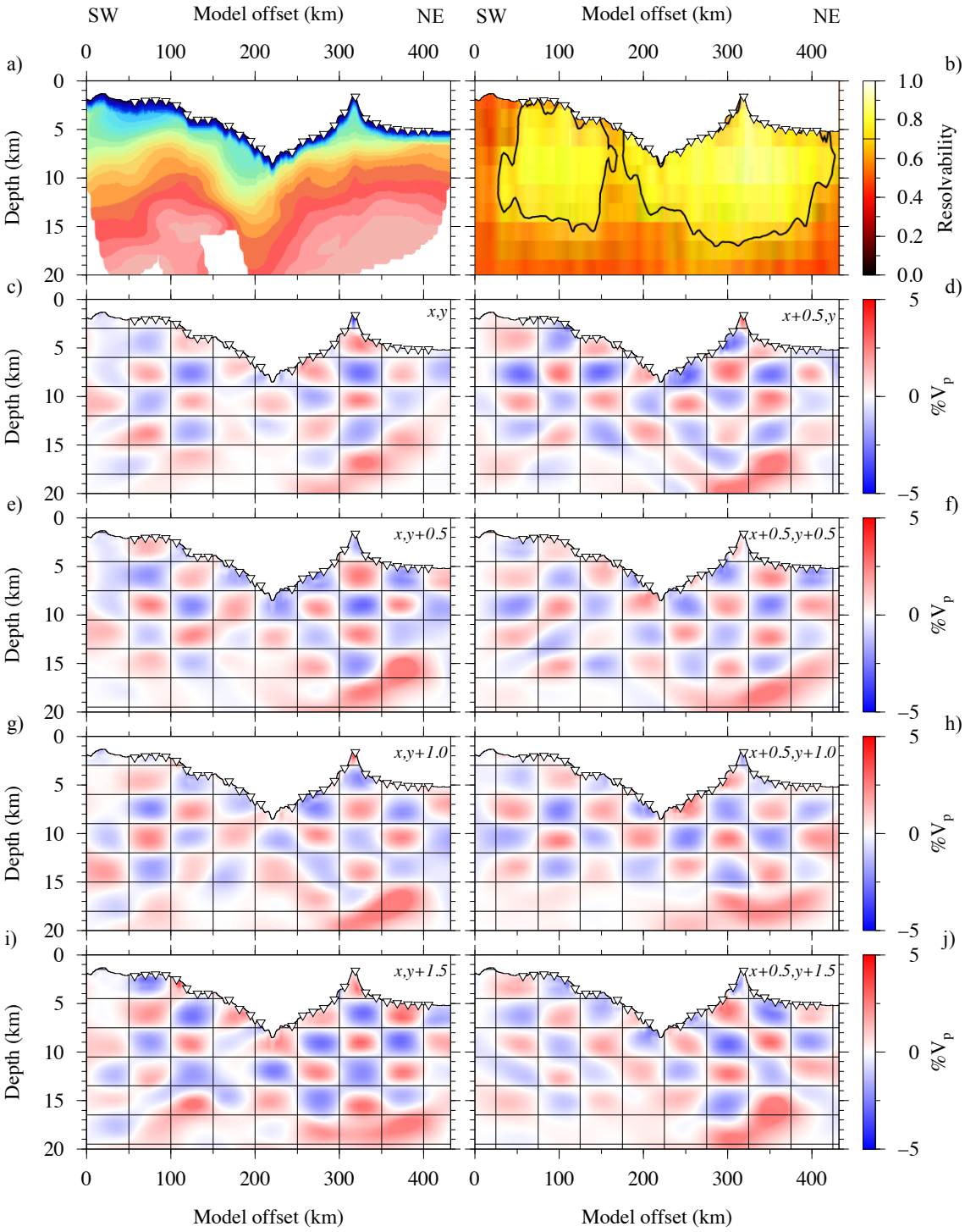

Figure E.11: Anomaly recovery testing using 50 km x 3 km, 5% anomaly, offset checkerboards. a) Final inversion velocity model. b) Average resolvability with regions exceeding the 0.7 threshold outlined by a contour if applicable. c)-j) Recovered checkerboards. Lateral and vertical checkerboard offsets, in checkerboard wavelengths, are indicated in the top righthand corner of each panel. Note that the grid overlay for c)-j) indicates the expected boundary of individual checkers within each test board.

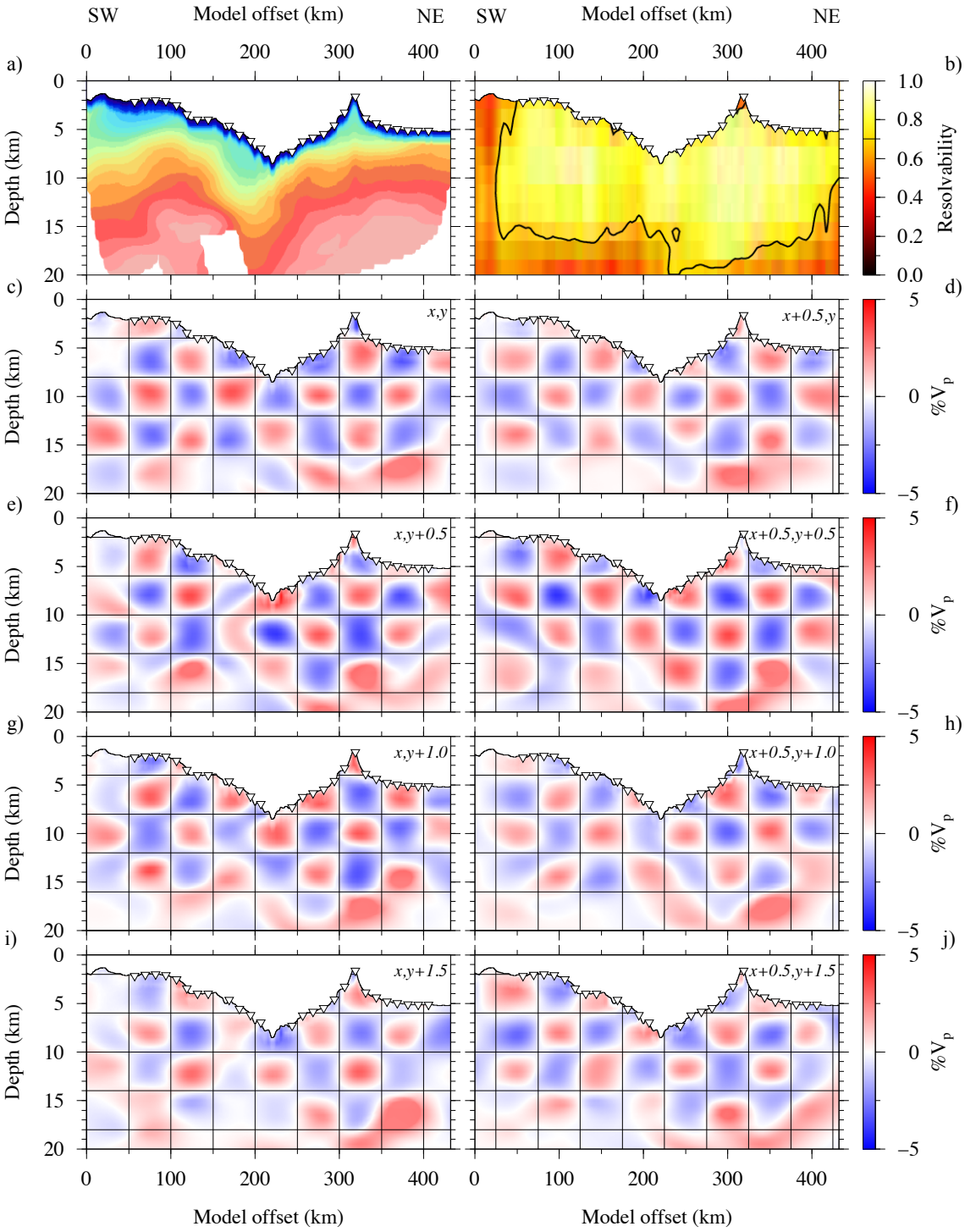

Figure E.12: Anomaly recovery testing using 50 km x 4 km, 5% anomaly, offset checkerboards. a) Final inversion velocity model. b) Average resolvability with regions exceeding the 0.7 threshold outlined by a contour if applicable. c)-j) Recovered checkerboards. Lateral and vertical checkerboard offsets, in checkerboard wavelengths, are indicated in the top righthand corner of each panel. Note that the grid overlay for c)-j) indicates the expected boundary of individual checkers within each test board.

Appendix F

To assess the along-arc crustal variations more objectively and in the context of other global examples the crustal area of each of the published velocity-depth models along the Tonga-Kermadec subduction system was calculated. The models were divided into the upper (2.9-6.0 km s^{-1}), middle (6.0-6.5 km s^{-1}), and lower (6.5-7.4 km s^{-1}) crustal layers between the trench and the edge of the backarc basin, where data were available. For profiles that did not sample crust over this entire region, such as Profile M3 which starts 30 km arcward of the trench, or Profile B that ends at the active volcanic ridge, an additional volume factor was added to the total crustal area based on analogous regions from adjacent profiles. This method neglects the volume of volcanic material present in the extinct backarc along the Lau-Colville ridge, as the crust is not well sampled that far west of the trench, although follows the method used by other authors (e.g. Calvert *et al.*, 2008; Takahashi *et al.*, 2008; 2009). It also fails to consider volcanic material currently being produced at the Kermadec arc south of the 32°S boundary, as the current volcanic line is currently located in the Havre backarc basin, although this material is not thought to be significant based on models presented by Bassett *et al.* (2016).

Table F.1: (Next page) Volumes of the upper, middle, and lower crustal units, as well as the whole crust, per kilometre along arc length (i.e. km^3/km. Data from the Tonga-Kermadec arc was calculated through this study, and examples from other arcs are taken directly from the quoted references. Note that for the Tonga-Kermadec subduction system, Profile Cr (Crawford *et al.*, 2003) was excluded becauses the Moho is not sampled and PC (Robinson, 2017) because the profile did not image a sufficient length of the forearc-arc. Model type definitions are shortened for brevity in the table: 2D and 3D denote 2-dimensional and 3-dimensional, respectively; V and G indicate whether velocity or gravity modelling were used to develop the crustal model; and F and I indicate whether the model was improved using the forward or inversion method, respectively. To account for layer definition inconsistencies and modelling errors, all volumes should be considered with a 10% uncertainty estimate.

Arc, *profile*	Reference	Model type	Upper crust 2.9-6.0 km s^{-1}		Middle crust 6.0-6.5 km s^{-1}		Lower Crust 6.5-7.4 km s^{-1}		Total crust 2.9-7.4 km s^{-1}
			Vol.	%	Vol.	%	Vol.	%	Vol.
Tonga-Kermadec									
Tonga, *P02*	Contreras-Reyes *et al.* (2011)	2D V I	823	25	503	15	1938	59	3264
Tonga, *PA*	Stratford *et al.* (2015)	2D V F	950	32	299	10	1753	58	3002
Tonga average			887	28	401	13	1846	59	3133
Kermadec, *PB*	Funnell *et al.* (2017); this study	2D V F	647	31	467	22	1006	47	2120
Kermadec, *M4*	Bassett *et al.* (2016)	2D V F	984	49	140	7	889	44	2013
Kermadec average (<32°S)			816	40	304	14	948	46	2067
Kermadec, *M3*	Bassett *et al.* (2016)	2D V F	439	26	278	16	986	58	1703
Kermadec, *M2*	Bassett *et al.* (2016)	2D V F	987	51	123	6	832	43	1942
Kermadec average (>32°S)			713	38	201	11	909	50	1823
Izu-Bonin-Mariana									
Izu	Suyehiro *et al.* (1996)	2D V F	-	-	-	25	-	>30	-
Izu	Takahashi *et al.* (2008)	2D V F/I	732	18	963	23	2455	59	4150
Bonin	Takahashi *et al.* (2009)	2D V F/I	465	17	715	26	1547	57	2727
Mariana	Takahashi *et al.* (2008)	2D V F/I	588	23	591	23	1349	53	2528
Mariana	Calvert *et al.* (2008)	3D V I	646	27	369	15	1376	58	2391
Aleutian									
Aleutian	Grow (1973)	2D G F	-	-	-	-	-	-	2300
Aleutian	Holbrook *et al.* (1999)	2D V	-	-	-	-	-	-	5500
South Sandwich									
South Sandwich, *line 34*	Larter *et al.* (2003)	2D G F	-	-	-	-	-	-	2132
South Sandwich, *line 36*	Larter *et al.* (2003)	2D G F	-	-	-	-	-	-	2582